Modélisation du stockage de chaleur par changement de phase d'alliages à composition binaire soumis à un refroidissement contrôlé

Abraham Moreno Reyna

To cite this version:

Abraham Moreno Reyna. Modélisation du stockage de chaleur par changement de phase d'alliages à composition binaire soumis à un refroidissement contrôlé. Mécanique [physics]. Université de Bordeaux, 2018. Français. NNT : 2018BORD0012 . tel-02102859

HAL Id: tel-02102859

https://theses.hal.science/tel-02102859

Submitted on 17 Apr 2019

THÈSE PRÉSENTÉE

POUR OBTENIR LE GRADE DE

DOCTEUR DE
L'UNIVERSITÉ DE BORDEAUX

ÉCOLE DOCTORALE DES SCIENCES PHYSIQUES ET DE L'INGÉNIEUR SPÉCIALITÉ MÉCANIQUE

Par Abraham MORENO REYNA

MODÉLISATION DU STOCKAGE DE CHALEUR PAR CHANGEMENT DE PHASE D'ALLIAGES À COMPOSITION BINAIRE SOUMIS À UN REFROIDISSEMENT CONTRÔLÉ

Sous la direction de : Cédric LE BOT

(Co-Encadrant : Elliott BACHÉ)

Soutenue le **9 Novembre 2018**

Membres du jury :

Mme. PALOMO del BARRIO Elena	Professeur des Universités	Université de Bordeaux	Pésidente
M. BEDECARRATS Jean-Pierre	Professeur des Universités	Université de Pau	Rapporteur
M. GINESTET Stéphane	Maître de Conférences, HDR	INSA Toulouse	Rapporteur
M. ZALOZNIK Miha	Chargé de recherche	Université de Lorraine	Examinateur
M. AZAIEZ Mejdi	Professeur des Universités	Bordeaux-INP	Examinateur
M. LE BOT Cédric	Maître de Conférences, HDR	Bordeaux-INP	Dir. de thèse
M. BACHE Elliott	Ingénieur de recherche	Solute, Madrid Espagne	Invité

ABSTRACT

THERMAL STORAGE MODELING IN BINARY ALLOY PHASE CHANGE MATERIALS SUBMITTED TO A CONTROLLED COOLING RATE

Latent Heat Thermal Energy Storage (LHTES) shows high storage density compared to sensible thermal systems. For high temperature applications, the use of alloys as phase change materials presents many advantages. Principally, varying alloy composition allows controlling the storage\discharge of thermal energy through an expected temperature range (defined by the heat source), and the high thermal conductivity gives suitable heat transfer properties to the system that receives/supplies the energy. However, some systems need a specific temperature range to correctly operate. In such conditions, subcooling (also known as undercooling) and segregation are undesirable phenomena in alloys when they are used as PCM. In the present work, we propose a method to predict the latent heat release during phase transformation of a binary alloy submitted to a controlled cooling rate, including subcooling, segregation and variation of composition. This thesis describes the physical models that apply when heat is released from such a material. We take into consideration the cooling rate applied to the PCM, the solidification velocity, convective phenomena, melting temperature and subcooling. In the present work, phase diagrams and the CALPHAD methodology are used to determine the temperature range for phase change (or constant temperature value for isothermal transformation) by minimizing the Gibbs equilibrium energy. The Gibbs free energy minimization has been implemented in a homemade numerical code. The material can be screened with different compositions for equilibrium or off-equilibrium solidification allowing quick selection of the optimal material for the specific heat source. In the proposed method, the solidification velocity is obtained from the cooling rate. Then, variation in microstructure is driven by the solidification velocity using the local non-equilibrium diffusion model. Based on the local nonequilibrium model that depends on the partition coefficient variation, the subcooling degree, wich is derived from the applied cooling rate is predicted. A bibliographic study has been carried out and a numerical comparison has been undertaken to ensure the capacity of our code to reproduce the phase change of various materials that include phenomena such as subcooling and recalescence. The results highlight that the cooling rate is one of the most important parameters in the performance of the thermal storage, having a large effect on segregation and subcooling degree. Moreover, we show the influence of partition coefficient on the time evolution of solid fraction, considering a constant or a composition-dependent value. We can conclude that the latent heat release can be correctly predicted provided that the method correctly predicts the phase diagram and the variable partition coefficient. This work helps to accelerate the design and development of thermal storage systems and lays the foundation to continue exploring other kinds of materials (e.g. paraffins).

Keywords: Latent heat, thermal energy storage, CALPHAD, phase change, undercooling, subcooling, cooling rate, solidification rate, segregation, alloy phase change, Gibbs energy, phase diagramme

I2M - Institut de mécanique et d'ingénierie –
Université de Bordeaux
ENSCBP bât A, 16 avenue Pey-Berland, 33607 PESSAC Cedex

RÉSUMÉ

Modélisation du stockage de chaleur par changement de phase d'alliages à composition binaire soumis à un refroidissement contrôlé

La thèse est centrée sur la modélisation de la physique du comportement d’un alliage binaire et l’implémentation du meilleur modèle mathématique pour simuler le changement de phase liquide solide en tenant compte de la vitesse de refroidissement, la vitesse de solidification, la ségrégation, la convection naturelle et la surfusion afin d’optimiser la capacité de stockage de chaleur d'un tel matériau. Dans le présent travail, les températures pour lesquelles le changement de phase s'opère sont estimées grâce aux diagrammes des phases et la méthodologie CALPHAD qui retraduisent les différentes phases d'un alliage binaire, y compris la transformation isotherme. Pour cela, la minimisation de l'énergie de Gibbs est résolue dans un code de calcul développé à cette occasion et aboutit à l'identification des phases stables du matériau. Pour un intervalle de température souhaite le code permet d'estimer rapidement la décharge de chaleur pour la composition de l'alliage sélectionné en équilibre ou hors équilibre. Dans la méthode proposée, la vitesse de refroidissement du système permet de calculer la vitesse de solidification. Puis, celle-ci établit la relation entre la cinétique globale et la macrostructure. Basé sur le modèle de non-équilibre local, qui dépend de la variation du coefficient de partition, le degré de surfusion est prédit à partir de la vitesse de refroidissement appliquée. Une étude bibliographique a été réalisée pour amener une comparaison numérique et assurer la capacité de notre méthode à reproduire le changement de phase, en incluant des phénomènes spécifiques tels que la surfusion et la recalescence.

Mots clés: Chaleur latent, stockage d’énergie thermique, CALPHAD, changement de phase, surfusion, vitesse de refoidissement, vitesse de solidification, segregation, changement de phase des alliages, énergie de Gibbs, diagramme de phase.

I2M - Institut de mécanique et d'ingénierie
Université de Bordeaux
ENSCBP bât A, 16 avenue Pey-Berland, 33607 PESSAC Cedex

ACKNOWLEDGEMENTS

This work would not have been possible without the financial support of the National Council of Science and Thecnology (**CONACYT**), public agency of Mexico. This work was carried out in the I2M (Institut de Mécanique et d'Ingénierie de Bordeaux) at the TREFLE laboratory (Transferts Ecoulements Fluides Energétique). I wish to express my deep gratitude to all the TREFLE laboratory who have made possible the accomplishment of this work.

I would like to thank my advisor Cédric Le Bot for his kindness, generous guidance and assistance. My sincerely gratitude and appreciation to my co-advisor Elliott Baché. Without their persistent guidance and motivation this dissertation would not have been possible. Thanks to both, my friends.

Quisiera agradecer a mis amigos con quienes comenzamos la aventura en la maestría, Luis, Diego, Juan de Dios, Arturo y Memo; con quienes he encontrado una parte de mi familia. Gracias por su soporte, ayuda y hacer este viaje increíble y emocionante. Quisiera agradecer especialmente a Luis que en cada momento he encontrado su apoyo e increíble amistad. También quisiera agradecer a Samantha por estar presente con su soporte y ánimos, los viajes y momentos vividos, además de su increíble amistad a lo largo de los años.

Incluyo en estos agradecimientos a Arely que desde la universidad hemos sabido seguir siendo los mejores aliados y testimonios en todas nuestras aventuras, agradesco sus palabras y consejos que me han ayudado tanto a lo largo de este tiempo. También me es imposible olvidar que durante el desarrollo de mi doctorado he encontrado a personas fantásticas, en especial quisiera agradecer a Janeth por mostrarme la bondad y alegría de Burdeos así, como los instantes por los que uno debe sonreír, con suerte el universo traerá una taza de té.

También quisiera dar mi más sincero y profundo agradecimiento a Laurence por su infinito cariño, ayuda y comprensión; especialmente en la recta final de mi trabajo de tesis en donde sé que no ha sido sencillo; en donde se ha demandado tolerancia y sobrellevar las diversas dificultades que implico terminas este trabajo de tesis. Por todo eso y más, gracias por estar conmigo.

Y finalmente quisiera agradecer a mi madre, padre y hermano. Innumerables los motivos para agradecerles su incondicional apoyo, sus palabras de aliento, su compañía en esta aventura, su presencia, su guía, su esfuerzo, su dedicación y un largo etcétera de motivos por los cuales les podría agradecer. Pero principalmente gracias por su infinito amor y su constante sostén en cada proyecto que he realizado. Solo gracias a ellos podría explicar por qué estoy aquí, solo gracias a ellos podría explicar la culminación de este trabajo de tesis. A ellos tres, gracias con infinito amor, respeto y admiración.

1. Contents

List of Figures

Nomenclature

ΔG	Driving force	Equation	1	
ΔS	Difference in entropy	Equation	2	
ΔH	Difference in enthalpy	Equation	4	
G	Gibbs free energy	Equation	10	
μ	Chemical potential	Equation	13	16
Gm	Gibbs free energy per mole	Equation	14	
Ω	Excess gibbs free energy	Equation	14	
k	Partition coefficient in equilibrium	Equation	17	
k_v	Partition coefficient in function of solidification velocity	Equation	61	
C	Composition			
Co	Initial composition			
C_{SM}	Maximum solubility in the solid solution			
C_s^k	Composition non-equilibrium			
m	Liquidus slope			
m_{Lv}	Non-equilibrium liquidus line slope	Equation	63	
fs	Solid fraction			
f_L	Liquid fraction			
V	Velocity			
Vs	Solidification velocity			
V_L	Velocity vector in liquid phase			
V_D	Limit diffusivity speed			
CR	Cooling rate			
TMK	Trivedi-Magnin-Kurz model			
LNDM	Local non-equilibrium diffusion model			
CGM	Continuous growth model			
REV	Representative element volume			
fl_r	Solid fraction in a REV			
T^*	Continuous temperature			
ΔTu	Undercooling degree			
ΔT_{scp}	Narrow interval of temperature for Cp_{ap}			
ΔT_R	Curvature undercooling			
ΔT_c	Constituitional undercooling			
ΔT_k	Kinetic undercooling			
ΔT_T	Thermal undercooling			
Cp	Heat capacity			
Cp_{ap}	Apparent heat capacity			
AHCM	Apparent heat capacity method			

R	Universal gas constant		
D	Diffusion		
P	Static pressure		
v	Flow velocity	Equation	35
ρ	Density		
β	Volumetric expansion coefficient	Equation	35
g	Acceleration of gravity		
γ	Thermal conductivity		
δ	Diffusion layer	Equation	60
Iv	Ivantsov function	Equation	66
Pc	Solutal péclet number	Equation	65
P_T	Thermal péclet number	Equation	71
a	Molecular interatomic		
Γ	Gibbs-Thomson coefficient		
α	Thermal diffusivity		
µ	Dynamic viscosity		
L	Latent heat		
L^{cp}	Latent heat released		
L^{ab}	Latent heat of binary alloy		
t	Time		
S	Source term, heat generation	Equation	51
F	Source term for the porous medium	Equation	37
Ils	Interface liquid/solid	Equation	52
CC	Cell center position	Equation	53

Subscript

s	Solid
L, l	Liquid
A, a	Element A
B, b	Element B
M	Melting temperature
V	Solidification velocity
o	Reference value
e	Eutectic point
ap	Apparent heat capacity
ls	Liquid-Solid phase
x	X-axis direction
y	Y-axis direction

Superscript

a	Element A
b	Element B

Chapter 1 Introduction and context

Since 2012, in France industry represents 21 % of the total energy consumption, ranking third after residential buildings and transport. 71 % of this consumption is devoted to heat production, mainly in the food industry through ovens and dryers that allow food transformation processes[1]. The low efficiencies of thermal processes, that can reach up to 50 % or 60 %, lead to a heat loss considered as waste heat, since it has been produced but does not participate in the desired processes[1], [2]. Waste heat is a global term corresponding to the heat lost by a process. This heat may be possibly recovered and used under another form. For ovens or dryers, for which the efficiency remains relatively low (as low as 50%), the waste heat could be recovered and could be introduced in other industrial activities to limit energy consumption. Figure 1 shows the temperature at which waste heat is rejected by industrial processes and confirms the necessity to limit the consumption.

Two kinds of waste heat can be mentioned [1]: High temperature waste heat concerns applications with an operating temperature above 300°C, like the steel industry that needs to supply high heat to form materials. Such applications are subjected to heat recovery. On the contrary, low temperature applications, like chemistry applications, paper or food industries, have less potential heat recovery which represents a source of future improvement. The most difficult waste heat sources to recover are the diffuse ones, due to low insulation. As shown in Figure 1, thermal rejection appears for a large range of temperatures. The ADEME Agency [3](Agence de l'Environnement et de la Maitrise de l'Energie) devoted to environment energy control, estimated that the annual waste heat in France, due to applications at temperatures above 100°C, reaches 51TWh, with 50 % of waste heat due to 100°C to 200°C temperature applications.

Reuse of the waste heat can be accomplished by two methods. The first one consists in recovering heat. The waste heat produced from a given process can be supplied to a similar process, operating at a lower temperature. The second one is thermal storage. When waste heat repurposing is not possible, its reuse can be considered through heat storage systems that capture energy for later use. Storage systems can be based on sensible heat when related to a

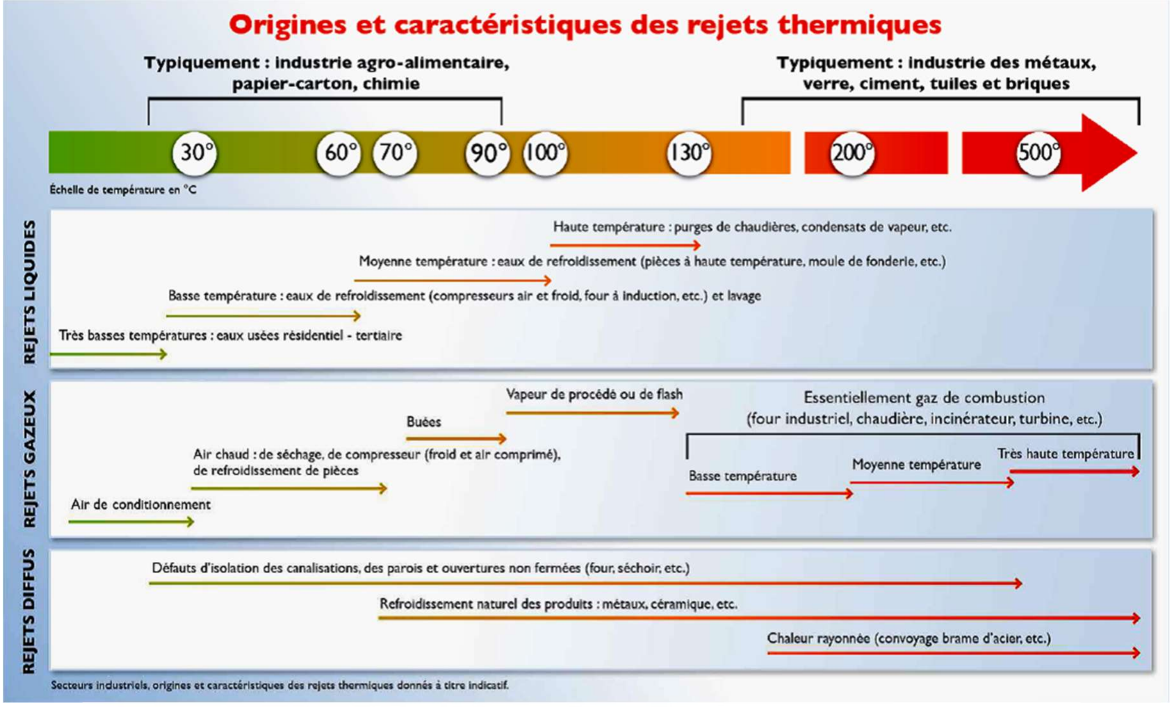

Figure 1 Typical temperature range for waste heat processes in France industry [1]

temperature evolution, or latent heat if the discharge is expected to occur at a constant temperature. In general, sensible heat storage, where charging and discharging are obtained by varying the system's temperature, is used more often than latent heat storage, where the phase change can occur at a constant temperature or through a temperature range. The two storage systems are of interest but they don't show the same thermal density. In both scenarios, however, the heat can be transported to another place. In both scenarios, however, the heat can be transported to another place.

Metal, glass and cement industries operate at high temperatures (above 400°C) and recovery of the generated waste heat is usually neglected [4]. For this waste heat, reuse is important, not only from an economic point of view, but also for environmental considerations. Nowadays, thermal energy storage and transport are key points of responsible industries development. Transportable high temperature latent heat storage tanks can be used to feed industrial processes requiring energy at a lower temperature. For example, the industrial waste heat represents an interesting heat supply for residential buildings, where temperatures of around

Figure 2 Commercial LHTES made by Latherm

50°C to 70°C are generally needed [2]. As another example, during winter, heat can be use on farming applications to avoid freezing of crops.

Nowadays, different heat storage and transport systems are being developed. They are based on the use of heat exchangers immersed in a phase change material (PCM) that stores and discharges latent heat during melting or solidification. One of the first transportable heat storage systems was developed and designed in Japan in 2008 [5]. This system is fed by thermal oil that serves as heat transfer fluid and erythritol that composes the material dedicated to heat storage with a capacity of 5.3GJ. The melting point of such a system corresponds to a temperature of 110°C, which allows waste heat recover above 180°C. This heat can be discharged in applications where the operating temperature is up to 90°C, which is largely convenient for residential buildings for example. These systems, (also know as trans-heat system), are used, when the heat source and heat demand are not on the same location.

The German company Latherm [6] has started to investigate economical advantages of such a system. They have found that a PCM characterized by a melting temperature of 60°C helps to store waste heat produced by sources at temperatures above 100°C. They commercialize this waste heat into transportable heat storage (see Figure 2). Most storage systems are based on a temperature range that allows benefiting both latent and sensible heats, so that the combination of the two storage modes supplies heat for applications requiring temperatures below 50°C, like swimming pools or office buildings.

Of the two possibilities, the more efficient way to store energy is based on latent heat thermal energy storage (LHTES). The operating principle of latent heat storage is based on the heat absorption and subsequent release through phase change materials (PCM).

1.1 Latent heat thermal energy storage

In Figure 3, the stored heat as function of the temperature is illustrated, comparing a typical phase change material with an one, where only sensible heat is stored. Basically, for a similar temperature difference, the phase change material involves a higher stored heat than the inertial one, especially on a small temperature scale around the melting temperature Tm. While the PCM is totally solid (temperature below Tm) or liquid (temperature above Tm), the material efficiency is related to the heat capacity Cp, by storing or releasing heat through a temperature variation (see Figure 3). Consequently, this kind of charge or discharge depends on the operating temperature range. When the material melts or solidifies, the captured or released heat corresponds to the latent heat, which is a material property.

Selecting a PCM and developing a LHTES is not an easy task. The use of these materials has three requirements: i) a melting point in the desired temperature range; ii) an efficient heat exchanger to transfer heat and iii) a suitable container compatible with the PCM. Consequently, the design of an efficient storage process involves the understanding of three essential subjects: phase change materials, container materials and heat exchangers.

Different type of storage system [7] are involved in the development of a latent heat storage system as shown in Figure 4. It shows how the selected material has an important role to develop a heat exchanger. Firstly, the PCM is chosen from its working temperature range, desirable thermophysical properties, kinetics and chemical stability. PCM selection can define

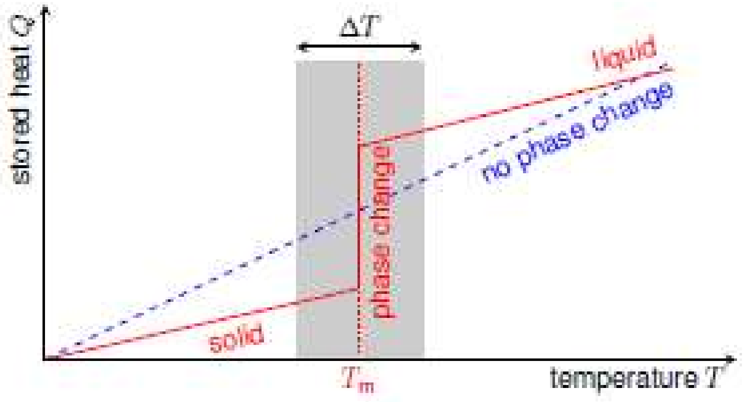

Figure 3 Comparison of heat stored between a PCM material and a sensible heat storage material

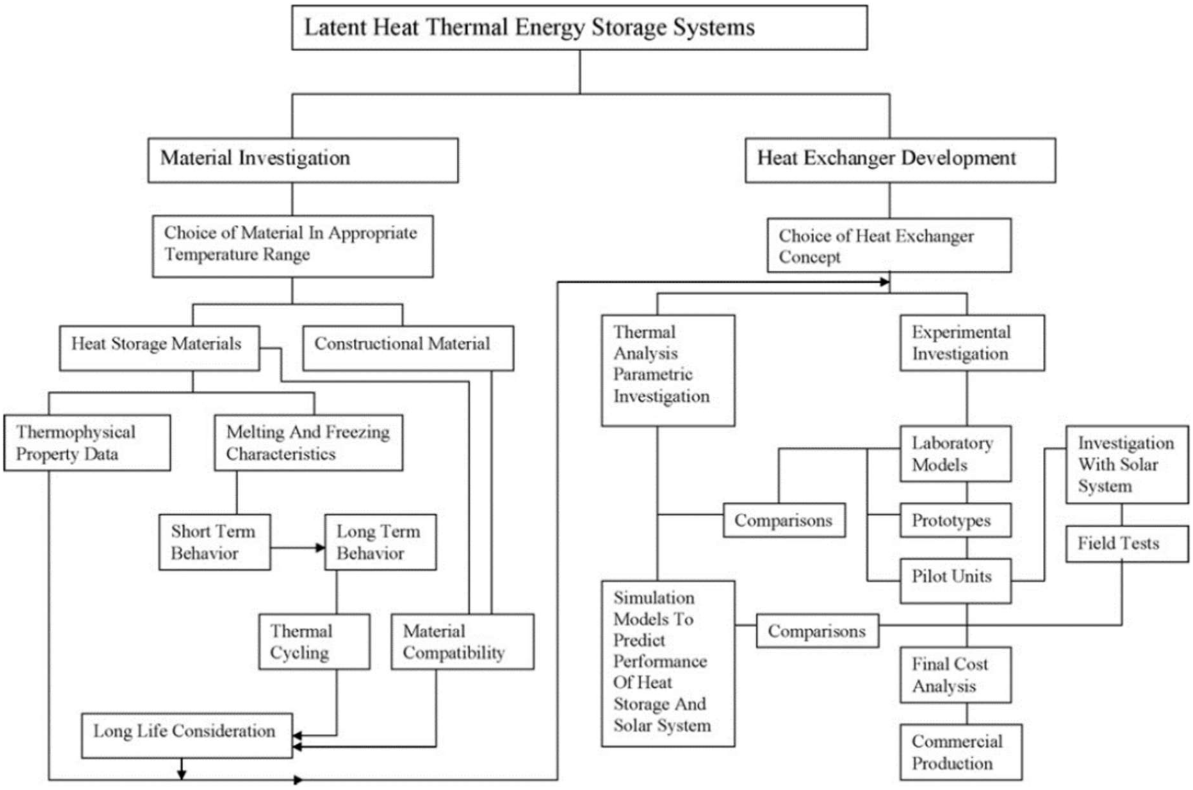

Figure 4 Algorithm of the different stages involved in the development of a LHTES [5]

the success of the thermal energy storage system. For example, if the PCM transition temperature is above the charging temperature, the material can exploit all its capacity to store energy. On the other hand, if the PCM transition temperature is under the cooling temperature (discharge), only a few degrees are sufficient to interfere with a proper heat extraction, resulting in an inefficient LHTES.

A suitable PCM will give the best heat charge and discharge, with the following characteristics[8]: maximal thermal density (stored energy per unit mass), adequate charge/discgarge power to ensure an effective heat transfer, low material cost and low toxicity of the material. It will also have adequate thermophysical properties, principally high thermal conductivity of the PCM and thermochemical stability to keep the same thermal density over charge/discharge cycles. Generally, such a criterion is obtained through a heat exchanger immersed in the PCM combined with a suitable heat transfer fluid that directs the heat flow. Most of PCM used for temperatures below 300 °C have low thermal conductivity, which must be improved by means of a suitable conductive system.

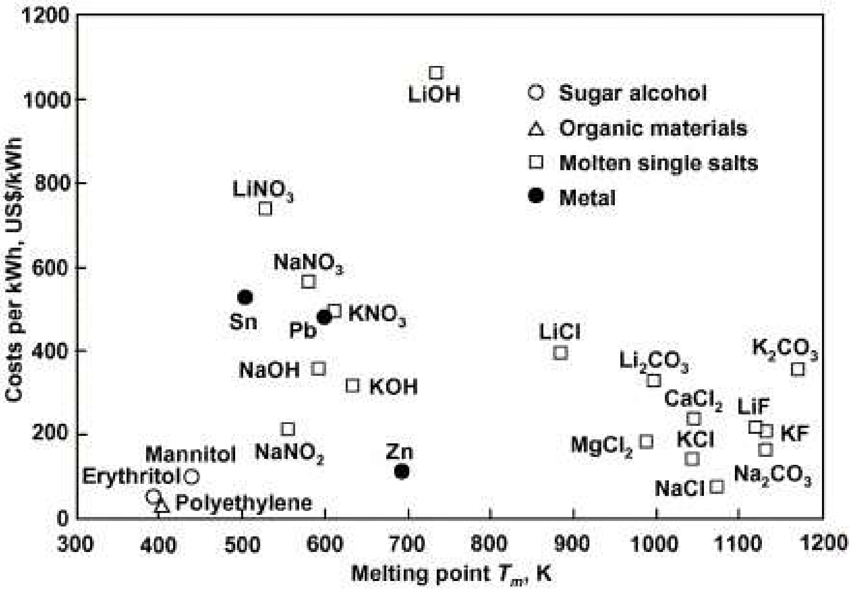

Figure 5 PCM cost and its melting temperature [10]

For LHTES, the melting temperature Tm is inside the operating temperature range. These storage systems are particularly interesting for systems where the operating temperature is around Tm and the stored heat is nearly entirely supplied during phase change. In such a situation, the main thermal properties or constraints can be identified:

- The melting/solidifying point must be within the operating temperature range to charge/discharge using latent heat.
- The PCM must have a large latent heat and specific heat.
- The PCM must have a high thermal conductivity to transfer heat efficiently.
- The volume expansion of the PCM during phase change must be low as the PCM is generally in a container that should not be submitted to constraints.

Another criterion to consider while designing a storage system that uses latent heat is the cost. Various PCMs are presented following their melting temperature and their media cost per kWh [9] as shown in Figure 5. This graphic shows that the concerned PCMs exhibit a large range of melting temperatures, with a large range of costs, so that various waste heat storage systems may benefit from PCM. The PCM must be carefully selected to be financially feasible.

On the other hand many authors have analyzed PCMs and categorized them by their melting temperature and their latent heat, as shown in Figure 6.[10]This figure exhibits some materials with a melting temperature above 600°C. They can be found in solar plant applications that involve high heat concentration and high temperature systems to convert heat into electricity via heat transfer fluids under pressure. On the contrary, paraffins are usually used for systems such as heat exchangers for food applications that require a moderate temperature as their melting temperature does not exceed 120°C.

The paraffins mentioned above are not the only PCM considered for heat storage. The advantages of metals and alloys as PCMs are their higher heat storage capacity per unit volume and their higher thermal conductivity [11]. Metals and alloys are expensive but when space availability is a criterion, they become one of best choices for LHTES due to their higher thermal density. Also, they represent good sensible heat storage materials as liquid or solid metal and their latent heat can be close to paraffins or even higher (≈565 [kJ/kg] for AlSi12). Another technical advantage is that alloys have a large range of melting temperature as can be seen in Figure 5.

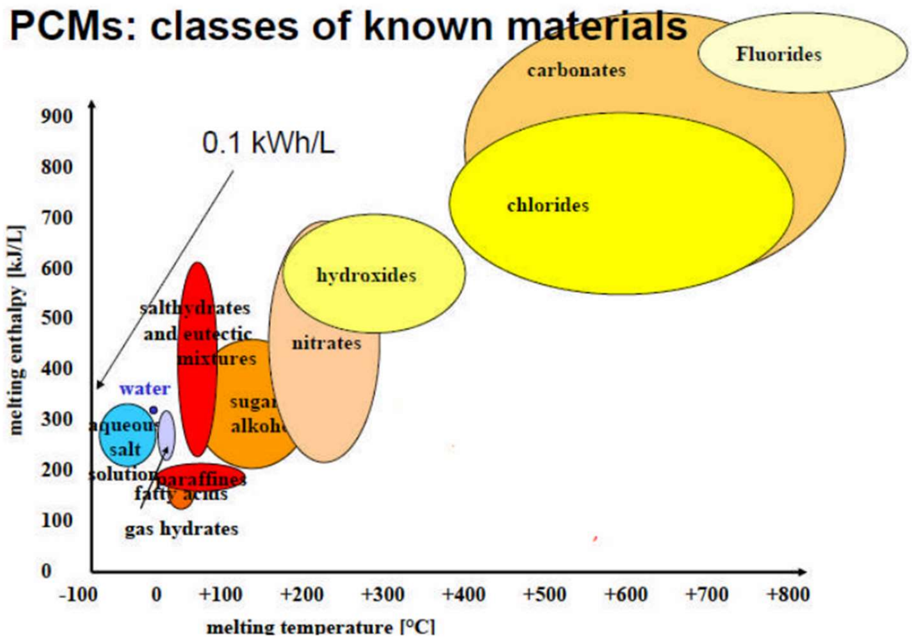

Figure 6 Melting enthalpy for types of PCM [11]

1.2 Problems associated with LHTES

Many studies can be found for paraffines on LHTES applications. These studies estimated and consider the potential use of PCMs but also the potential issues while involving PCMs. Depending on the application and the operating temperature, undercooling can represent an advantage or a drawback. The undercooling phenomenon directly influences the temperature evolution and the moment the latent heat starts to be released. This is one of the main problems stated in literature. Undercooling represents the capacity of the material to remain at liquid state while its temperature is below the melting temperature. This means that the latent heat is not released as expected at the melting temperature. This is a metastable state (liquid) that can be broken (when a first steady solid germ appears) by an external perturbation, the addition of impurities or by lowering the temperature until the nucleation temperature. Depending on the application, undercooling is able to improve or to limit efficiency of the storage system. The improvement can be effective when the system needs to reach a temperature below the melting point before releasing heat. For applications that requiring release/store heat at a particular temperature (the melting temperature Tm), Shama et al. [12] mention that a undercooling degree of about 10°C can prevent the correct operation of the PCM storage system. In practice however, controlling the undercooling degree is still a challenge.

In her doctoral work, Soupart Caron [13] investigated the mechanics of heat transfer involved in the design of a heat storage system. She concluded that in such an application, the undercooling can stop the recuperation of the heat storage. Thus, controlling both nucleation and crystallization is the key issue to determine which PCM material will be optimal. Nevertheless, the potential undercooling present on PCMs are not reported in commercial materials such paraffines and complicate the selection of the best PCM. Supercooling is also an issue and in pure metals or binary mixtures can be as high as 100 °C for homogeneous nucleation in Mg and Al metals. Therefore, metal alloys for LHTES systems are complex and a thorough understanding of metallurgy is needed.

Although metals and alloys have great potential as high temperature PCMs, many issues need to be taken into consideration. After repeated thermal cycles, metals and alloys can undergo modifications in their microstructure due to precipitation, oxidation, segregation etc. It can change their properties including phase change temperature and latent heat. They require an inert atmosphere to prevent oxidation, but these inert gases themselves may be absorbed by metals during the melting and solidification cycles and these retained gases can affect the thermophysical properties of metals alloys. Metal alloys have shown thermochemical stability. Li et al.[14] conducted a study on the suitability of aluminum–silicon alloys when used as PCM. They found that aluminum–silicon alloys are relatively stable through multiple heating and cooling cycles. Zhengyun et al. [15] evaluated the thermal storage performance and thermal cycle stability of Al-Si alloys and showed that the latent heat of Al-12Si decreased from 499.2 KJ/kg to 493.4 [KJ/kg] after 1000 cycles while the phase change temperature was essentially constant, but they did not study the performance with different cooling rates. All their samples were heated from 500°C to 650°C at 10[°C/min] and 6 [°C/min].

Table 1 Problems associated with PCMs

Problem	Classification
Segregation	Thermophysical
Low thermal conductivity	Thermophysical
Supercooling or undercooling	Kinetic
Long term stability	Chemical

For the reasons mentioned above, numerical studies devoted to thermodynamic simulation of a material is fundamental to select the best material. Usually in literature, numerical simulation is used to predict thermophysical properties and PCM behavior. These models often propose simplifications through numerous assumptions and exclude important thermophysical, kinetic and chemical phenomena. Some of them are listed in Table 1. The design and development of LHTES is a challenge, requiring extensive experimental characterization and many cycles of charge/discharge. Also, thermodynamically the behavior can be different if the LHTES is scaled to a big system or the heat exchanger is modified.

One of the main challenges to predict the phase change in an alloy is the definition of the parameters that contribute to an accurate description of the phenomena to model: composition evolution, convection phenomena, undercooling and cooling rate. To demonstrate the feasibility of our method, we develop our own software based on the Gibbs free energy and the CALPHAD

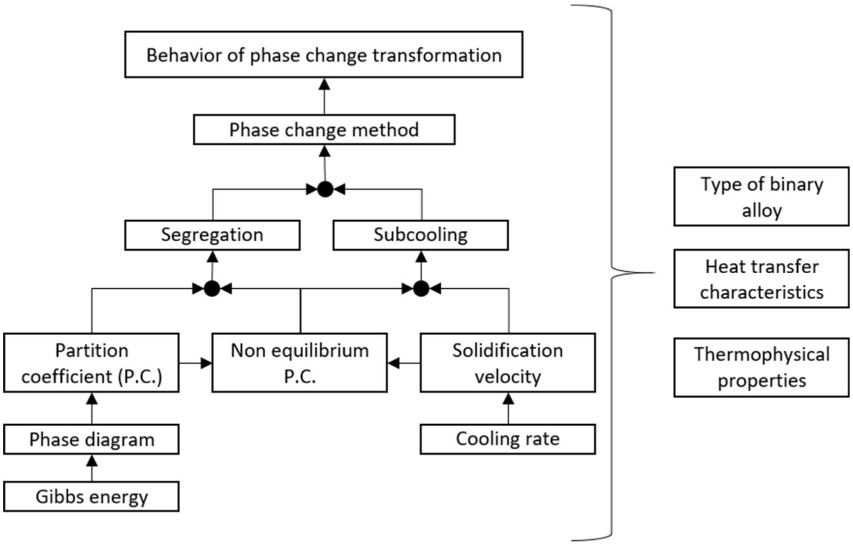

Figure 7 Phase change specifics included in the proposed method

methodology [16] to obtain the phase diagram information. At this moment, our software is limited to binary phase diagrams and the Gibbs free energy contained in the SGTE database [17]. The main reason to develop our software is the possibility to extend the methodology to other non-metallic mixtures.

To simulate phase transformation, we used the ANSYS software[18]. This is a general-purpose software, used to simulate interactions of different disciplines of physics, structural, vibration, fluid dynamics, heat transfer and electromagnetic for engineers. We used the commercial software ANSYS to test the implementation of our method and then evaluated the feasibility to be implemented in others simulation software. Figure 7 illustrates the general approach implemented for the phase transformation. This considers all the parameters and characteristics for the metallic alloy and integrated in the software. The simulation results are compared with experimental results from literature.

1.3 Aim of the present work

Even if some authors propose that the use of alloys metals are feasible as PCMs for industrial processes in LHTES [19]–[22],. it seems that the available literature still lacks system studies. Cardenas et al. [23] claimed that the use of metal alloys as PCM have been underestimated by researchers even though they have desirable properties. Others authors as [12], [24], [25] claim that these materials have not yet been seriously considered for PCM technology. For thermal storage the procedure that includes material selection and latent heat estimation is not developed in literature.

For these reasons the main objective of our research is to develop a method that predicts the thermal behavior of metal binary alloys used as PCM, considering segregation and undercooling phenomena. The proposed method has the intention of optimizing the development of new LHTES using PCM metallic mixtures and even set the stage for studying other non-metallics mixtures.

The first chapter is dedicated to the description of LHTES and the motivation to use alloys as PCMs. The purpose is to explain the different phenomena and how they affect the LHTES.

The second chapter is dedicated to the phenomena involved in phase change of materials submitted to a large cooling rate. From this description, the aim is to propose the definition of the physical basis to predict the materials' behavior during solidification.

The third chapter is devoted to the numerical models of a binary alloy phase change. The methodology describes the steps of a numerical method dedicated to the estimation of heat supply during solidification or melting of a particular material for heat storage. Also, this method consists in simulating the phase change processes and then describing the thermal behavior for an alloy used to store thermal energy, considering the variation of the proportion of the mixture and the cooling rate when the recuperation of the heat stored occurs. This methodology, will be useful to develop enhanced numerical models which can be easily translated into various programming languages such as Python, C, C ++, Fortran, or implemented as an add-on in multi-physics numerical simulation programs like Ansys or Abaqus.

The fourth and last chapter is the application of the model described in the previous chapter. Validations are carried out by parts as our model is composed of several functional blocks that represent successive phenomena. Several validation cases are proposed, based on different materials as it is difficult to find a reference that integrally validates all the steps of our method. As Information concerning metal behavior where the phase transformation and the undercooling degree are controlled by the cooling rate are very rare. The last part of the chapter describes the solidification of Al-Si alloys. Unfortunately, we could not find experimental results published to validate our numerical results. This simulation model uses functional blocks and models previously validated and these left us to suppose a good approach in our results.

A general conclusion and perspectives will conclude the document.

Chapter 2 Definition of the physical model.

This chapter aims to describe the physical phenomena and associated numerical models. The step concerning the solidification corresponds to the latent heat and represents a critical stage of LHTES application as recovering the latent energy is a complex step. We aim to select the optimal material that maximizes the heat source. To do so, the thermal density of the different candidate materials must be estimated considering the operating temperature range. Then, we can improve our selection adding more criteria (and constraints) like economic, environmental factors or improve the system design.

Solidification of an alloy is a complex phenomenon starting with the adequate initial composition to find a desired phase change temperature. From a microstructure point of view the most basic solidification begins with the existence of a crystal nucleus in an undercooled liquid melt. Then, the crystal nucleus grows to initiate the formation of solid phase. In almost all binary alloys, materials also have other solid to solid phase transitions, and these correspond to the transformation from one crystal structure to another. Understanding all of these transformations has been the key topic of many studies such as the design of steels or the improvement of strength in aluminum alloys [26]–[28]. The comprehension of these transitions is fundamental to determine the mechanical properties and to design the correct material for the specific application [29], [30].

The mechanism of kinetic transformation for both of these types of transformation is studied in almost the same way. Solid-liquid or solid-solid phase transition occurs with nucleation and/or crystal structure growth under condition of thermodynamic equilibrium. A first order phase transition involves two distinct phases physically separated by a sharp interface. In this interface, an energy exchange between both phases occurs.

The phase transitions for most solid-liquid or solid-solid transformation are usually studied at constant pressure. These mechanisms of phase transitions are complex and, in most cases, difficult to investigate via experiments [30]–[32]. The atomistic mechanism of transformations is poorly understood. For example, it was unexpected for Peng et al.[33] to discover polymer

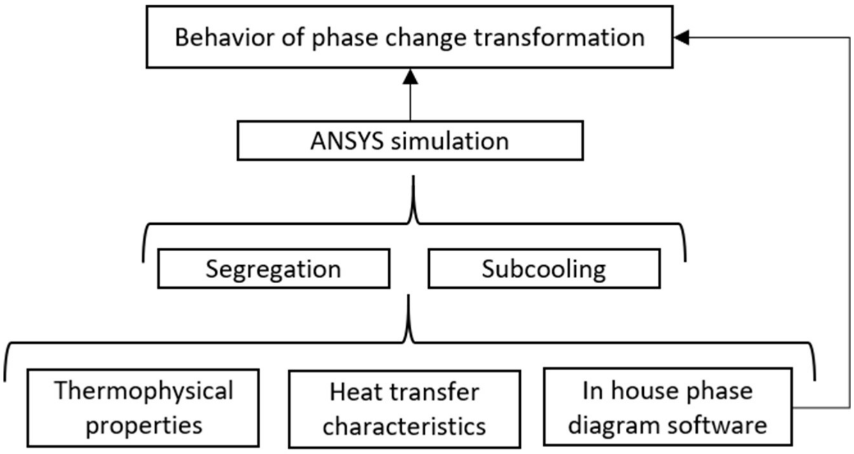

Figure 8 Implementation of the proposed method in ANSYS.

particles of an intermediate liquid phase transitions between solid to solid phase transition at molecular range. In their conclusion they suggest it may also occur in metals and alloys and this can play an important role to define molecular morphologies or defects in alloys.

For these materials the main difficulty is the rapid crystallization during phase transitions. Measurements of thermodynamic data at the high speeds present during phase transformation have been possible only with small scale samples [34] [35]. The conditions of these small samples don't allow considering any degree of liquid movement and this phenomenon has been well known to affect phase transformation in macrosamples. The material and physical properties of alloys (and other kind of materials with crystal structure) are governed by the microstructure, which is mainly governed by the nucleation growth and its morphology. Actually, in practice, it is very difficult to characterize the nucleation behavior that will define macrostructures. Moreover, if a largely different composition and material are considered, the prediction of the nucleation behavior is very difficult.

Different theoretical approaches of solidification behavior were defined from the beginning of the 20th century and the main advance in this subject appeared in the works of Kaufman and Hillert and theirs coworkers [36] [37]. They present the foundation of the CALPHAD method to model phase diagrams and thermodynamic properties. Phase diagrams use theoretical modelling to predict which phases should be expected for given conditions [36]. These involve temperature, pressure and overall composition of the alloy. They are a very useful tool for prediction of macrostructure phases, melting temperatures and final behavior of its morphology. The phase diagram is based on the knowledge of thermodynamic properties, and they estimate the metastable phases at their equilibrium state. The crucial information used in the calculation of phase diagrams is the Gibbs free energies of all phases and for all constituents existing in the studied mixture. For this reason, the use of an established and reliable description of the Gibbs free energy is fundamental to predict the thermodynamic characteristics and solidification behavior.

2.1 Gibbs free energy

In terms of energy that describes the kinetics of phase transitions, each phase is represented by its Gibbs free energy as a function of temperature, pressure and composition. Phase transformation occurs in a system in equilibrium favoring the phase with the lower Gibbs free energy. The equilibrium state can be found from the Gibbs free energy dependence on temperature and composition at constant pressure for a cooling rate slow enough to assume an equilibrium transition.

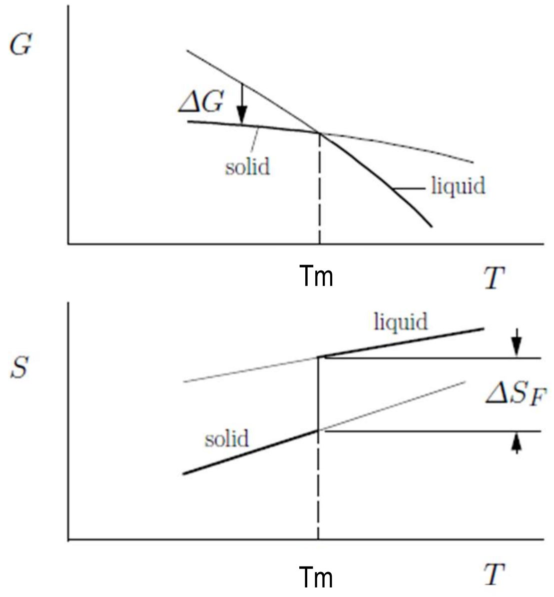

Figure 9 Gibbs free energy and entropy curves for a liquid-solid phase change

The Gibbs free energy curves of liquid and solid intersect at the melting temperature (Tm), as is shown in Figure 9. This figure shows a continuous curve with a slope change between the phase transformation defined as:

$$\Delta G = G^{Liquid} - G^{Solid} \tag{1}$$

where ΔG is the driving force for the transformation. In the bottom graph of Figure 9, the entropy shows a discontinuity change at the transition point, Tm. This is given by:

$$\Delta S = \left(S^{Liquid} - S^{Solid}\right) = \left(\frac{\partial G^{Liquid}}{\partial T} - \frac{\partial G^{Solid}}{\partial T}\right) \qquad (2)$$

Assuming that the heat capacities are equal in both phase transitions, the driving force ΔG can be estimated as

$$\Delta G = \Delta H - T\Delta S \qquad (3)$$

where ΔH is the difference in enthalpy between both phases, expressed as:

$$\Delta H = H^{Liquid} - H^{Solid}\big|_{T=Tm} \qquad (4)$$

and at T=Tm → Δ G=0. Then from Equation 3:

$$\Delta H = Tm\Delta S \qquad (5)$$

hence with Equation 3 and Equation 5:

$$\Delta G = \Delta H - T\Delta S = \Delta H - T\left(\frac{\Delta H}{Tm}\right) = \Delta H\left(\frac{Tm - T}{Tm}\right) \qquad (6)$$

Equation 6 is known as the Turnbull extrapolation. It is valid in almost all solidification situations except under rapid cooling for large undercooling effects. The heat capacity can be defined as the change in enthalpy per change in temperature:

$$Cp = \frac{\partial H}{\partial T} = T\frac{\partial S}{\partial T} = -T\frac{\partial^2 G}{\partial T^2} \qquad (7)$$

The derivation of the molar enthalpy from Equation 6 using Gibbs free energy can be used to estimate the latent heat of solidification as:

$$H = G - T\frac{\partial^2 G}{\partial T^2} \qquad (8)$$

Hence:

$$L = H\left(T_{Liq}\right) - H(T_{Sol}) - \int_{T_{Liq}}^{T_{Sol}} Cp \cdot dT \qquad (9)$$

where T_{Liq} and T_{sol} are the liquidus and solidus temperature of an alloy respectively. This equation can be used in the heat transfer calculation. The validation of these formulations was studied by F. Richter [38] [39] where enthalpy and specific heat data are compared for 30 low-alloyed steels. Figure 10 shows the good agreement of their results between calculated region and experimental data [39].It's important to note that the variation reported between both was about 10 percent higher for the calculated enthalpy and 0 to 7 percent lower for calculated specific heat.

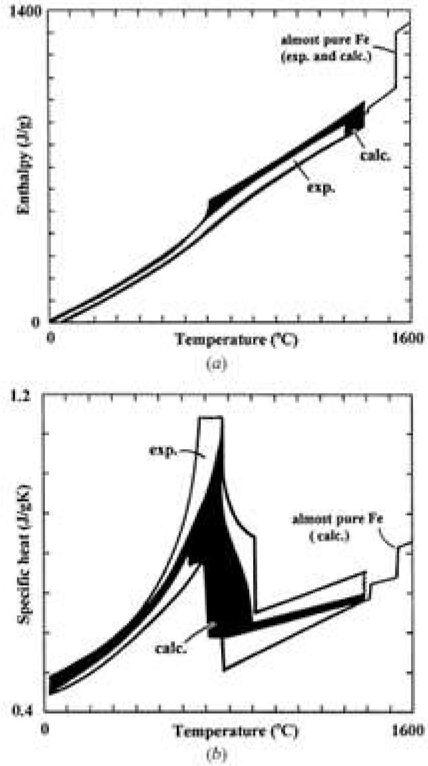

Figure 10 Experimental and calculated regions of a) enthalpy and b) specific heat for 30 low-alloyed steels [24]

The calculated latent heat should be considered as an approximation. The latent heat obtained by experiment is very close to those calculated [40], [41] for some casting and pure materials. The main difficulty is the usual impurity found in all materials that can modify physical properties and the procedure to measure enthalpy excess. This has been confirmed thanks to another set of experimental data for the same material [42].

The utilization of Equations 6, 7 and 8 focuses on the description of the equilibrium phase transformation for metastable phases of multicomponent and multiphase systems. As mentioned before, the equilibrium criterion is attained when the Gibbs free energy is at a minimum. Another fundamental concept to define an equilibrium phase transformation is the chemical potential.

2.1.1 Chemical potential

Until now the phase transformation was considered with constant mass in a homogeneous phase. The addition of a variation in its mass through the number of moles (ni) of component i gives the concept of chemical potential that increases the Gibbs free energy when the component i is added to form a mixture. This is associated in chemistry to the transfer of matter represented as the molar flow from one phase to another for all the components. A complete formulation and explanations can be found in [43] and [44].

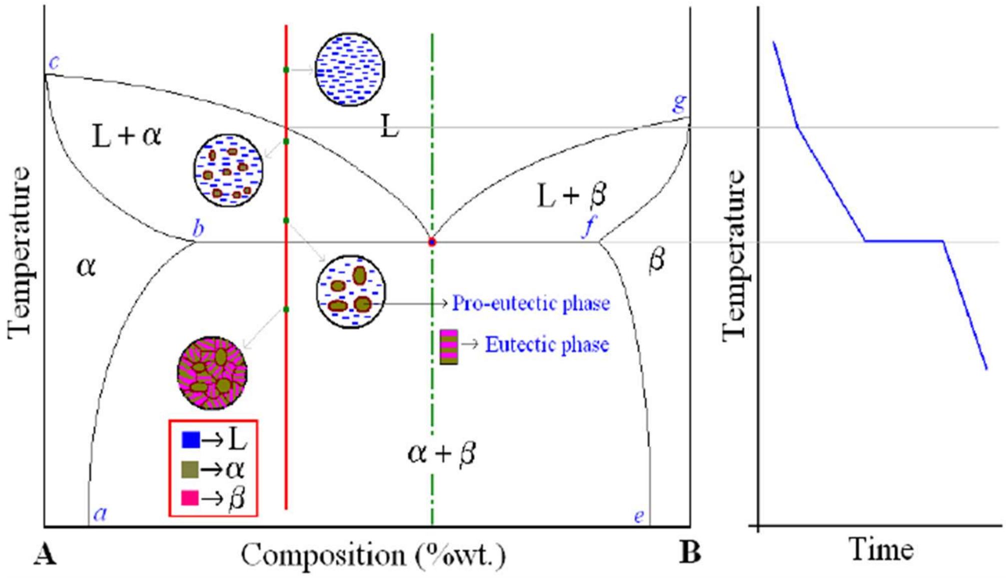

Figure 11 (left) Microstructure development during the solidification of a hypothetical alloy with alpha and beta phases. (right) Cooling curve for a hypo-eutectic alloy.

Figure 11 shows a system in equilibrium, this phase diagram has three single phase regions namely liquid(L), alpha (α) and beta (β); also, we can see three two-phases regions L+

α, L+ β and α+ β. The eutectic composition is identified with the dotted green line. Their Gibbs free energy for a phase with composition A and B is defined as:

$$G = n_A G_A + n_B G_B \tag{10}$$

To explain the use of chemical potential as an equilibrium criterion for binary alloys, only two metastable phase α and β are considered as can be seen in Figure 11. If an amount dn of component A is transferred from phase α to phase β at constant temperature and pression (equilibrium phase transformation) the change in Gibbs free energy associated with each phase by composition is:

$$dG_A^{\propto} = \mu_A^{\alpha} dn \tag{11}$$

$$dG_B^{\beta} = \mu_B^{\beta} dn \tag{12}$$

and since at equilibrium, the Gibbs free energy is equal to 0 using $G=n_A G_A + n_B G_B$ it follows that:

$$0 = \mu_A^{\alpha} - \mu_B^{\beta} \tag{13}$$

This gives another condition of equilibrium transformation: the chemical potential of each component must be the same in all phases. The principal assumption of equilibrium is that reaction rates at the interface are rapid compared to the rate of interface advance. This implies a chemical potential in equilibrium before an advance in the phase transformation interface. Experimentally this concept has been demonstrated for alloys but only for solidification velocities up to 5 m/s [38], [44], [45]. For common alloys submitted to this solidification velocity an equilibrium transformation cannot be achieved and some modification of the phase diagram or the equilibrium equations must be performed.

2.1.2 Phase calculation

Using the assumptions of local thermodynamic equilibrium (same temperature at the interface) the liquid and solid composition of alloys can be determined using an equilibrium phase diagram. These equilibrium phase diagrams describe the structure of a system as function of composition and temperature assuming the thermodynamic equilibrium and consequently, that the diffusion rate is infinitely fast. Such phase diagrams are based on experimental cooling curves for selected compositions.

From phase diagrams the principal information obtained is:

- According to the initial composition: initial liquidus and solidus temperature.
- The melting temperature at the eutectic point.
- Initial composition of formation during crystallization.
- Partition coefficient and liquidus slope.

Based on equilibrium criteria, the calculations of the chemical potential and the minimization of Gibbs energy of multicomponent and multiphase systems can predict phase formation and their compositions for constant temperature and pressure. The calculation of the phase diagrams can be formulated and solved as optimization problems. This technique has been largely studied in [46]–[49]. The calculations of the chemical potential and the Gibbs free energy sometimes lead to numerical complications. The first and most complex is the number of phases for a mixture changing from liquid to solid and metastable phases changing from solid to solid. Each metastable phase is an equation, and these give a number of equations that can lead to an unstable equilibrium point [50], [51]. To solve these instabilities the convex hull model helps to find the thermodynamic equilibrium point [52]

The convex hull algorithm is used to search for two-phase equilibria in multicomponent alloys. The first step is based on the determination of the convex hull for the two-phase Gibbs free energy. Then, at each composition the lowest Gibbs free energy is determined as illustrated in Figure 12. The Gibbs free energies are discretized into grids of Nd nodes, where N is the number of nodes along one species axis and d is the number of independent species. The minimization of the Gibbs free energy is the approach used by Hildebrandt et al. [53].

For each phase the discretization is first carried out regularly from 0 to 1 along the site fractions (yi) of the independent species. For a given phase (liquid, solid alpha, solid beta, etc.) nodes are discarded if their Gibbs free energies are greater than the Gibbs free energies of the other phases at the same compositions. Moreover, nodes belonging to non-convex regions are detected by computing the equilibrium criterion (defined by the chemical potential [16]) and discarded if they do not belong to the phase equilibrium of the binary system. The optimization to find the convex hull for the set of nodes is carried out by a Quick-hull algorithm [54], which has been shown empirically to be the fastest for multidimensional space and thus for multicomponent alloys. The implementation of these algorithms is found in the SciPy Python open-library [55]. For these reasons we chose to compute the convex hull of the Gibbs hypersurfaces with the Quick-Hull algorithm.

The most accepted correlation between thermodynamics and phase equilibria is the CALPHAD method. This uses the definition of the Gibbs free energy (established by J.W. Gibbs [56]) and the foundation established by Kaufman and Bernstein [16], [57]. This method is used to obtain the phase diagram and the solidification behavior.

2.2 The CALPHAD methodology

Recent works using CALPHAD tools are accelerating the design and development of new alloys [58]–[60] including the prediction of phase equilibrium for complex multi-component systems. These tools are included in many commercial software packages, such as ThermoCalc [61], FactSage [62] and Pandat [63]. These become important for the characterization or in the development of new materials and products.

To define the phase change, we used the CALPHAD method that consists in describing the Gibbs free energies of the different phases in a given system as a function of thermodynamic variables: composition, temperature and pressure. The CALPHAD approach [16], [36] is derived from the original work of Kaufman et al.[57] by adding assumptions such as a regular solution for dilute alloys**.** The CALPHAD method is an extensively used semi-empirical technique for phase diagram calculation and modeling. As mentioned before, Equation 3 is the main equation of the Gibbs free energy. In the CALPHAD methodology this is fundamentally represented by Equation 14, which contains all the thermodynamic functions that may be easily derived, e.g. enthalpy, entropy, heat capacity and molar volume.

The Gibbs free energy per mole of a liquid or a substitutional solid solution is:

$$G_m = \sum_{i}^{c} x_i G_i^0 + RT \sum_{i}^{c} x_i ln x_i + \sum_{i}^{c-1} \sum_{j}^{c} x_i x_j \Omega_{ij} \qquad (14)$$

where the molar Gibbs free energy and universal gas constant are Gm and R respectively; x represents the mole or mass fraction of components i in a system with c components; and Ω is the excess Gibbs free energy. The first term on the right-hand side of Equation 14 is the Gibbs free energy of pure component elements at a given temperature (T) and constant pressure (P) of 1 atm, the second term is the ideal Gibbs free energy of mixing and the third term is the excess Gibbs free energy describing the real behavior of the phase. This third term has been formulated by Redlich-kister in their algebraic representation [64] where Ω are the model parameters normally obtained only by experimentation. This parameter describes the influence of the mutual interactions between constituents i and j.

The first term of Equation 14 (Gibbs free energy of pure element) is commonly found in its standardized form of the Scientific Group Thermodata Europe [17](SGTE) equation of the Gibbs free energy as:

$$G = a + bT + cTlnT + \sum_{2}^{n} d_n T^n \qquad (15)$$

where n is an integer typically equal to 2 or 3 or -1. The parameters a, b, c and d are optimized fitting experimental and theoretical data by a least squares minimization method. These material parameters are standardized by the SGTE [17].

Using the SGTE database of pure element and Equations 14 and 15, we can calculate the Gibbs free energy of binary compositions for a specific temperature at constant pressure. The Gibbs free energies are calculated for the different phases. For example, for a mixture that solidifies with two different crystal structures α and β, the Gibbs free energy can be calculated for the liquid phase and the α-β solid phase. They are then used to calculate the chemical potential.

For the equilibrium points of compounds A and B, the chemical potential is used to identify the tangent of each curve representing the phase's Gibbs free energy in function of composition x. Figure 12 shows two Gibbs curves, one for liquid and another for solid phases, where in the illustration (i) all the material is liquid at the initial X_o composition. The second illustration (ii) illustrates Gibbs free energy curves for a lower temperature with the presence of liquid and solid phases. The chemical potential is represented by the intersection of two lines formed by the tangent of the Gibbs free energy curve at compositions X_L (liquid phase) and X_S (solid phase). At this point μ represents the chemical potential equilibrium criterion for the phase transition defined as:

$$\mu_A^S = \mu_A^L \quad and \quad \mu_B^S = \mu_B^L \qquad (16)$$

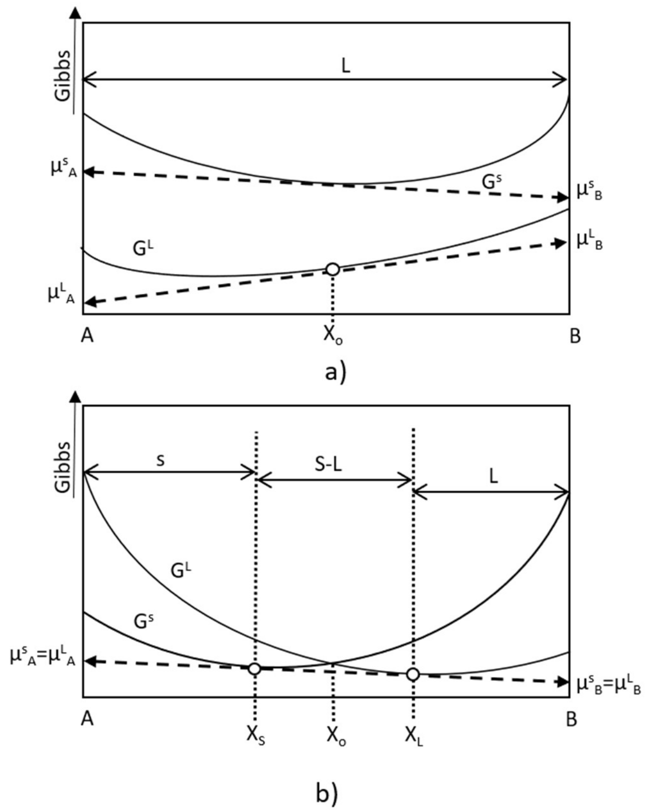

Figure 12 Relationship between Gibbs free energy and chemical potential in a binary system A-B with initial composition Xo. i) Liquid phase at Ti; ii) Mushy region containing liquid and solid phases, with X_s *and* X_L *compositions respectively and equal chemical potential in both phase*

In the system at equilibrium, Figure 12ii) the composition of solid and liquid phases are X_S and X_L respectively and these are the compositions estimated with Gibbs free energy minimization of the system at the specific temperature. Figure 13 shows the graphical construction of a phase diagram using μ. This system has two Gibbs free energy curves for solids: phase α (G_α) and phase β (G_β); and another for the liquid phase (G_L). Each curve is defined by Equations 14 and 15. As we can see in Figure 13, these Gibbs free energy curves are calculated for all compositions at a given temperature. The tangent point formed between them by the chemical potential criterion is the equilibrium phase where the tangent compositions are the liquidus and solidus lines in the phase diagram.

These general principles for Gibbs free energy are sufficient for common materials to model all metastable phases (liquid and solids) and to define the phase diagram. However, for some materials there are other parameters that can modify the description of the phase diagram.

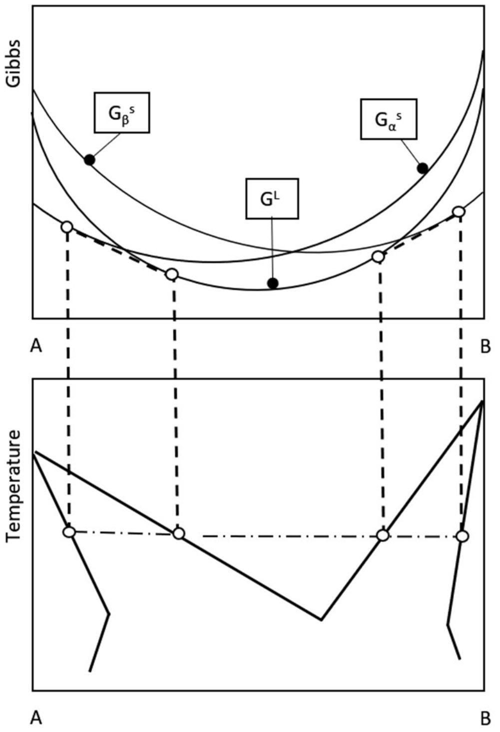

Figure 13 Gibbs free energy minimization to determine all the liquidus and solidus compositions

For example, the magnetic contribution and surface energy may be considered. Furthermore, specific models with complex crystallography and/or particular physical properties are defined with difficulty in a phase diagram. More detailed descriptions for some special cases and their typical treatment can be found in [16], [36], [65] . Nevertheless, for most materials the phases can be modeled with Gibbs free energy and the CALPHAD methodology, using the SGTE database for Gibbs free energy of pure elements. Using the SGTE database and Equations 14 and15 based on the CALPHAD methodology we develop our software to trace the phase of a binary system.

2.3 Partition coefficient in equilibrium

Phase diagrams are unavoidable when modeling alloy phase change. They give temperature and composition evolution during phase transition and the corresponding physical properties. Figure 14 shows a region of a phase diagram for a solid solution [45]. The ratio between the solid composition and the liquid composition at the interface is called the equilibrium partition coefficient, expressed as:

$$k = \frac{C_S}{C_L} \tag{17}$$

C_s and C_L are respectively the solid and liquid compositions, and Csolidus and Cliquidus are the composition of the solidus and liquidus lines. The partition coefficient is constant only when the liquidus slope ($m=dT_L/dC$) is constant. Though in almost all phase diagrams m is variable and thus k is variable, for mathematical simplicity in most calculations m and k are assumed constant. This approximation is often reasonable for common alloys (the variation between constant and variable coefficient partition is rarely reported).

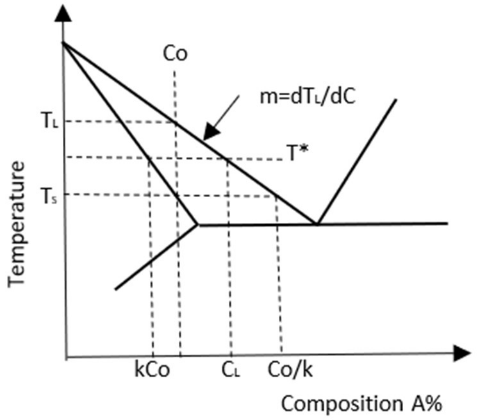

Figure 14 Equilibrium phase diagram for an alloy. k the is partition coefficient; m is the liquidus slope

When the left-hand corner of a phase diagram is considered as in Figure 14, the partition coefficient in equilibrium (ke) is always lower than 1.

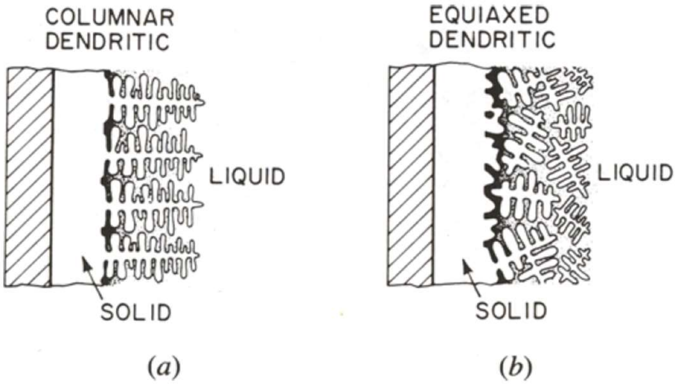

Figure 15 Almost all metal alloys solidify with a) columnar dendritic structure; b) equiaxed dendritic structure

Understanding the role of phase diagrams in the solidification process of an alloy is essential to predicting the related transport phenomenon. The partition coefficient based on the particular phase diagram is essential to consider segregation phenomena, and this can be considered as the link between microsegregation and macrosegregation phenomena. The corresponding concept will be discussed in details later.

2.3.1 Alloy microstructure evolution

The internal structure of alloys is described by the nature of their solute distribution occurring during solidification. In casting the main objective is to control crystallization to maintain a uniform composition and thermodynamic equilibrium during solidification. Almost all metal alloys solidify with columnar or equiaxed dendritic structures [66]. As shown in Figure 15 the interface pattern between liquid and solid is defined by dendrite tip radius and liquid with a modified composition between dendrite arms. The dendrite arms result in the formation of cells, where some “fingers” protrude from the cell. These “fingers” are called primary dendrite arms. The side branches on the primary arm are the secondary arms. Dendrite spacing has a significant influence on mechanical properties. Several analytical models have been proposed in the literature to predict the growth of the primary dendrite arm and the radius at the tip for binary alloys. Understanding the characteristics of dendrite arm, tip radius and microsegregation behavior during solidification is of great importance to predict metallurgical solidification defects

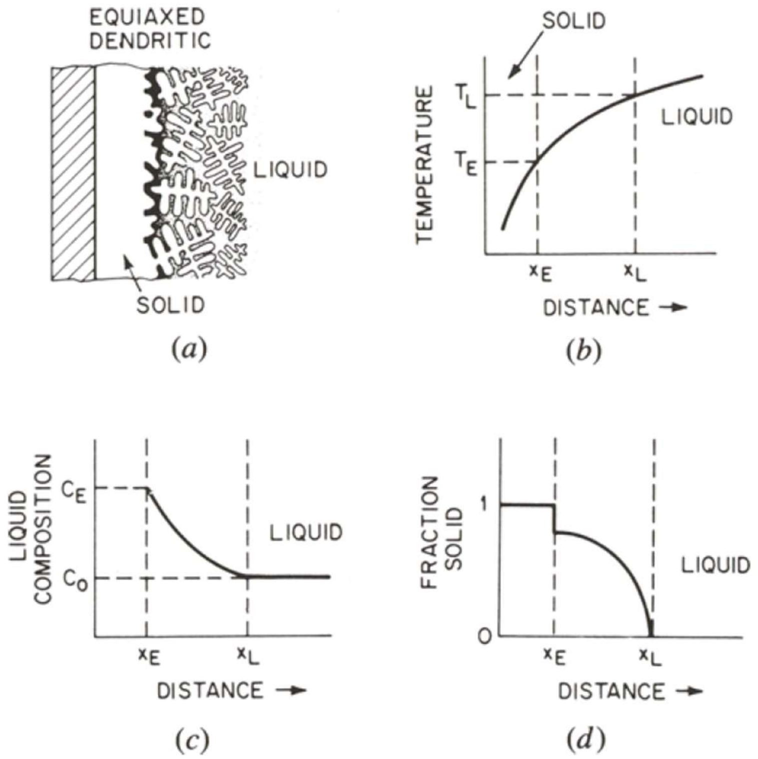

Figure 16 Physical evolution of solidification for a) equiaxed dendritic microstructure; b) temperature distribution at x distance; c) solute composition distribution at x distance; d) solid fraction distribution at x distance.

such as microporosity and macrosegregation, freckling [67], [68] and undercooling degree [69]. We will use dendrite arm information to estimate the undercooling.

Equilibrium of a mixture is defined by uniform chemical potentials [45] across the liquid-solid interface during solidification as shown in Figure 14. The interface between the solid and liquid phase, defined respectively with the solid composition C_s and liquid composition C_L, has a continuous temperature T*. Equilibrium solidification is the base of every phase diagram where the principal assumption is that the material has enough time to completely diffuse solute in both solid and liquid phases. In such a situation the composition becomes uniform throughout the solid. The two main conditions to obtain an equilibrium solidification are: a) slow solidification times with very slow cooling rates, b) very fast solid and liquid diffusion.

The physical relationship between microstructure, solute composition, temperature and liquid fraction is shown in Figure 16, where the solidification microstructure evolution is represented in Figure 16a. For a given temperature distribution (Figure 16b), the liquid composition at any location within the liquid-solid zone is defined by the liquidus line of the alloy system at equilibrium solidification (Figure 16 (c)). The solid fraction at a given location in the liquid-solid zone (Figure 16 (d)) is given by the relation between temperature and solute distribution.

In literature, usually the liquid-solid interface is divided in four stages function of the solidification velocity [94], [114], [115]. (shown in Figure 17). *The first stage* of the transformation is full diffusional equilibrium with uniform phase composition and where the lever rule is applicable. This step is represented in Figure 17 as dendritic structure with null solidification velocities and without undercooling. For this condition all the information generated by the CALPHAD method corresponds to an equilibrium solidification, and the phase transformations are described by the phase diagram.

The second stage shown in Figure 17 is the transition between dendritic and banded structure. It considers undercooling and liquid diffusion effects. The phase diagram can be used but needs corrections such as the Gibbs-Thomson effect or Scheil-Gulliver scheme (to be discussed later in more detail) due to the interface curvature in the solidification or melting process. Undercooling serves to start the nucleation. The solidification forms dendritic or eutectic structure with segregation effects. This second stage represents one of the challenges of this work.

The banded structure shown in Figure 17 is *the third stage* where the undercooling effect increases due to a greater solidification velocity[45], [66], also known as supercooling. Consequently, the cellular/dendritic stable phase cannot nucleate or grow sufficiently fast to reach the phase indicated in the phase diagram. This kind of transformation can occur normally at solidification velocities exceeding 0.1 m/s [45] depending mainly on the properties and composition of the material. The partition coefficient can reach the limit value of one corresponding to a zero solutal diffusion in liquid and solid and a final solid composition equal to the initial liquid composition.

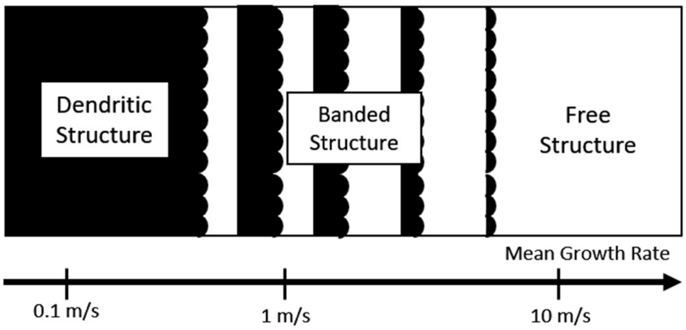

Figure 17 Common cases of microstructures transition for growth rates of absolute stability

In *the fourth stage* shown in Figure 17 new metastable phases can form or go directly to phases described in the phase diagram without passing intermediate stable phases [45], [66], [70], [71]. Due to this new metastable phase, composition and undercooling have strong differences in comparison with the other stages, the solidification velocity is above 5m/s or even at cooling rates exceeding 100K/s [41], [72]. Under these conditions only experimental investigations can predict the final metastable phase and its microstructure due to the occurrence of a new metastable phase or directly jump to another phase described in the phase diagram.

While considering the composition variation during solidification, a fundamental stage consists in calculating the partition coefficient (for liquidus and solidus lines). This is done under equilibrium considerations following the CALPHAD method. A modification of this parameter helps to perform the composition variation for the second and third stages described before in Figure 17.

For some castings, non-equilibrium solidification may be considered when the phase transformation velocity exceeds 0.01 m/s [45]. Solidification occurring at rates above this value is named rapid solidification. This rate is directly related to the amount of undercooling and could be used to differentiate rapid and equilibrium transformations.

2.3.2 Equilibrium solidification

The equilibrium solidification behavior is described by the classical lever rule defined as[45]:

$$Cs = \frac{kCo}{1-(1-k)fs} \tag{18}$$

$$Csfs + C_L f_L = Co \tag{19}$$

$$fs + f_L = 1 \tag{20}$$

$$m = dT/dC_L \tag{21}$$

This leads to an expression of the solid fraction with temperature:

$$\begin{gathered} f_s = \left(\frac{T_L - T*}{(T_{MA} - T*)(1-k)}\right) \\ T_L = T_{MA} + mCo \end{gathered} \tag{22}$$

where f_s and f_L are the mass solid and liquid fractions respectively. T_{MA} is the melting temperature of element A, T_L is the temperature at which the composition starts to solidify, and k is known as the equilibrium partition coefficient (less than 1). T* is the calculated temperature and m is the liquidus slope. Cs and C_L are the concentrations of the liquidus and solidus at the same temperature T*. The principal characteristic in equilibrium is that the solute concentrations can be attained between the liquid and the solid through the partition coefficient. Actually, the partition coefficient is a function of temperature, but in practice a constant value is assumed, which constitutes an acceptable assumption for a low concentration.

The utilization of these equations is shown in Figure 18, where liquidus and solidus lines represent equilibrium solidification, and the initial composition is Co. At T1, solidification begins with a composition C_L =Co. Using the partition coefficient (k) the first solid formed will have the

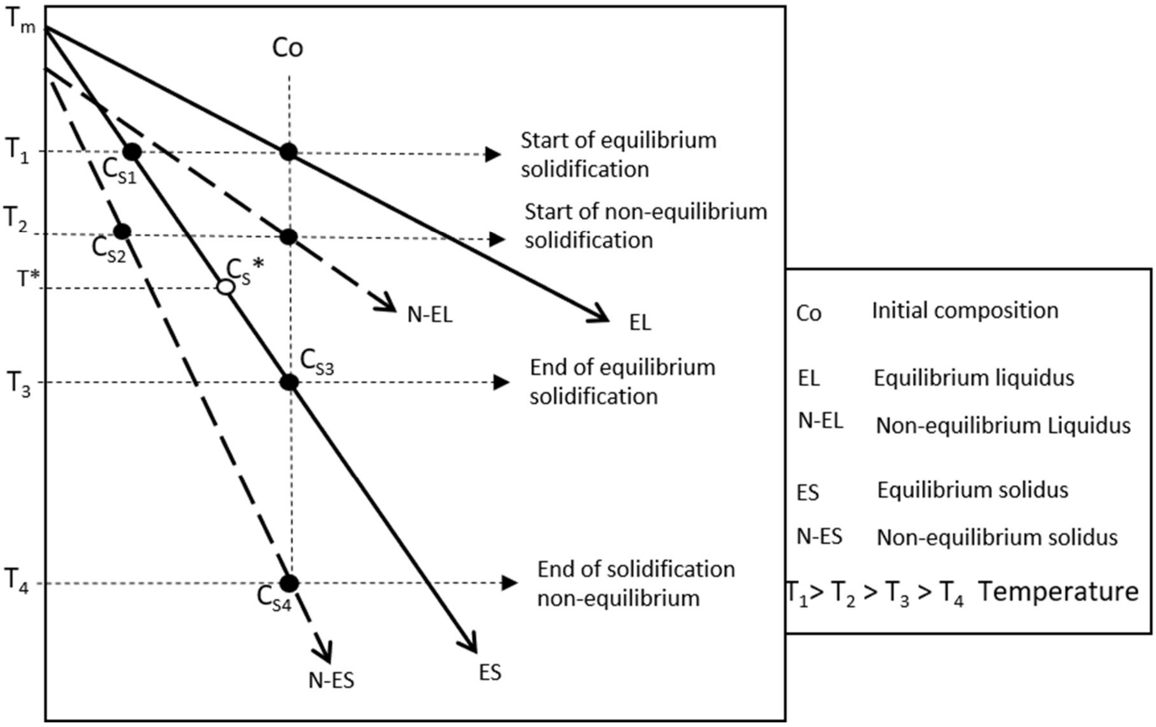

Figure 18 Comparison of equilibrium and non-equilibrium phase diagram. T_1 and T_3 are the temperature at which under equilibrium solidification begins and ends respectively. T_2 and T_4 are the start and end of solidification under non-equilibrium solidification. The difference between T_1 and T_2 is undercooling due to the rapid solidification. Tm is the melting temperature of pure element A.

composition C_{S1}= kCo, shown in Figure 18 at the temperature T1. At a subsequent instant during the solidification, T* in Figure 18, the composition of solidus has grown (Cs*>kCo) and the liquidus composition has risen to C_L*>Co. At the end of solidification under the assumption of infinite solid diffusion the material presents a uniform composition. This homogeneity is only true before and after the solidification process.

The assumption of equilibrium solidification assumes complete mixing in both liquid and solid at every instant of solidification. It also supposes local thermodynamic equilibrium at the interface of solid and liquid. Such an assumption is acceptable for a very slow process (solidification velocity → 0) or where diffusion is very rapid in both solid and liquid phases (Ds and Ds →infinite). However, in practical applications, equilibrium phase transformation is a complex task due to the required very slow cooling rates.

Case a) in Figure 19 shows the solute redistribution during equilibrium solidification, where C_S is represented by kCo at the beginning of equilibrium solidification. During redistribution of the

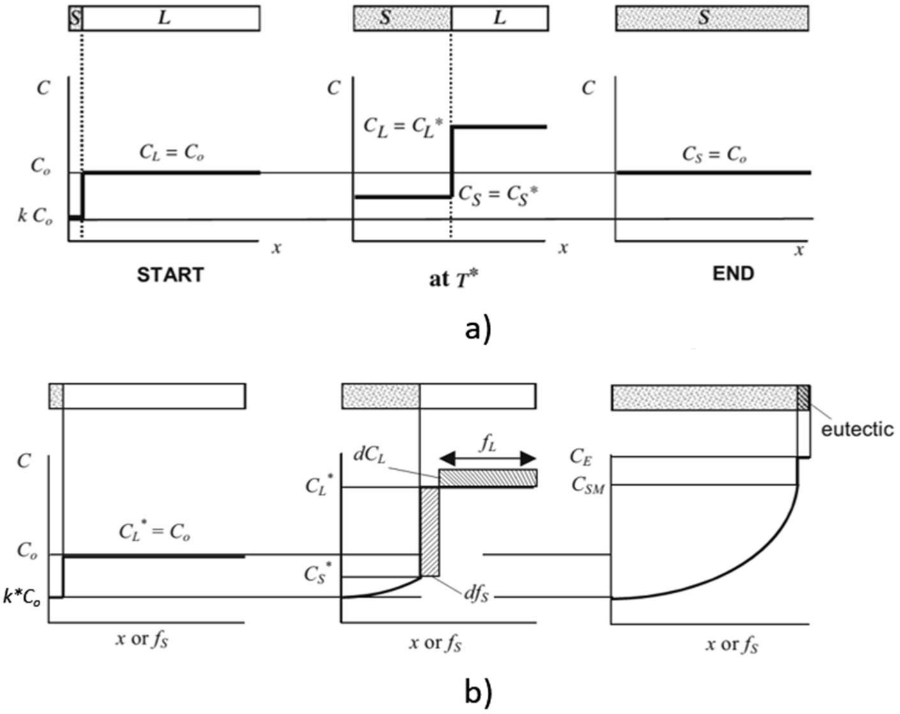

Figure 19 Solute redistribution in a directional solidification. Case a), equilibrium solidification. Case b), non-equilibrium solidification [45]

composition, segregation occurs and can change the behavior of solidification and heat release. On further cooling at T* shown in Figure 19 (case a) is in a equilibrium solidification), all the solid has the composition Cs* due to an infinite solid diffusion. The temperature-concentration evolution follows the solidus line described in the phase diagram shown in Figure 18 as a continuous line. The same situation continues through the process of equilibrium solidification until the entire solidification at T_3, reaching a final composition C_{S3}=Co. During a non-equilibrium phase transformation, solidification ends at T_4 (Figure 18). This is represented by the dotted line with a final solid composition C_{S4}=Co.

Figure 20 shows a schematic evolution of composition at the liquid-solid interface representing an equilibrium solidification of a non-isothermal transformation. The concentration of C^*_L will decrease according to the concentration gradient until the composition will be that of the bulk liquid Co. A diffusion boundary layer will exist. Assuming no convection in the liquid phase, the diffusion layer can be defined as $\delta = D_L/V$ where D_L is the diffusion in liquid and V is the solidification rate. The diffusivity is one of the parameters that define the behavior of solidification as mentioned before and this is different for each material. If the solidification rate increases the diffusion layer becomes thinner until a partition coefficient of unity, this means that $C_s=C_L=C_o$ for the phase transformation.

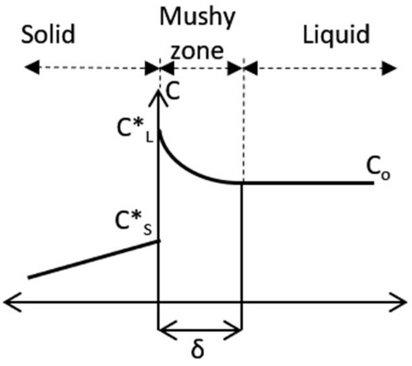

Figure 20 Evolution of composition at the solid-liquid interface [45]

2.4 Segregation and non-equilibrium partition coefficient

To take into account non-equilibrium solidification, different models can be proposed based on different assumptions. Under real conditions the diffusion in the solid is not considered complete (infinite). This leads to the apparition of microsegregation in alloys. This phenomenon leads to a coarse and inhomogeneous microstructure that will result in poor mechanical properties.

One of the first attempts to describe microsegregation quantitatively is the Scheil-Guilliver equation [45], [73]. It assumes i) that there is complete mixing of the solute in the liquid but no diffusion in the solid; ii) that local thermodynamic equilibrium exists at the solid-liquid interface described by a constant equilibrium partition coefficient; iii) undercooling is not present. With these assumptions, the multi-component and multi-phase solidification problem can be implemented as a simple and robust numerical procedure, where thermodynamic equilibrium using Scheil-Guilliver is calculated repeatedly for small temperature decrements. To define the solidification process with macrosegregation the Scheil-Guilliver approach is used.

Macrosegregation is the result of coupling two phenomena: microsegregation at the scale of dendrites and internal movement in the mushy region due to internal convection or sedimentation [66], [74]. Microsegregation results from the solidification of solute enriched liquid in the interdendritic space. In equilibrium this microsegregation is removed during subsequent solidification and recalescence. Macrosegregation causes disorderly composition in large-scale samples causing problems in alloy quality. The segregation pattern is closely linked to morphological features (grain structure), its internal properties and solidification behavior. This is one of the biggest topics researched in metallurgical domains and it has been largely studied in the last 50 years where we can find excellent reviews in [45], [66], [75]–[79]. All of these references describe the basic principles of formation of microsegregation and macrosegregation.

When solidification is not in equilibrium, the solidification velocity exceeds the diffusive speed of solute atoms in the liquid phase and the solute is trapped into the solid at levels exceeding the equilibrium solubility. Liquid and solid chemical potentials across the interface are not equal and consequently the information of the phase diagram can’t be used directly. Figure 18 shows a comparison for a hypo-eutectic phase diagram between equilibrium and non-equilibrium solidification at the initial composition Co. In an equilibrium assumption, the mixture begins the solidification process at the temperature T_1 and the first solid formed has a composition C_{S1}. However, on non-equilibrium with undercooling phenomenon the phase transformation begins at T_2 and the first solid formed has a composition C_{S2}.

The difference between an equilibrium solidification and a non-equilibrium solidification is shown in Figure 19. As the behaviors are different, the partition coefficient obviously needs to be modified to model the non-equilibrium phase transformation. Figure 19 case b) shows the solute distribution during non-equilibrium solidification using a partition coefficient k* considering the solidification velocity. When the eutectic temperature is reached with a remaining liquid fraction, the rest of liquid fraction continues to solidify at the eutectic temperature (isothermal transformation). The variation in the composition is due to a practically null diffusion in the solid and consequently the composition does not change during solidification as shown in Figure 19.b). A concentration gradient will be established between the initial solid composition kCo and the solid composition at the intermediate time (or temperature, $T*$), which is $CS*$. In the liquid phase the composition is homogeneous and equal to $C_L* > Co$ since diffusion is very rapid. The composition of the solid will continue to grow till the end of solidification and will finally reach the maximum solubility in the solid solution on the phase diagram, C_{SM} in Figure 19 case b). The basic equation as a function of the solid fraction is the Scheil-Gulliver equation defined as:

$$\begin{aligned} Cs &= kCo(1-f_s)^{k-1} \\ C_L &= Co(1-f_s)^{k-1} \end{aligned} \tag{23}$$

$$fs = 1 - \left[\frac{(T_{MA} - T_L)}{(T_{MA} - T*)}\right]^{\frac{1}{1-k}} \tag{24}$$

When fs=1 this equation gives Cs=∞ but the composition of the solid can only increase to the maximum solid solubility at the eutectic temperature.

Some other analytical equations besides the Scheil Gulliver equation have been studied and include different assumptions. A summary of major hypotheses used in these different mathematical models are given in Table 2. The main difference between these and the Scheil equation is how the diffusivities in liquid and solid are modeled. The Brody and Fleming model, for example, is more accepted recently. This model’s principal characteristic is that the solid state diffusion is quantified in the intermediate regime between the Scheil and lever rule.

Table 2 Different mathematical models for non-equilibrium solidification

Model	Solid Diffusion	Liquid Diffusion	Partition coefficient
Lever Rule	Complete	Complete	Variable
Scheil	No	Complete	Constant
Brody-Flemings	Incomplete	Complete	Constant
Kobayashi	Limited	Complete	Constant
Nastac-Stefanescu	Limited	Limited	Variable

2.4.1 Segregation and cooling rate

A link can be observed between microstructure and cooling rates, as shown in Figure 17. This shows various phases that the material can present during solidification at different cooling rates. As mentioned before, the first one is equilibrium solidification. The second one presents a small undercooling (neglected) with a controlled segregation and the third one has a huge undercooling and segregation is more linked to convection phenomena. Especially in common alloy materials, non-equilibrium phase transformation with neglected undercooling (second zone) is a typical situation because solidification is a long process (with very low cooling rates).

The cooling rate (CR) is the main key in solidification behavior. Non-equilibrium solidification becomes relevant when a huge CR is imposed. A significant undercooling is present before solidification begins, and the equilibrium partition coefficient increases with interface velocity and tends to unity. This phenomenon is known as solute trapping and occurs when V>>DS/ao where DS is the diffusivity in the solid and ao is the atomic jump distance. The non-equilibrium liquidus & solidus lines are the same. This means that the composition becomes uniform across the interface $C_S = C_L$. The interface temperature is significantly undercooled with

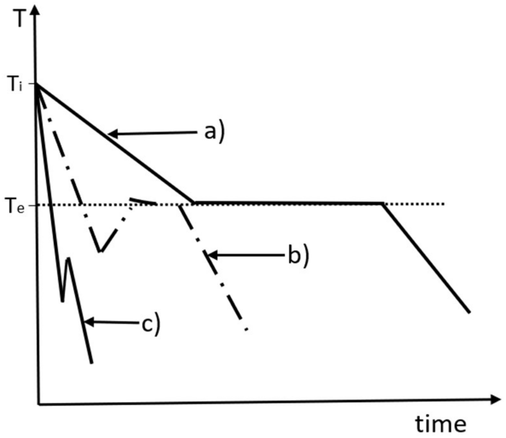

Figure 21 Effect of the cooling rate during solidification of a eutectic mixture. 1- Isothermal equilibrium solidification; 2- Undercooling effect present, the solidification starts below the eutectic temperature Te; 3- Strong undercooling effect due to cooling rate, high solidification velocity and the heat delivered is practically instantly absorbed by CR.

respect to the temperature at which equilibrium solidification should start. The solidification temperature can start below eutectic temperature and the effect of the latent heat release can be insignificant due to the operating CR (Figure 21 third case). The temperature at which the partition coefficient is one is defined as the *To temperature*, where the molar free energies of the solid and liquid phases are equal for a given composition. The locus of To over a range of compositions constitutes a curve between the liquidus and solidus lines where the liquid and solid phase compositions are equal along the curve.

The next section explains the equations used to model solidification of a undercooled alloy with a given cooling rate, calculating the non-equilibrium partition coefficient considering undercooling phenomena. The main objective is to obtain the partition coefficient for non-equilibrium and the dendrite tip radius value. These are both necessary to calculate the amount of undercooling present and composition during solidification. These are used to estimate the latent heat released.

2.5 Undercooling degree

In most cases phase change occurs with equilibrium considerations. When solid-liquid phase change occurs, the solidification is usually seen as a transition at a given temperature: the melting temperature Tm. This state where liquid and solid phases are in equilibrium means that the free energies of the solid and the liquid are equal when the material is at temperature Tm. For a pure material, when the temperature is below the melting temperature the solidification is accompanied by extraction of latent heat. For a temperature below Tm, the solidification is seen as a variation of free energy as

$$\Delta Gv = \Delta H(T - Tm)/Tm \tag{25}$$

Depending on the material properties and the cooling process (fast or slow cooling for example), solidification may occur at a temperature below Tm. The material can then remain at liquid state under the melting temperature. This state called **undercooling**, but also commonly called **subcooling**, is not stable and can be disturbed to initiate solidification. Then, the material comes back to a stable equilibrium and in such considerations, the liquid-solid interface tends to reach the melting temperature Tm through the recalescence process.

Many authors have studied this phenomenon from various points of view. From thermodynamics considerations undercooling corresponds to a negative ΔGv, this corresponds to T<Tm as was presented by H. Biloni et al. [41]. In this case, Tm-T is called the undercooling or undercooling degree (ΔTu) and the initial solidification is composed by two steps. During the first step the material is undercooled (T<Tm). Figure 22 shows the undercooled zone defined by ΔTu. Nuclei may appear in the bulk to form a micro germ. When these reach a critical radius r* [41] the nucleated germ grows constantly to form the solid. This step is considered as micro-solidification and occurs at the nucleation temperature. In the second step, crystal growth governs the solidification process. The nucleation temperature T<Tm, increases during solidification toward Tm, which represents the equilibrium melting temperature, and the remaining liquid solidifies as shown in Figure 22. During this step, the latent heat release is tied to the solidification velocity and macrosegregation. From a macroscopic point of view the undercooling is mainly seen as a delay in latent heat release t_s in Figure 22. This release depends on the material

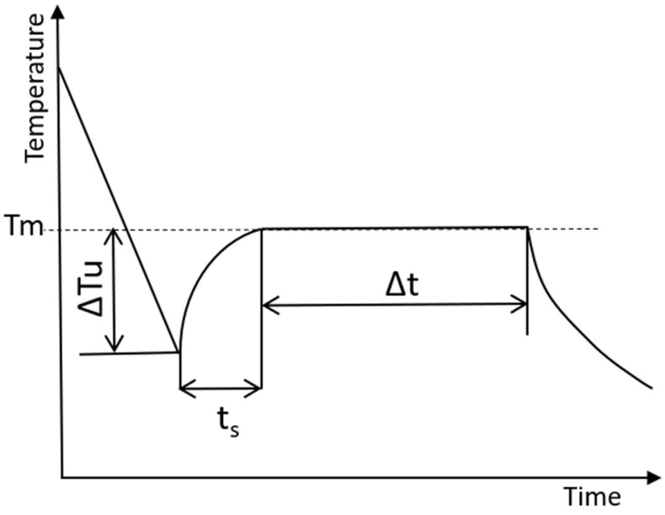

Figure 22 Schematic illustration of a cooling curve during the solidification of an undercooled material

properties and cooling conditions. Experiments are usually useful to quantify the relations between temperature and solidification rate. Our work is focused principally on macro-solidification.

When solidification starts at the nucleation temperature, the material solidifies in a quasi-constant rate until it reaches Tm. This rapid solidification can be considered as quasi-adiabatic, where the latent heat release acts as a heat sink with a small amount of heat transferred to the environment. This released heat leads to an increase of temperature (recalescence effect) consuming latent heat. Then, the remaining fraction of latent heat is released at its melting temperature during the plateau regime (Δt in Figure 22). At Tm the solidification rate is controlled by the heat extraction~~.~~

Figure 23 shows a cooling curve during solidification for a non-eutectic material. The crystallization begins below its liquidus temperature T_L and after an undercooling amount (ΔTu), the recalescence leads the temperature toward equilibrium conditions (1). The remaining melt solidifies at equilibrium conditions. Such behavior shows that LHTES needs precision in calculating properties of the PCM. If undercooling occurs, the start of solidification is delayed and for the typically small operating temperature range of LHTES applications, this is an undesirable behavior [80]. The heat used in recalescence reduces the system performance and this behavior leads to a great discrepancy between theoretical calculations (using constant melting temperature) and application results [81]. An important conclusion observed by different

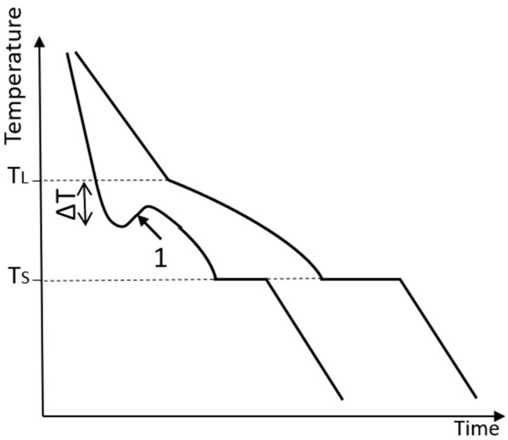

Figure 23 Schematic illustration of a cooling curve during the solidification of undercooled non-eutectic material

researchers [80], [82]–[85] is that the solidification temperature decreases due to high heat flux and hence the presence of a undercooling increase. Also, this confirms that a large amount of undercooled material is used in the recalescence process. This results in the apparent availability reduction of the latent heat. Consequently, the LHTES performance is reduced

Many works demonstrated that any solidification process presents an undercooling degree. The undercooling requirement to start the solidification process for most liquids is larger than 0.15Tm (Tm being the melting temperature) [86]. Therefore, the solidification process normally considered isothermal at Tm actually occurs in a small range of temperature. The material nature also plays a role in undercooling degree. For example for the metallic crystalline structure face centered cubic (FCC) and body centered cubic (BCC), a undercooling degree of approximately ≈0.18Tm has been estimated to start the solidification process [86]. Quantifying the undercooling degree is a challenge. The solidification and undercooling are affected by the different techniques used. For example, the droplet emulsion technique [70] demonstrated a undercooling almost twice as large as that obtained with the same material in previous works that used other experimental apparatus. Research finds new parameters to explain these differences but these data are less reliable due to change in material purity or changes in their general experimental conditions. In commercial alloys, homogeneous nucleation is virtually inexistent. Even if micro-solidification and macro-solidification are represented separately, both are necessary to understand and develop new theories involving rapid solidification processes or changes at macro scale in molecular structure. The undercooling is subject to many causes and controlling this behavior remains a hard task.

Table 3 Principal conclusions in literature to define the undercooling process over phase change materials.

Reference	**Conclusion**
[87]	The solidification process depends significantly on the heating/cooling rate and the size of the sample used
[88]	For numerical simulations if natural convection is omitted, the PCM temperature heats much more slowly compared to experimental result
[89]	The inlet coolant temperature affects the start of solidification, the undercooling degree and the time for charging/discharging.
[89]	The coolant flow rate did not have any effect on the undercooling degree
[83]	Internal natural convection can make a uniform temperature in all internal positions, the solidification apparently starts over all the positions.
[81]	The heat used in the recalescence process reduce the LHTES performance and leads to a great discrepancy between theoretical and application results.
[80], [83], [85], [89]	The solidification temperature decreases due to the high heat extraction flux and hence a strong undercooling are present
[80], [83], [85], [89]	Recalescence uses a fraction of the latent heat, which results in the apparent availability reduction of the latent heat for the LHTES
[90], [91]	Temperature and position of nucleation have a probabilistic behavior. The higuest probability to start the nucleation is in the coolest and roughest wall.

Normally, the effect of a small undercooling to start the solidification is neglected. Neglecting this effect is a practicable approach if undercooling is small compared to the modifications of temperature in an application. On the other hand, in the presence of significant undercooling, the results can be completely wrong. In such cases undercooling has to be included in the numerical model. Nevertheless, a mathematical model to predict undercooling degree in metal alloys considering composition and boundary conditions does not exist. Figure 22 shows the principal four parts for a temperature-time profile during the solidification of a undercooled material: i) the undercooling zone until the nucleation temperature (ΔTu), ii) recalescence after the start of the solidification, iii) phase transformation considered as an isothermal solidification when the temperature reaches Tm and finally iv) post-solidification.

A brief summary of the publications relative to the undercooled material and their principal conclusions is presented in Table 3. In the assembly of this literature we conclude that the cooling rate can be used to define the undercooling degree. Also, it is necessary to define if the convective flux homogenizes the internal temperature as was demonstrated by Solomon et al. [83] , where consequently the solidification apparently starts at all locations. Otherwise, in the presence of a stronger cooling rate, the temperature gradient favors the appearance of a solidification front driven by a solidification velocity. Solidification of binary alloys presents other challenges in comparison with organic/inorganic PCMs. Additional phenomena occur, like segregation or significant differences in thermal diffusivity coefficients or solidification velocity. Hence, in most cases it’s more difficult to predict the undercooling degree or the general behavior of phase change.

2.5.1 Cooling rates and undercooling degree

Many experimental studies are focused on understanding undercooling effects due to specific conditions. Arkar and Medved [87] conducted a differential scanning calorimetry (DSC) analysis at various cooling rates of 0.1, 1 and 5 K/min. They reported that the shape of the DSC curve depended significantly on the heating/cooling rate and the size of the sample used. Undercooling effects were surely in part responsible for this. In their experimental study, Solomon et al. evaluated the effects of undercooling due to the surface heat flux and the location of the PCM in the tested section. They concluded that at a higher cooling rate, the undercooling effects are more significant. Consequently, the undercooling degree is not the same for all locations and depends on the advance of the solid frontier. The sample shows high temperature gradients, and the start of solidification occurs at different times. This is driven by the solidification rate, material

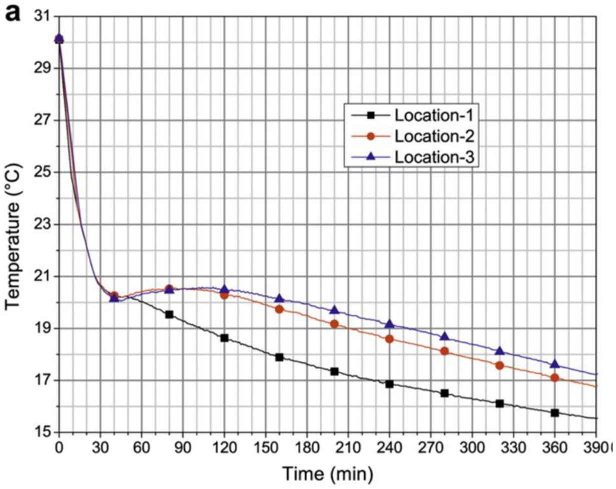

Figure 24 Temperature history at various radial positions. All of them have the same temperature before the start of solidification. Solidification starts massively [88]

properties, cooling rate and heat extraction. Furthermore, as shown in Figure 24, on their experimental work Solomon et al. [83] reduce the cooling rate in their experimental work. The natural convection homogenizes the internal temperature before the solidification process begins. Hence, considered as a massive solidification process in the entire sample the nucleation process initiates apparently at the same time. This is possible if the temperature of solidification is uniform over the different locations in the sample and if the sample dimensions allow convective flows. Once the solidification process is initiated, the latent heat released at the closest position to the cooled wall (location 1 in Figure 24) acts as thermal insulation for the rest of the internal locations. Then, the other locations stop the solidification process and only heat extraction drives solidification rate. Solomon et al.[83] conclude that the time of the temperature plateau shown in Figure 24 depends on the undercooling degree and the rate of the heat extraction. [89]

Also, statistical studies [92], [93] have shown that the beginning of solidification (nucleation temperature) is not completely defined with precision and has a probabilistic distribution. Moreover, it is influenced by the volume of the sample, the presence of foreign bodies or surface treatment, the thermal cycle of charge/discharge and principally the cooling rate.

2.5.2 Microstructure and solidification velocity by undercooling effects

Despite the difficulty, normally the central role of undercooling an alloy is to influence its microstructure [75], [79]. The challenge to define all the parameters that define microstructure in metals continues to be an attractive research field, where these are principally focused on new experimental methods to understand solidification behaviors, characterization techniques and modeling approaches in microstructure or new metastable phases to improve materials for specific applications [94], [95].

Grain structure was largely studied in the last 50 years [96] to define growth laws at the solid liquid interface. The solidification processes are mainly governed by the temperature field, natural convections effects and solute diffusion. Further, these are not the only parameters: solute trapping, solidification speed, interface kinetics or impurities into the melted alloy may become important to avoid equilibrium solidification [75], [79]. The classical theory related to the undercooling is about the solid-liquid interface in metallurgical or crystal growth. Growth undercooling is not the same as nucleation undercooling. The nucleation undercooling is difficult to define or control due to the numerous sites and a probabilistic behavior. In literature the difference between them is not clearly defined when microstructures are studied. The quantitative evaluation of undercooling is defined in literature by the equation of the interface undercooling [97], [98]. Accordingly, the total undercooling measured in their experiments are expressed as the sum of the thermal, the constitutional, the curvature and the kinetic undercoolings.

The main interest of many researchers is focused on nucleation, crystallization growth and definition and prediction of intermediate phases and their mechanical physical characteristics due to kinetic transformation. The most important examples of research interest from an industrial point of view are Fe-C systems, copper and aluminum alloys, nickel-based superalloys and titanium aluminides. Many of these studies track the nucleation and crystal growth to trace the microstructure transformation described in phase diagrams for equilibrium solidification. These studies relegate thermal properties below mechanical properties or omit information relative to undercooling cooling rates.

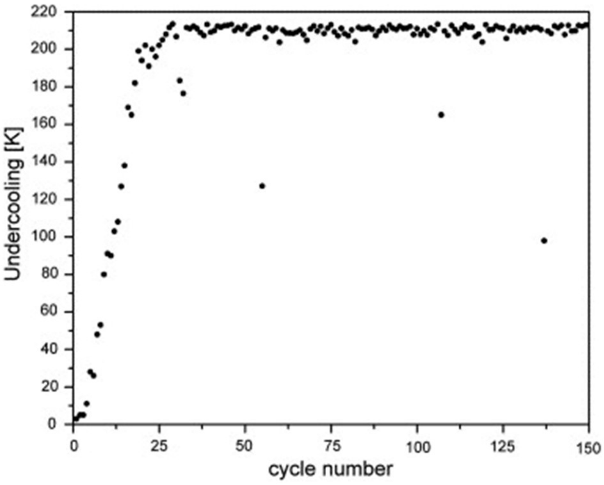

Figure 25 Change in undercooling reponse after phase change cycle in an Au sample [101]

In all of these works, it is well known that the increase in nucleation undercooling was attributed to an increase in the thermodynamic driving force for the formation of the new phase (liquid to solid, solid to solid). This leads to higher reaction and transformation kinetics. This undercooling degree depends directly on solidification conditions that are the key parameters to predict/control the microstructure morphology in alloys [75], [79], such as cooling rate, thermal gradient, composition and internal natural convection. Unfortunately, even if some reports concerning the influence of undercooling in alloys for industrial process [94], [99], [100], can be found, satisfactory explanation has not been available to account for this effect in LHTES. Moreover, research prioritizes the relation between cooling rate and solidification velocity to define microstructural morphology in alloys, and the relation between cooling rate and undercooling for macro solidification is not reported.

The relation of microstructure and undercooling are strongly linked. G. Wilde et al. [101] present a new model based on thermodynamic considerations and on the nucleation kinetics. Their experiments show how the undercooling response in gold changes significantly after 25 cycles of phase change, as shown in Figure 25, this result contrasts with the following cycles where a quasi-steady state of undercooling response is observed. They confirmed that the presence of 50 ppm oxygen in the inert Ar atmosphere delayed the onset of the quasi-steady state undercooling. They conclude that the melting/solidification cycle is necessary to characterize the undercooling degree in an alloy even with materials of 99.9999% purity. Also,

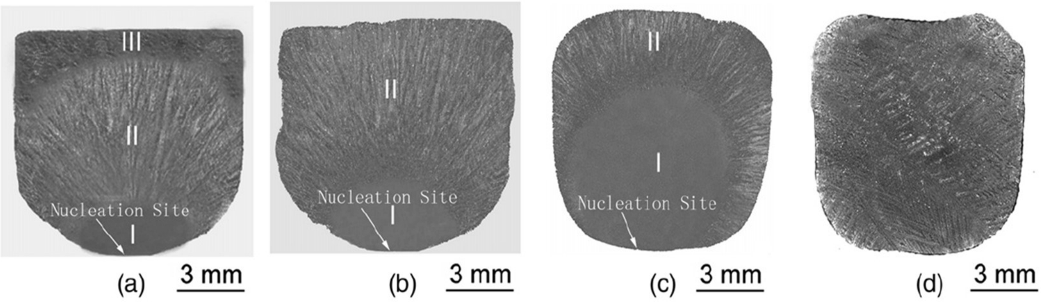

Figure 26 Microstructure sample with different undercooling: a) 10K b) 15K c) 70 K d) 100K; "I, II, III" indicate the three regions: refined, columnar and equiaxed grains. [102]

they suggest that impurities are almost always responsible for nucleation. Consequently, in the first melting/solidification cycles the impurity considerably reduces the undercooling degree. This demonstrates that nucleation agents are not tenable during its thermal cycles.

A remarkable study based on the relation between undercooling, cooling rate and microstructure was presented by Zhao et al. [102]. They used the glass flux method to study the microstructure of Ag-Cu eutectic alloy. They reported three types of microstructures shown in Figure 26: i) the refined grain area near the nucleation site, ii) columnar grains and iii) equiaxial grains. They observed how the region i) is enlarged at high undercooling and region iii) disappears. They concluded that solidification velocity gradually decreases from the nucleation site but is still faster than that during equilibrium solidification.

Also Zhao et al. [102] studied the undercooling effect and solute excess and they affirm the same behavior reported in [71], [103], [104] that the growth velocity can cause significant solute trapping. Then, more solute excess is incorporated into the microstructure formation at high undercooling degree. This deviation from the equilibrium solidification is more severe at the initial undercooling point. When recalescence occurs, some part is remelted. For this reason, if little undercooling and low velocity growth are present, equilibrium solidification can be considered. The Zhao et al. experimental works give us the bases to use microstructure solidification to predict the undercooling degree.

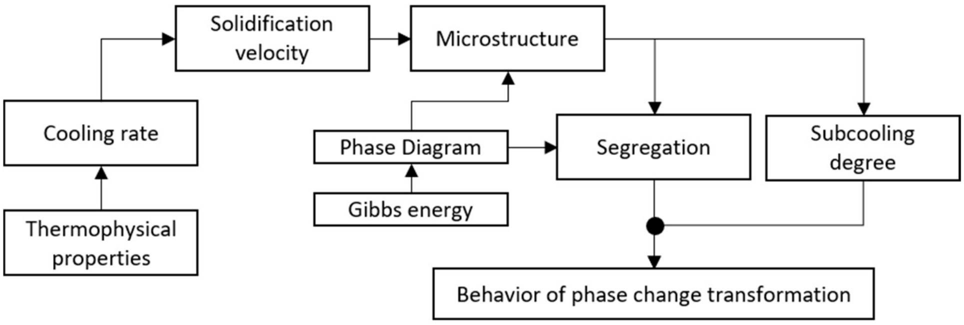

Figure 27 Representation of interaction during solidification

Pryds et al. [105] show powder particles of stainless steel with dendritic or cellular structure depending of undercooling degree. Their work shows microstructure variation at different solidification velocities across individual powder particles. The explanation is that at the beginning of the solidification the initial growth may occur very fast (phenomena described also in Figure 26). The interface velocity decreases as the Solidi-Liquid interface moves through the alloy because the release of the latent heat reduces the cooling rate across the powder particles. Hence, the microstructure also changes. When the cooling rate is enough to reduce the recalescence during phase transformation, the solidification velocity can be supposed constant. Moreover, the microstructure rests unchanged with the same solidification velocity. These considerations are true until the equilibrium melting temperature is reached where the solidification of the melted alloy is thus limited by the heat transport to the surroundings. As stated before, the undercooling degree depends on the cooling rate present.

The dependence of solidification velocity by cooling rates as been largely studied, principally for steels, where effects of cooling on the structural features has been the main topic on [75], [106], [107]. Figure 26 shows the dependency of the solidification velocity with the cooling rate, and the material's microstructure depends on the solidification velocity. Even if the solidification velocity depends on cooling rates and thermophysical properties, it must be defined before the start of solidification to estimate the undercooling degree and the advance of the solid/liquid interface.

To explain the link between solidification velocity and microstructure shown in Figure 27, it is necessary to understand the phase transformation process. The solid phase forms after the nucleation of the melt. Solidification is a process during which molecules from the liquid phase rearrange and become part of the solid phase. For every molecule that becomes part of the solid phase a fixed amount of latent heat is released. That heat raises the temperature of the mixture surrounding the phase front and depending on the properties of liquid and solid. This increase in temperature can be seen in some of the cases shown in Figure 28. If the heat transport is slow compared with the solidification, the propagation of the phase front is inhibited and a distinct temperature plateau is formed (cooling curve 2 as opposed to cooling curve 1). If the heat transport is fast compared with the solidification, the melting temperature is not reached during the phase change and the plateau is apparently suppressed, represented by the cooling curve 3 in Figure 28. These effects have a strong impact on the storage performance and should be considered in the design of storage systems.

M. Carrard et al. [107] shows in Figure 29 a section of the phase diagram showing the equilibrium liquidus and solidus temperatures (solid line) for an Al-Fe system. The equilibrium solidification has a zero velocity. The increase of the solidification velocity draws the liquidus and solidification temperatures closer. These tend to converge around the To temperature where the partition coefficient increases to reach unity at the maximum growth velocity (for Al-Fe, 5 m/s [95]). The fourth zone described before in Figure 17 represents the maximum growth velocity with a partition coefficient >= 1. The To curve is the locus of compositions and temperatures where the Gibbs free energies of the two phases are equal. Then the liquid and solid phase composition are equal along the To curve [95].

There are 4 stages depending on the solidification velocity (described in detail in 2.3.1 Alloy microstructure evolution). We propose that the solidification velocity is predicted by the cooling rate present before the nucleation temperature. Then, this solidification velocity serves to define the change in the microstructure of the alloy, as shown in Figure 26. Based on this microstructure variation, we can formulate a prediction of the subrcooling degree. We use the theory of microstructure variation by solidification velocity to predict the undercooling degree. Our research considers some physical phenomena described in their works (summarized in Table 3) to develop a model that can be used in LHTES.

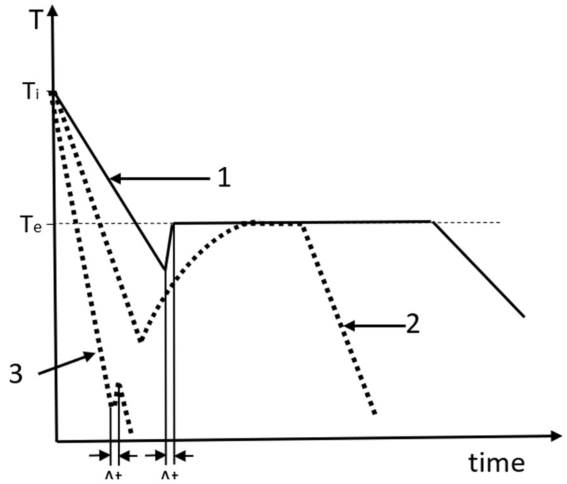

Figure 28 Distinct temperature plateaus. 1, small undercooling degree; 2, Significant undercooling degree reduces the temperature plateau. 3, The release of latent heat is almost insignificant, temperature plateau is practically inexistent.

2.6 Cooling rate and solidification velocity method

In the last four decades significant works have been done to perform several theoretical, experimental and numerical models to describe the various parameters that affect crystal growth and solidification. Mathematical models/methods have been largely developed such as phase field [108], [109] [44] level set [110] or enthalpy based techniques [111] among others [45]. These follow different theoretical criteria such as maximum growth criterion [45], marginal stability criterion [112], micro solvability theory [113] or even the effect of natural convection in growth velocity [114], [115]. All of these are used to define/develop theoretical models in nucleation growth defining undercooling effect, growth rate, convection, thermal and composition diffusivities. This can be complex work especially if this implies nucleation dynamics. All of these have the objective to predict microstructure formation under effects such as undercooling or variation in its solidification velocity. An example of this complex work to predict the microstructure can be seen in Ebrahimi's PhD thesis [116] where he developed a micromechanical phase-field model to assess the eutectic solidification in Ti-Fe alloys with coherent elastic misfit. Loginova's PhD thesis [117] developed a phase field method based on the Gibbs free energy function to track morphological evolution of dendrites, grains and widmanstätten patterns for phase transformation in Fe-C compositions.

The analysis of undercooling in binary alloys requires careful experimental design and as mentioned previously, the numerical approach requires a large amount of experimental data even for one specific composition. Hence, it's not surprising that current nucleation theory/models do not accurately predict the phase transformation kinetics when applied to different alloys. The definition of nucleation behavior or microstructural solidification are not our priority as was studied by Ebrahimi [116] and Loginova [117], even if this can explain many phenomena in undercooling problems.

With this point of view and additionally at the conclusions resumed in Table 3, we define the undercooling in alloys with these hypotheses:

- In undercooling, the beginning of nucleation is not tracked or predicted. The nucleation is considered massive at microscale.

- Microstructural morphology is not tracked or predicted. On the other hand, the solidification velocity and how it affects the microstructural morphology defines the nucleation temperature.
- Undercooling degree depends on cooling rate and composition concentration. Impurities or container wall roughness are not considered.
- The presence of recalescence does not remelt the alloy or change its composition.
- •Solidification always begins at the point of lowest temperature

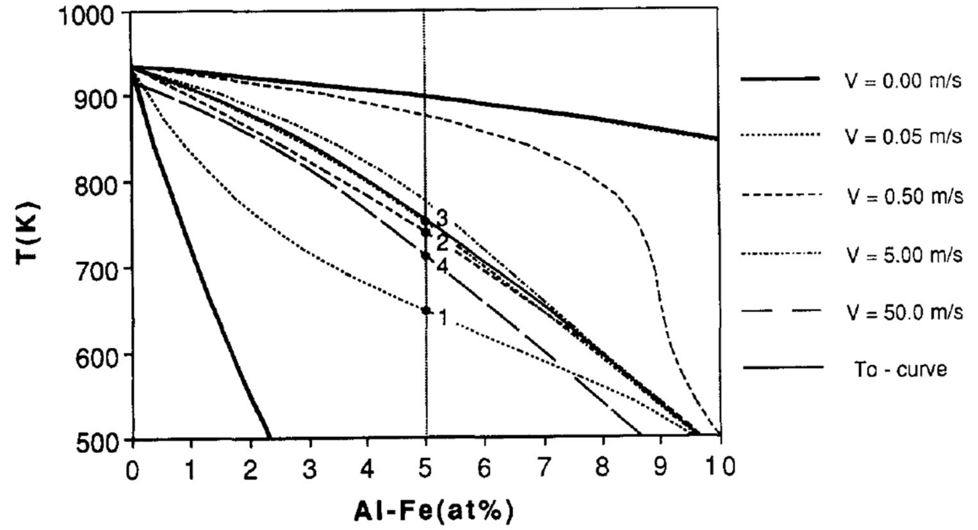

Figure 29 Evolution of the stable and metastable phase diagram with different growth rates for the Al-Fe system. The points 1,2,3 and 4 indicate the solidus temperature for an Al-5 % Fe alloy [125]

To represent the consecutive steps of solidification of an undercooled material several assumptions have been proposed in literature. Some authors consider that nucleation starts everywhere in the material at the same time and leads to the solidification of the entire volume avoiding the existence of a liquid-solid interface. In fact, the solid phase grows from a nucleus and forms a liquid-solid interface that evolves with a velocity depending on the crystal growth rate and the heat dissipation rate. The validity of the homogeneous solidification without explicit interface depends on the liquid-solid interface velocity that must be high enough compared with the material size to consider the previous approach. To control this variation, in our method the solidification velocity is controlled artificially by introducing the degree of solidification in function of cooling rate. At each time step the new degree of solidification is determined according to the current speed of solidification, which depends on the imposed cooling rate. Another approach is to fix a constant growth rate that implies a constant solidification rate.

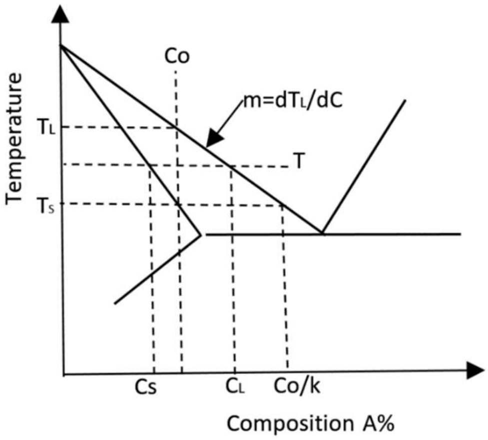

Figure 30 Schematic region of a phase diagram for an alloy. k is the partition coefficient; m is the slope liquidus

2.6.1 Our method

To investigate the material behavior during heat discharge due to solidification we have developed an algorithm based on a high cooling rate model, this includes the subsequent undercooling. The description of the method considers the rapid solidification of a binary alloy. The rapid solidification depends on the composition and its variation during the phase transformation. When considering global equilibrium, which truly exists only when solidification takes a very long time [44], [95], the fraction of phases can be calculated with the lever rule and the phase diagram gives the uniform composition of the liquid and solid phases, shown in Figure 30. Neverthlees, in most cases of casting, the overall kinetics can be described using equilibrium phase transformation with some modification (ex. Scheil-Gulliver). We can approximately estimate the temperature and compositions at the interface.

The solidification velocity depends mostly on the cooling rates (topic treated in the section 2.4.1 Segregation and cooling rate and 2.5.1Cooling rates). Figure 27 shows the interactions of

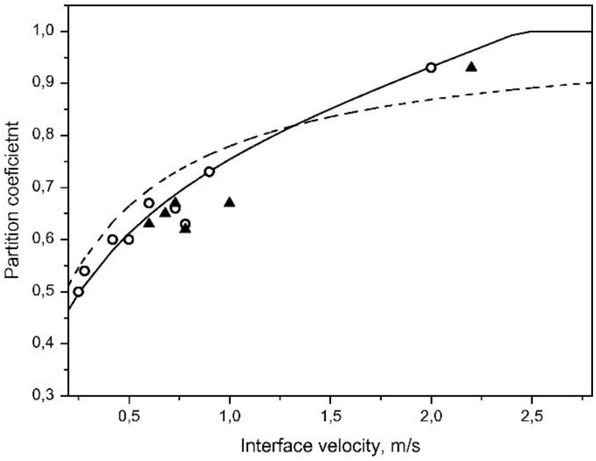

Figure 31 Partition coefficient as a function of interface velocity for Si-As alloys. Data points are experimental values. The dashed curve is k calculated with the CGM model. The solid curve is k calculated with the LNDM mode [101]

solidification velocity with other phenomena. Even if the microstructure can define the solidification velocity present experimentally, we assume that the solidification velocity drives the microstructure behavior. As mentioned before, microstructure characteristics (dendrite radius tip and spacing principally) define the macrosegregation and the undercooling degree. Figure 27 shows the connections between different phenomena.

The evolution of the partition coefficient is directly tied to the growth velocity and growth morphology. As pointed out before, the undercooling degree depends of many factors such as thermophysical properties, alloy composition, impurities, natural convection, vibration or external elements. On experimentation, the undercooling degree due directly to the solidification velocity can be obtained under the strictest material composition purity. The undercooling degree predicted can be considered as the maximum value and then as a reference value for the worst situation.

Each material has a limit solidification velocity for the To curve. Sobolev [118] studied the Si-As systems and the solute drag effects. Their results showed that the solidification velocity varies under solutal drag effects. They used the local nonequilibrium diffusion model (LNDM) [98] to predict the solidification velocity and the variation in its partition coefficient. Since the importance of solute drag in rapid alloy solidification is still under discussion, solute drag is not taken into consideration. In any case at high interface velocity (V) all liquidus and solidus slopes

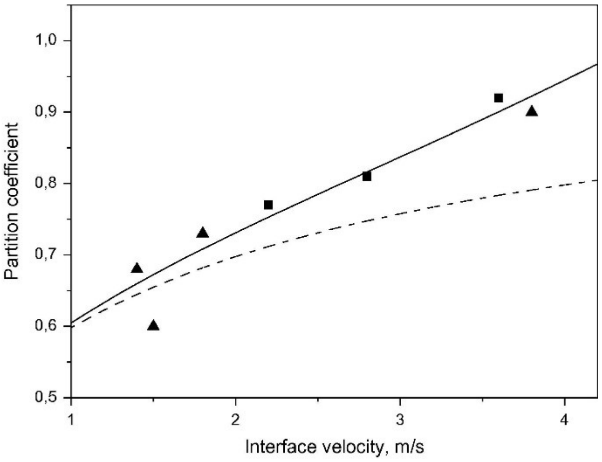

Figure 32 Partition coefficient as a function of interface velocity for Si-Ge alloys. Data points are experimental values. The dashed curve is k calculated with the CGM model. The solid curve is k calculated with the LNDM model [101]

converge and the solute drag effects can be dismissed. Sobolev [118] demonstrated that the solute drag effects have influence when V tends to the diffusive speed of the material (VD). VD is defined as the ratio of solute diffusivity at the interface to the interatomic distance. It is clear that the limit velocity (VD) (where the To curve is reached) varies for each material. For example: for Al-Fe systems it is 5 m/s [95] and for Al-Si systems it is 2.5 m/s [118]. Both values deduced from experimental results and analytical models. A review of some analytical models can be found in [98] but the LNDM and the Continues Growth Model [119] (CGM) are the most accepted in literature.

The partition coefficient also depends on the solidification velocity. Figure 31 and Figure 32 show the partition coefficient as a function of interface velocity [98]. These compare the analytical model LNDM, the CGM model with experimental values. We can see that LNDM shows a better correlation in the Si-As and Ge-Si alloys. Also, we can see two different values of the interface velocity: Si-As with 2.5 m/s and the Ge-Si alloy with 4.2 m/s. For these reasons as was shown in Figure 27, we define the liquidus and solidus slopes and partial coefficient as a function of solidification velocity when a rapid solidification occurs. Thus, the solidification velocity needs to be defined previusy.

We proposed define the solidification velocity expressed as function of the cooling rate as:

$$V_S = A_v \cdot CR^3 + B_v \cdot CR^2 + C_v \cdot CR + D_v \qquad (26)$$

where A, B and C are constant for the specific mixture and CR is the cooling rate in kelvin per seconds. These constants can be found in literature or using a quadratic fit in experimental data to obtain the constants as is illustrated in Figure 33. The validity of Equation 26 is limited for values of partitional coefficient K<1.

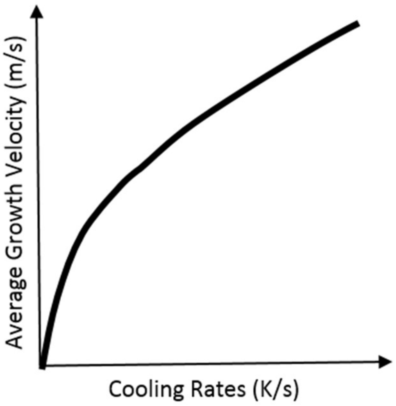

Figure 33 Solidification velocity as a function of cooling rate

In our algorithm the solidification velocity is controlled by the cooling rate imposed at the boundary condition. At each time step the cooling rate is updated and then the solidification velocity is determined using Equation 26. The first node closest to the boundary condition cools down fastest and starts to solidify, and the neighboring nodes that are more distant from the boundary condition solidify later. Then, the solidification velocity controls the progress of the phase transformation when a undercooled phase transformation occurs.

The model that we have developed takes into account the conclusions that Pryds et al [105] have suggested. As a consequence, in our model we define a critical value of the cooling rate. When the cooling rate overcomes this value the solidification velocity is set to a defined constant value. Unfortunately, these parameters are not found in literature. We infer them from experimental cooling curves.

Also, it can be possible to directly predict the amount of undercooling degree by the cooling rate present. Based in Equation 26; Equation 27 can be used:

$$\Delta Tu = A_T \cdot CR^3 + B_T \cdot CR^2 + C_T \cdot CR + D_T \qquad (27)$$

However, the use of Equation 27 to predict the undercooling degree does not define the solidification rate. Hence, the recalescence process can be defined by a solidification rate constant or can depend on the applied cooling rate. This solidification rate directly depends on the material and as mentioned previously, the solidification velocity can depend on the cooling rate present over the recalescence process.

Chapter 3 Methodology and mathematical model

This chapter aims to describe how the temperature field evolves during cooling of a phase change alloy and its solidification, with or without undercooling. Tracking the temperature field supplies the time evolution of latent heat discharge for a given cooling rate imposed by the operator. Discharge of latent heat is submitted to successive steps corresponding to distinct phenomena.

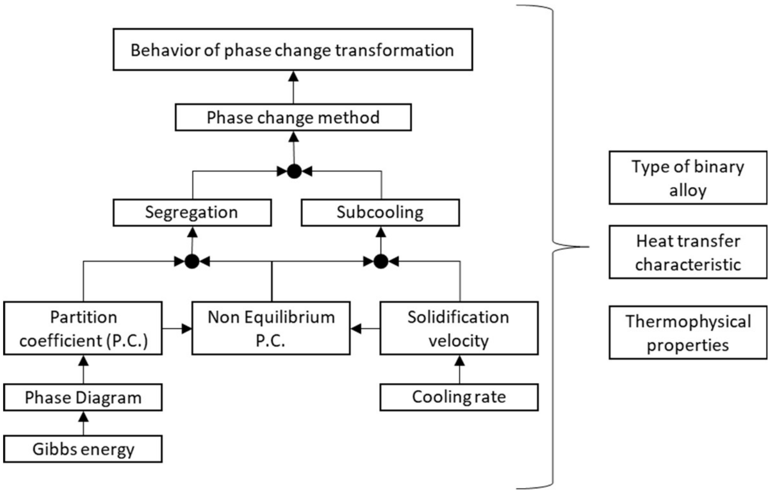

Figure 34 Relationship between phase change transformation the development of the method

Figure 34 illustrates the relationship between the different phenomena and the development of our method to predict them. At the extreme right, the three blocks comprising the method are shown. On the other side, each block defines a topic that need to be considered and defined: Gibbs free energy and phase diagram, partition coefficient, solidification velocity and cooling rate. The figure clearly shows that the performance of the binary alloy and its properties are intertwined and significantly influence each other. Clearly a large number of factors must be considered. For example, to define segregation, the partition coefficient in non-equilibrium must be defined. This in turn requires the equilibrium partition coefficient, which in turn is defined by the phase diagram. To extract this information from the phase diagram it is necessary to use the Gibbs free energy and the CALPHAD methodology. In the same way, undercooling depends on the solidification velocity, the non-equilibrium partition coefficient and the cooling rate.

The methodology consists in describing the models that have been chosen to represent the physical phenomena and the associated numerical methods to solve the temperature field in time. The material cooling (under liquid or solid states), the undercooling, the solidification and the recalescence are represented, depending on the cooling rate imposed by the operator. Since the cooling rate influences the occurrence of equilibrium or off-equilibrium solidification, these two possibilities must be considered in the general method. For the description of the model, the different steps have been split into Functional Blocks that represent the material behavior and the associated numerical method to evaluate the temperature field.

We develop our software to trace phase diagrams. This implements the CALPHAD method. The Functional Block named *FB-Calphad* corresponds to the information generated by this software. For the others Functional Blocks, we decided to implement the method into the commercial Software Ansys. However, all the Functional Blocks and the method can be implemented in other programming languages like C, C++, Fortran, or using commercial numerical codes (e.g. Ansys, Abaqus, Comsol).

Figure 35 shows the general architecture of the algorithm that gives the heat discharge in time, provided that the the user supplies suitable input information concerning the material properties and the cooling rate. This algorithm couples the different phenomena described in Chapter Two like undercooling or segregation that depend on cooling conditions. The results of this method aim to predict the material behavior for LHTES applications as a function of the cooling rate or replacing the phase change material with a more appropriate one. As mentioned previously, the general method is described as several Functional Blocks (FB). Each one is devoted to the resolution on one specific phenomenon. The relations between the successive functional blocks are submitted to particular conditions to activate it. Therefore, each FB is defined along with the input data necessary to activate it, mathematical modelling represented as a set of equations to solve and output data that will serve the next functional block as activation criterion or as input data.

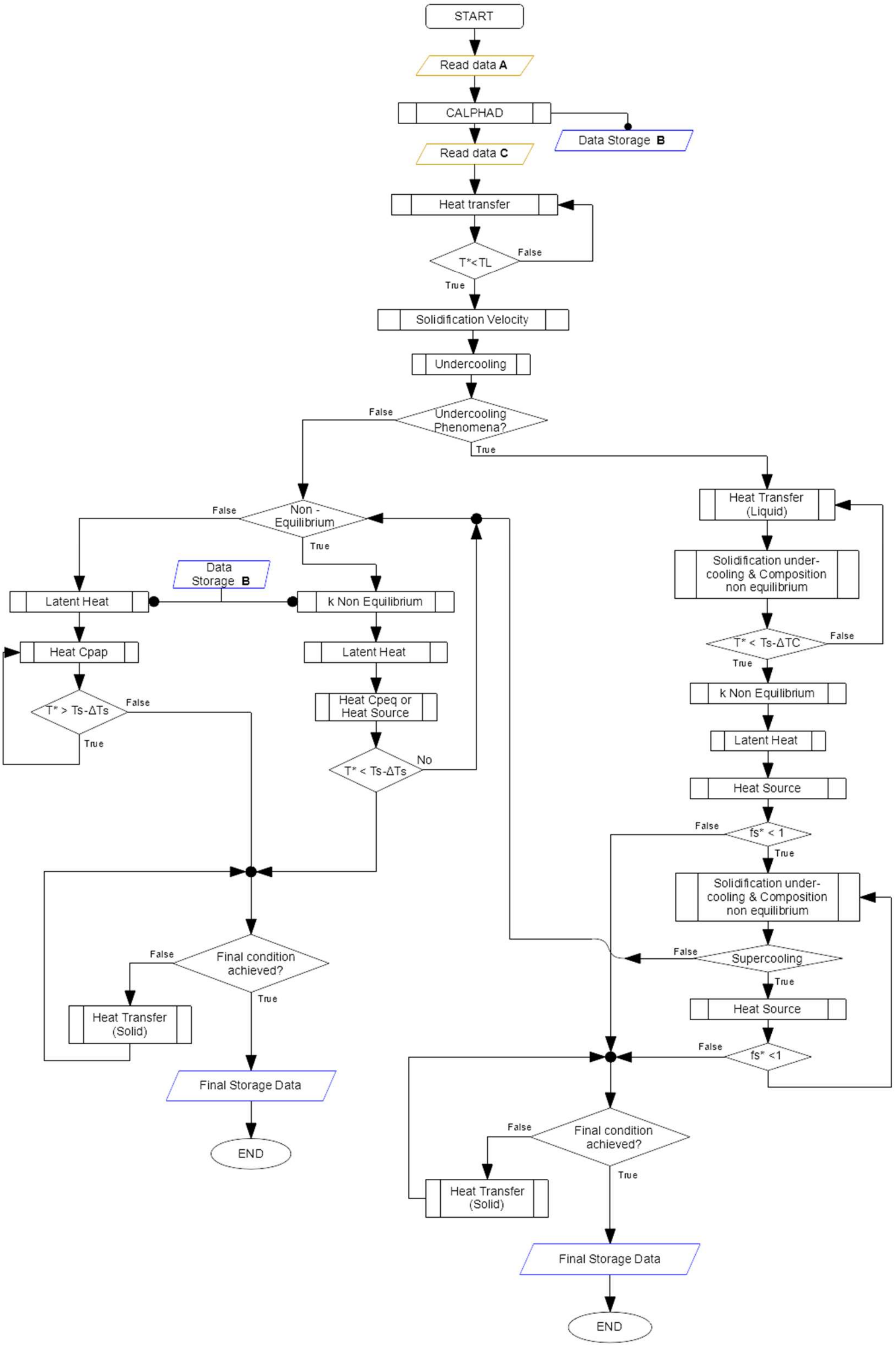

Figure 35 Algorithm of our method

3.1 General description of Functional Block

Each FB has its own function and finality. The process inside each FB can be seen as a black box needing input data and giving output data. The list of all the functional blocks is illustrated in Figure 36. The different components are:

- The required data (named Data Read) that can be generated by a previous functional block or given by the operator.
- Specific functions (Functional Block) that model the target phenomenon (with a specific name as illustrated on the right of figure 43)
- The output data (named Data Storage) obtained by the resolution of the set of equations and provided to the next functional blocks or corresponding to final data.

In this section, all the functional blocks are first described, followed by the development of the corresponding mathematical modeling.

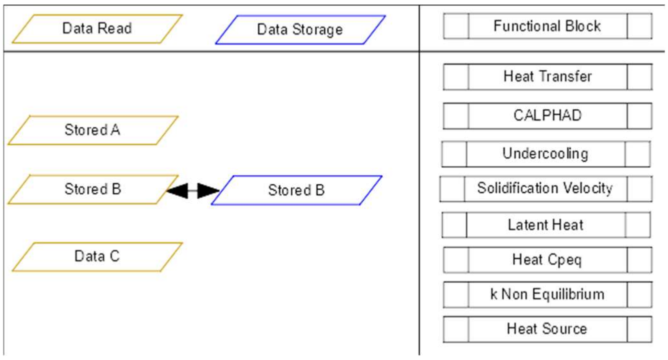

Figure 36 List of Functional Block of the method

3.1.1 Functional Block definition

FB-Calphad: This functional block aims to describe the phase diagram of a binary alloy. From this description, for a given temperature, the FB is able to estimate the liquidus temperature depending on the composition that corresponds to the beginning of solidification from an entirely liquid material. It also supplies the temperature corresponding to the end of solidification (eutectic or solidus temperature). It also gives the main characteristics of the phase diagram, the eutectic point, (temperature/composition) the liquidus slope that indicates the limit between entirely solid and liquid-solid material and the partition coefficient that defines the liquid-solid ratio. The FB-

Calphad calculations are based on the description of a binary alloy phase diagram under equilibrium considerations and for a given initial composition. For a cooling rate sufficiently slow an equilibrium solidification is an acceptable assumption and that solidification can be modelled directly from the phase diagram information in terms of composition and temperature. As a consequence, this functional Block does not consider undercooling, which will be described in another functional block.

The input of this functional block are:

- Initial temperature
- Initial composition

and the outputs are:

- liquidus temperature and slope
- Temperature of solidification: eutectic or solidus temperature
- Eutectic point: temperature and composition
- Partition coefficient in equilibrium

FB-Heat Transfer Liquid or Solid: This functional block aims to determine the temperature field in the material considered as an entirely liquid or solid domain. Under these considerations, phase change is not activated. Heat transfer is generated only by conduction in the solid and conduction and convection in the entirely liquid domain. This FB is solved through the energy equation that has been extensively studied and validated in literature. Many numerical codes are available to compute this FB. We implement this FB in Ansys software.

The input of this functional block are:

- Temperature of phase (liquid or solid)
- Thermodynamic properties

and the outputs are:

- Temperature of phase (liquid or solid)

***FB-Heat Cpap*:** When phase change occurs, the classical energy equation is not sufficient to estimate the temperature field. The aim of this functional block is to propose a method to estimate the solid fraction evolution assuming off-eutectic equilibrium solidification or that phase change operates at a constant temperature: the thermodynamic melting temperature Tm. Many techniques exist in literature to treat such a situation. The apparent heat capacity formulation is one of the preferred methods due to its simplicity and ease to implement in numerical simulation [120]–[123]. The main advantage of this method relies on the description of the latent heat during phase change in a small temperature interval around the melting temperature. Hence, by controlling the interval thickness the phase transformation will be a quasi-static isothermal process [124]. Since the latent heat is explicitly described as a function of temperature, generally in polynomic form, it can be included in the heat capacity term, resulting in an equation of the same form as the energy equation of FB-Heat Transfer Liquid or Solid.

The input of this functional block are:

- Melting temperature Tm
- Thermodynamic properties
- Temperature interval for the phase change
- Latent heat

and the outputs are:

- Temperature

FB-Heat Source: In many cases phase change occurs in a non-isothermal situation. This FB aims to solve the solid fraction evolution with a numerical method based on the description of the phase change with a source term that represents the heat released or trapped during solidification added to the classical energy equation [125], [126]. If non-isothermal phase change is considered with undercooling, this functional block replaces the previous one (FB-Heat Cpap). This FB operates from the low temperature undercooled material (Ts) to the melting temperature T_m. Both temperatures define the undercooling degree ($\Delta T=T_m-T_s$). The source term adds the latent heat released in the term source, then the temperature increase during solidification by recalescence.

The input of this functional block are:

- Melting temperature Tm

- Thermodynamic properties
- Solid/Liquid fraction
- Amount of latent heat added at the source term

and the outputs are:

- Temperature
- Solid/liquid fraction

***FB-Solidification velocity*:** This functional block aims to relate the cooling rate with the solidification velocity. Figure 37 shows three hypothetical phase transformations at different cooling rates. The first case a) corresponds to equilibrium solidification. For the second case, b), the cooling rate is high at the beginning and the undercooling degree is more significant. Once the solidification has begun the heat propagation into the material implies a temperature increase. As mentioned before, the solidification velocity decreases if the cooling rate decreases as many sources have stated [72], [105], [127], [128]. An amount of the latent heat during the phase transformation is used to raise the temperature to Tm. For c) in Figure 37 the cooling rate is stronger in comparison with the cases a) and b) and undercooling phenomena are notorious. The phase front propagation is inhibited by a stronger solidification velocity despite the high cooling rate. Hence, a distinct temperature plateau is formed. If the thermophysical properties favorize a faster heat transport (fast compared with the solidification velocity), the melting temperature is not reached during the phase change and the plateau is suppressed.

Natural convection plays an important role during solidification. This internal liquid movement takes an amount of heat released during the phase transformation and diffuses it to the surroundings. Hence, when convection phenomena are stronger, they homogenize the internal temperature, as studied by Solomon et al [83] (see Figure 24). Also, the interactions

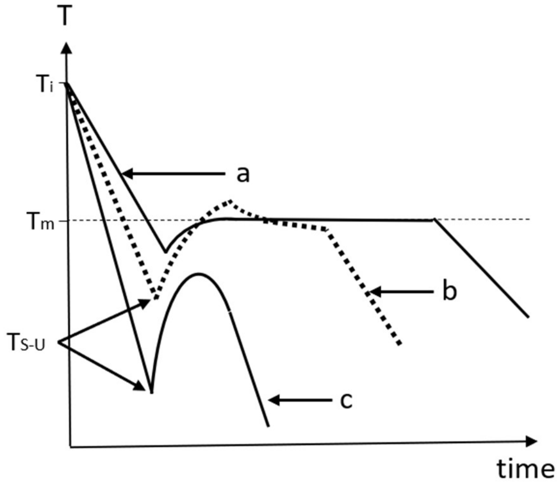

Figure 37 Three hypothetical cooling a) Equilibrium solidification. b) Undercooling solidification, a quantity of liquid fraction is used to raise temperature to the melting temperature. c) Strong cooling rate, solidification velocity is faster in comparison with the other two. The heat released is not enough to raise the temperature to the melting temperature. Ti is the initial temperature. T_m *is the melting temperature.* T_{S-U} *is the undercooled temperature where the phase change begins.*

between solidification velocity and convection phenomena depend on thermophysical properties. For example, natural convection can reduce heat transport.

For off-eutectic composition alloys Figure 38 shows three cases: 1) cooling curve for an equilibrium solidification, where at T_L the phase change begins and finish at the eutectic temperature Te; 2) cooling curve for a non-equilibrium solidification and segregation, where the phase change starts at T_L and the undercooling degree is dismissed on macrosegregation problems; 3) non-equilibrium solidification with undercooling, where the solidification begins at T_{L-U} and the eutectic temperature is undercooled at T_{S-U}. Under this case, if the latent heat released reduces the cooling rate before the eutectic temperature, the undercooling degree can be avoided and the phase change will finish at the eutectic temperature as is shown on case 1 or 2.

Defining the relation between cooling rate and solidification velocity for binary systems is a hard task. We did not find research where this relation is properly studied and where the relation between cooling rate and solidification velocity in function of composition change is defined. Almost all studies define other relations (e.g. solidification velocity/microstructure), but they rarely

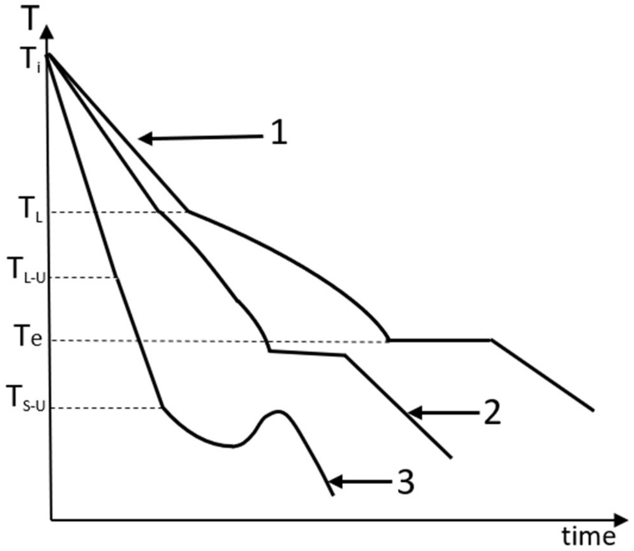

Figure 38 Different cooling curves for a non-eutectic composition. 1 Equilibrium solidification; 2 Non-Equilibrium solidification without undercooling; 3 Non-equilibrium solidification with undercooling. T_L is the equilibrium temperature to start the solidification. T_{L-U} is the undercooled temperature where the solidification begins, Te is the eutectic temperature and Ts-u is the eutectic temperature undercooled

report imposed cooling rates. Moreover, small samples are used to limit convective phenomena, which is a very significant phenomenon and should be considered.

The effects of the cooling rate on solidification times are usually found in studies on paraffins including segregation and solidification velocity phenomena. For almost all alloys this information is usually not reported whereas the imposed cooling rate is necessary to obtain an equilibrium phase transformation.

The input of this functional block are:

- Cooling rate
- Temperature
- Constants for the specific mixture (Equation 26)

and the outputs are:

- Solidification velocity for the specific mixture at the cooling rate present

***FB. Undercooling*:** This functional block is dedicated to the estimation of the undercooling degree (ΔTu). This is estimated thanks to the previous functional block (FB-

Solidification velocity). This is a function of alloy CR, thermophysical properties and composition. The undercooling degree ∆Tu is the difference between the ideal equilibrium temperature of phase change Tm in Figure 37 or T_L in Figure 38 and the temperature undercooled to starts the solidification ($T_{s\text{-}u}$ in Figure 37 or $T_{L\text{-}U}$ in Figure 38). As mentioned previously, the phase diagram is not sufficient to correctly describe the material temperature and the phase transformation behavior when undercooling phenomena is present. Then for a given temperature initial composition and liquidus slope (from FB-Calphad), the variation of material composition is calculated with FB k non-Equilibrium with FB Solidification velocity.

The input of this functional block are:

- Non-equilibrium composition
- Thermophysical properties
- Initial composition
- Solidification velocity
- Non-equilibrium partition coefficient
- Non-equilibrium liquidus slope
- Peclet solutal number
- Dendrite tip radius
- Ivantsov function
- Or if is the case, the constants for the specific mixture (Equation 27)

and the outputs are:

- Undercooling degree

FB--k non-equilibrium: If the cooling rate is high enough to induce a non-equilibrium solidification, it is necessary to add modifications to the composition behavior during phase transformation. The estimation of a partition coefficient and the liquidus slope from the FB-CALPHAD is not sufficient to correctly describe the solid fraction evolution; in such circumstances solidification is not completely obtained from the phase diagram that reproduces only the equilibrium state. The composite material species diffusion during the transformation affects the solidification behavior which can be altered by segregation. Based on the information generated by the FB-Calphad and the solidification velocity, this FB estimates the variation of composition and the subsequent variation in latent heat. Segregation may occur at different space scales. The microsegregation is directly linked to the composition variation and is used to predict macrosegregation. The macrosegregation gives information of composition variation at macro scale and can be calculated using the formulations described before (Scheil Gulliver, Brody and Flemings and Koyabashi) and in function of solidification velocity. As a consequence, the properties of the phase diagram must be modified when undercooling occurs.

The input of this functional block are:

- Initial composition
- Solidification velocity
- Diffusive speed
- Thermophysical properties of the mixture
- Equilibrium partition coefficient
- Equilibrium liquidus slope

and the outputs are:

- Non-equilibrium composition
- Non-equilibrium partition coefficient
- Non-equilibrium liquidus slope
- Peclet solutal number
- Dendrite tip radius
- Ivantsov function

***FB-Latent heat*:** The aim of this functional block is to estimate the latent heat discharge knowing the solidification velocity and the composition variation. From FB-Calphad, the composition change is estimated during solidification as a function of temperature and initial composition. Moreover, thanks to the FB-k non-equilibrium the composition can be predicted when undercooling effects are present, which alters the latent heat discharge time evolution. This released het is calculated in function of the liquid to solid transformation for a non-isothermal phase transformation. In the case of an isothermal transformation, the FB-Latent heat is linked to the FB-Heat Cpap since this one estimates the solid fraction evolution for an equilibrium solidification.

The input of this functional block are:

- Latent heat of mixture and for each element on the composition
- Initial composition
- Current temperature T*
- On isothermal phase change, the range of temperature for the phase transformation
- Liquidus slope (equilibrium or non-equilibrium)
- Partition coefficient (equilibrium or non-equilibrium)
- If is the case: Ivantsov function, solidification velocity and diffusive speed.

and the outputs are:

- Amount of latent heat released during the phase transformation

Read and Storage data. The previous functional blocks need different kinds of information to run correctly. Some must be supplied directly by the operator (the numerical code user), whereas some others come from the calculations of a previous functional block. The data provided by the operator concern the domain geometry, some material thermal properties or some numerical parameters like the suggested mesh grid size. These input data can be separated into three main topics:

Initial condition (IC): initial temperature distribution in the domain and boundary conditions that affect the cooling rate.

Material properties (MP): These represent the thermodynamic and physical properties. Some of them can be taken as constant or in function of temperature. They can also depend on the phase as liquid and solid can exhibit different properties. In the next chapter the MP are defined depending of phase transformation type.

Mesh and time step (MT): An overwhelming number of numerical methods to solve the governing equations are based on a linearization from the time and space discretization. The solution accuracy depends on the mesh size and time step as they directly impact the derivative terms of the governing equations. Detailed discussions can be found in literature [129]–[131] on the numerical methods based on coupled space and time discretization. The mesh covers the entire domain that represents only the phase change material. Basically, even if the procedure (succession of functional blocks) suits all kinds of numerical discretization (finite elements or finite volumes), we have decided to propose a finite volume discretization, as it fits well with the source term and the apparent capacity methods.

Phase diagram (PD): this topic gives all the information necessary to describe the equilibrium transformation, mainly the liquidus and solidus temperatures, the composition changes, the partition coefficient, the Gibbs free energy and the eutectic point (by composition and temperature).

3.1.2 Solidification undercooling & off equilibrium

Figure 39 represents the algorithm sequence to calculate the undercooling degree. *Solidification undercooling & off equilibrium* englobe these 4 blocks necessary to estimate the undercooling degree:

- FB-Calphad to describe the equilibrium phase diagram
- FB-Solidification Velocity (to model the solidification process
- FB-k non-equilibrium to consider a cooling rate influence
- FB-undercooling to estimate the undercooling degree

These are grouped as a new FB and this calculates solidification velocity, their respective compositions, non-equilibrium partition coefficient and undercooling degree. The input data for this algorithm (Figure 39) are:

- The current temperature (T*) obtained as a result of the heat transfer simulation (*FB-Heat Transfer*)
- The cooling rate, extracted from the *FB-Heat transfer*, defined as the rate of cooling per second into the element that arise the melting temperature.

Concerning the *FB solidification velocity* (see Figure 39) contains the function that relates the cooling rate with the solidification velocity.

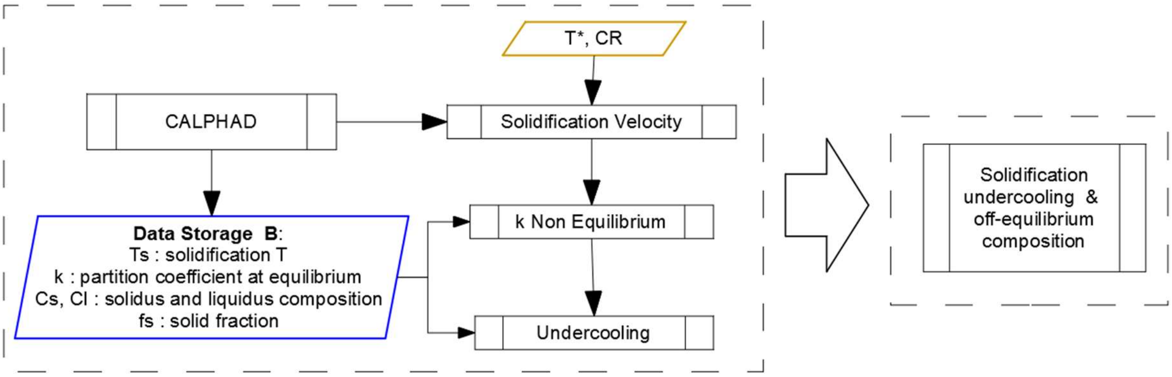

Figure 39 Routine defining the amount of undercooling

3.2 Description of FB mathematical modelling

For all functional blocks specific equations and expressions have been introduced to supply information on the temperature, solid fraction and composition evolutions in time and space. Many numerical developments have been conducted in this thesis. Their applications have been carried out using the commercial CFD code ANSYS Fluent[18]. This commercial finite volume package uses the Design Modeler and ANSYS Meshing for the creation of geometry and meshing respectively. The ANSYS Fluent model is a 2-D model. FLUENT can be used to solve fluid flow problems involving solidification.

Instead of tracking the liquid-solid front explicitly, we use an enthalpy-porosity formulation [132]. Essentially, the liquid-solid mushy zone is treated as a porous zone with porosity equal to the liquid fraction and appropriate momentum sink terms are added to the momentum equations to account for the pressure drop caused by the presence of solid material. The liquid-solid interface is not tracked explicitly. The local liquid fraction is estimated in each cell of the domain and at each time iteration based on an enthalpy balance. The nodes where the liquid fraction is between 0 and 1 correspond to the liquid solid interface position. With that, the movement of the phase change interface is tracked by the specification of a nodal liquid fraction.

The use of phase diagrams to calculate the liquid fraction and the heat released assumes the existence of a thermodynamic equilibrium for the alloy, which is a true condition under low cooling rates and equilibrium solidification. The use of the Scheil equation in the calculation of the latent heat release requires solving a species equations system constituted of N equations for N alloy components for an off-eutectic composition, as was explained in the use of Gibbs free energy and phase diagrams. Also, the purpose of this study is not to model the grain growth or the morphological microstructure and their effect on the heat release. Instead, the purpose is to show how the latent heat released is affected by different cooling rates, temperature distribution, fluid patterns and solidification patterns from the point of view of LHTES.

3.2.1 Solution procedures Fluent Ansys

Fluent Ansys software solves the governing integral equations for mass, momentum and energy. A control-volume-based technique is used that consists of:

- Division of the domain into discrete control volumes using a computational grid.
- Integration of the governing equations on the individual control volumes to construct algebraic equations for the discrete dependent variables (unknowns) such as velocity, pressure, temperature and conserved scalars.
- Linearization of the discretized equations and solution of the resulting linear equation system to yield updated values of the dependent variables.

The governing equations are solved sequentially (Momentum, Continuity and finally Energy). Because the governing equations are non-linear (and coupled), several iterations of the solution loop must be performed before a converged solution is obtained.

Linearization

The discrete, non-linear governing equations are linearized to produce a system of equations for the dependent variables in every computational cell. The resulting linear system is then solved to yield an updated flow-field solution. The governing equations are linearized with an “implicit" form with respect to the dependent variable (or set of variables) of interest. For a given variable, the unknown value in each cell is computed using a relation that includes both existing and unknown values from neighboring cells. Therefore, equations are compiled and must be solved simultaneously to give the unknown quantities.

A point implicit (Gauss-Seidel)[18] linear equation solver is used in conjunction with an algebraic multigrid (AMG) method to solve the resultant scalar system of equations for the dependent variable in each cell. The procedure of these methods in Ansys Fluent can be found in the theory solver manual for Ansys [18] and dedicated books as [133].

Spatial Discretization

Ansys Fluent uses a control-volume-based technique to convert the governing equations to algebraic equations that can be solved numerically. Figure 40 illustrates the component of a cell. This is an example of such a control volume. Discretization of the governing equations is applied to each cell in the computational domain. Then, Ansys Fluent stores discrete values of the scalar solution at the cell centers (see Figure 40). However, face values are required for the

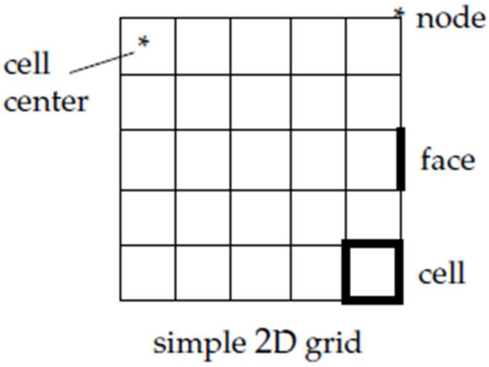

Figure 40 Mesh Components

convection terms, and these are interpolated from the cell center values. This is accomplished using an upwind scheme.

Time Discretization

The time-dependent equations must be discretized in both space and time. The spatial discretization for the time-dependent equations is identical to the steady-state case. Temporal discretization involves the integration of every term in the differential equations over a time step Δt. The integration of the transient terms is straightforward, as shown below. A generic expression for the time evolution of a variable is given by:

$$\frac{\partial \phi}{\partial t} = F(\phi) \tag{28}$$

If the time derivative is discretized using backward, the first-order accurate temporal discretization is given by:

$$\frac{\phi^{n+1} - \phi^{n}}{\Delta t} = F(\phi^{n+1}) \tag{29}$$

where ϕ is a scalar quantity, n+1 is the value at the next time level (t+Δt), n is the value at the current time level (t), $F(\phi^{n+1})$ is evaluated at the future time level.

Pressure Interpolation Schemes

The body-force-weighted scheme is used in all the simulations [133]. This scheme is good for high-Rayleigh-number natural convection flows. Our simulations are expected with natural convection but the point where the flow becomes fully turbulent is unknown a priori. The body-force-weighted scheme computes the pressure values at the faces by assuming that the normal acceleration of the fluid resulting from the pressure gradient and body forces is continuous across each face. This works well if the body forces are known explicitly in the momentum equations, and in this situation the buoyancy calculations are used.

As another recommendation, the PRESTO! Scheme should be used for cavities with high swirling flows with natural convection [133]. The PRESTO! Scheme uses the discrete continuity equation to calculate the pressure field on a mesh that is geometrically shifted so that the new cell centers are where the faces of the ordinary mesh are placed, this means that the pressures on the faces are now known. Because we use buoyancy calculations and the Reynolds numbers are unknown a priori, the body-force-weighted scheme is used.

The momentum and continuity equations are solved sequentially. The continuity equation is used as a pressure equation. It is clear that pressure does not appear explicitly for incompressible flows since density is not directly related to pressure. To introduce the pressure into the continuity equation, the SIMPLE algorithm (Semi-Implicit Method for Pressure-Linked Equations) [133]. is used. This reduces the computational time for laminar flux and converges more quickly.

In order to proceed further, it is necessary to relate the face values of velocity to the stored values of velocity at the cell centers. Linear interpolation of cell-centered velocities to the faces results in unphysical checker-boarding of pressure. In Ansys Fluent, we use a procedure based on the Rhie and Chow work [134] to prevent checker boarding. The face value of velocity is not averaged linearly; instead, momentum weighted averaging is performed.

Pressure-velocity coupling is achieved in the Ansys Fluent software using the SIMPLE-pressure-velocity coupling algorithm. The SIMPLE algorithm uses a relationship between velocity and pressure corrections to enforce mass conservation and to obtain the pressure field.

Algorithm solver

The solver in Fluent uses a solution algorithm where the governing equations are solved sequentially. Because the governing equations are nonlinear and coupled, the solution loop must be carried out iteratively in order to obtain a converged numerical solution, illustrated in Figure 41. These steps are continued until the convergence criteria are met.

The numerical modeling is based on the following assumptions:

- The transport processes are laminar
- The properties of the solid or liquid phases are homogenous and isotropic.
- The solid regions are rigid and thermal stress is not considered.
- The density for the solid phase is constant and for the liquid phase, the Boussinesq approximation is applied.
- Any casting defect is not considered: gas porosity, shrinkage defects, pore formation or mold contamination.
- Initial temperature is uniform and all the domain is in the liquid phase
- The problem is two-dimensional
- No impurity or external nucleation agents are considered
- The model uses atmospheric pressure and the liquid domain is incompressible

The integration of FBs into the ANSYS Fluent is achieved through the User Defined Functions (UDFs)[18]. UDFs allow us to customize ANSYS Fluent. Essentially UDF is a function written in C programming language and compiled into the Fluent program to be executed into the simulation process and perform new task.

The UDF is used to define material properties, source terms, initial solution and the internal process to define parameters that will be used in the different FBs. The UDF uses macros provided by ANSYS Fluent. These ANSYS Fluent macros allow us to access solution process data and functions at every step of the resolution. Figure 42 illustrates the solution process using these UDFs in ANSYS Fluent. The variables solution is stored at cell center location where data is stored (See Figure 40) where every cell has an identification ID used to access or provide the cell information

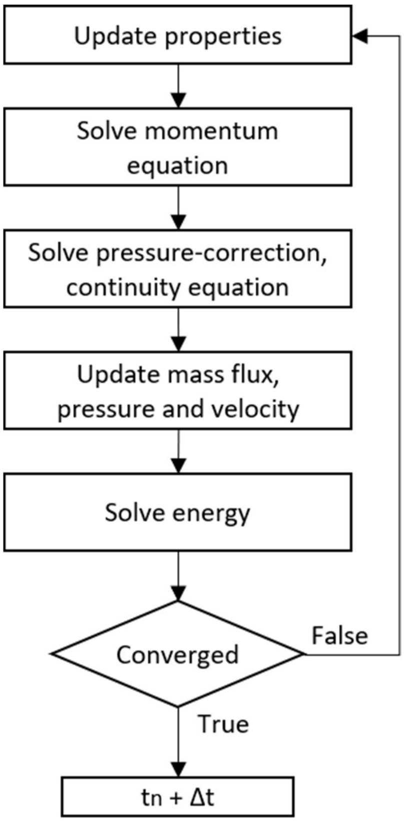

Figure 41 Algorithm for each numerical iteration used in the Ansys Fluent Software

The FB integrated into this UDF are:

- FB-Heat Cap
- FB-Heat Source
- FB-Solidification velocity
- FB-k non-equilibrium
- FB-Latent Heat

The UDF file can be found in the Annex 3 UDF File.

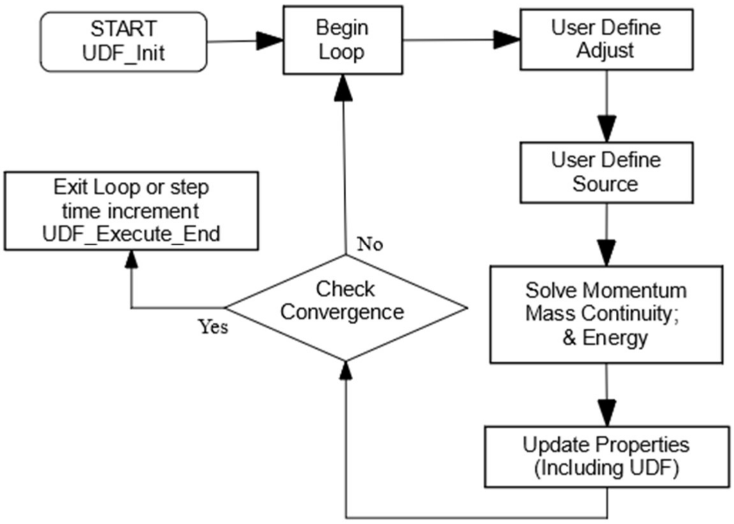

Figure 42 Solution procedure integrating UDFs (only for ANSYS Fluent)

3.2.2 FB-Calphad

The works of Gaye et al. [135], [136] are the bases to apply Newton-Raphson techniques on phase diagrams. These principally use experimental techniques to calculate equilibrium points and trace the phase diagram as a function of temperatures. The graphical procedure is illustrated in Figure 11. Based in these works, Cahn and Carter [137] developed the construction of phase diagrams tracking the Gibbs free energy during mixing of two or more phases with convex hull representation for chemical equilibrium.

The use of these computational libraries enables calculating the thermochemical equilibrium from compound representation of free energy functions. Equations 1, 9, 10, 14, 15, 16 are the mathematical basis to trace the phase diagram.

Equation 15 is highly important because it is the source of the Gibbs free energy of a pure element:

$$G = a + bT + cTlnT + \sum_{2}^{n} d_n T^n \tag{15}$$

As described before, a, b, c and d are the parameters that drive the temperature dependence of the Gibbs free energy of a pure element in a particular phase. The next step is to integrate the Equation 14 for a single-phase alloy. This equation is expanded into its constituents (π phases) by the expression:

$$G_{sys}(T) = \sum_{i}^{\pi} G_i(T) \tag{30}$$

Where $G_{sys}(T)$ is the total Gibbs free energy of the binary system for all its constituents, and $G_i(T)$ is the Gibbs free energy of the constituent i (Equation 14). Then, the thermodynamic function for phase equilibrium calculations is expressed as a linear combination of the chemical potential (Equation 16) of each component c in each constituent π:

$$0 = \sum_{i}^{\pi} \sum_{j}^{c} n_{ij} \mu_{ij} \tag{31}$$

Where n_{ij} and μ_{ij} are respectively the number of moles and chemical potential of component j in constituent i. The chemical potential is defined by the partial derivative of Gibbs free energy (Equation 30) with respect to xi as G'. The equilibrium composition results from satisfying Equation 16. Equation 32 contains the information where a single tangent line intersects the Gibbs free energy curve at the phase equilibrium compositions xi for the constituent i≠i+1.

$$\left(\frac{\partial G_{sys}}{\partial x_j}\right)^{i} = \left(\frac{\partial G_{sys}}{\partial x_j}\right)^{i+1} \quad j = 1, \dots, c \quad i = 1, \dots, \pi - 1 \tag{32}$$

Figure 43 illustrated the values of the minimization of Equation 30 and the chemical potentials of Equation 32 for an initial composition z and two constituent i and i+1. The values of composition x_1 for the constituent i and i+1 are the phase composition in equilibrium.

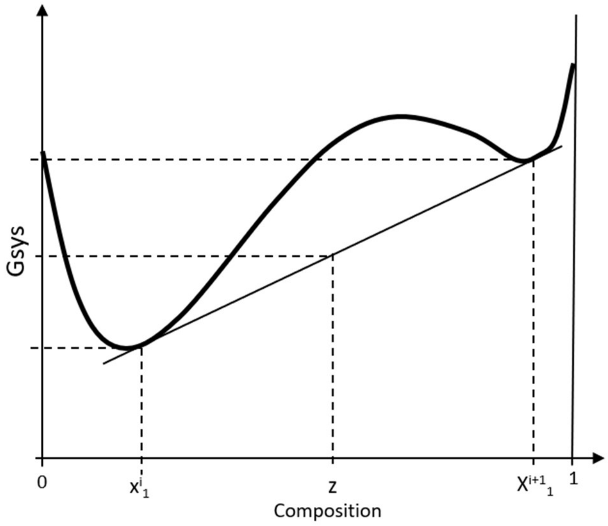

Figure 43 The Gsys function of composition at constant T, with a representation of the tangent plane.

As was shown in Figure 13 and Figure 43, the equilibrium system can be found by tangent line intersects. Accordingly, it is necessary to find a non-negative set of values x_i that minimizes Equation 30 and satisfies the mass balance constraint:

$$\sum_{i}^{\pi} n_{ij} = x_i n_F \quad , \qquad j = 1, \dots, c$$

$$0 \leq n_{ij} \leq x_i n_F \quad , \quad i = 1, \dots, \pi \quad j = 1, \dots, c \tag{33}$$

where n_F is the total number of moles in the binary system and x_i is the mole fraction of component j.

Hence, the equilibrium conditions in a closed system with one mole of atoms at a given temperature T and at constant pressure requires the minimization of Equation 30 and finding the constrained amounts of compositions to solve the nonlinear systems of Equations 31, 32 and 33.

In the present work, the convex hull algorithm has been implemented in a python script subroutine based on the works of [53], [54], [138]. It uses a number m of binary composition samples (composition between 0-1) to calculate chemical potential and Gibbs free energy minimization with the nonlinear system of Equations 31, 32 and 33 to calculate the chemical potential by the Gibbs free energy minimization. The library of the convex hull algorithm and the computational improvement by the Quick-hull algorithm can be found in the open source code, Python [139]. The source code for both is integrated into the library Scipy [55]. These libraries aim to estimate the chemical potential, temperature and composition that minimize the Gibbs free energy. For each couple, Composition/Temperature, the material phase is then defined.

We develop an in-house script in Python code to plot the phase diagram of binary compounds alloys and to define the solidification behavior in equilibrium. It also gives the partition coefficient, liquidus and solidus temperatures, eutectic compositions and temperature field.

The main advantage to trace the phase diagram using the SGTE databases [17] is that we can modify or add the thermodynamic information associated and develop an adequate software for our purposes. Another advantage using the present software is the integration of the solidification modelling by initial composition based on the lever rule and/or the Scheil-Gulliver model.

The general architecture of own script is illustrated in Figure 44. The .TDB file contains all the information of Gibbs free energy in its standard representation. The Cu-Ag binary mixture and Al-Si alloy TDB raw file can be found in Annex 1 as an example of the structure of this type of files.

The construction of the binary model is the representation of the molar Gibbs free energy function for each phase. This procedure requires the minimization of Equation 30 and finding the constrained amounts of compositions to solve the nonlinear systems of Equations 31, 32 and 33. The convex hull and Quick hull algorithms are implemented for all the variation of compounds and temperature to estimate the chemical potential, composition, eutectic temperature, eutectic composition, enthalpy and entropy, relative to the minimal Gibbs free energy. When these parameters are calculated for all coordinates (composition-temperature), the phase diagram is traced.

This code is associated to a graphical user interface we have coded to easily supply all the information of interest. In Annex 2 Phase Diagram Software the use of our software is explained in detail.

The data obtained from the phase diagram performed by our software are:

- Solidus and Liquidus temperature
- Eutectic temperature

- Partition coefficient
- Slope liquidus
- Solidus and eutectic composition

These data are used into the subsequent Functional Block described in the method.

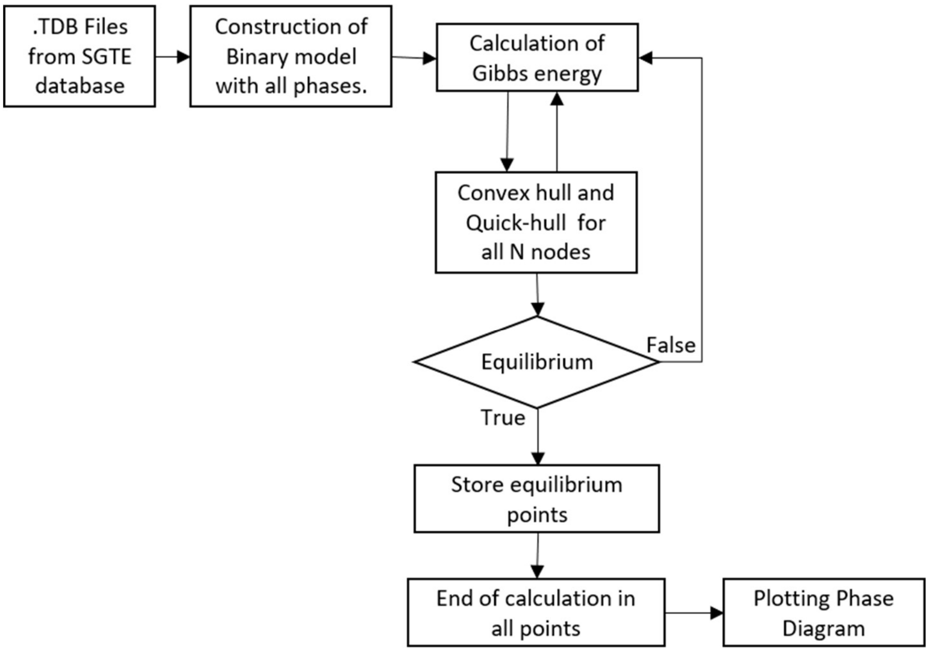

Figure 44 General algorithm to trace the phase diagram of a binary alloy

3.2.3 FB-Heat Transfer Liquid and Solid

This Functional Block aims to determine the temperature field as a function of time considering that no phase change occurs (completely liquid or solid domain). The Functional Block is based on the resolution of the classical energy equation that gives the temperature field. The resolution of the governing equations is carried out with the finite difference method using the commercial CFD code ANSYS Fluent performed as described before.

This block requires the heat capacity, the thermal conductivity and the density for the solid and liquid phases. As a result, this gives the temperature field in time and the local cooling rate in the whole domain.

The liquid phase is potentially submitted to fluid flow. The determination of the liquid velocity is based on conservation laws. The mathematical representation of the liquid region without phase change was assumed to be Newtonian and incompressible. The numerical discretization and solution implemented is outlined below.

Mass Conservation Equation

The equation for conservation of mass (also called the continuity equation) for an incompressible fluid reduces to:

$$\nabla \cdot \vec{v} = 0 \tag{34}$$

Momentum equation

Transport of momentum in the ith direction in an inertial (non-accelerating) reference frame is described by the Navier-Stokes equations. The Boussinesq approximation is valid if the density variation is small, and it provides faster convergence than other temperature dependent models. This model assumes constant density in all the terms of the momentum equation except for the body force term where it is modeled based on a reference density (ρ_o) at the reference temperature (T_o) and the volumetric expansion coefficient (β). With these considerations, the momentum equation is defined as:

$$\begin{gathered} \frac{\partial}{\partial t}(\rho_o \vec{v}) + \nabla(\rho_o \vec{v}\vec{v}) = -\nabla P + \nabla \cdot (\bar{\bar{\tau}}) + \rho_o \beta (T - T_o)\vec{g} + \vec{F} \\ \bar{\bar{\tau}} = \mu(\nabla \vec{v} + \nabla \vec{v}^T) \end{gathered} \tag{35}$$

where P is the static pressure, F contains the source terms, $\bar{\bar{\tau}}$ is the stress tensor, v is the flow velocity which depends on time and space and μ is the viscosity.

Energy equation

The energy equation for a fluid region can be expressed by:

$$\rho_o Cp \frac{\partial T}{\partial t} + \nabla \cdot (\rho_o CpT\vec{v}) = \nabla(\gamma \nabla T) + S \tag{36}$$

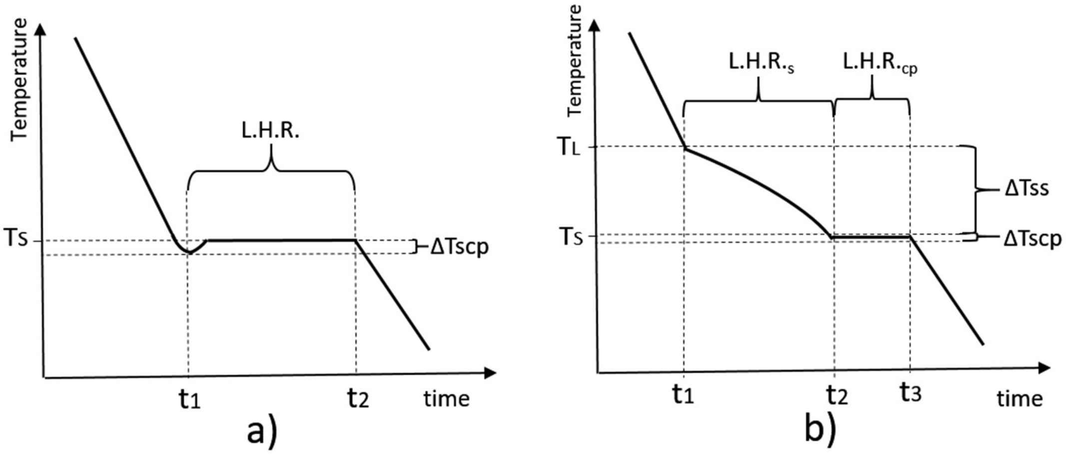

Figure 45 a) Isothermal solidification at the eutectic point. b) Range of temperatures at which solidification takes place (case a & b in Figure 46)

Where γ is the thermal conductivity, ρ is the density, Cp is the specific heat and T is the temperature. S is the source term that includes any volumetric heat sources. Without phase transformation S=0. In solid regions, where $\vec{v} = 0$, a simple conduction equation is solved that includes heat flux due to conduction and the source term (without phase change) is zero (S=0)

Many sources can be cited about how the resolution is done [140]–[142]. The diffusion in the solid is taken as null (Ds=0). This means that when a finite region completely solidifies, the composition does not change.

3.2.4 Heat Transfer during the phase change: FB-Heat Cpap & FB Heat Source

When solidification begins, the material starts to release a quantity of heat (latent heat). This heat is considered in the energy equation with two different methods: *i) Apparent Heat Capacity Method (AHCM) for isothermal phase transformation and ii) Heat Source Method (HSM) for non-isothermal phase transformation.* Each method is integrated into two Functional Blocks: FB-Heat Cap that involves the AHCM and the FB-Heat Source.

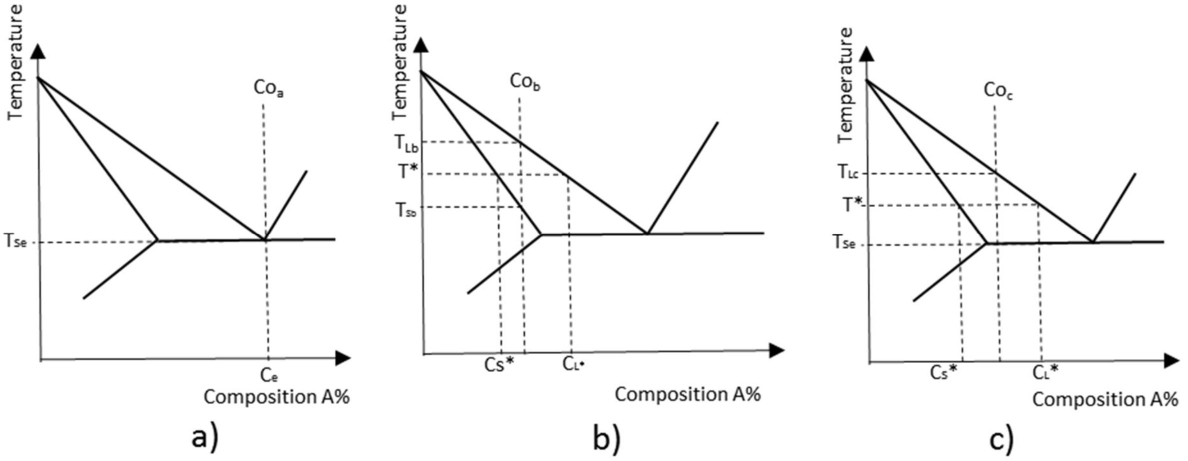

Figure 46 Different types of equilibrium solidification according to the initial composition. a) Eutectic composition, b) & c) hypo-eutectic composition

These two Functional Blocks are expressed as a function of the initial composition. Figure 46 shows a hypothetical eutectic phase diagram section with three different initial compositions. This illustrates the difference between a eutectic solidification (diagram a) with an initial composition Co_a and two hypo-eutectic solidifications with composition Co_b and Co_c (diagram b & c respectively) where T* is an arbitrary temperature between the liquid phase and solid phase. T_{La} & T_{Lb} are temperatures at which solidification begins, T_{se} is the eutectic temperature and T_{se} & T_{sb} are the temperatures when solidification ends. CL* and CS* are compositions at temperature T* for the liquid and solid respectively.

FB-Heat Source is used when the solidification has a undercooling degree. When the temperature rises until equilibrium temperature for case b and c in Figure 46, the rest of liquid is added to the FB-Heat Cap. For equilibrium solidification or segregation (Scheil Gulliver model) without undercooling, the FB-Heat Cap is used.

Figure 45 illustrates the cooling curve for these three cases: a) shows the eutectic solidification, where all the latent heat is released near the eutectic temperature (Ts) within a narrow interval of temperatures ΔT_{Scp}.

For an off-eutectic composition, the phase transformation (case b in Figure 45) has two transitions. The first occurs between the liquidus and solidus temperature, and the second occurs for the remaining liquid that solidifies at the solidus temperature (Figure 46 c diagram) or eutectic temperature (Figure 46 b diagram).

The phase diagram is used to define the liquidus and solidus temperature off eutectic composition and eutectic temperature for eutectic compositions.

Momentum equation in phase change

For the numerical solution of the momentum equation of the phase transformation, the porosity model developed by Brent et al. [132] is applied. In this model the entire domain is considered as a pseudo porous medium where the liquid fraction is introduced into the momentum equation. This takes the value of 1 in the liquid phase and 0 in the solid phase. The liquid fraction has a value between 0 and 1 for the phase transformation in the finite region. A source term representing the porous media is added to Equation 35, where the there is a pressure loss due to the solidification of the alloy. This additional source [132] is expressed as:

$$\vec{F} = \frac{(1-f_l)^2}{f_l^3+\epsilon} vA_{mush} \tag{37}$$

and Equation 35 is defined for the phase transformation as Equation 38:

$$\frac{\partial}{\partial t}(\rho\vec{v}) + \nabla(\rho\vec{v}\vec{v}) = -\nabla P + \nabla\cdot(\bar{\bar{\tau}}) + \rho_o\beta(T-T_o)\vec{g} + \frac{(1-f_l)^2}{f_l^3+\epsilon} vA_{mush} \tag{38}$$

where ε is a small computational constant used to avoid division by zero. *Amush* is a constant reflecting the mushy zone morphology that describes how steeply the velocity is reduced to zero when the material solidifies, this constant is a large number usually between 10^4 and 10^7. A value of 10^5 is commonly used. When the material in a cell is completely solidified, the porosity becomes zero and the velocity drops to zero.

As a cell can exhibit a totally or partially liquid and/or solid state, the average physical parameters are weighted with the liquid and solid fractions f_L and f_S as follows:

$$\begin{aligned} &f_L + f_S = 1 \qquad \rho = f_L\rho_L + f_S\rho_S \qquad \gamma = f_L\gamma_L + f_S\gamma_S \\ &V_L = (ui + vj)f_L \end{aligned} \tag{39}$$

Where subscripts S and L denote solid and liquid respectively. ρ is density of alloy, γ is the thermal conductivity of alloy and V_L is the velocity vector on liquid phase from their component ui and vj.

Local solute redistribution equation

When equilibrium solidification is supposed, complete diffusion in liquid and solid is assumed and no segregation phenomenon occurs. Therefore, the lever rule (Equation 48) is used to define the local average composition or the phase diagram data can be used directly.

As described before, when K<1 solute atoms are rejected from the solid/liquid interface. These rejections form a boundary layer which has higher solute than of the liquid bulk. If no convection phenomenon is supposed, the diffusion and solidification velocities control the solute redistribution. This is usually referred to as microscale phase transformation.

At macroscale, the basic assumption is that liquid diffusion is very rapid (D=∞), which is often true when convection in the liquid is present. This condition represents almost all experimental cases of macro phase transformation.

The Scheil Gulliver Equation 49 uses the assumption of no diffusion in the solid and infinite diffusion in the liquid. The differential time form of Equation 23 is expressed by:

$$f_L \frac{\partial C_L}{\partial t} = Co(1-k)\frac{\partial f_s}{\partial t} \tag{40}$$

When the natural convection is added in Equation 40 based on their work of Flemings and co-workers [143], [144]. They derived a local solute redistribution equation relating the change in liquid volume fraction, within the volume element to the change in liquid composition within the element and the local flow velocity vector, Equation 41:

$$f_L \frac{\partial C_L}{\partial t} = Co(1-k)\frac{\partial f_s}{\partial t} - V_L \nabla C_L \tag{41}$$

Equation 41 indicates that the variation of solute in the liquid phase at a given volume element should be equal to the net loss or gain of solute due to interfacial reaction (Scheil model) and convection phenomena. The diffusion boundary layer assuming constant diffusivity is included in Equation 41, then Equation 42 is defines as:

$$f_L \frac{\partial C_L}{\partial t} = Co(1-k)\frac{\partial f_s}{\partial t} - V_L \nabla C_L + \nabla(D\nabla C_L) \tag{42}$$

After completing the solidification, the phase composition does not change. Equation 42 is the most accepted to predict the solutal distribution in macrosegregation. Experimental segregation results are very close to the Scheil Gulliver calculation when the diffusivity in solid is much smaller than the solidification velocity. Equation 42 is widely used for the prediction of the solutal solid phase like in foundry applications. An increase in solidification velocity tends to reduce the boundary layer significantly and the solutal composition tends to increase. This change due to high solidification velocity is included in the partition coefficient (FB k non-equilibrium). The maximum solidification velocity is at the critical point of complete solute trapping (k=>1).

3.2.5 FB-Heat Cap

When referring to an abrupt liquid solid interface (equilibrium phase change), Stefan problems are usually mentioned. The Stefan problem involves the solidification or melting of a pure material and is characterized by a distinct moving phase change boundary at which a heat balance condition has to be met. A detailed derivation of the governing equations for the Stefan problem can be found in Crank's book [145]. In a heat-conduction-controlled Stefan problem the domain of interest consists of a solid region and liquid region separated by a sharp-moving interface (Γ(t)) which coincides with the phase change temperature isotherm T=Tm. Then the Stefan condition is the heat balance at the solid/liquid moving interface.

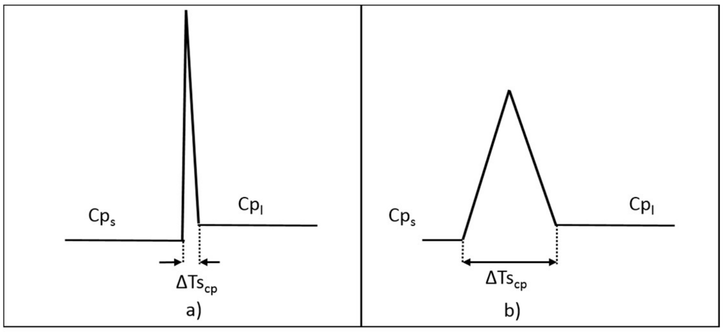

Figure 47 Variation of heat capacity using the apparent heat capacity in the interval ΔTscp, a) Eutectic composition; b) non-eutectic composition

Different methods exist to solve the Stefan condition, the one implemented in our method is the Apparent Heat Capacity Method (AHCM). The main objective of the Apparent Heat Capacity Method (AHCM) is to include the latent heat into an apparent heat capacity (Cp_{ap}) term in a narrow interval of temperatures (ΔT_{Scp}) as shown in Figure 47. Cp_{ap} replaces the heat capacity in energy Equation 36

For isothermal solidification (e.g. paraffins or pure elements) the range ΔTScp is a small difference of temperature between the liquid and solid phase, illustrated in Figure 48. The amount of latent heat released (L^{cp}) added to the Cp_{ap} is obtained using the expression:

$$L^{cp} = L^{ab} fl_l \tag{43}$$

Where fl_r is the remaining liquid fraction at the beginning of the isothermal phase transformation (for eutectic composition fl_l=1) and L^{ab} is the material latent heat. Then the Cp_{ap} can be calculated with:

$$Cp_{ap} = \left(\frac{L^{cp}(fl_r)}{\Delta T_{scp}} + Cp_{ls}\right) \tag{44}$$

The amount of latent heat liberated by alloy solidification is assumed to be proportional to the fraction of formed solid. The amount of latent heat for the alloy (L^{cp}) and the fraction of solidified material (fs) are calculated using the *FB-Latent heat*. Cp_{ls} is the heat capacity of liquid (Cp_l) and solid (Cp_s) in the mixture calculated with the expression:

$$Cp_{ls} = Cp_s fs + Cp_l(1 - fs) \tag{45}$$

Using the energy equation described before (Equation 36); the heat capacity during the isothermal solidification is defines by Equation 46:

$$Cp = \begin{cases} Cp_L & T > T_m + \Delta T_{scp} \\ Cp_{aq} & T - \Delta T_{scp} < T_m < T + \Delta T_{scp} \\ Cp_S & T < T_m - \Delta T_{scp} \end{cases} \tag{46}$$

where T_m is the melting temperature, or the eutectic temperature in eutectic compositions.

A bad selection of the temperature range ΔT_{Scp} would result in computational errors and simulation distortion of the real problem. It is largely recommended to verify that this range agrees with the type of composition simulated. For equilibrium eutectic composition, ΔT_{Scp} should be as small as possible (shown in Figure 47.a) usually <2K; but if an isothermal generic material is present (ex: paraffins), ΔT_{Scp} can become larger in comparison with an equilibrium isothermal composition. In paraffins we found that literature [120], [146] uses a ΔT_{Scp} between 2 and 5K., as shown in Figure 47. These variations can drastically affect the behavior of thermal storage material. In our simulation for alloys we use ΔT_{Scp} = 2K, for other materials ΔT_{Scp} = 5K is used.

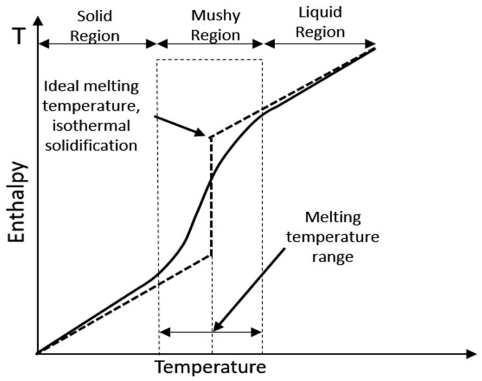

Figure 48 Enthalpy-temperature performance curve for ideal and common PCMs

In Equation 45, for off eutectic equilibrium solidification the solid or liquid fractions can be obtained by the lever rule, given by the Equation 22:

$$f_s^T = \frac{T_L - T*}{(T_{MA} - T*)(1-k)} \qquad 22$$

Where f_s^T refers to the solid fraction in the entire domain (see Figure 49).

The use of the AHCM for a long freezing range alloy requires additional consideration. The heat capacity for any alloy at off eutectic composition and equilibrium solidification is obtained using Equation 47:

$$Cp_{ap} = L\frac{df_s^T}{dT} + Cp_{ls} \qquad (47)$$

The variation of the AHCM with temperature was determined experimentally by Veinik [147]. As described before, it is known that in off eutectic binary alloys a significant portion of solid can be formed below the liquidus temperature. Figure 49[148]illustrates the solidification for two off eutectic solidification in equilibrium. In both cases, the phase transformation starts below the liquidus temperature and the remaining liquid solidifies at the eutectic temperature (left) or solidus temperature (right), as can be seen in Figure 49.

The amount of latent heat is provided by the FB-Latent heat. Assuming that the amount of latent heat delivered by solidifying alloy is proportional to the solid fraction formed and differentiating Equation 22 with respect to T and substituting into Equation 47:

$$Cp_{ap} = L^{cp}\frac{T_{MA} - T_l}{(T_{MA} - T*)^2(1-k)} + Cp_{ls} \qquad (48)$$

where L^{cp} is the latent heat of the binary alloy and varies according to the phase diagram. This latent heat considers the variation of composition in the phase transformation. This is defined in the FB-Latent heat by Equation 80. The main difference between Equation 46 (Stefan consideration) and Equation 48 is the ΔT_{Scp} assumption. Equation 48 is defined by the phase diagram for equilibrium solidification of an off-eutectic calculation. In Equation 46, a small temperature range is defined and then the latent heat release is linearized between these small temperature ranges (<5K).

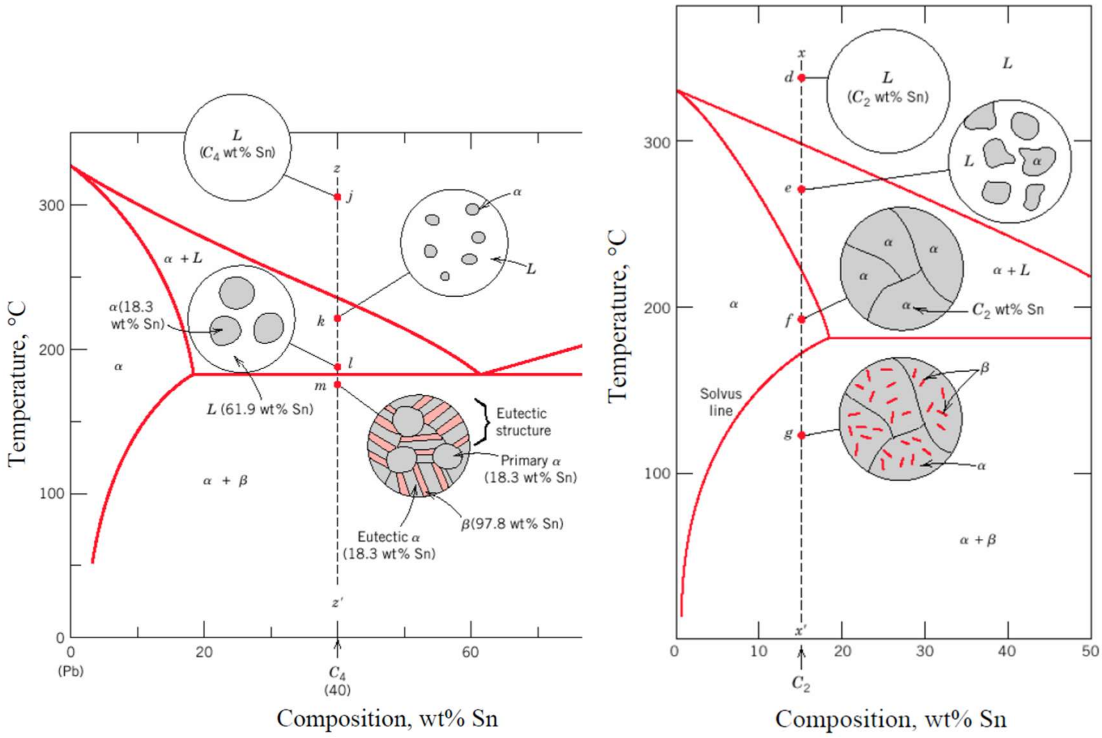

Figure 49 Phase diagram for Sn-Pb with off eutectic solidification. Left, solidification starts at the liquidus temperature at the initial composition and finishs the phase transformation at the eutectic temperature. Right, solidification starts at liquidus temperature and finishs at its solidus temperature. [153]

The basic assumption for a non-equilibrium solidification without undercooling is that liquid diffusion is very fast (uniform composition in liquid) and the diffusion in solid is null. For a phase transformation without undercooling the solidification starts at the liquidus temperature following the phase diagram information. Then, since there is no diffusion in solid, a concentration gradient will be established between the initial solid composition kCo and the solid composition at the intermediate time (with calculated temperature T∗), which is CS∗ (illustrated in Figure 19 case B). In the liquid zone, the composition is homogeneous and equal to CL∗ > Co since diffusion was considered infinite. The composition of solid will continue to grow and at the end of solidification the solid composition finally reaches the maximum solubility defined in the phase diagram at the eutectic temperature. This off-eutectic solidification behavior is illustrated in Figure 20. The maximum solubility is identified as C_{SM} in Figure 19 case B. The basic equation based on solid fraction is known as the Scheil-Gulliver model (Equation 23), [45], [95] defined as:

$$Cs = kCo(1 - fs)^{k-1} \tag{23}$$

Without undercooling, the kinetic solidification is calculated with the Scheil equation instead of lever rule. According to the Scheil model, the solid fraction is defined by Equation 24:

$$f_s^T = 1 - \left[\frac{(T_M - T_L)}{(T_M - T*)}\right]^{\frac{1}{1-k}} \tag{24}$$

When fs=1, Equation 24 calculates Cs=∞ (k <1), but the composition of the solid can only increase to the maximum solid solubility in the binary composition (C_{SM}.), illustrated in Figure 22 case b. This limit value of solubility is obtained by the phase diagram (FB-Calphad). The Equations 24 and 23 knows as Scheil-Gulliver model are largely accepted for alloys transformations[45], [95].

Following the same procedure as for Equation 48, Cp_{ap} is also proportional to the solidified fraction. Differentiating Equation 24 with respect to T and substituting into Equation 43, the expression for the AHCM off equilibriums without undercooling is defined by Equation 49:

$$Cp_{ap} = L^{cp} \frac{(T_{MA} - T_l)^{\frac{1}{1-K}}}{(1-k)(T_{MA} - T*)^{\frac{2-k}{1-k}}} + Cp_{ls} \tag{49}$$

Where L^{cp} is the latent heat at a non-equilibrium composition. Equation 49 does not consider the change in the composition during solidification. The arguments described for Equation 84 are used in the FB-Latent heat. We can write Equation 49 using AHCM in a non-equilibrium solidification, off-eutectic, as:

$$\begin{aligned} Cp_{ap} = & \frac{(L_B - L_A)kCo}{(1-k)(T_{MA} - T_l)} \left[\frac{T_{MA} - T_l}{T_{MA} - T*}\right]^{\frac{k}{1-k}} \\ & + \frac{L_A}{(1-k)(T_{MA} - T_l)} \left[\frac{T_{MA} - T_l}{T_{MA} - T*}\right]^{\frac{1}{1-k}} + Cp_{ls} \end{aligned} \tag{50}$$

An implicit method is used to compute Equation 50. The calculated temperatures are solved by an iterative scheme described above in 3.2.1.

The FB- Latent heat gives the variation of latent heat that will be included in Equations 48 and 49. The partition coefficient, liquidus temperature and solidus temperature are obtained by the FB-Calphad. The FB Heat Cap and its methods are incorporated into Fluent with the User Defined Functions (UDFs) method.

Although the Scheil-Gulliver equation is largely accepted, some other models exist. A summary of these models and the associated assumptions are presented in Table 2. The main difference between these models and the Scheil equation (Equations 24 and 23) concerns the assumptions on the diffusivities in liquid and solid and the sample size that activates convection. Our work is focused on solving the Scheil Gulliver equation and the corresponding assumptions.

3.2.6 FB-Heat Source

The source method has become more popular because this method can be easily implemented or adapted to existing numerical codes. Also, the overall accuracy for non-isothermal phase change problems is fairly good with a high computational efficiency, since the latent heat is directly linked to the temperature of the discretized element. This method was initially proposed by [149], [150] and their entire formulation implemented into a finite element scheme can be found in [129], [151], [152].

This method consists in adding any heat from a particular behavior to the energy equation as an extra term. In our methodology, the source term is the quantity of latent heat delivered during solidification. Usually, the energy equation with a source term is expressed by Equation 36. The second term S is the heat generation as:

$$S = \frac{\partial fs}{\partial t}\, L^{ab} \qquad (51)$$

where L^{ab} depends on the local composition solidification rate ($\partial f_s^T / \partial T$). The latent heat effects are naturally activated only in phase change zones. S is calculated with FB-Latent heat where composition variations are considered.

While considering undercooling effects, a material region submitted to phase change does not release the latent heat at the equilibrium melting temperature but keeps it below this value.

Equations 48 and 49 cannot be used in such a case. The solidification rate ($\partial fs/\partial t$) is controlled by the solidification velocity and the heat released is considered as a heat sink (see Figure 28). This heat raises the temperature of the alloy surrounding the phase front. Depending on the transport properties of liquid and solid alloy, the temperature can increase in the phase front to the melting temperature. However, if heat transport is slow compared with the solidification, the propagation of the phase front is inhibited and a distinct temperature quasi-plateau is formed. If the heat transport is fast compared with the solidification, the melting temperature is not reached during the phase change, and the plateau is suppressed. Also, it is assumed that the solidification velocity depends on cooling rate, so the heat released changes due to the imposed cooling rate. Then the rate of solidification varies spatially.

The FB-Solidification velocity is used to calculate the solidification velocity. Then, the FB k non-equilibrium and FB-Undercooling are used to define the liquid fraction that will be added to the source term. This procedure is represented in Figure 55.

3.2.6.1 Numerical solution

The resolution of temperature and solid fraction from the source term method is based on the succession of several steps and an iterative algorithm. The assumptions are:

- The simulation onset with a complete liquid phase and a temperature in all the domain over the solidification temperature. Hence the source term is zero.
- An undercooling degree is present.
- The solidification process begins at least at the third time iteration, since the CR equation (Equation 59) uses temperatures at two previous time steps. This defines the solidification velocity at the third time iteration (Vs) Equation 26.
- Solidification starts at the coolest zone (boundary cooled) cells situated at the wall boundary.
- Then, the phase transformation for cells away from walls is controlled by Vs and the heat transports.
- Shrinkage allowance is not considered.

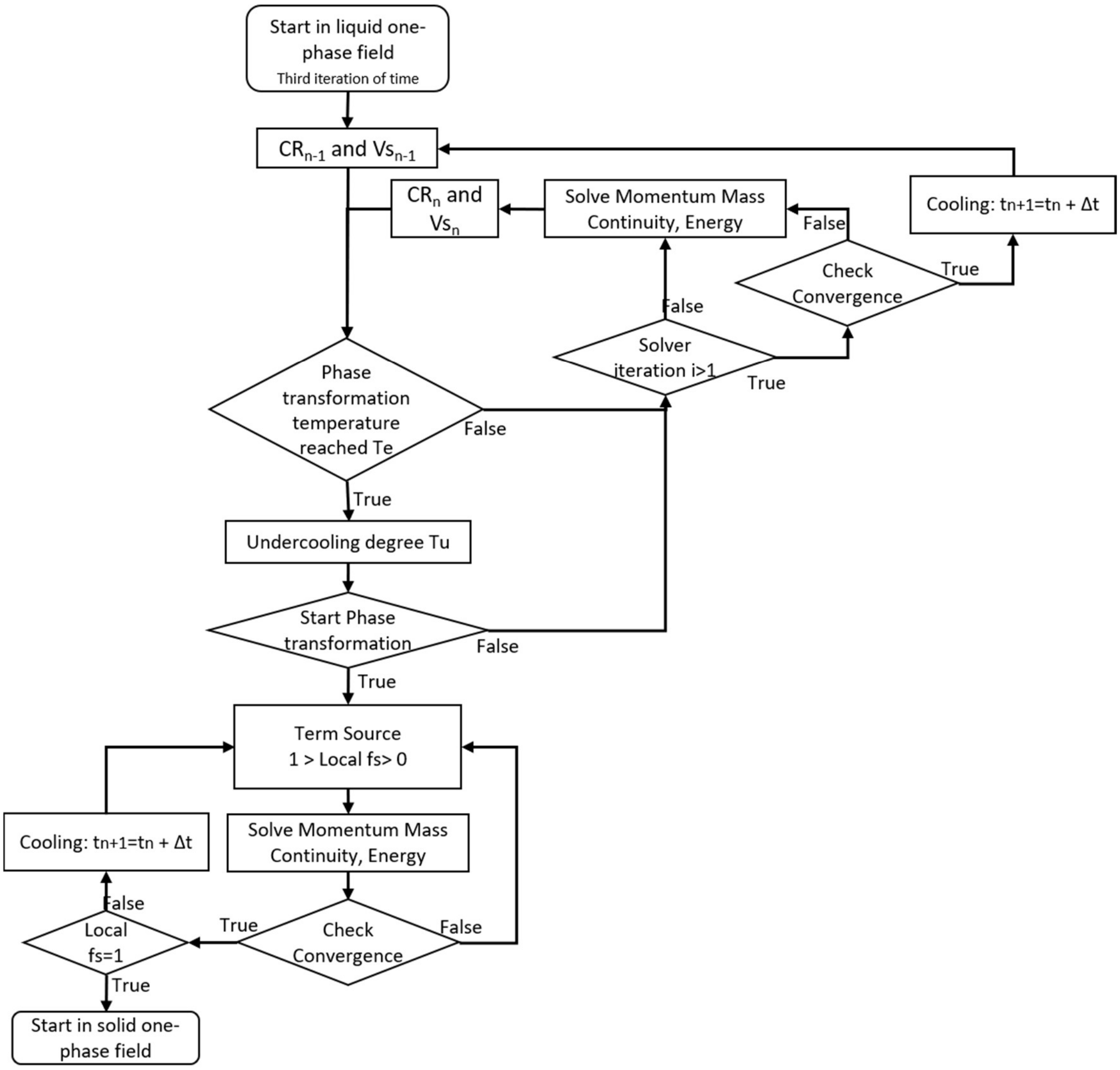

Figure 50 Algorithm to calculate the solid fraction in cells at the cooled wall frontier

From FB-Calphad the following are known: the temperature for the onset of solidification (equilibrium temperature Te) and CR_{n-1} and Vs_{n-1}, T_{n-1} from previous time iteration (n-1) for the discretized element. Figure 50 shows the algorithm to calculate the beginning of solidification on boundary cells to define the source term. This algorithm describes the process for cells on the wall boundary.

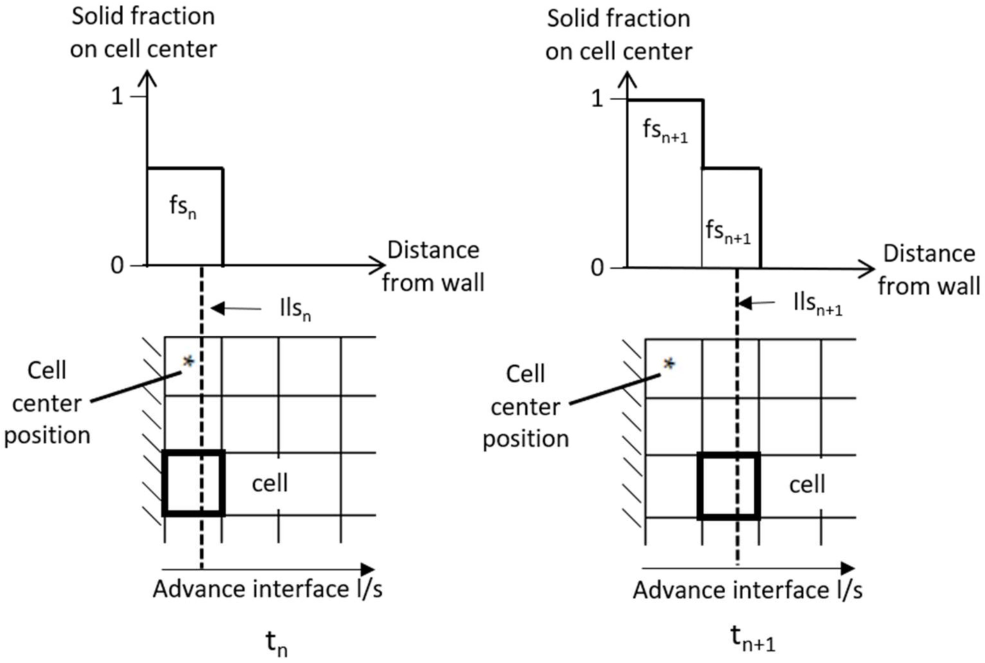

Figure 51 Advance of the liquid/solid front. Left at time tn, right at time t_{n+1}

If T_{n-1} reaches the solidification temperature the undercooling degree is calculated and a new undercooled temperature is calculated at solver iteration i ($T^i u$). This $T^i u$ defines the onset of the undercooled solidification.

If T_{n-1} does not reach $T^i u$, the solver runs a numerical iteration (i+1) and solves the governing quations (34, 35,36) algorithm shown in Figure 50. Then the CR and Vs are updated at the solver iteration (i+1) and evaluated at the time step (n). Now, if T_n is under Te (ot Tm), the undercooling degree is calculated. Then $T^{i+1}u$ is updated at the i+1 numerical iteration.

If $Tu<T_n<Te$, the tolerance factor controls the convergence of the nonlinear solver. If the converge criteria are met, it advances to the next time step.

Starts of solidification

At the time iteration n, if T_n or T_{n-1} =< Tu<Te the undercooling degree is achieved and solidification starts. Equation 57 expresses the local solid fraction thanks to the calculated solidification velocity. Then if Vs is solved at the first solver iteration (i), Vs_{n-1} is used. Otherwise, following the algorithm in Figure 50 Vs is calculated at the i+nth iteration, then Vs_n is known. The time at which the solidification occurs (ts) is stored and this is used to calculate the advance of the interface liquid/solid (lls) defined by:

$$Ils_n = Vs(t_n - t_s) \quad , \quad tn > ts \tag{52}$$

Ils is the movement of the interface through the domain. The time ts is defined only when the boundary cell (wall cells) starts to solidify (Figure 51).

Equations 34, 38 and 36 are solved and the convergence criterion is evaluated. Vs remains constant for the entire local undercooled solidification velocity. Once solidification has started, the interface boundary goes forward at the same calculated solidification velocity (Vs). Equation 57 expresses the local solid fraction at each time iteration, this is defined at the cell center. Then, the source term of expression 51 is estimated and introduced into the energy equations (Equation 36) to compute the temperature Tn+1. The last section of the algorithm in Figure 50.

After that the solidification started at the time *ts*, Ils (Equation 52) advance at a constant solidification velocity over the domain. The left of Figure 51 shows the liquid/solid interface advance on the 2D grid cells at the instant tn>ts according to Equation 57 fs >0 at instant tn at the cell center.

In Figure 51, the right side shows the advance of Ils position from Ils_n to Ils_{n+1}. The next cell starts to solidify if Ils_{n+1} is greater than the cell center position (CC) normal to the wall boundary minus Δx/2. Then, the local solid fraction for a cell beyond the wall boundary is estimated with the expression:

$$fs_n = \frac{Ils_n}{CC + \left(\frac{\Delta x}{2}\right)} \quad , \quad Ils_n > CCP - \left(\frac{\Delta x}{2}\right) \tag{53}$$

Where CC is the normal cell center position to wall. Equation 53 express the local solid fraction at each iteration time beyond the cell adjacent to the wall boundary.

Cooling rate over two walls

One special situation occurs when two different cooling rates are imposed on the left and bottom 2D grid. Figure 52 shows the 2D domain where a CRx is imposed on the left (x-axis direction and a CRy is imposed bottom (Y-axis direction). With $CR_x > CR_y$, the liquid solid interface advances at a different solidification velocity ($Vs_x \neq Vs_y$). Consequently, Equations Equations 52 and 53 under these conditions are expressed by:

$$\begin{aligned} Ils_{n;\,x} &= Vs_x(t_{nx} - t_s) \\ Ils_{n;\,y} &= Vs_y\left(t_{ny} - t_s\right) \end{aligned} \tag{54}$$

$$\begin{aligned} fs_x &= \frac{Ils_{n;\,x}}{CC_x + \left(\frac{\Delta x}{2}\right)} \\ fs_y &= \frac{Ils_{n;\,y}}{CC_y + \left(\frac{\Delta y}{2}\right)} \end{aligned} \tag{55}$$

$$fs = fs_x + fs_y(1 + fs_x) \tag{56}$$

Where subscripts x and y refer to left and bottom phase front respectively and fs is the solid fraction in the cell. CR is calculated independently with Equation 59 for the bottom and left walls. The solidification velocity for both walls is calculated with Equation 26. Equations 54 and 55 defines the solid fraction for each solidification velocity. Figure 52 shows both solid fractions ($fs_x \neq fs_y$) over the cell at the j position. Then Equation 55 express the local solid fraction in each axis direction. Equation 56 is used to express the solid fraction at the cell element. Then, the source term Equation 51 is estimated and introduced into the energy equation (Equation 36) to compute the temperature T_n.

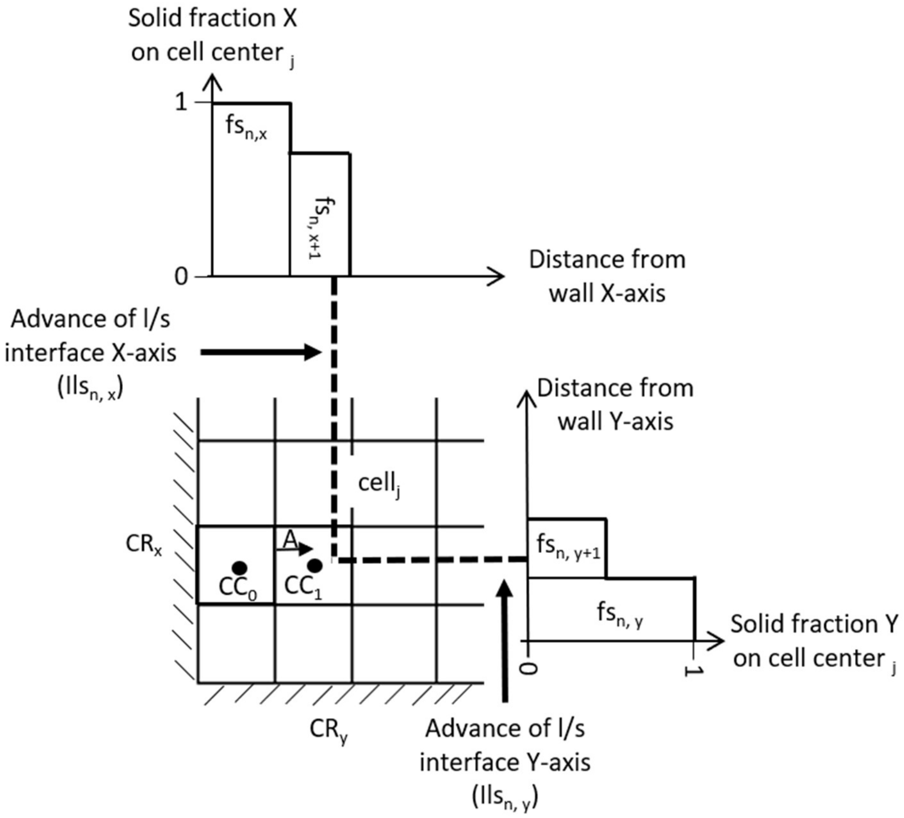

Figure 52 Liquid/solid (l/s) front interface over the domain for two different CR imposed at the left and bottom domain

Figure 53 shows the algorithm to define the source term depending on the cell position. At the beginning, Vs is calculated at the first numerical iteration with the CR_{n-1}. For the subsequent numerical iteration, CR_n is used to define Vs. Following the algorithm in Figure 53, the undercooling degree is calculated for wall cells. Otherwise, the position of the solid/liquid interface is evaluated. For wall cells Equation 57 is used to estimate the solid fraction. To start the solidification in cells at the wall (shown in Figure 51 and Figure 52) Equations 54 is evaluated. If the condition: $Ilsn > CC-\Delta x/2$ is true, solidification starts in the evaluated cell. Hence Equations 55 and 56 defines the solid fraction added into the source term. The sequences described in Figure 50 and Figure 53 are implemented in the UDFs script into the Ansys Fluent software for solving the undercooling phase transformation.

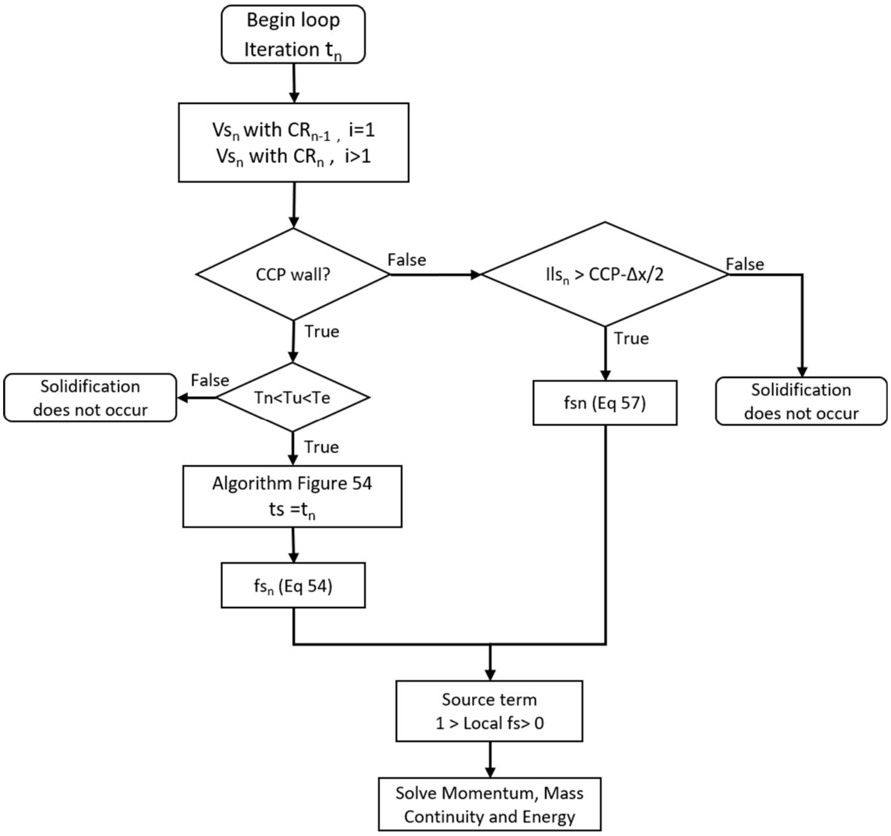

Figure 53 Algorithm for selection of cells to define source term

3.2.7 FB-Solidification velocity

As discussed before, the solidification velocity is function of the cooling rate (CR) and can be expressed by Equation 26:

$$V_S = A_v \cdot CR^3 + B_v \cdot CR^2 + C_v \cdot CR + D_v \qquad (26)$$

Hence, the solidification velocity is added to a discretized element by the rate of solidification expressed by Equation 57:

$$fs_n = fs_{n-1} + \frac{\Delta t \cdot V_s}{\Delta x} \qquad (57)$$

where fs_n is the solid fraction at the time n, Δt and Δx are the time step and discretized element size and V_s [m/s] is the solidification velocity.

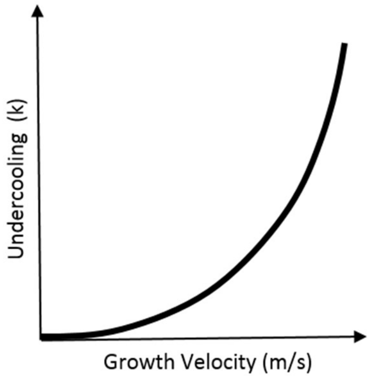

Figure 54 Undercooling vs growth velocity. This relation is only under ideal conditions. Impurities or mixture degradation could modify it

Experimental research [70], [72], [98], [105], [107] demonstrated that when the cooling rate is high enough to reach complete solute trapping (k=1), the solidification velocity can change abruptly and consequently may lead to the apparition of new metastable phases or skip some of those described in the phase diagram. This behavior is still unknown for almost all materials and only experiment can help predict the final microstructure and how solidification has been performed. As an example, tempered process for steels are confronted to a high cooling rate that induces the omission of metastable phases. In thermal storage, higher cooling rates at a higher heat flux increase the undercooling effect. [24], [78], [99], [100]

Figure 54 shows the relation between solidification velocities and undercooling degree. It shows that at higher velocities the undercooling degree increases exponentially. This behavior needs to be considered as a reference because the final relation actually depends on other parameters such as thermophysical properties, impurities, wall container roughness, etc. In practice, the amount of undercooling principally depends on two aspects: the thermophysical properties of material (alloy, paraffin, salt, etc.) and presence of impurities (see Figure 25). These two aspects change during charge/discharge cycling and are not considered in our research.

In the explicit simulation method, the solidification velocity is limited by the time step. Equation 57 accelerates or decreases the phase transformation on the discretized element. The time step is thus a key parameter to define. The time step is selected by the criterion:

$$\Delta t \cdot V_s < \Delta x \tag{58}$$

Usually Δx is very small and in our experience to maintain a good convergence the spatial discretization is often Δx<2e-3m. For example, if we take the solidification velocities showen in Figure 29, the maximum solidification velocity before complete solute tramping is 5m/s [95]. This limit velocity gives us a Δt maximum of $4x10^{-4}$. As another example, the critical to have complete solute trapping on Al-Si systems is 2.5 m/s [118], then the maximum Δt that can be use is $8x10^{-4}$s. Furthermore, Equation 57 is limited at the phase transformation where the undercooling effect is present. In other cases, FB-Heat Cap is used.

The cooling rate and solidification velocity will be limited by the partition coefficient k<1. However, when undercooling is present the latent heat composition changes. The prediction of this compositional variation at the phase transformation is done by the FB k non-equilibrium. The partition coefficient is modified to consider the increase in the solidification velocity

The temperature to start solidification in equilibrium is provided by the FB-Calphad. When the temperature Tm is reached, the cooling rate is calculated using the expression:

$$CR = \frac{T_{l\,n-1} - T_{l\,n}}{\Delta t} \tag{59}$$

where T_l is the temperature at which the solidification begins (equilibrium solidification liquidus temperature). $T_{l\text{-}\Delta t}$ is the temperature at the previous time step. Equation 59 is used with Equation 26 to calculate the solidification velocity.

Figure 39 shows the routine to determine the degree of undercooling. The CR is defined at Tm and this CR is an input into the FB- Solidification Velocity. The solidification velocity is used in the FB-K Non-Equilibrium and the output information is used in the FB-Undercooling.

As mentioned previously, the interface velocity has another critical point. This is the point that defines an off-equilibrium phase transformation without undercooling and phase transformation with undercooling.

This value is defined experimentally and defines the solidification velocity limit where the Scheil Gulliver method is in good agreement with the experimental segregation solidification. For

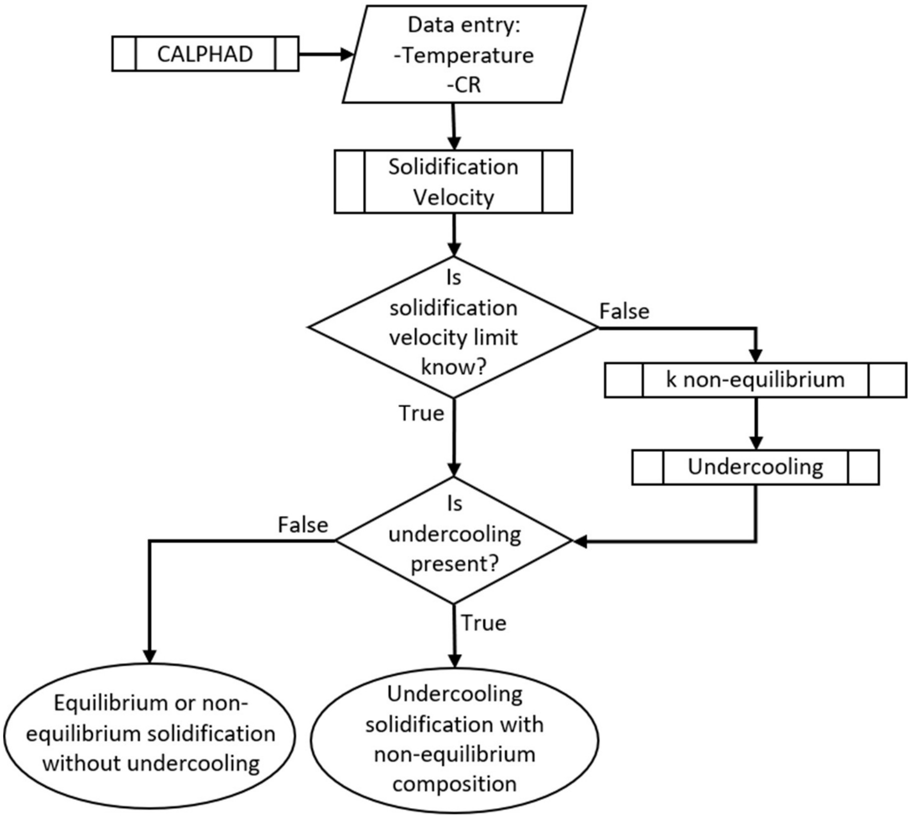

Figure 55 Algorithm to define the type of phase transformation

some castings, the solidification velocity limit is below 0.3 m/s but for others it can be as low as 0.1 m/s or as high as 5 m/s [45], [95], [105], [106]. This parameter can drastically change depending on the type of material (alloy, salt, paraffin, etc.). Moreover, this critical point and the final macrosegregation in the solid depends on many factors previously described such as: nucleation temperature, impurities, cooling rate, vibration and wall roughness among others. Furthermore, the solidification velocity/cooling control is a main problem in casting production. Unfortunately, no formulation nor model exists to predict the solidification velocity limit when the undercooling effect is enough to limit the validity of the Scheil Gulliver model. This critical point of solidification velocity is defined by the user at the beginning of the simulation. When this value is known, the undercooling degree is not dismissed.

If we do not know the solidification velocity limit, the undercooling process cannot be dismissed. One possibility is using a limiting value of undercooling. This limit works in the same way as a critical solidification velocity value. We knows that the undercooling degree is defined by the solidification velocity and microsegregation phenomena, as was reported by [71], [102], [103], [127]. If we use the solidification velocity/microstructure composition relation we can estimate the undercooling amount. Figure 55 shows the algorithm to predict the undercooling amount in function of the microsegregation present in the discretized element. This process is done through the FB-k-non-equilibrium. Obviously, the procedure shown in Figure 55 is used when the solidification velocity critical point is unknow.

Figure 55 shows the algorithm to define the type of phase transformation. The initial solidification temperature is obtained from the phase diagram (FB-Calphad) and the CR is calculated at the instant that the solidification starts (Equation 59). Then, the CR data is used with Equation 26 to calculate the solidification velocity. As previously explained, if the critical point of the solidification velocity is known, we can directly define the type of phase transformation. The question is: *Is the solidification velocity known?* If this is not known, the procedure to define the amount of undercooling is used. Consequently, the FB k Non-equilibrium and FB-Undercooling are used. Then, in Figure 55, the question: *Is undercooling present?* This will define if FB-Heat Cap (without undercooling) or FB-Heat source (with undercooling) is used.

3.2.8 FB k non-equilibrium

FB k non-equilibrium calculates the change in the composition when the cooling rate affects the solid composition and a non-equilibrium solidification is present. Non-equilibrium solidification is when the diffusion is insufficient to homogenize the composition across the liquid/solid interface under a fast cooling rate. When this is the case, the information contained in the phase diagram isn't valid. The FB depends on the solidification velocity and cooling rate. Hence, the solidification velocity exceeds the diffusive speed of solute atoms in the liquid phase and the solute is trapped into the solid at levels exceeding the equilibrium solubility. Chemical potential across the interface isn't equal and consequently the phase diagram can't be used directly.

The solidification interface can have four stages in function of the solidification velocity (see Figure 17). These are defined by the cooling rate and the composition present. The third stage is where the undercooling effect increase due a stronger solidification velocity. Consequently, the cellular/dendritic stable phase cannot nucleate or grow sufficiently fast to reach the phase indicated in the phase diagram. This kind of transformations can occur normally at solidification velocities exceeding 3 m/s; depending mainly on the type of properties and composition of the material. An important characteristic is the partition coefficient, this can reach the limit value of one and this limit represents that the diffusion in liquid and solid are zero and the initial liquid composition is the same at the final solid composition.

Following the algorithm in Figure 55, when the melting temperature is achieved the next step is to calculate the solidification velocity. This value will drive the evolution of the composition and the rate of phase transformation. This value is also necessary to estimate the amount of latent heat delivered during solidification.

Non-Equilibrium Partition coefficient with undercooling

During non-equilibrium solidification, solute redistribution presents a segregation that can change how the material solidifies and heat is released. The partition coefficient drives this redistribution during solidification. The cooling rate and solidification velocity are key elements to determine the modification of the partition coefficient. Assuming no convection in the liquid, the diffusion layer in the mushy zone is defined by:

$$\delta = \frac{D_L}{Vs} \tag{60}$$

where D_L is the diffusion in the liquid and Vs is the solidification rate. As previously mentioned, the diffusivity is one of the parameters that define the solidification behavior and is different for each material. If the solidification rate increases, the diffusion layer decreases until a partition coefficient of unity. This means $kCs=C_L=Co$ for the phase transformation.

The research by Lipton et al [153] laid the foundation to understand solidification in relation with its undercooling degree. They establish the undercooling (ΔTu)-growth velocity (Vs)-dendrite tip radius relationship by a combination of Ivantsov solutions for the thermal and solute diffusion fields. This relationship is illustrated in Figure 56. From their work , many other models have been developed from the Lipton model [153]. This modification has been the extension to consider different kinetics effect, for example the Jackson-Hunt model is applicable only to small undercooling predictions, and the Trivedi-Magnin-Kurz (TMK) was developed to consider the dependency of the growth velocity on the lamellar microstructure. This dependence of the microstructure on the growth velocity was described before on the Chapter two (Figure 56). On

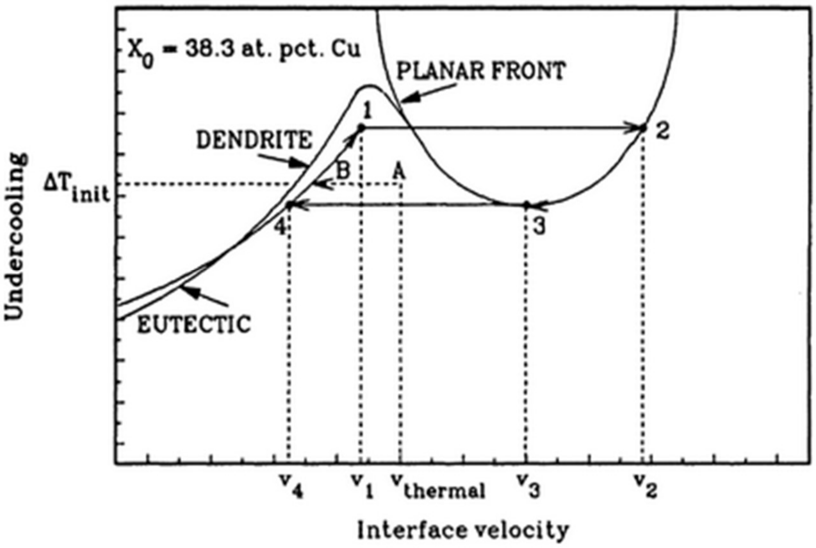

Figure 56 Diagram illustrating the interrelationship of undercooling (ΔTu)-growth velocity (Vs)- microstructure change, for a Ag-38.3% Cu alloy[73]

the other hand, results demonstrated that the TMK model is valid only in the intermediate undercooling range [77].

One of the most recent models is the local non-equilibrium diffusion model (LNDM) [154] where is based on the Continuous growth model (CGM) [119]. This model is used to predict the phase growth in terms of the interface temperature and composition. The CGM is able to reproduce the phase diagram at zero velocity. The LNDM modifies the solute trapping model with different solid-liquid interface kinetics. The main advantage is that this takes the local equilibrium of a solute in bulk liquid to the solute concentration and solute flux in bulk liquid under local non-equilibrium conditions. The LNDM identifies the abrupt transition from diffusion-limited to purely thermally controlled solidification. At this limit, complete solute trapping is present (K=1), and the growth velocity achieves the limit diffusivity speed (V_D) as seen in the fourth stage described in Figure 17. The liquid diffusion is zero (D_L=0) at the To temperature.

We examine a system with non-equilibrium rapid solidification to evaluate the latent heat change and to estimate the temperature at which the phase transformation occurs. The cooling rate modifies the solidification velocity, generating sub-cooling effects and a variation in solidification composition, modifying the microstructure and presenting an opportunity to exploit the structural control and property enhancement for energy storage. The composition at the solidification boundary linked to Rapid Solidification Process (RSP) is defined by the partition coefficient in function of velocity (k_V), which can be defined as:

$$k_v\,(V) = \frac{k_e\Psi + V_s/V_D}{\Psi + V_s/V_D}\,, \qquad V_s < V_D \tag{61}$$

Ψ=1-Vs^2/V_D^2

$$k_v\,(V_s) = 1, \qquad V_s \geq V_D \tag{62}$$

where, Vs is the solidification velocity and V_D is the diffusive speed, interpreted as the maximum speed solute-solvent redistribution across the interface. When Vs overcome V_D, the partition coefficient is 1, the limit of this methodology. The tangent of the non-equilibrium liquidus line slope (m_L) as function of non-equilibrium solute partitioning and the solidification velocity (m_{Lv}) is defining as:

$$m_{Lv}\,(V_s) = \frac{m_e}{1-k_e}[1 - k_v + ln(k_v/k_e) + (1-k_v)^2(V_s/V_D)]\,, \qquad V_s < V_D \tag{63}$$

The composition for non-equilibrium, defining the solid concentration C_S^k at the tip of the solute dendrite in function of k_v is described as:

$$\begin{aligned} C_S^k &= \frac{C_o\,k_v}{1-(1-k_v)Iv(Pc)} && \mathrm{V_s} < V_D \\ C_S^k &= C_o\,, && \mathrm{V_s} \geq V_D \end{aligned} \tag{64}$$

where Pc is the solutal Peclet number defined by:

$$Pc = \frac{V_s \cdot Rr}{2D} \tag{65}$$

Iv is the Ivantsov function [155], [156] defined as: Iv(Pc)=Pexp(P)Ei(P), typically, for casting solidification P<1 where P is the solute Péclet number, solved using the following approximation:

$$Iv(P) = Pexp(P)[a_0 + a_1P + a_2P^2 + a_3P^3 + a_4P^4 + a_5P^5 - ln(P)] \tag{66}$$

where ao=-0.57721566, a1=0.99999193, a2=-0.24991055, a3=0.05519968, a4=-0.00976004, a5=0.00107857 [45], [99]. For limiting values of the Péclet number, the Ivantsov function can be approximated as:

$$\begin{gathered} for\ \ P \ll 1:\ \ Iv(P) \approx -Pln(P) - 0.5772P \\ for\ \ P \gg 1:\ \ Iv(P) \approx 1 - 1/P\ + 2/P^2 \end{gathered} \tag{67}$$

The Ivantsov transport solution describes steady state transport of the heat surrounding a branch with dendrites growing in an infinite, quiescent supercooled melt. More details on the Ivantsov solution can be found in the works of Z. K. Liu et al [156] and G. Müller et al [157].

The dendrite tip radius (Rr) is a fundamental parameter to estimate the undercooling temperature. Using the marginal stability criterion [158], [159] in combination with the transport solution of Ivantsov, molecular structural features are linked to RSP, Rr is defined as:

$$Rr = \frac{\Gamma}{\sigma^*}\left(\frac{P_T \Delta H \xi_L}{Cp} - \frac{2m(1-k_v\,)C_oPc}{\Psi[1-(1-k)Iv(Pc)]}\xi_C\right)^{-1} \quad V_s < V_D \tag{68}$$

With

$$\xi_C = 1 + \frac{2k}{1 - 2k_v\ - [1 + \Psi/\sigma^* Pc^2]^{1/2}} \qquad V_s < V_D \tag{69}$$

$$\begin{gathered} \xi_T = 1 - \left(1 + \frac{1}{\sigma^* P_T^2}\right)^{-1/2} \\ \sigma *= 1/4\pi 2 \end{gathered} \tag{70}$$

where σ* =1/4π2 denotes a stability constant and P_T is the thermal Péclet number defined:

$$P_T = \frac{V_s \cdot Rr}{2\alpha} \tag{71}$$

Where α is the thermal diffusivity.

V_D define the critical point when the complete solute trapping occurs (K=1) and its value depends on material properties, purity of material during phase change, pressure and cycle of charge/discharge. However, the value V_D can be approximated using the expression:

$$V_D = \frac{D_i}{a} \qquad (72)$$

where D_i is the diffusion coefficient for the alloy and <<*a*>> is the molecular interatomic separation. Usually this is estimated for alloys to be between 0.5 to 5 nm [160].

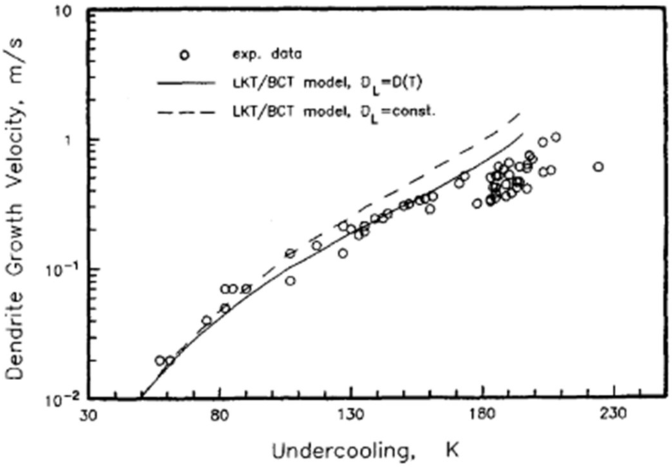

Figure 57 Comparison between experimental results and calculated solidification velocity at Co-20%Sb (hypoeutectic alloy). LKT model using constant D and D as a function of temperature. [161]

At microscale simulations, for example in phase field simulations, the assumption of constant solute diffusion coefficient is invalid for rapid solidification, especially for alloys with large undercooling. The dependence of D (diffusion coefficient m^2/s) on dendrite tip velocity (Equation 65) directly affects the non-equilibrium partition coefficient. If V_D is used as a function of a and D (Equation 72), then the interface velocity is clearly affected (see Figure 56). The inclusion of a solute diffusion coefficient depending on temperature requires always knowing the temperature at the discretized element. This is thus an iterative method to calculate the tip temperature and the subsequent equations involving the diffusivity to obtain k_V, mL, Rr and C_S^k (Equations 61, 63, 68, 64 respectively). Nevertheless, for macrosimulations the inclusion of D as a function of T does not show an improve in result and its inclusion generate convergence instabilities. Figure

57 shows a comparison between the LKT model using constant D and D as a function of temperature with experimental data for Co20%Sb. Even if we can see a difference between their results, since macrosimulation is neglected, this can be correct where microstructure interface tracking is the main objective (e.g. in phase field simulations). In our calculation we assume the diffusivity D constant.

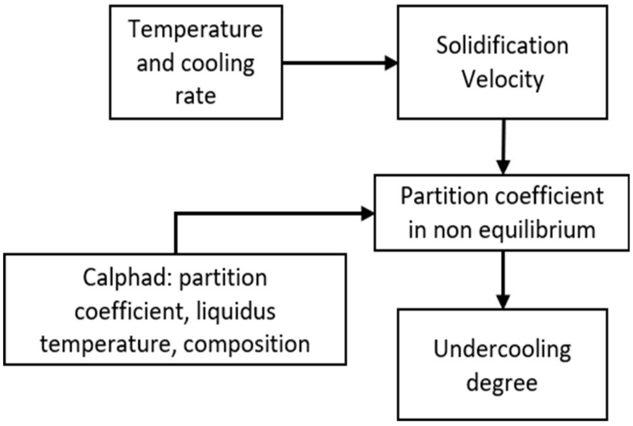

Figure 58 The FB k-non-equilibrium needs information from FB-Calphad and FB-Solidification velocity.

Figure 55 shows the algorithm to define the degree of undercooling. When we do not know the relationship between the solidification velocity and undercooling degree, we follow the sequence to calculate the amount of undercooling that can be present in function of the solidification velocity: cooling rate → solidification velocity → off-equilibrium partition coefficient → undercooling degree. The flux of information is show in Figure 58

The solidification of undercooling melts occurs at a wide range of velocities. Figure 59[162] shows the interrelationship between solidification velocity and undercooling for nickel. The undercooling percent is the percent of melting temperature (10pct undercooling = 173K). Also,

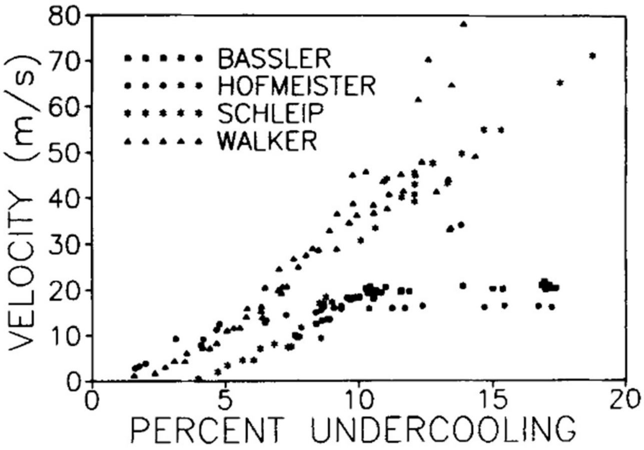

Figure 59 Nickel experimental results reported by Bassler, Hofmeister, Schleip and Walker. Solidification velocity vs percent undercooling [162]

we can see different results for the same material. For the Basseler et al. results, the sample has a weight of 1+-0.05 grams. The phase transformation was made in electromagnetic levitator. The sample size is too small to consider convective phenomena, and the wall roughness acts as a nucleation agent. Hence, these results shown in Figure 59 can be interpreted as the worst situation even if experimental result shows important variation.

However, for all solidification conditions, the interface velocity affects the solute diffusion, the interface kinetics and heat conduction from equilibrium solidification. Thus, as explained before, the solidification velocity can be used to define the deviations from equilibrium following the increase in solidification velocity:

Vs= 0; full equilibrium. The composition of the phases is uniform, and the phase diagram describes solidification behavior. The lever rule is applied.

$V_s << V_D$, local equilibrium. The concentration and temperature gradients change the full equilibrium. The phase diagram information needs correction. The Scheil Gulliver equation is used with local assumption (no diffusion in solid, infinite diffusion in liquid). The use of other equations and their assumptions are described in Table 2.

$V_s<V_D$, Non-equilibrium interface kinetics. There is no local equilibrium at the interface and the partition coefficient depends on the interface velocity. The diffusion D(Vs) tends to zero with complete solute trapping (k=1). For macro simulations, D is considered constant.

Cases of V>VD are not considered in this methodology.

Table 4 Data used in FB-Undercooling

Non-equilibrium partition coefficient (kv),	Equation 61
Non-equilibrium liquidus slope (m_L)	Equation 63
Non-equilibrium composition (C_s^k)	Equation 64
Peclet solutal number (Pc)	Equation 65
Ivantsov function, (Iv(P))	Equations 66 and 67.
Dendrite tip radius (Rr)	Equation 68
Latent heat and heat capacity of alloy	thermophysical properties

3.2.9 FB Undercooling

FB-Undercooling has the finality to predict the amount of undercooling for a non-equilibrium solidification. The data needed in the FB-Undercooling are listed in Table 4.

The interface temperatureis not only a function of composition (following phase diagram information). The local heat and solute diffusion affect the local temperature, moreover the local undercooling degree. Thus, the amount of undercooling ΔT_U is constituted for five undercooling components: curvature undercooling ΔT_R, constitutional undercooling ΔT_C, kinetic undercooling ΔT_K and thermal undercoolings ΔT_T and ΔT_N. The difference between equilibrium and non-equilibrium liquidus temperature is thus defined as:

$$\Delta T_U = \Delta T_R + \Delta T_C + \Delta T_K + \Delta T_T + \Delta T_N \qquad (73)$$

where:

$$\Delta T_R = 2\Gamma/Rr \tag{74}$$

$$\Delta T_C = m_L C_o \frac{(1-k_v)Iv(Pc)}{1-(1-k_v)Iv(Pc)} \tag{75}$$

$$\Delta T_K = V_S/\mu \tag{76}$$

$$\Delta T_T = (\Delta H/Cp)\ Iv(P_T) \tag{77}$$

$$\Delta T_N = (m_e - m_{Lv})C_o \tag{78}$$

With solidification velocity (Equation 26) and the FB-k non-equilibrium, the undercooling is predicted. Figure 60 and Figure 61 compare experimental results for a Ni0.7%B [163], [164] alloy with models described before. In Figure 60, Equations 73-78 are used to predict the undercooling degree in function of solidification velocity compared with experimental values from [163], [164]. Figure 61 shows results of Equations 61-64 and 73. It is clear that for 250K undercooling solute tramping occurs.

Following the algorithm described in Figure 55, the undercooling degree is calculated giving the type of solidification: undercooled or not

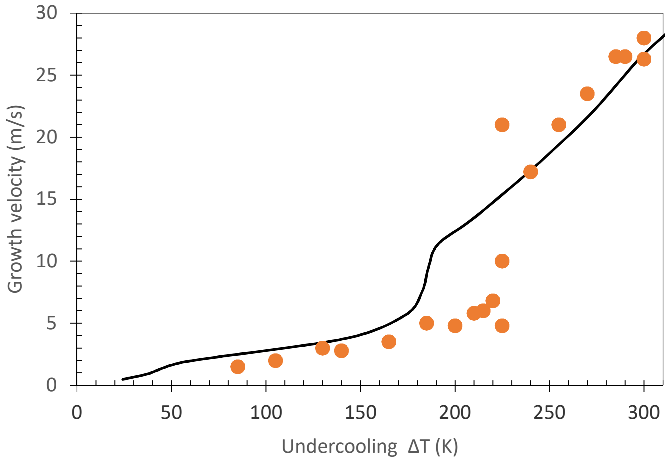

Figure 60 Solidification velocity vs. undercooling ΔTu for Ni 0.7% B alloy. Circles: experimental data [162], [163]; Solid line represents the mathematical model from FB-Undercooling

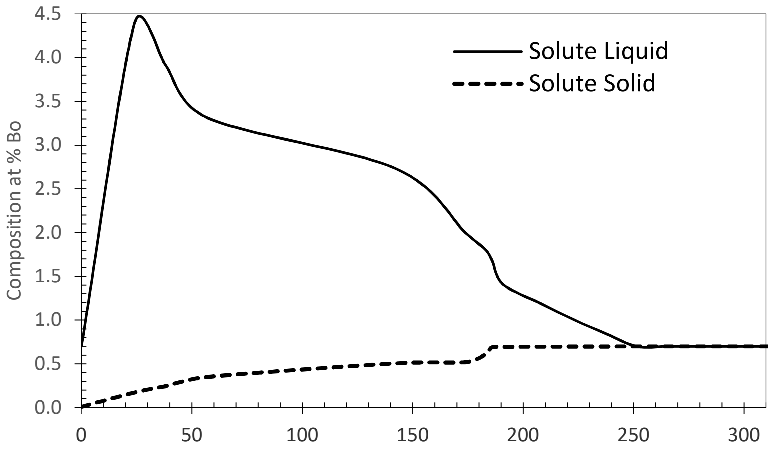

Figure 61 Result of FB-k non-equilibrium and FB-Undercooling. Evolution of the solute concentration in the liquid and solid for an alloy at Ni 0.7% B

3.2.10 FB-Latent heat

The latent heat L^{ab} is a material property. During phase change, this heat is not necessarily instantaneously and completely released. This functional block aims to determine the evolution of latent heat release as a function of temperature and solid fraction. Three cases are described:

- Case 1: Eutectic composition and equilibrium solidification

- Case 2: Off eutectic situation and equilibrium solidification

- Case 3: Off eutectic situation and non-equilibrium transition.

Congruent solidification of a pure material (metal, paraffin, or eutectic alloy) corresponds to the latent heat release at a particular temperature (melting temperature). In such considerations, the liquid solid interface, responsible for the latent release, remains at temperature Tm. Considering a representative element volume (REV), when solidification occurs under conditions of case 1, the temperature is equal to Tm. The solid fraction is between 0 and 1. To estimate more accurately the instantaneous solid fraction fs, one common assumption consists in linearizing the temperature during phase change, by supposing that solidification occurs in a thin temperature range ($\Delta T = T_L - T_S$) instead of a constant Tm, as represented in Figure 48. For a REV submitted to phase change, where the solid fraction fs is between 0 and 1, the released heat L is a part of the total latent heat L^{ab} and is expressed with Equation 79:

$$fl_r = \frac{T_L - T*}{T_L - T_s} \tag{79}$$

Where T_L and T_S represent the range ΔT_{Scp}, described in FB-Heat-Cap and illustrated in Figure 47, and T* is the current REV temperature (ideally equal to Tm). For binary alloys, Equation 79 can be used only for eutectic composition without undercooling.

However, such assumptions, for off eutectic composition binary alloys, give several errors when the phase diagrams of the mixture are not linear. These errors are incremented mainly when non-equilibrium solidifications are present.

For off eutectic phase transformation corresponding to case 2, the latent heat depends on the solute concentration that varies in time and space due to solute rejection and diffusion during the solidification process. Veinik [147] reports that the law of additivity can be applicable for alloys. Using this law, we define the latent heat of a binary alloy of composition Co of constituent B and consisting on components A and B as the Equation 80:

$$L^{ab} = [L_B C_o + L_A(1 - C_o)] = [(L_B - L_A)C_o + L_A] \tag{80}$$

where L_A and L_B is the latent heat of component A and B respectively. Equation 80 is used in Equation 48 substituting L^{cp} par L_{ab}.

During non-isothermal evolution, the composition varies and differs from Co. The latent heat is obviously altered by this behavior and must be considered in the model 80. Thus, when a solid has the composition Cs* ≠Co, the latent heat released is expressed by:

$$L^{ab} = [(L_B - L_A)Cs * + L_A] \tag{81}$$

A small variation of the solid fraction dfs affects the small latent heat release dL assuming that the REV remains at the composition Cs*. Then, dL can be calculated with:

$$dL = [(L_B - L_A)Cs * + L_A]\, df_s \tag{82}$$

Diving both sides by dT* that represents the temperature variation (under Tm) we obtain the equation:

$$\frac{dL^{ab}}{dT} = [(L_B - L_A)Cs * + L_A]\, \frac{df_s}{dT} \tag{83}$$

The assumptions of case 3 need to complete Equation 83, which is the general equation to calculate the amount of latent heat released for phase transformation of an off-eutectic composition material. The derivative of dfs with respect to temperature was described for Equation 49. Then, Cs* is substituted into Equation 23 using the Scheil Gulliver model. The latent heat equation for an off-eutectic composition in a non-equilibrium solidification, using the derivation of df_s from Equation 49 and substituting Equation 23, we obtain the Equation 83:

$$L^{ab}{}_{of} = \frac{(L_B - L_A)kCo}{(1-k)(T_{MA} - T_l)}\left[\frac{T_{MA} - T_l}{T_{MA} - T*}\right]^{\frac{k}{1-k}} + \frac{L_A}{(1-k)(T_{MA} - T_l)}\left[\frac{T_{MA} - T_l}{T_{MA} - T*}\right]^{\frac{1}{1-k}} \tag{84}$$

Where $L^{cp}{}_{of}$ is the latent heat released in the phase transformation for an off-eutectic composition solidification and non-equilibrium solidification without undercooling.

Undercooling affects the composition and the solidification behavior. Variation in composition of a mixture generates different initial melting temperatures and consequently alters the amorphous characteristic solidification structures, changing thermal properties. It is clear that in Equations 79, 83 and 84, the diminution of temperature drives the solidification behavior. For undercooled solidification the heat released increases the temperature, and this does not follow the phase diagram data. Then, as previously described, the solidification velocity drives the phase transformation in function of cooling rate and thermophysical properties.

As mentioned in the FB-k non-equilibrium the composition can be expressed in function of solidification velocity. Then, Equations 64 and 61 are substituted in 81:

$$L^{ab} = \left[(L_B - L_A)\left(\frac{C_o}{1-(1-k)Iv(Pc)}\right)\left(\frac{k_e\Psi + \frac{V_s}{V_D}}{\Psi + \frac{V_s}{V_D}}\right) + L_A\right] \qquad \Psi = 1 - \frac{{V_s}^2}{{V_D}^2} \tag{85}$$

The temperature change is caused by the amount of solid formed. The rate of this change depends on thermophysical properties and imposed conditions. Moreover, we can infer that this rate of solidification implies a coexistence of solid and liquid phases at the equilibrium temperature over the finite REV at a time t.

Equation 57 and Equation 85 define the amount of heat that will be added into the source term Equation 51.

Table 5 englobes the hierarchy of equations described before. Equations 80, 83 and 85 depend on the solidification behavior. Equations 83 and 85 can be used in the same simulation. For example, at the beginning of the phase transformation, recalescence elevates the temperature until the point where a solidification non-equilibrium without undercooling can be considered. It is only then 83 when will be used.

Table 5 Hierarchy of equations for the FB-Latent heat

	Solidification behavior	Equations on FB-Latenth heat
Increasing undercooling / solidification velocity	Full diffusional, global equilibrium.	76
	Composition in phases is uniform	
	Lever rule applicable	
	Local interface equilibrium, No diffusion in solid, full diffusion in liquid. No undercooling	80
⇩	Phase diagram information is used: partition coeficient, liquidus temperature, liquidus slope	
	Corrections made: Scheil Gulliver model	
	Interface non-equilibrium with undercooling	82
	Phase diagram fails to give temperature and composition at the interface	
	Solidification velocity drive the segregation phenomena	
	Strong undercooling degree is present	

Chapter 4 Method validation

The performance of alloys as phase change materials for thermal storage are the subject of few experimental studies, representing a difficulty to validate the complete methodology described in the previous chapter. Instead, we use specific references to validate the different parts of our method. This chapter describes the validation cases that have been performed. The last section is devoted to the analysis of a specific material (an Al-Si alloy), which has attractive properties to be considered as material for energy storage, by evaluating its capacity to be used as a phase change material for latent heat thermal energy storage (LHTES). The validation has been splitted in four sub sections following the represented phenomena: i) CALPHAD; ii) Isothermal phase change; iii) Undercooling; and iv) Segregation.

In-house software Calphad: the objective is to validate the CALPHAD methodology we have integrated. The phase diagrams drawn from the Gibbs free energy are compared with those obtained with the ThermoCalc Software. This software is widely used and validated.

Isothermal phase change. The purpose of this section is to validate the isothermal phase change model. Due to the lack of publications that experimentally evaluate the alloys we want to consider; paraffin wax has been used in a first step. This material has been extensively studied and is one of the main materials used for the phase change below 373K. The experimental test described in [165], is often used to evaluate paraffin as latent heat thermal energy [166].

Undercooling. Experimentally, this phenomenon is commonly related with microstructure, but rarely with cooling rate. In general, the principal lack in information on binary alloys is the cooling rate applied to the sample when microstructure is studied with natural convection in the alloy. For this reason the experimental results [167] obtained by using paraffin are used to compare with the results obtained from the simulation model based on the methodology described above.

Off-eutectic solidification, segregation model. In this section the Scheil-Gulliver segregation model is validated considering convective flows. The results are compared with the bibliography that describes macrosegregation [99], [168], [169]. Unfortunately, most of the studies about segregation are focused on Fe-XX alloys (steels), or aluminum ternary alloys. A binary Al-Cu is a commonly studied alloy ([170]–[173]), however, different results are reported. A generalized segregation behavior is identified to validate the macrosegregation model .

In a second stage, the methodology for an Al-Si binary alloy is tested and the thermal behavior for energy storage is predicted. Numerical simulations are carried out for a eutectic composition Al-12% Si, as well for an off-eutectic composition Al-05% Si. The results in terms of phase change material behavior will help to optimize energy storage systems by latent heat. Additionally, the results provide the necessary information for the design of a heat exchanger for energy storage.

4.1 In house software Calphad

The CALPHAD method aims calculate the phase diagram and the corresponding specific data:

- Solidus and Liquidus temperature
- Eutectic temperature
- Partition coefficient
- Slope liquidus
- Solidus and eutectic composition
- Behavior of latent heat during the phase change

The validation of the Calphad method has been performed by comparing our results with the database of the commercial software Thermo-Calc [174].

Thermo Calc is a software and database package for phase equilibrium, phase diagram and phase transformation calculations. The application is oriented to the fields of chemistry, metallurgy, material science, alloy development, etc. Their algorithm is based on the work of Mats Hiller [175] to find the equilibrium state of a system. The first version of Thermo-Calc was released in 1981. There has been an update almost every year and the most recent version is used to compare our results with it (2018a Limited version). The most recent description and documentation are available at [174].

For our research in LHTES systems, temperatures of phase change solid/liquid and eutectic points are the main information to know. An Ag-Cu alloy has been selected to validate our code by comparing several data with the Thermo-Calc software results:

- Solidus and Liquidus temperature
- Eutectic temperature
- Eutectic composition

As previously described, the common tangent construction is used to represent the equilibrium between two phases. The work of Cahn and Carter [137] demonstrated that the convex hull algorithm is valid for the common tangent construction in the Gibbs free energy for binary alloys represented by the chemical equilibrium.

The silver copper system

The Silver-Copper phase diagram is one of the simplest and has been elected to compare our results with Thermo-Calc software. The phase diagram calculated with the Thermo-Calc software is shown in Figure 62.

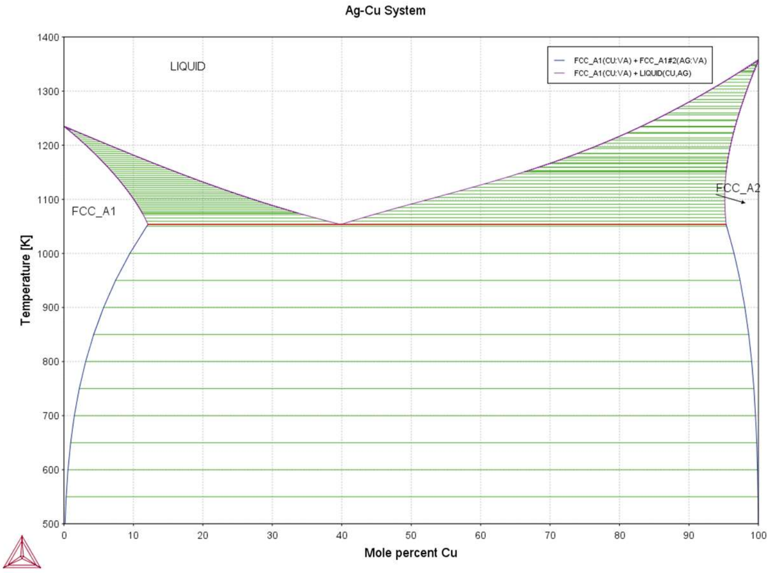

Figure 62 Ag-Cu Thermo-Calc phase diagram

According to Figure 62 Thermo-Calc phase diagram, the present phases are liquid and solid with two allotropes: Ag-rich face centered cubic (FCC_A1) and Cu-rich face centered cubic (FCC_A1). The composition of Ag and Cu at the eutectic temperature of 1053.01 K is 39.8 mole pct. Cu. At the eutectic temperature, the observed maximum solubility of Cu in Ag is 12.09 mole pct. Cu. On the Cu rich side, it is 4.6 mole pct. Ag. The Ag solidus is approximately a straight line between the melting point of Ag (1254.93 K) and the eutectic temperature. The Cu solidus has been represented by a straight line between the melting point of Cu (1357.7 K) and 1200 K. Under this temperature a slight curvature is present up to eutectic temperature. The Ag-rich liquidus is a straight line between the melting temperature Ag and the eutectic point. The Cu-rich liquidus is approximately a straight line between the melting point of Cu and the eutectic point.

We have obtained the phase diagram Ag-Cu using the TDB file presented in annex 1. The first data presented in the file concern the thermodynamic properties of the material in terms of allotropic phases, molar mass, enthalpy and entropy for each phase (liquid or solids):

```
$........................................................... mass [g/mol]     enthalpy_298   entropy_298
 ELEMENT VA   VACUUM                 0.0000E+00     0.0000E+00        0.0000E+00!
 ELEMENT AG   FCC_A1                1.0787E+02      5.7446E+03       4.2551E+01!
 ELEMENT CU   FCC_A1                6.3546E+01     5.0041E+03        3.3150E+01!
```

Equation 14 expresses the Gibbs free energy of the system for the specific phase.

$$G_m = \sum_i^c x_i G_i^0 + RT \sum_i^c x_i ln x_i + \sum_i^{c-1} \sum_j^c x_i x_j \Omega_{ij} \qquad (14)$$

The first term in Equation 14 is the Gibbs free energy of pure component for Ag and Cu materials. These are defined in the TDB file following the standard notation (Equation 15) defined by the SGTE group [17] as *FUNCTION GHSERAG* and *GHSERCU*:

Equation 15 for Ag:

```
FUNCTION GHSERAG    2.98150E+02  -7209.512+118.202013*T-23.8463314*T*LN(T)
    -.001790585*T**2-3.98587E-07*T**3-12011*T**(-1);  1.23493E+03  Y
     -15095.252+190.266404*T-33.472*T*LN(T)+1.412E+29*T**(-9);  3.00000E+03
     N !
```

Equation 15 for Cu:

```
 FUNCTION GHSERCU    2.98150E+02  -7770.458+130.485235*T-24.112392*T*LN(T)
    -.00265684*T**2+1.29223E-07*T**3+52478*T**(-1);  1.35777E+03  Y
     -13542.026+183.803828*T-31.38*T*LN(T)+3.642E+29*T**(-9);  3.20000E+03
    N !
```

Then, the definition of the first term in Equation 14 using Equation 15 for the liquid phase in the TDB file annex 1 are the PARAMETER G(LIQUID,AG;0) and PARAMETER G(LIQUID,CU;0). For the solid phase with the allotropy FCC_A1, the Gibbs free energy phase are the PARAMETER G(FCC_A1,AG:VA;0) and PARAMETER G(FCC_A1,CU:VA;0) for the Ag and Cu respectively.

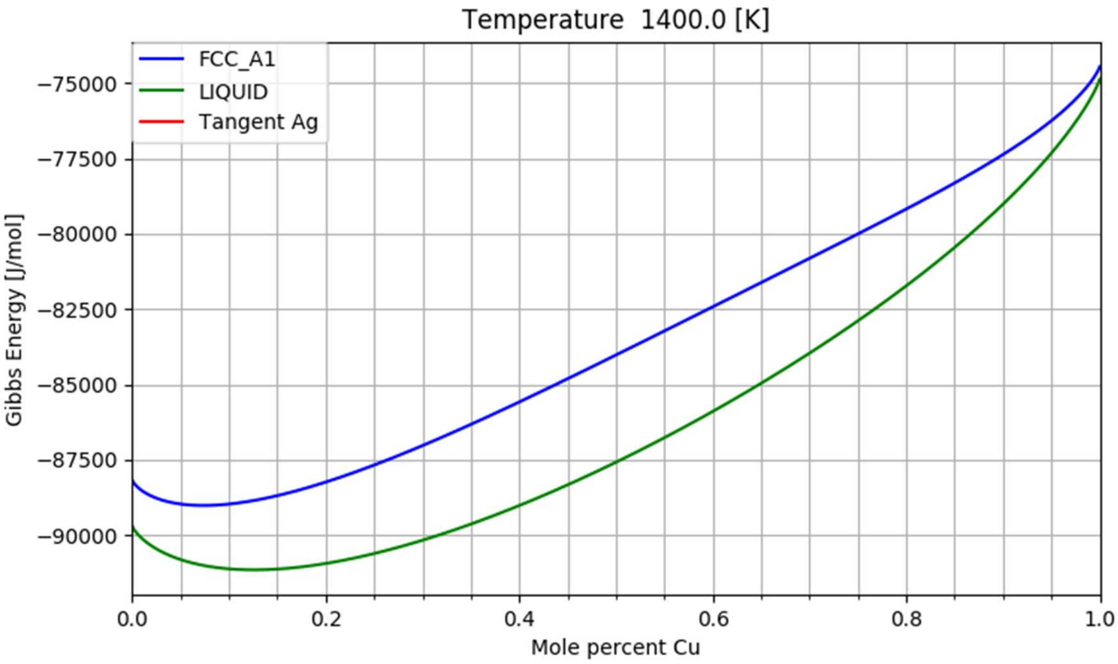

Figure 63 Gibbs free energy calculation for two phases

The second term in Equation 14 corresponds to the variation in composition satisfying the mass balance constraint (Equation 33).

The third term in Equation 14 is the excess Gibbs free energy. This is defined in theTDB file for the liquid phase as:

```
 PARAMETER G(LIQUID,AG,CU;0)  2.98150E+02  +17323.4-4.46819*T;
6.00000E+03   N !
 PARAMETER G(LIQUID,AG,CU;1)  2.98150E+02  +1654.38-2.35285*T;
6.00000E+03   N  !
```

For the solid phase:

```
 PARAMETER G(FCC_A1,AG,CU:VA;0)  2.98150E+02  +36061.88-10.44288*T;
6.00000E+03   N  !
 PARAMETER G(FCC_A1,AG,CU:VA;1)  2.98150E+02  -4310.12;   6.00000E+03   N !
```

For each phase, one Equation 14. Then, the Gibbs free energy is calculated for liquid and FFC_A1 phases using the convex hull algorithm for a temperature range of 400 to 1400 K with a temperature step of ∆T=1K.

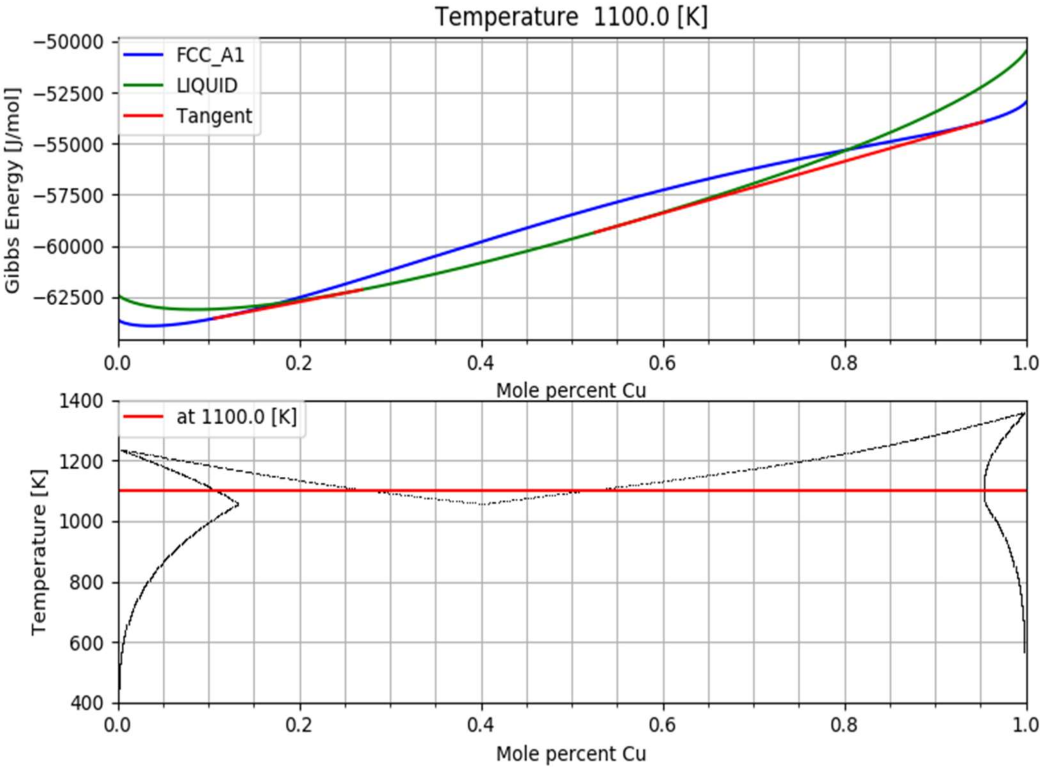

Figure 64 Calculation of the phase diagram. Top, tangent line at solid-liquid phase at 1100 K, bottom, phase diagram of Ag-Cu alloy

At each temperature the Gibbs free energy for each phase. Figure 63 shows the Gibbs free energy of Equation 14 for Liquid and FFC_A1 phase at 1400 K. It shows that at this temperature, the two curves do not cross each other and the tangent line traced from minima points cannot be created.

Figure 64 shows the Gibbs free energies calculated for the FCC_A1 and liquid phases for a temperature of 1100K. At this temperature, the tangent can be built and shows that several phases must be considered. From such representations at various temperatures, the phase diagram is built and is represented in Figure 64. The red line represents the temperature of 1100K and shows the phase transitions with concentration. The general method described before to solve the nonlinear system of Equation31, 32 and 33 is used to finally trace the phase diagram shown in Figure 65.

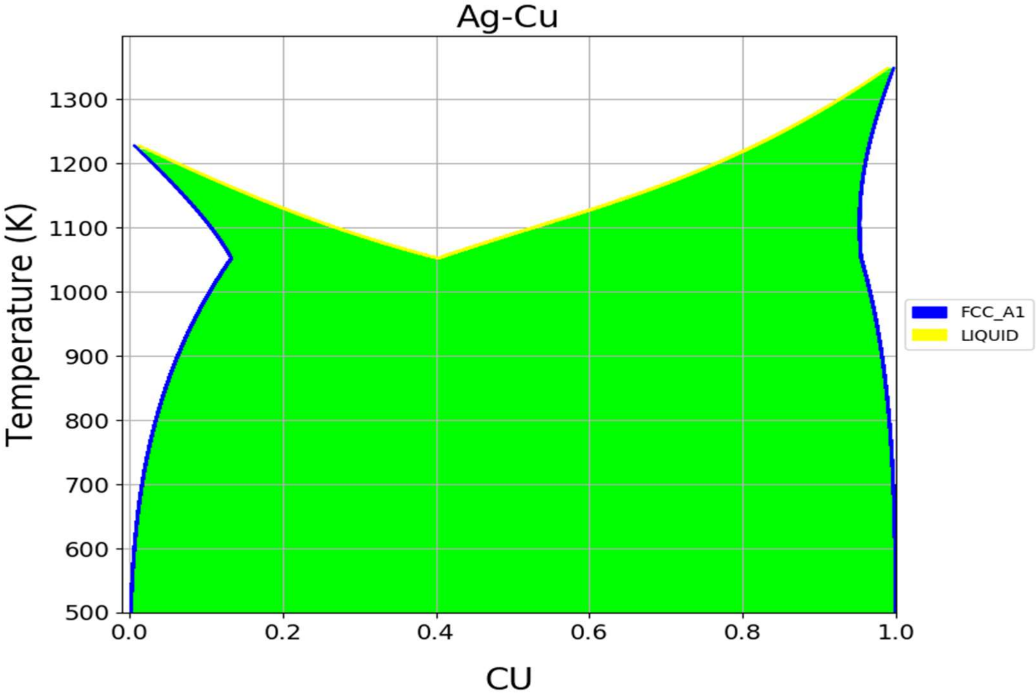

Figure 65 Final phase diagram calculation, AgCu alloy

According to Figure 65 the phase diagram traced with our script exhibits liquid and solid with two allotropes: Ag-rich FCC_A1 and Cu-rich FCC_A1 delimited by blue points. The eutectic temperature is traced at 1052.26 K. The eutectic composition of 40.2 mole pct. Cu is obtained, as shown in Figure 66. The observed maximum solubility of Cu in Ag is 13.2 mole pct. Cu as is shown in Figure 68. On the Cu rich side, it is 4.5 mole pct. Ag at the eutectic temperature shown in Figure 67. The Ag solidus has the same straight line between the melting point of Ag (1254.93 K) and the eutectic temperature. The Cu solidus also has been represented by a straight line between the melting point of Cu (1357.7 K) and 1200 K. Under this temperature a slight curvature is present up to eutectic temperature. The Ag rich liquidus is a straight line between the melting temperature Ag and the eutectic point. The Cu-rich liquidus is approximately a straight line between the melting point of Cu and the eutectic point. Both solidus lines match the Thermo-Calc phase diagram Figure 62

To confirm the accuracy of our numerical procedure, the Al-Zn binary system has also been selected. This system has 1 liquid phase and two solid allotropes: HCP and FCC. Figure 70 shows the phase diagram obtained with Thermo-Calc software. The eutectic temperature is at 653.99 K, the eutectic composition is 88.35 mole pct. Zn. Figure 69 shows the phase diagram traced with our script. The eutectic temperature that has been found is at 654.01 K. The eutectic composition is 88.3 mole pct. Zn at the eutectic temperature.

Both Al-Zn phase diagrams (Figure 69 and Figure 70) from our code and Thermo-Calc have the same lines delimitating the allotropes solid phases.

In Table 6 we summarized the difference between our software and ThermoCalc of the eutectic point for the Ag-Cu and Al-Zn binary systems. The maximum difference noted between our results and them of Thermo-Calc is 1%.

Table 6 Difference between phase diagrams calculated with our script and Thermo-Calc software.

	Ag-Cu			Al-Zn		
	Thermo-Calc	Our software	Difference	Thermo-Calc	Our software	Difference
Eutectic Temperature	1053.01	1052.3	**0.071%**	653.99	654.01	**0.003%**
Eutectic Composition	39.8	40.2	**1.0%**	88.35	88.3	**0.057%**

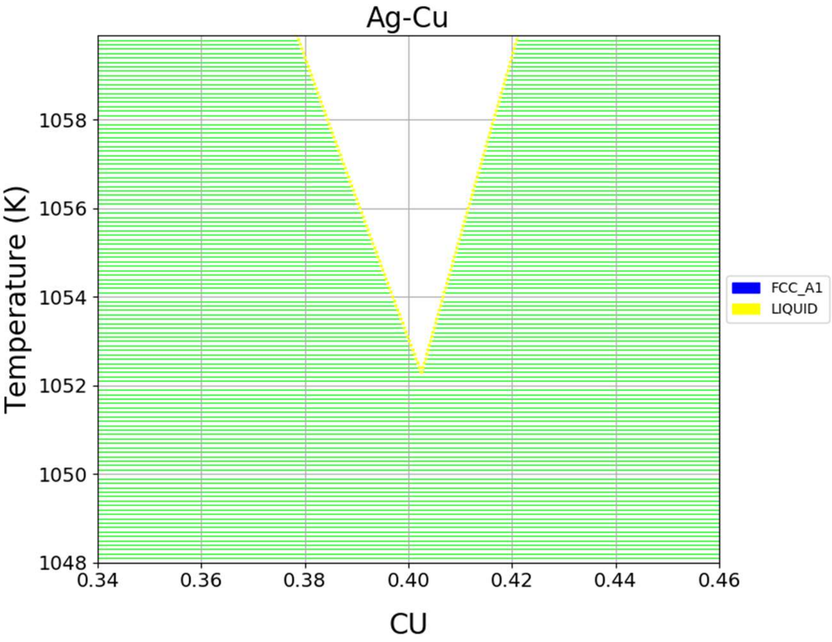

Figure 66 Eutectic point calculated for the Ag-Cu alloy

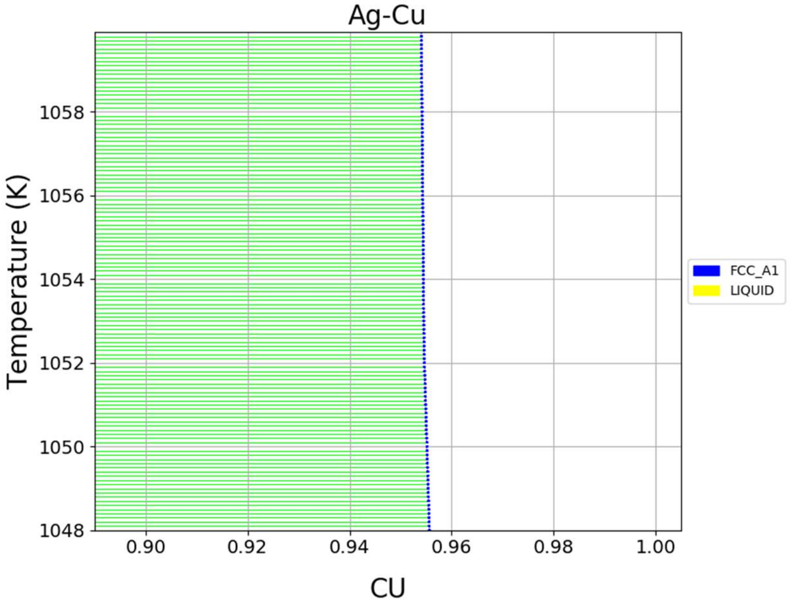

Figure 67 Cu rich Ag-Cu alloy at the eutectic temperature

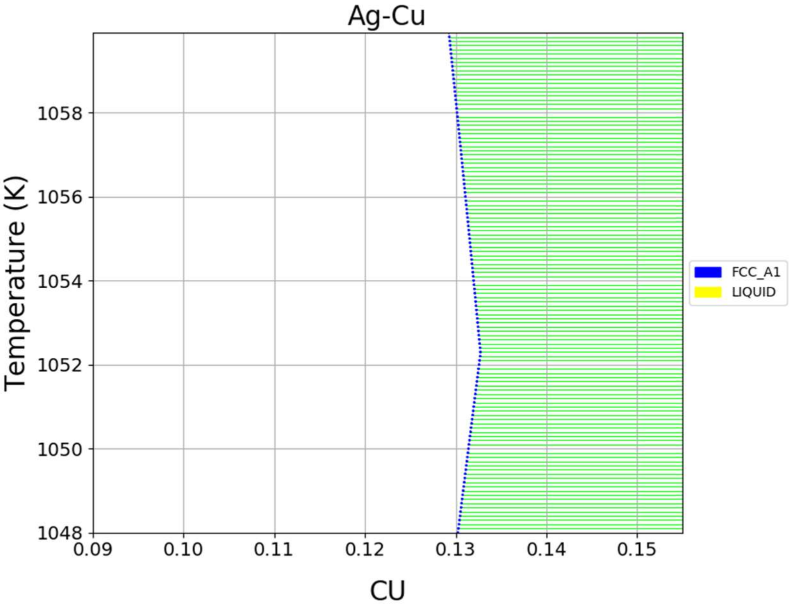

Figure 68 Ag rich Ag-Cu alloy at the eutectic temperature

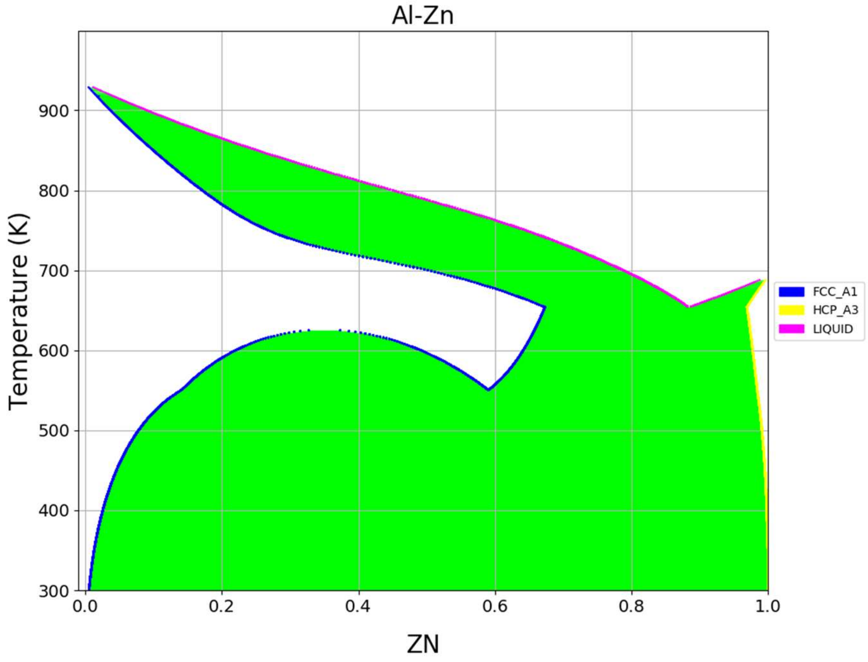

Figure 69 Calculated Al-Zn phase diagram

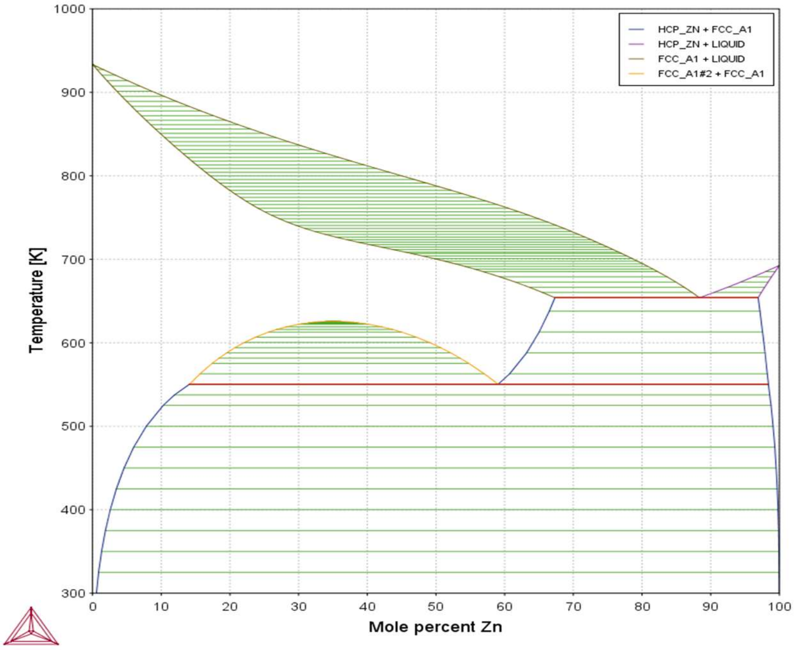

Figure 70 Thermo-Calc Al-Zn alloy phase diagram

4.1.1 Analysis of the phase diagram: latent heat

The phase diagram is the basis for obtaining the necessary information of the binary alloy and for the simulation of the phase change. For the LHTES systems the most relevant points are the liquid and solid states, as well as the phase transition. To calculate them and using the binary Ag-Cu system, the lever rule (Equation 22)and Scheil Gulliver (Equation 24) formulations have been used through the phase diagram and the initial composition.

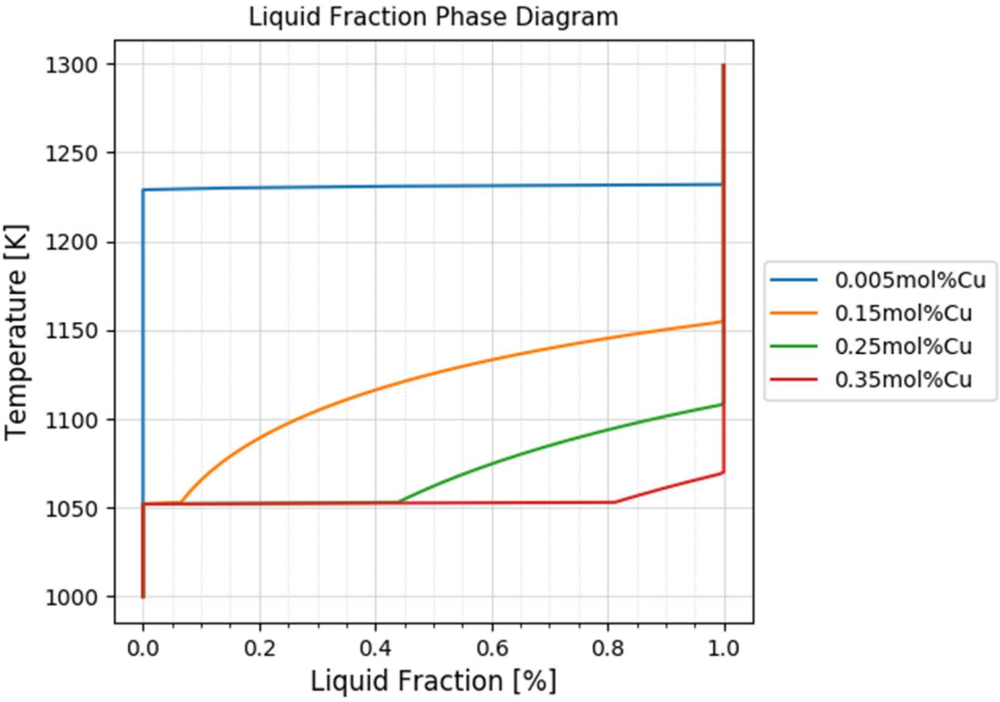

Figure 71 Lever rule liquid fraction at 0.5, 15, 25 and 35 mol% of Cu.

The thermal properties of a binary alloy depend on its composition. The temperature at which we consider the material phase change starts is obviously one of the main parameters to identify. Then, the solid fraction and the associated heat discharge via the latent heat can be estimated.

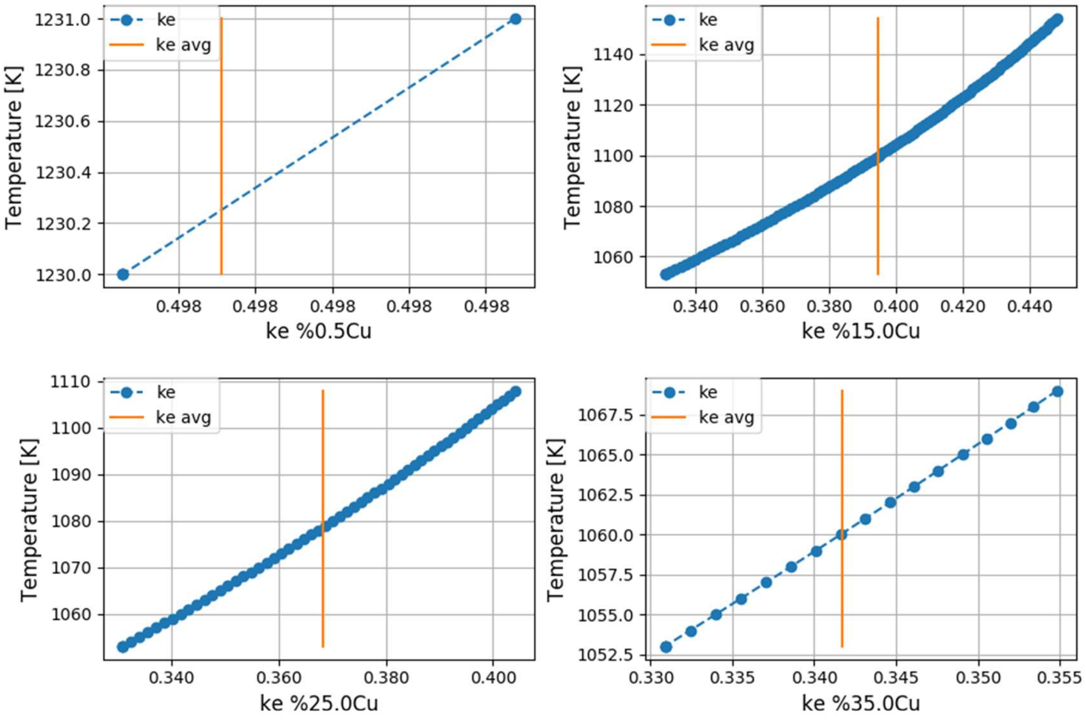

Figure 72 Partition coefficient for four different compositions of Al-Cu: 0.5, 15, 25 and 35 mol% Cu. Solid line is the average partition coefficient, round dote line is the variation of the partition coefficient following the phase diagram

From the phase diagram of Ag-Cu alloy and the lever rule formulation, we have estimated the liquid fraction and the temperature evolution for several compositions at 0.5, 15, 25 and 35 % mol Cu. Results are reported in Figure 71. It is observed that for a binary composition of 0.5 mol pct. Cu practically all the material solidifies at the solidification temperature of the pure aluminum element (quasi-isothermal solidification). For compositions 0.15 and 0.25, the solidification begins above the eutectic temperature, at 1109 and 1155 Kelvin respectively. For both cases, the solidification started at a higher temperature. Therefore, a quantity of material has solidified before reaching the eutectic temperature and solidifying completely. For the composition 0.15% mol Cu, at least 92% will have solidified before reaching the eutectic temperature when calculating with Lever Rule. If the Scheil Gulliver formulation is used for the same initial composition (at 0.15 %mol Cu) with a constant partition coefficient, 75% of the material solidifies above the eutectic temperature (this includes taking into account segregation). Contrarily, for a composition at 0.35 mol pct. Cu, less than 20% has solidified before reaching the eutectic temperature, as shown in Figure 71. This gives a general behavior of material solidification under equilibrium considerations.

The partition coefficient is another key element to describe solidification behavior (Equation 17). This value is used in the Scheil-Gulliver equation and in the undercooling degree evaluation. The partition coefficient for the same four binary compositions is calculated (0.5, 15, 25 and 35 mol pct. Cu). The use of a constant partition coefficient considers the solidus and liquidus lines as straight lines. This assumption is invalid for binary materials with non-linear variations in liquidus and solidus temperatures. Figure 72 shows the variation of the partition coefficient with different compositions, as well as its average value. In this figure, the blue dots are the partition coefficient evaluated at each temperature using the compositions of liquidus and solidus from phase diagram. The Ag-Cu phase diagram, (Figure 65) shows a curvature in the Ag-rich solidus line. This makes the partition coefficient vary notably at intermediate compositions. The orange solid line is the average value of the partition coefficient for the corresponding initial composition.

As shown in Figure 72, at the compositions 0.5 and 35 mol% Cu, the partition coefficient is practically constant. Otherwise is present for intermediate compositions (at 15 and 25 mol% Cu). The partition coefficient varies from 0.331 to 0.448 at 15mol% Cu and from 0.331 to 0.404 for the composition 25mol% Cu. These variations mean changes of 16.4% and 10.5% for the partition coefficients respectively. The composition of 15% mol Cu, is the one with the most variation with respect to the average partition coefficient.

Figure 73 shows the variation of the partition coefficient for different hypo-eutectic compositions of Ag-Cu alloy, the average value of the partition coefficient (blue line) and the maximum and minimum values (orange and green dotted lines). Consequently, the compositions calculated with the average partition coefficient in equations such as Lever Rule and Scheil-Gulliver can vary considerably to the compositions defined in the phase diagram. Another aspect is the variation of the partition coefficient that is not linear with respect to the initial composition of the alloy. Figure 73 shows two lines of different slopes can be identified for the average value. The first one starts from the pure element Ag, up to a composition of 15 mol pct. Cu. This composition corresponds to the maximum solubility of Cu in an Ag-Cu alloy. From this composition, the slope of the partition coefficients to the eutectic composition exhibits a change.

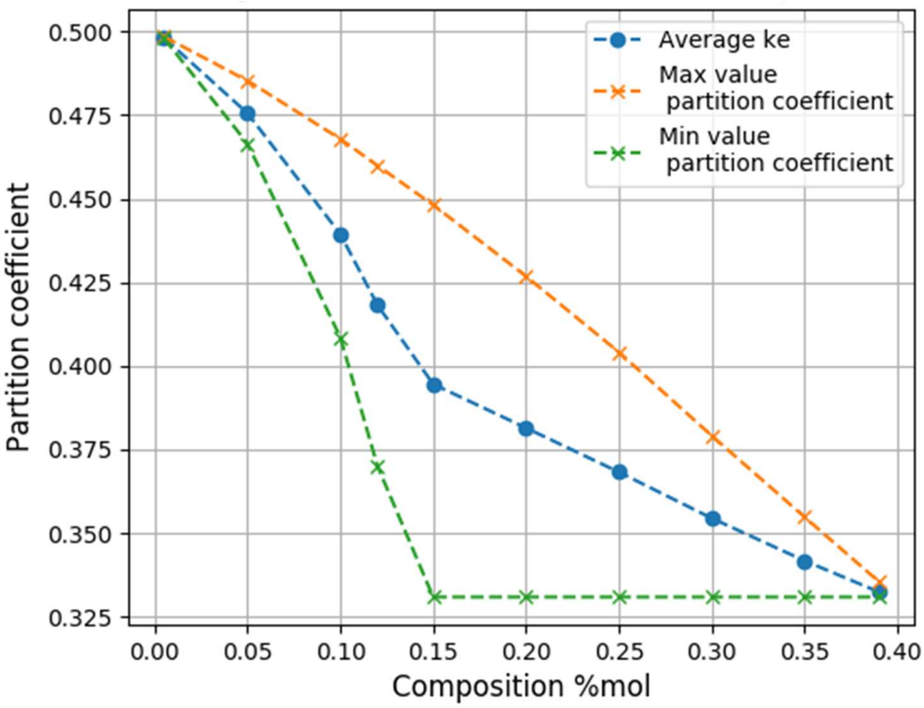

Figure 73 Blue round dote line is the average partition coefficient. Orange and green dashed line are the maximum and minimum value of the partition coefficient for the hypoeutectic composition on Ag-Cu alloy.

The use of a constant or variable partition coefficient changes the composition during solidification into the Lever Rule and Scheil-Gulliver formulations through the modification of the composition during the solidification. To compare this variation, using Equations 81 for the lever rule and Equation 84 for the Scheil-Gulliver, the latent heat calculated during the temperature decrease (solidification) for an initial composition at 15% mol Cu is shown in Figure 74. The upper graph of Figure 74 estimates the release of latent heat using the Scheil-Gulliver formulation. The lower graph uses the Lever Rule formulation. The solid line is obtained for calculations implying the average partition coefficient, whereas the blue dotted line is built from calculations with the variable partition coefficient from the phase diagram (blue points in Figure 72). The orange line corresponds to latent heat when an average constant partition coefficient of ke=0.95 is used for both models (Scheil-Gulliver or Lever rule).

For a composition at 15 mol pct. Cu the total latent heat is 99.2x10^3 [J/kg]. As shown in Figure 73 the initial composition at 15% mol Cu has the maximum variation of the partition

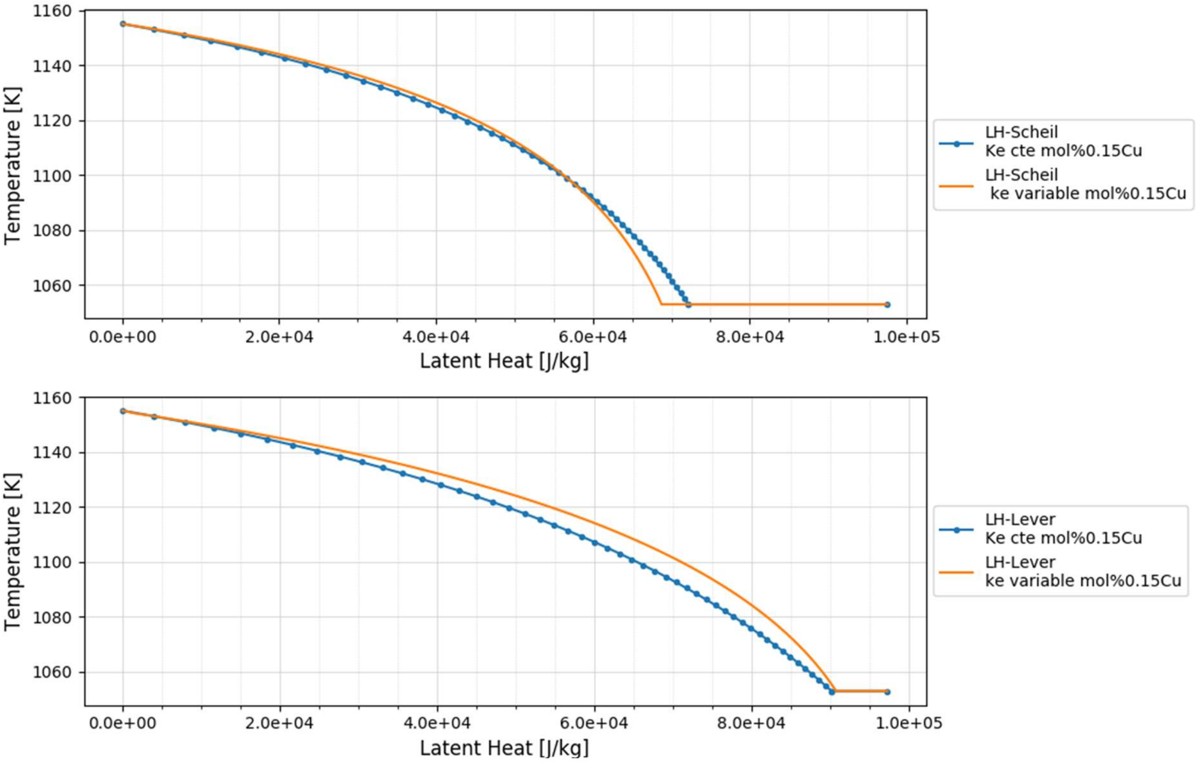

Figure 74 Variation of the latent heat calculated with the Scheil-Gulliver (Top) and Lever rule formulation (bottom). Comparison using a constant and a variable partition coefficient for an initial composition of 15 mol% Cu

coefficient with respect to the average value (up to 16.4%). This composition reveals the maximal difference between latent heats obtained respectively with a constant partition coefficient and a variable partition coefficient. Figure 74 shows that the same compositions are present with no discrepancy between variable or constant partition coefficient models. The total amount of latent heat given once the entire material is at solid state is almost identical regardless of whether the Scheil-Gulliver or Lever rule is used, as expected. However, as shown in Figure 74 the lever rule implies variations of latent heat under the 1100 K temperature until the eutectic temperature is reached.

Using lever rule Equation 81 with a variable partition coefficient to calculate the Cs, the total amount of 81.5x10^3 [J/kg] of latent heat is calculated once the eutectic temperature is reached. This amount represents 81.9% of the total latent heat that was released before the eutectic temperature during the solidification. On the other side, when a constant average partition coefficient is used (ke = 0.395), a part of latent heat of 90x10^3 J / kg is discharged before the eutectic temperature is reached. This represents 90.1% of the total latent heat. The difference between both is 9%.

The variation of latent heat release between the use of constant or variable partition coefficient must be analyzed depending on the initial composition in the alloy. Also, it depends on the phase diagram and whether the liquidus or solidus temperatures are linear or not. The variation of the composition during solidification implies variation of latent heat released during the solidification using Equation 81 for the lever rule.

However, as shown in Figure 74 top graphic, it seems that calculations based on a variable or a constant partition coefficient do not cause significant discrepancy while using the Scheil Gulliver formulation. Even for the maximum partition coefficient, the variation is minimal and lower than that used with the lever rule (bottom graph). With a constant partition coefficient, 72.5x10^3 [J / kg] of latent heat is released when the eutectic temperature is reached, this represents about 72.8% of the total latent heat released. Using the variable partition coefficient, latent heat of 69.5x10^3 J/kg is released when the eutectic temperature is reached. This represents 69.8% of the total latent heat. These differences of released heat using constant or variable partition coefficients are under 3% and can be considered negligible. The use of constant or variable partition coefficient in the Scheil-Gulliver formulation does not meaningfully alter how the latent heat is released during the solidification.

The most noteworthy in Figure 74 is the difference between the fractions calculated with the lever rule and Scheil Gulliver formulations. In general terms, compared to the Lever rule, the Scheil Gulliver equation induces a delay in the solid fraction progression before the eutectic temperature is reached. As shown in Figure 74, it is estimated that 72.5% of the latent heat has been released before reaching the eutectic temperature using the Scheil Gulliver equation. For the Lever rule equation, it estimates that over 85% of the latent heat has been released when the eutectic temperature is reached. Naturally, the use of Lever rule or Scheil-Gulliver formulation needs to be selected carefully as it depends on specific assumptions, mainly the species diffusion of the alloy.

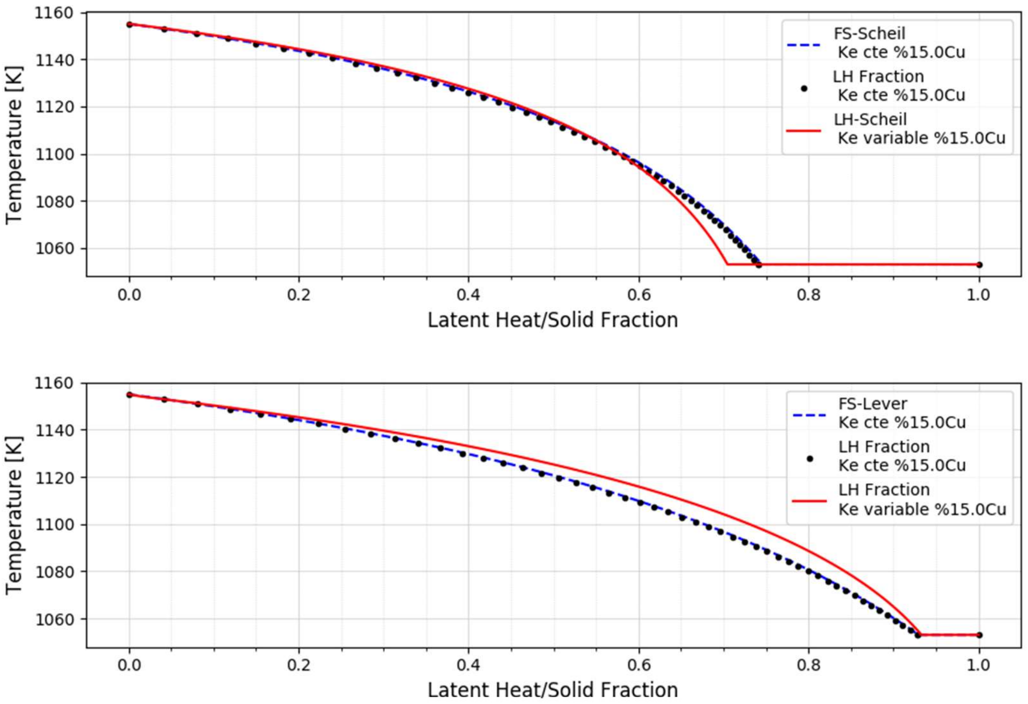

Figure 75 Blue line is the solidified fraction. Dotted and solid lines are the latent heat fraction released during the solidification calculated with ke variable or constant respectivetly. Top: Scheil Gulliver formulation. Bottom, Lever rule formulation. Ag-15%mol Cu alloy

Usually the amount of the latent heat released (LH_r) during the solidification directly relies on the amount of material solidified:

$$LH_r/dt = LH \ \cdot fs/dt \tag{86}$$

where LH is the total latent heat of the system, fs is the solid fraction and t is time.

Equation 86 is often used in literature. This defines the solid fraction linearly between the liquidus and solidus temperature. However, the inclusion of the compositional variation through the partition coefficient results in variation of the amount of latent heat released during the phase transformation and also the total amount of latent heat.

Equation 83 is the general form to consider the compositional variation during the solidification process. Cs* is calculated using the Lever rule or Scheil-Gulliver formulation during the solidification process.

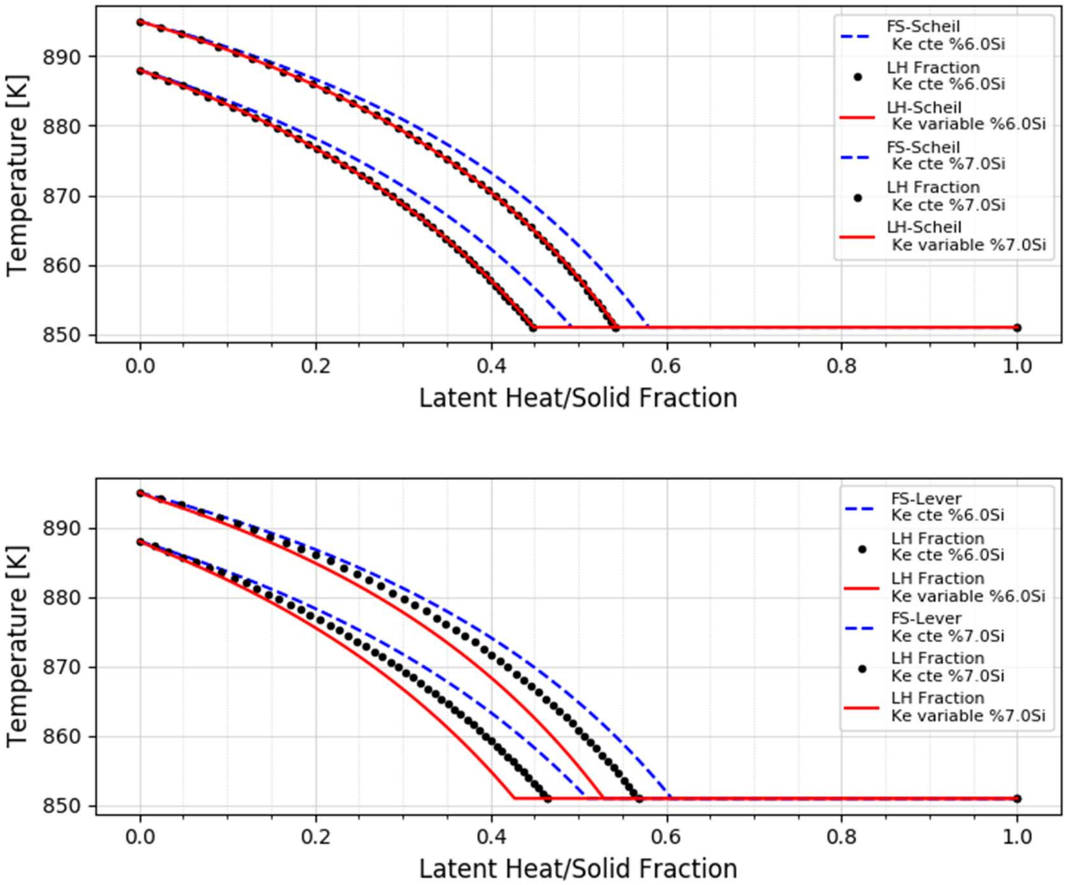

Figure 76 Two alloys: Al-6%Si and Al-7%Si. Blue dashed line is the solidified fraction. Dotted and solid lines are the latent heat fraction released during the solidification. Top, Scheil Gulliver formulation. Bottom, Lever rule formulation.

The maximum variation of the partition composition is situated at 15%mol Cu, as shown in Figure 73. At this composition Figure 74 shows the difference in the utilization of Equations 86 and 83 that considers the composition of the solid part. The blue dashed line is the solid fraction during the solidification process calculated with the Lever rule (lower in Figure 74) and Scheil Gulliver formulation (upper in Figure 74). Round black dots represent the latent heat fraction released during the solidification process using Equation 81 for the lever rule (lower graph) and Equation 84 for the Scheil Gulliver (upper graph). In both cases a constant partition coefficient is used. The red solid line comes from Equations 81 and 84 for lever rule and Scheil Gulliver respectively and implying a variable partition equation.

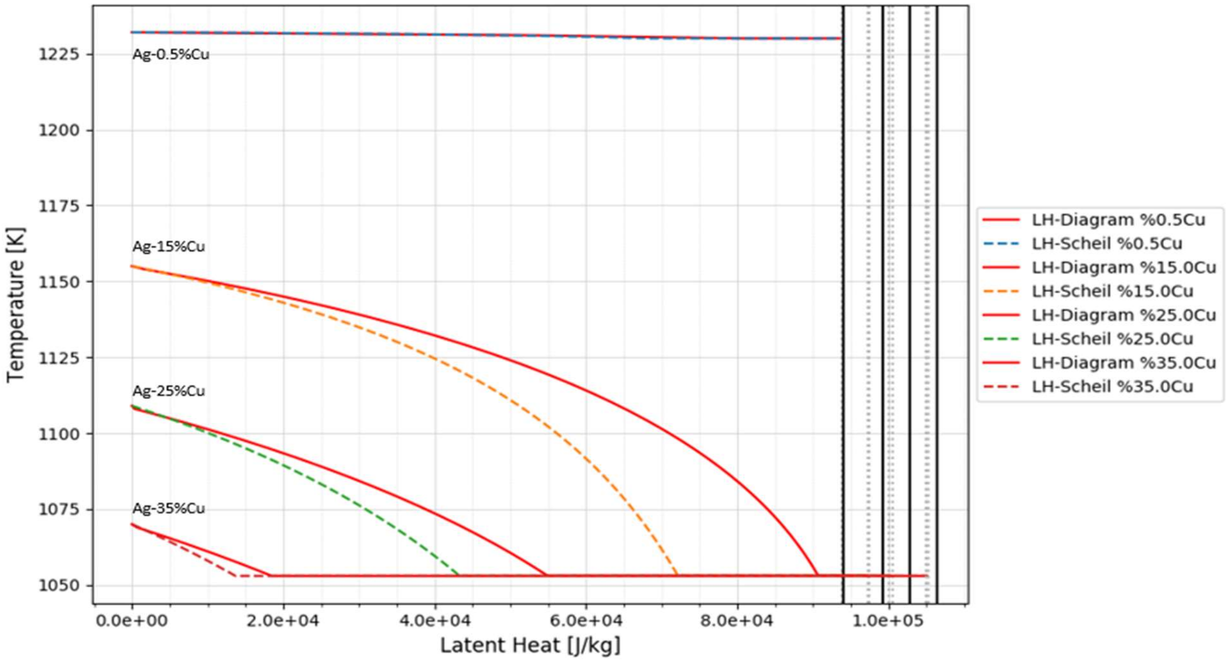

Figure 77 Latent heat release for Ag 0.5, 15, 25 and 35 mol% Cu compositions. Dotted line with crosses Scheil-Gulliver formulation with constant partition coefficient. Dotted line with points Lever rule formulation with variable partition coefficient

When a constant partition coefficient is applied, the solid fraction and the latent heat fraction exhibit the same curve, as seen in Figure 75. Nonetheless, the maximum difference found comes from the use of a constant partition coefficient or a variable partition coefficient. The maximum difference using the Scheil-Gulliver formulation (Figure 75 upper graph) is closer to the eutectic temperature. Using the lever rule, we can observe minimum differences in almost all solidification processes. These differences are under the 2% regardless of whether the lever rule or the Scheil Gulliver formulation is used. These differences are not significant. If another material is analyzed, the results are different.

The same analysis is carried out in the binary Al-Si alloy. The results are significantly different. For compositions at Al-6%mol Si alloy and Al-7%mol Si Figure 76 shows the solid fraction and the latent fraction released for the solidification process. As in the case of the Ag-15%mol Cu alloy (Figure 75), the lever rule and the Scheil Gulliver formulation are used with the variation on the partition coefficient: constant and variable.

Using Scheil Gulliver formulation, Figure 76 upper graph shows a different result from the one found with the Ag-Cu alloy. There is no difference in the latent heat released for constant partition coefficient or a variable one (contrary to Ag-Cu Figure 75).

Using the lever rule formulation, Figure 76 bottom graph shows that all results present differences between the solid fraction and the calculated latent heat released, independently of whether a constant partition coefficient or variable partition coefficient is used.

Table 7 summarizes the results Figure 75 and Figure 76. The table shows the amount of solid fraction solidified when the alloy arrives at the eutectic temperature and also the fraction of latent heat released during the solidification when the alloy comes to the eutectic temperature. These were calculated using a constant partition coefficient and a variable partition coefficient. The lever rule and Scheil-Gulliver formulations have been considered to compare their influence.

Table 7 Solid fraction and fraction of latent heat released when the eutectic temperature is reached

Amount calculated when the eutectic temperature is reached				
	Formulation	Solid Fraction	Fraction latent heat released	
			Constant ke	Variable ke
Ag-15%mol Cu	Lever Rule	**93%**	**93%**	**93%**
	Scheil-Gulliver	**74%**	**74%**	71%
Al-6%mol Si	Lever Rule	52%	47%	43%
	Scheil-Gulliver	49%	**45%**	**45%**
Al-7%mol Si	Lever Rule	60%	57%	53%
	Scheil-Gulliver	58%	**55%**	**55%**

As can be seen in Table 7 results, it is not possible to define a general behavior for all three alloys. For example, if the lever rule formulation is used, the Ag-Cu alloy shows the sames amount of solid fraction and latent heat indistinctly if a constant or a variable partition coefficient is used. On the other hand, for the Al-Si alloys shows differences up to 9 % if a constant or a variable partition coefficient is used. Thus, these difference in Al-Si alloys cannot be dismissed.

For an Al-Si alloy, only considering the amount of solid fraction to predict the amount latent heat released (Equation 86) does not seem to be completely correct. The difference between solid fraction and latent heat using a variable partition coefficient are 9% and 7% at Al-6%mol Si and at Al-7%mol Si respectively. Due to these differences, it can be assumed that for hypereutectic or hypoeutectic Al-Si alloys the variation of the composition in the solidified material must be considered to predict the amount of latent heat released

As can be seen in Table 7, the amount of solidified material and the released latent heat are the same using the Scheil-Gulliver formulation in the Ag-Cu alloy with a constant partition coefficient. However, with a variable partition coefficient the amount of heat released is 3% less than calculated with a constant partition coefficient. We consider that for energy storage calculation this can be dismissed. Thus, for the Ag-Cu alloy in hypereutectic or hypoeutectic composition the calculation of the solid fraction with a constant partition coefficient predicts well the amount of the latent heat released.

Figure 77 shows the latent heat released during solidification for four initial composition Ag-Cu alloys: 0.5 %, 15%, 25% and 35% mol Cu. The dotted line with crosses was calculated with the Scheil-Gulliver formulation and a constant partition coefficient. The dotted line with points is calculated with the Lever rule formulation using a variable partition coefficient.

For compositions close to the pure element or to the eutectic composition, Figure 77 shows that the relation between temperature and latent heat is similar. Obviously, this corresponds to a sharp liquid/solid interface for which the material is only solid or liquid without a mushy zone. However, a composition at 15 % mol Cu, shows the biggest difference between the curves for Scheil Gulliver with a constant partition coefficient. Once the eutectic temperature is reached, 71% of the material is solidified. In the case where the lever rule formulation is used with a variable partition coefficient, 85% of the material solidified when the eutectic temperature is reached. Comparing the Scheil Gulliver to the Lever rule, the observed discrepancy to the lever lever rule. Mainly, the time to complete the phase transformation using a variable partition coefficient will be different if the lever rule model or Scheil-Gulliver is used because when the rule of 14% in Figure 77 means that the alloy solidifies differently to the prediction done using the Scheil-Gulliver is used the amount of latent heat released is reduced before the eutectic temperature in comparison with the lever rule.

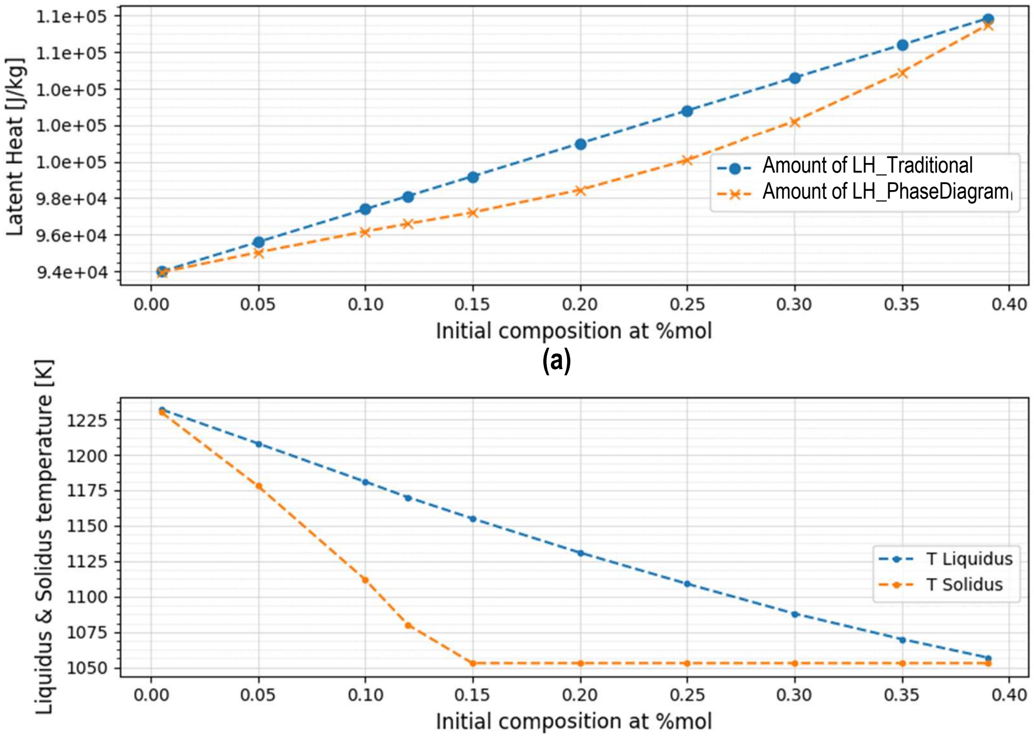

(a)

(b)

Figure 78 (a) Amount of latent heat at different composition Ag-Cu alloys, dotted line with crossed use variable composition (Equation 107), dotted line with points uses constant initial composition.(b) Liquidus and solidus lines at different compositions

The assumption that consists in defining the amount of latent heat released only by the solid fraction is not entirely correct (using Equation 80). Actually, this depends on the type of alloy and if its composition variation during solidification is relevant or not to calculate the latent heat released during the solidification process. The variation of composition during solidification influences and changes the general behavior of the material, as can be seen in Figure 77. It will be necessary to consider the composition variation because it can change the rate of solidification and the amount of latent heat released during the solidification. This assumption is not valid for compositions close to the eutectic composition or pure elements. Figure 77 does not show a significant difference between the latent heat released with a variable and a constant partition coefficient.

4.1.2 Partition coefficient: constant VS variable

Figure 78b shows the liquidus and solidus temperature as a function of the initial composition. For an Ag-Cu alloy Figure 78a shows the total amount of latent heat depending on composition variation. As we can see, the amount of latent heat calculated directly with Equation 80 (dotted line with points) is higher than the latent heat calculated with the variation of the composition with the lever rule and variable partition coefficient (dotted line with crosses). The maximal difference is almost 2.5% at 25%mol Cu composition.

These variations depend directly on the type of alloy. For example, Figure 79 shows the amount of latent heat for a binary Al-Si alloys. The dotted line with points is the total latent heat calculated using the initial composition Al-Si. The dotted line with crosses shows the total latent heat calculated by the amount of material that solidified using the lever rule and variable partition coefficient. As observed for the Ag-Cu system, the Al-Si alloy exhibits differences between these two amounts of almost 8% at 6mol% Si composition.

Estimating the latent heat released during the solidification is more complex than it appears, and possible sources of error need to be taken into account such as: the influence on the composition by the use of a constant or variable partition coefficient, variation in the amount of latent heat if a equilibrium solidification or off equilibrium solidification is calculated and if the composition is close to eutectic composition or pure element. To show this variation and its influence, Figure 80 compares the liquid fraction for the four previously defined compositions (0.5 %, 15%, 25% and 35% mol Cu). The liquid fraction is calculated using the Scheil Gulliver formulation (solid line) and the lever rule is used with a constant partition coefficient (dashed line) and with a variable partition coefficient (dotted line). As mentioned before, for an initial composition close to eutectic or pure element composition, the differences are not significant. However, for the intermediate composition, the variation is more significant and different if the Scheil-Gulliver or lever rule formulation is used.

Additionally, Figure 78a shows how the variation of the composition significantly affects the amount of latent heat that the material is able to discharge. As was shown in Figure 73 and Figure 78, it is concluded that for initial compositions that are not close to eutectic points or pure elements the latent heat must be quantified through the variation of composition that solidifies and not only by the liquid/solid fraction without composition variation. The differences are

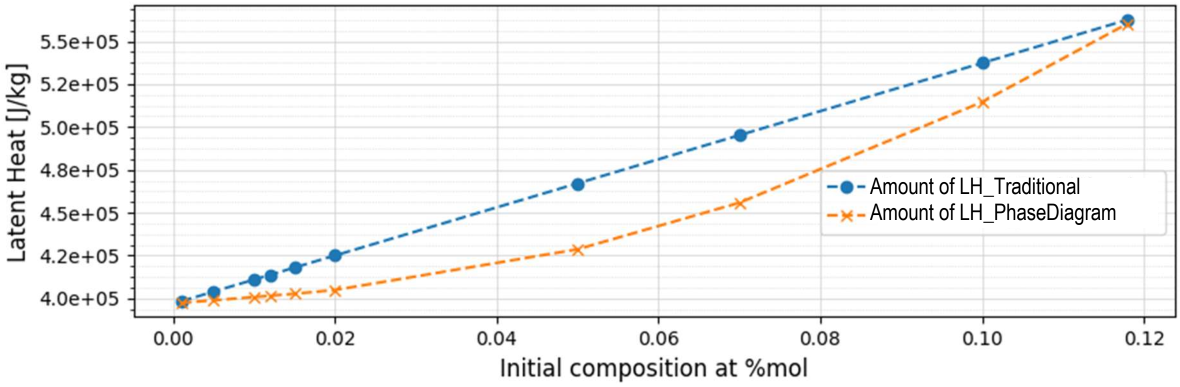

Figure 79 Amount of latent heat at different compositions for an Al-Si alloy, dotted line with crosses uses variable composition (Equation 107), dotted line with points uses constant initial composition

significant mainly when there are notable variations in the partition coefficient (see in Figure 73). When considering a new phase diagram that represents a new material, the influence of the partition coefficient must be evaluated.

Fortunately, the partition coefficient can be easily estimated using the phase diagram. Figure 73 compares the average values of the partition coefficient with its maximum and minimum values. The use of constant partition coefficient values can generate significant differences in terms of released latent heat with respect to the expected value estimated in the phase diagram. Therefore, it is concluded that this variation should be evaluated to define if this variation is insignificant and can be dismissed. For example, in compositions at 0.5 and at 35 %mol Cu the partition coefficient varies <4% from the average value. It is then possible to identify the range of composition where the partition coefficient variation must be taken into consideration.

In summary, when non-eutectic compositions are used, it is necessary to evaluate the following aspects:

- Using constant partition coefficients can significantly affect the composition that solidifies in the material. While simulating materials with compositions close to the solubility limits, it will be recommended to use variable partition coefficients as a function of temperature. Likewise, the significant variations that can be obtained if the Lever Rule or Scheil Gulliver formulations are used should be considered. Figure 81 compares both formulations to estimate the liquid fraction in four different compositions.

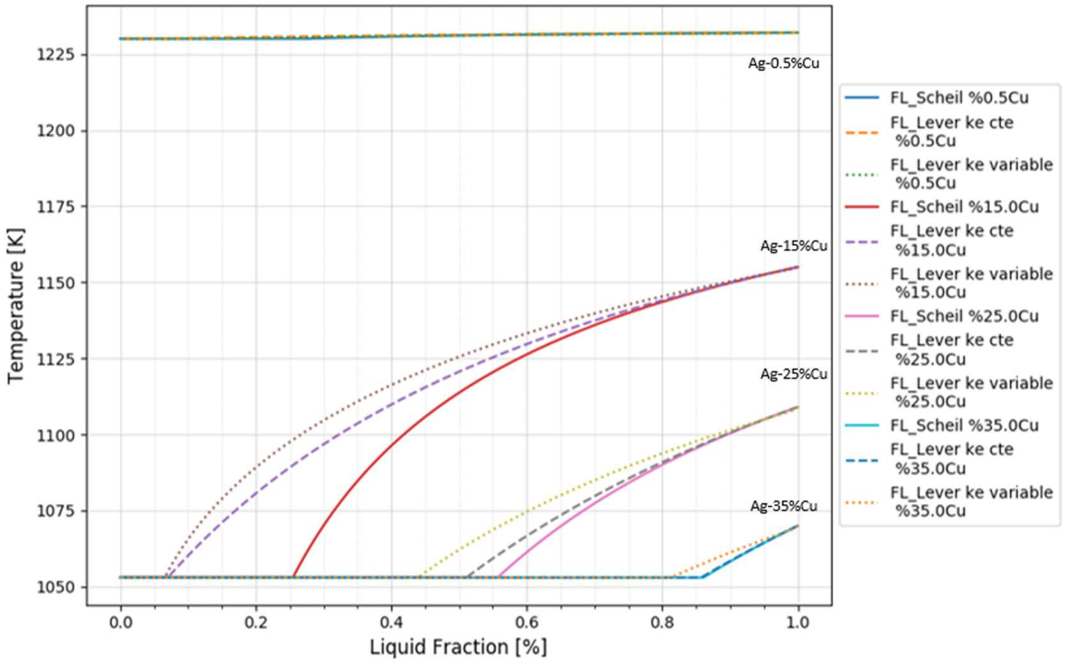

Figure 80 Solidification for four compositions Ag-Cu (0.5, 15, 25, 35 mol% Cu). Scheil Gulliver are liquid fraction solid line (ke const.). Dashed lines are liquid fraction lever rule (ke cte). Dashed lines are liquid fraction lever rule with variable partition coefficient

- Estimating the latent heat released only by the solidified fraction can be a source of calculation errors in the prediction of the phase change, principally for compositions close to the solubility limits. The variation in composition especially in compositions near the solubility limits can affect significantly the partition coefficient and consequently affect the amount of latent heat that remains when the material reaches the eutectic temperature.
- The partition coefficient plays an important role when undercooling effect is calculated. The use of variable or constant values directly affect this amount and need to be evaluated for every material to define which give less variation in the composition estimation.

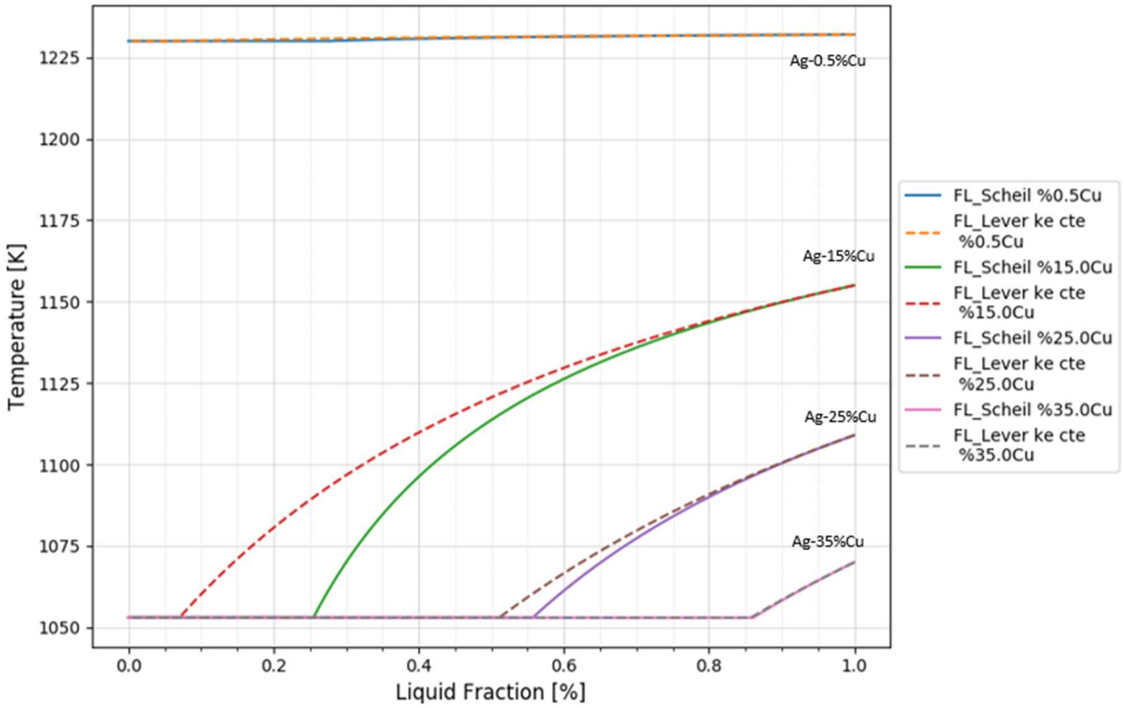

Figure 81 Difference betwen the lever rule and Scheil Gulliver formulation used to calculate the lilquid fraction during the solidification for AgCu alloys

4.2 Isothermal phase change.

Isothermal phase change has been numerically carried out through the numerical software Fluent as a quasi isothermal phase change (ΔTs=2 K). A first step has consisted in proposing a numerical verification of phase change of a pure material, by comparing the results with references from literature. Theoretical and experimental studies in the field of isothermal phase change (particularly for paraffin materials) and its applications have yielded extensive literature. Fluent has been widely validated and time and space convergences have been carried out and are available in literature. We have focused our attention on the comparison of our numerical method with corresponding experimental results.

Spherical Shell phase change

The spherical shell phase change experiment has been of great interest from the theoretical and experimental points of view for the characterization and comparison of PCMs for energy storage applications. A considerable amount of theoretical (Bareiss and Beer [176]–[178].) experimental (Katayama et al. [179]) and numerical (Saitoh and Hirose [180]), literature can be found on this subject.

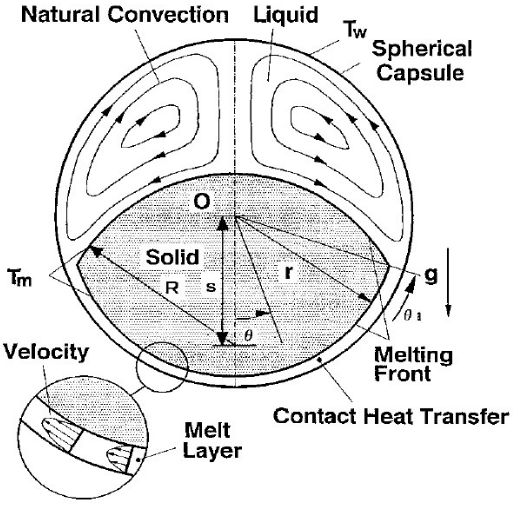

Figure 82 Melting process in a spherical capsule, from [181]

S. A. Fomin et al. [181] present the analysis of the melting process in spherical capsules. Figure 82 illustrates a sketch of their melting process. The principal characteristics are:

- A plexiglas sphere of radius R containing phase-change material is studied.
- Initially the phase change material is in the solid phase and entirely at melting point Tm or 1 K under Tm.
- The constant wall temperature is equal to Tw, which is higher than Tm (usually 10 K). As a result, inward melting of the solidification starts.

The motion of the solid bulk is accompanied by generation of liquid at the melting interface and the liquid is squeezed up through a narrow gap between the melting surface and the wall of the capsule to the space above the solid. The intrusion of some solid inside the phase change material (for example thermocouples) entirely changes the process, melting patterns and qualitative characteristics (concluded by Rieger et al., Khodadadi and Zhang, Katayama et al.). This is known as a constrained experiment. The spherical shell process is sub-divided into constrained and unconstrained, studied in F.L. Tan [182]. The constrained experiment includes thermocouple wires inserted into the enclosure. On the other hand, the unconstrained does not have any element inside. Our validation is done on unconstrained melting based on the study performed by E. Assis et al [183]. Their experimental setup can be found in [183].

Simulation Setup

Figure 83 shows the numerical model described by E. Assis et al. that was used to reproduce the experiment. An 80mm diameter sphere was used. The principal settings used are:

- The solid phase initially occupies 85% of the volume, having a flat top.
- The glass has a thickness of 2 mm.
- The PCM used was the RT27 paraffin wax (thermophysical properties are summarized in Table 8 and Table 9).
- The melting interval is ΔTs=2 K, Ts=301.15 K and TL=303.15 K.
- The wall temperature is set to a constant 10K above the mean melting temperature of the PCM.

We have carried out a numerical simulation with Fluent**.** A two-dimensional, axisymmetric model was created to reduce the computational complexity of the simulation. Both solid and liquid phases are assumed to be homogeneous and isotropic. The section of the PCM in contact with air was set at 10 K above the mean melting temperature of the PCM with a convective heat transfer coefficient of h=10 [W m^-2 K^-1] [184].Figure 83 shows the mesh that was used and the imposed frontier condition.

Table 8 Thermophysical Properties of paraffin

Wax Properties				
Property		Solid	Liquid	Liquid
		(273,15K-301,15K)	303,15 K	373,15 K
Density	(kg/m3)	870	760	734,3
Specific heat	(J/kg-K)	2400	1890	1890
Thermal Conductivity	(W/m-K)	0,24	0,21	0,21
Viscosity	(kg/m-s)	3,42E-03		
Thermal Expansion Coefficient	(1/K)	1,0E-03		
Pure Solvent Melting Heat	(KJ/kg)	179		

Table 9 Thermophysical Properties of plexiglass

Plexiglas properties		Solid
Glass Properties		(273,15K-301,15K)
Density	(kg/m3)	2500
Specific heat	(J/kg-K)	800
Thermal Conductivity	(W/m-K)	0,81

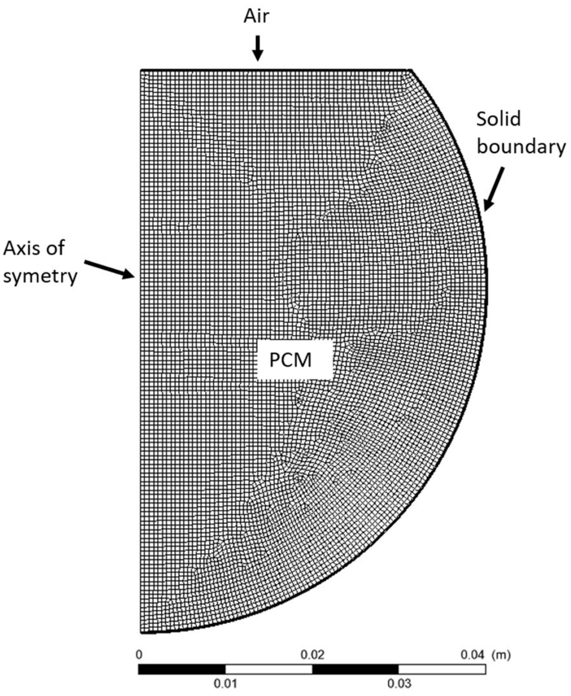

Figure 83 Computational domain

4.2.1 Validation results

Good agreement was found between the results of Assis et al and our results when replicating their study. Each simulation took approximately 24 hours to solve the 40 minutes of the entire simulation time. Figure 84 compares Assis results with our results. The temperature field, the solid fraction and the velocity field in the liquid have been compared to those of the referency study by Assis. The study shows that the solid PCM sinks to the bottom of the enclosure as the wax near the walls melts. The shapes of the solid PCM are consistent with those described by Assis [183]. Figure 84 shows how the solid phase typically descends. Our results exhibit very

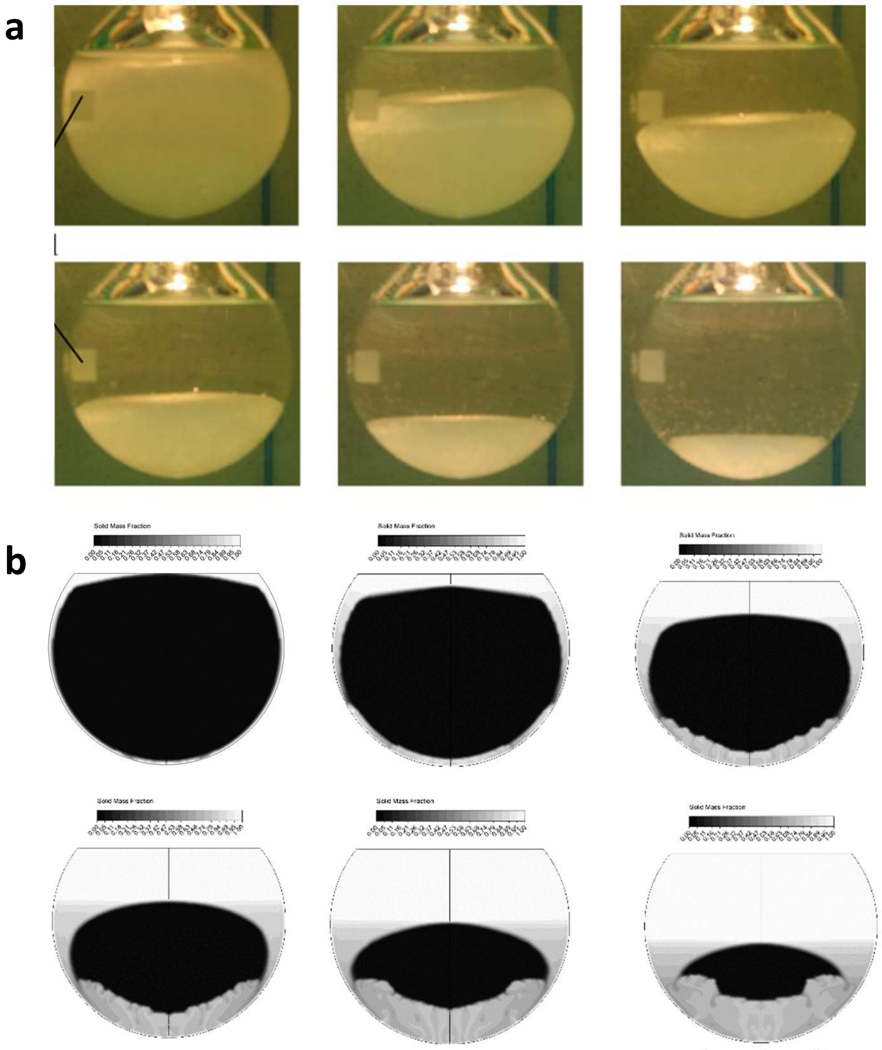

Figure 84 Experimental and numerical melting patterns, a) experimental result by Assis et al.[183]. b) Numerical results at 2, 5, 10, 15, 20 and 25 minutes since the start of the process

good agreement with the literature. Figure 85 shows the vortex flows and the phase change patterns. Also, the flow pattern shows that in the upper part of the melt, natural convection is initiated by the temperature difference between the heated wall and the relatively cold solid phase, as we can see in the left the temperature pattern. As a result, the liquid rises along the wall. In the lower part, a thin liquid layer is formed between the sinking solid and the shell. Flow patterns agree with theoretical and experimental results.

Figure 86 shows the measured experimental values by Assis and simulated melt fractions vs. time. One can see that the melting time is slightly shorter in the simulation. However, one can conclude that the agreement between the experimental and simulation values is very good. The results reported by Assis were accurately reproduced not only in overall parameters, but also in the details of the melting process (Figure 84).

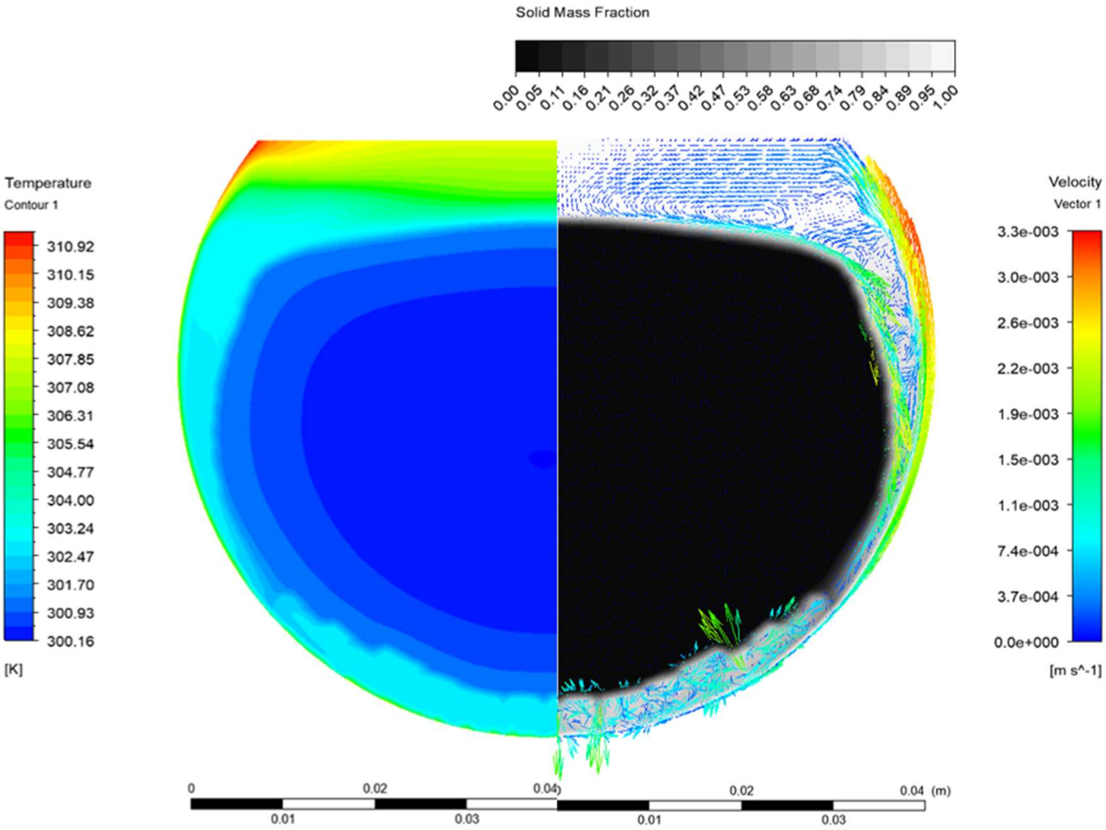

Figure 85 Right side, temperature patterns. Left side, mass fraction patterns and velocity vectors at 5 minutes since the start of solidification

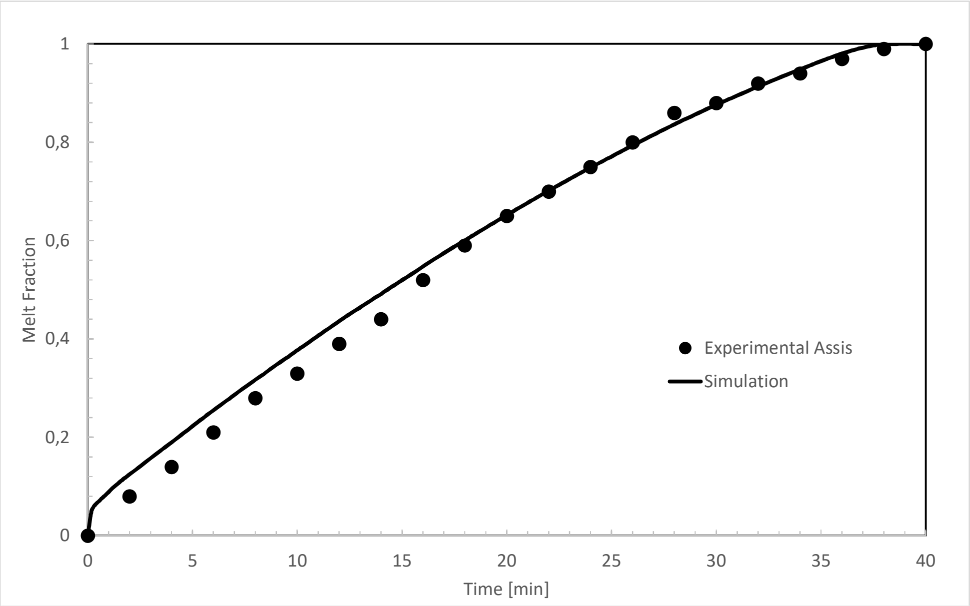

Figure 86 Comparison of the experimental results from Assis et al.[183] and numerical melt fractions

4.3 **Undercooling degree**

This section aims to validate the solidification process with undercooling. The degree of undercooling is considered random and probabilistic, depending on multiple aspects, such as presence of impurities, vibrations, wall roughness and degradation of the material. These aspects are not considered in our method and model. Undercooling is defined under the following hypothesis:

- Degradation of material by cycles of charge discharge is not considered.
- The degree of undercooling depends only on the cooling rate. At a higher cooling rate, the degree of undercooling is increased.
- At the moment of initiating the phase change during undercooling, the material releases latent heat. The solidification rate controls the rate of latent heat release. In this section, a constant rate of solidification is considered.
- The solidification rate is a characteristic of the material and the mixture proportions. This solidification rate has a maximum limit and varies from one material to another one.

The solidification process in a undercooling process is controlled mainly by two mechanisms: i) the rate of latent heat release and ii) the rate of heat removal. As the material solidifies, the latent heat is released and it may be, entirely or partly, consumed by the material itself (recalescence), depending on the rate of heat removal. These characteristics are evaluated imposing two different cooling rates.

There are only a few works that deal with an undercooled alloy. For paraffins, more studies are available. However, the experimental are not completely detailed in literature. For example the Yoshioka et al. [185] work reports an experimental study of the solidification of an undercooled alloy using Pb-Sn and Bi-Sn alloys. Although they do not report material properties, cooling rates, wall thickness of the container and its specific dimensions (they do not specify whether the stated dimensons are internal or external) and also relative information about thermal insulation of the wall. The lack of information prevents reproduction of the experiments in a numerical simulation.

Also, another shortcoming currently found in the literature is the questionable configuration of the experimental apparatus. In the Yoshioka et al. [185] work, their first

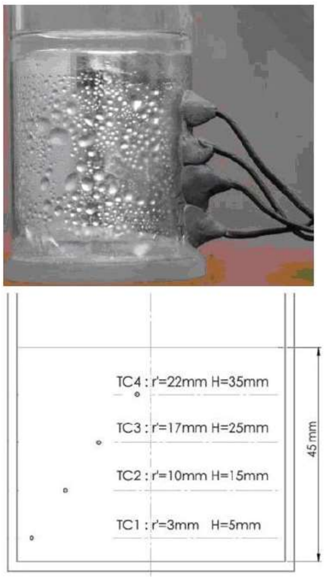

Figure 87 Thermocouple position in the undercooled gallium in the experimental configuration of Harary et al[189]

thermocouple is positioned in contact with the cooled wall in the sample and consequently this can induce a significant influence on the solidification/ undercooling process. The literature shows that when the solidification has some mechanical obstacle (e.g. impurities or thermocouples inside the PCM), melting patterns and qualitative characteristics for the process become entirely different (see Rieger et al. [186], Khodadadi and Tan works [187], [188]). Unfortunately, the undercooled alloy works found cannot be used to validate the model.

The comparison has been based on of Harary et al [189]. It is focused on the experimental heat transfer processes of undercooled gallium into cylindrical molds of two different materials (copper and polypropylene). The thermophysical properties and the setup of their experimental apparatus are detailed in [189]. The top wall is declared only to be exposed to ambient temperature. For the simulation model, the top wall was assumed to be at an ambient temperature of 300 K with a convective heat transfer coefficient of 10 W/m^2K based on [190]. Figure 87 shows the thermocouple positions in the experimental apparatus. The same positions are used in the numerical model to compare results.

Simulation Setup

The experimental apparatus described by Harary et al [189] consists in two thermostatic baths filled with 50% polypropylene glycol and 50% distilled water. One bath was used to heat the sample up to 50°C while the other one was used to cool the sample. The bath has continuous circulation to preserve a constant temperature the bath.

Table 10 Thermophysical properties of gallium, copper and polypropylene

Gallium Properties				
Property		**Solid**	**Liquid**	**Liquid**
		(273,15K-302,95K)	304,95 K	350 K
Density	(kg/m3)	5910	6075,8	6048,2
Specific heat	(J/kg-K)	366	366	366
Thermal Conductivity	(W/m-K)	40,6	40,6	40,6
Viscosity	(Pa s)		1,55E-03	1,37E-03
Thermal Expansion Coefficient (liquid)	(1/K)	1,2E-04		
Pure Solvent Melting Heat	(KJ/kg)	80,3		
Copper properties		**Solid**		
		(273,15K-301,15K)		
Density	(kg/m3)	8954		
Specific heat	(J/kg-K)	383		
Thermal Conductivity	(W/m-K)	380		
Polypropylene properties		**Solid**		
		(273,15K-301,15K)		
Density	(kg/m3)	855		
Specific heat	(J/kg-K)	1900		
Thermal Conductivity	(W/m-K)	0,17		

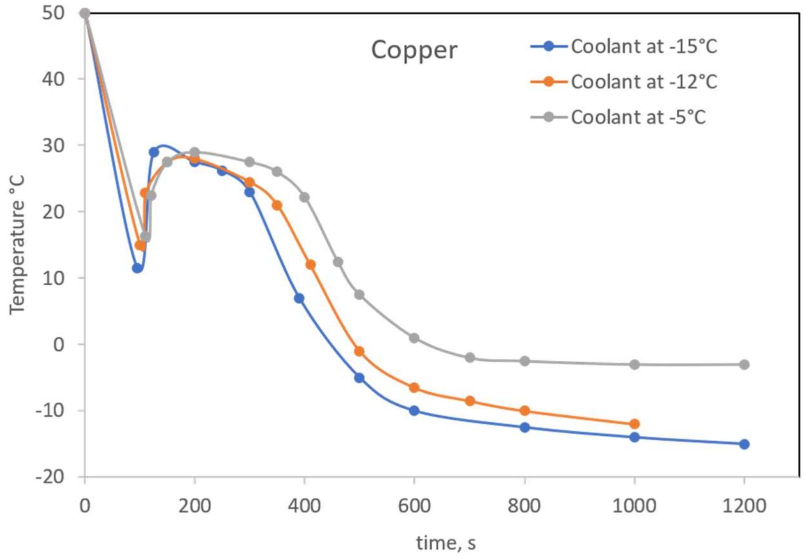

Figure 88 Experimental time dependent temperatures and melt fraction of gallium in copper shell for coolant temperatures at -15°C (blue), -12°C(orange) and -5°C (gray) [196]

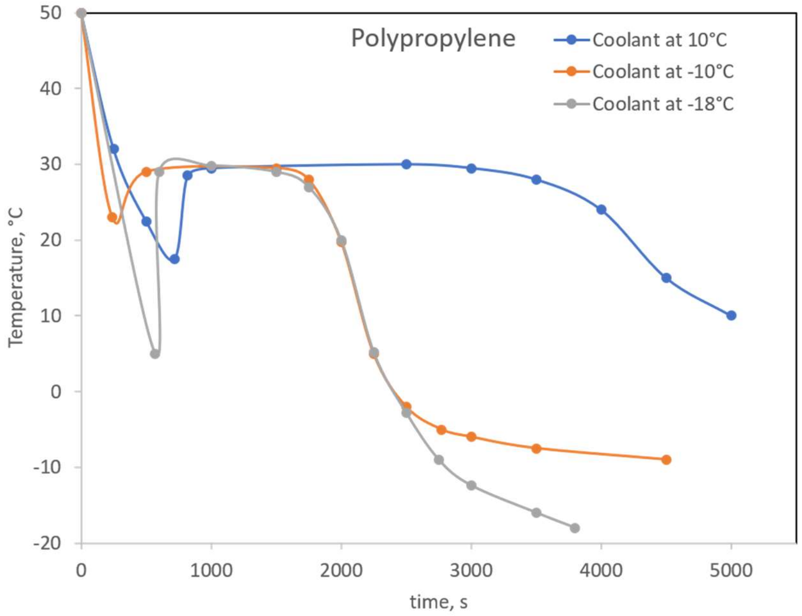

Figure 89 Experimental time dependent temperatures and melt fraction of gallium in polypropylene shell for coolant temperatures at 10°C (blue), -10 °C (orange) and -18°C (gray) [196]

The sample was commercial gallium contained in a cylindrical shell with a flat bottom and exposed to air at its top. Their experiments were performed in two shells, one in copper and other one in polypropylene. The inside diameter of the cylindrical shells was 50 mm, with the sample gallium rising to a height of 45 mm. The thermophysical properties are summarized in Table 10.

The initial temperature was 50°C. The sample is transferred into the cooling bath where the coolant temperature was maintained constant. The circulation of the coolant was intensified or slowed down to cope with the absorbed heat. Haravay et al. [189] reported that the convection heat transfer coefficient for the copper shell around the sample was h=240 W/m^2K in the gallium undercooling zone and h=370 W/m^2K in the solidification. For the polypropylene shell the convective coefficient h=57 W/m^2 in the undercooling zone and h=63W/m^2K in the solidification zone.

Haravay et al. use 3 constant coolant temperatures for the copper shell: -15°C, -12°C and -5 °C. For the polypropylene shell, the coolant temperatures 10°C,-10°C and -18°C are used. Figure 88 and Figure 89 show the experimental cooling curves for the copper and polypropylene shells respectively [189]. The temperatures are the average value for the four thermocouples shown in Figure 87. [189]

Gallium has a high thermal conductivity of k=40.6 W/mK. Then, the heat released by the phase change is almost entirely absorbed by the gallium, as can be seen in Figure 88 and Figure 89 by the quasi instantaneous (vertical) recalescence process that rises the temperature to the stable solidification temperature.

The experimental cooling rate with its cooling degree are summarized in Table 11, from the results from Haravay et al. The polypropylene shell (Figure 89) shows incoherent cooling curves. For the coolant at 10°C (CR of 0.045 °C/s), they reported a undercooling degree of 12.3 °C. However, with a lower coolant temperature of -10°C, (2.5 times higher CR 0.113 °C/s) the undercooling degree is lower (around the 6.8°C). This is a surprising result since at higher CR, a higher undercooling degree is expected.

Also, we found surprising that for the polypropylene shell with a coolant temperature of -18 °C they reported a undercooling degree of 25 degrees. This value is greater than any other values reported including the copper shell (Figure 88) that show greater cooling rates.

Based on the results shown in Table 11, we can see that for the polypropylene shell at a coolant temperature of 10°C and -18°C, cooling rate and undercooling degree do not have the same tendency as other results. For these reasons, these two experimental results are not considered.

Table 11 Experimental cooling rate in undercooling gallium zone

	Coolant temperature	Cooling rate	Undercooling degree
	°C	K/s	K
Copper shell	C at -15	0,405	18,3
	C at -12	0,350	14,8
	C at -5	0,307	13,6
Polypropylene shell	C at 10	0,045	12,3
	C at -10	0,113	6,8
	C at -18	0,079	24,8

As mentioned in the Cooling rate and solidification velocity method section, Equation 30 defines the relation between CR and solidification velocity. We do not have information about the solidification velocity, and based on the polynomial formulation (Equation 30) and the results of Haravay et al [189] we proposed the undercooling degree (ΔTu) as a function of cooling rate (CR) defined by the expression:

$$\Delta T_u = 1273.6 \cdot CR^3 - 1006.3 \cdot CR^2 + 276.33 \cdot CR - 13.369 \qquad (87)$$

Figure 90 shows Equation 87 and experimental results of Haravay et al [189].

In our numerical simulation Equation 87 drives the calculation of the undercooling degree as a function of the cooling rate as was described in the FB-Undercooling. Since gallium is not a binary alloy, the FB-k non-equilibrium and FB-Solidification velocity are not used.

As can see in Figure 90, at cooling rates over of 0.061 [K/seg] gallium starts to show a undercooling degree. Based in Equation 87, was can assume that for thermal energy storage we can dismiss a undercooling degree under 5 K. Then it can be modeled as isothermal phase change.

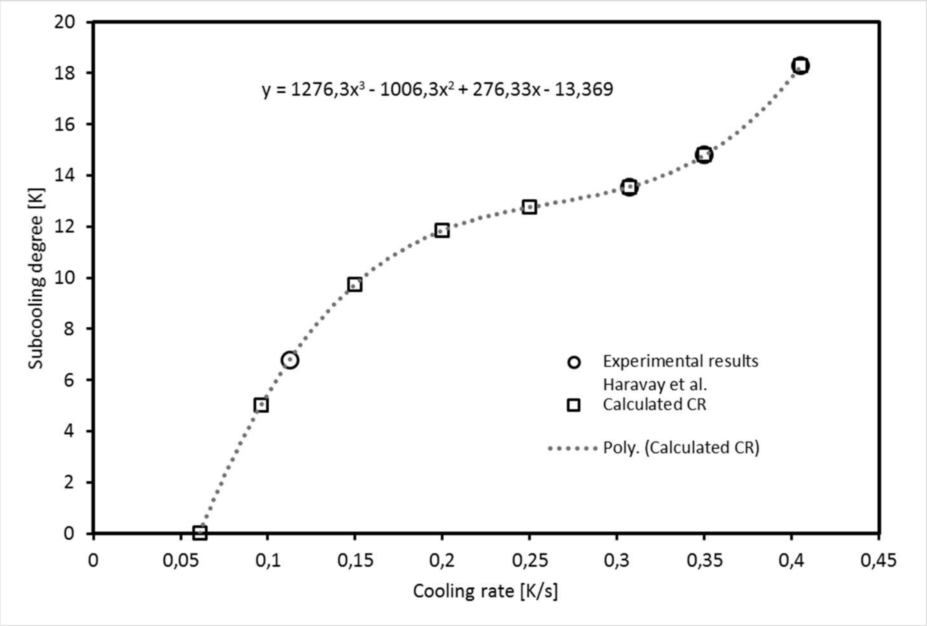

Figure 90 Undercooling degree dependent on cooling rate. Formulation obtained from the experimental data of Haravay et al. [196]

Using Equation 87, for the gallium material the limit cooling rate is 0.096 [K/s]. Over this value, the expected undercooling degree cannot be dismissed, as it will be greater than 5 K.

Boundary conditions

A two-dimensional, symmetric model was used to reduce the computational complexity of the simulation. It is assumed that both solid and liquid phases are homogeneous and isotropic. Figure 91 shows the simulation setup in the simulation model that replicates the experimental conditions of Haravay et al. [189]. The same dimensions of sample are used: bi-dimensional rectangle of 50 mm width (modeled with an axis of symmetry) and 45 mm length. A uniform spatial discretization of 0.2 millimeters is applied, giving 28476 nodes and 28125 elements, shown in Figure 91.

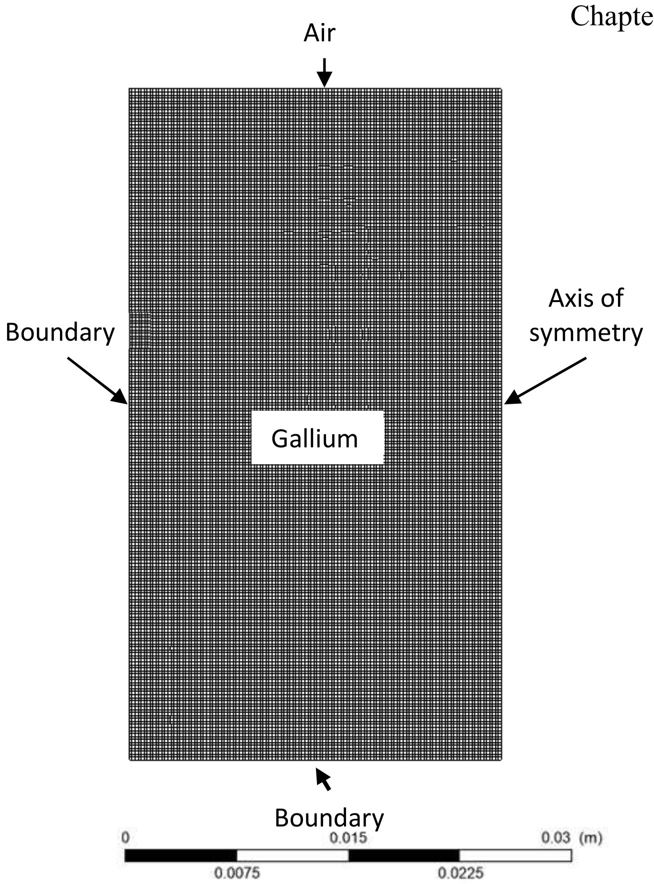

Figure 91 Simulation setup of undercooled gallium. Spatial discretization of 0.2 milimeters. Dimensions of 50 mm width and 45 mm length

Two coolant temperature experiments are replicated: constant coolant temperature at 258.15 K and at 268.15 K. These generate cooling rates 0.41 K/s and 0.31 K/s respectively. These cooling rates are applied on the left and bottom wall.

The boundary setup follows the experimental apparatus described by Haravay et al for two coolant temperatures:

- 0.2 millimeters of copper shell thickness and 2.25 millimeters of polypropylene shell thickness.
- The thermophysical properties are detailed in Table 11.
- The melting interval is ΔTs=2 K, with solidus temperature of Ts=302.955 K and liquidus temperature of TL=304.95 K.
- The wall section of the PCM in contact with air was set at 10 K above the mean melting temperature of the PCM with a convective heat transfer coefficient of h=10 [W m^-2 K^-1] [190].

A third simulation is configured where a cooling rate of 0.06K/s is applied to the left and bottom wall. The other parameters are the same. This corresponds to an isothermal phase change.

4.3.1 Undercooling validation

The two undercooled simulations took approximately 4-5 days to solve all the time indicated in each simulation model. Figure 92 and Figure 93. show the time dependent temperatures for the coolant at 268.15K (-5°C) and 258.15K (-15°C) respectively. These figures show the average temperature at the points situated in the same positions described in Figure 87.

Coolant at 268.15 K (-5 °C)

Figure 92 shows the average experimental temperature with a horizontal error bar at 2% that represents the maximum temperature difference with the simulation results (solid line). The temperature history shows good agreement before the start of solidification. The undercooling degree also is almost identical, 13K for simulations and approximately 13.6K for experimental undercooling. It seems that the initial 323.5K the temperature drops almost identically on both curves before the start of the solidification. However, at the beginning of phase change process, differences in temperature appear. The recalescence process is different.

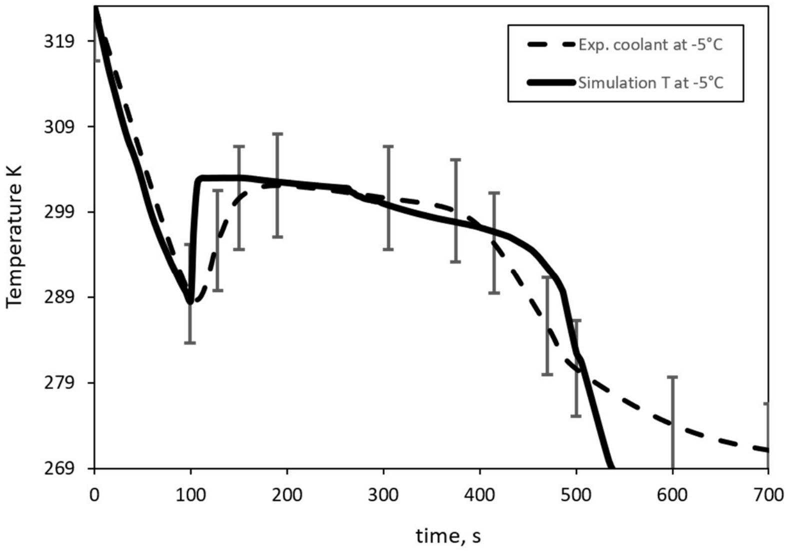

Figure 92 Time dependent temperatures of gallium in a copper shell for coolant temperature of -5°C (dash line) [196], simulation results (solid line). 2% vertical error bar in experimental results

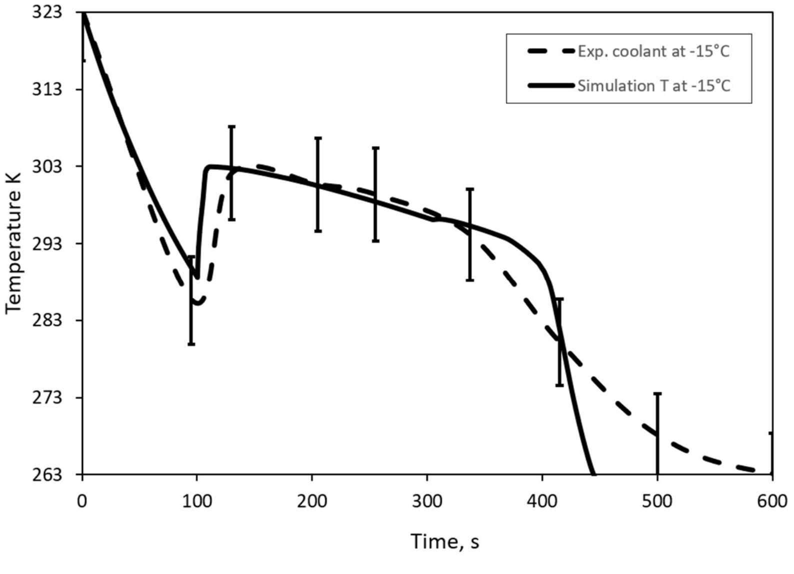

Figure 93 Time dependent temperatures of gallium in a copper shell for coolant temperature of -15°C (dash line) [196], simulation results (solid line). 2% vertical error bar on experimental results

The experimental results show a low increase of temperature until the melting temperature (303.15K). On the other hand, our results show the recalescence process occurs very rapidly. Nevertheless, the temperature difference is under 3%. The differences in the recalescence process are due to the solidification velocity. Equation 87 uses the cooling rate and the undercooling degree, but the solidification velocity is not defined. In our model, the solidification velocity was fixed at 1x10^{-3} m/s. This value seems to lead to release of latent heat in the simulation faster than that seen in the experiment.

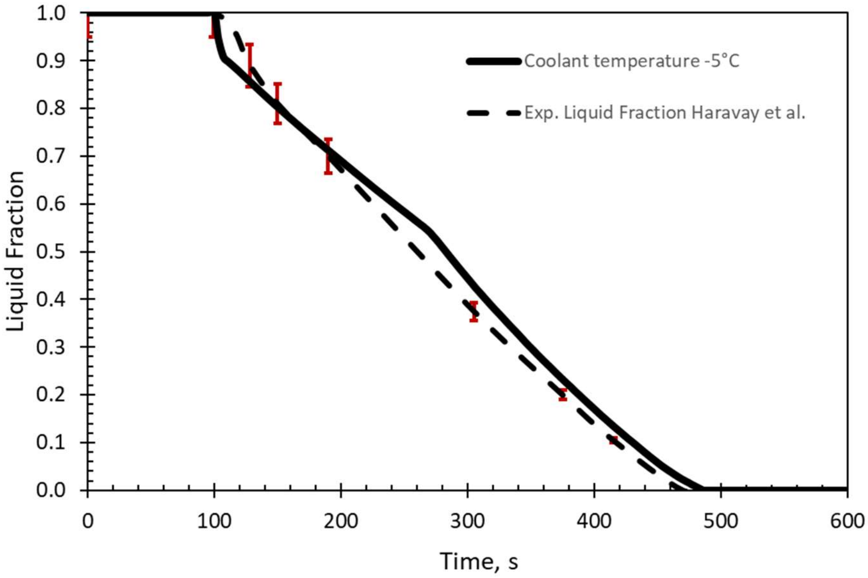

Figure 94 Liquid fraction for the coolant temperature of 268.15K; , dashed line is experimental results of Haravy et al. [196]. Solid line is numerical results. Horizontal error bar marks a difference of 5%

The differences of solidification velocity are also compared with the amount of solidification dependent on the time, shown in Figure 94. The vertical error bars define the limit of 5% liquid fraction difference from the experimental results. The numerical medium solidifies faster in the first 50 seconds, during wich the maximum differences in solidified volume occur. Afterwards, temperature rises until the melting temperature (303.15K). This continues as an isothermal solidification process. The difference between the numerical approach and experimental results in the isothermal phase change are above 5%.

At the end of solidification (below 10% of liquid fraction), the experimental temperature decreases slowly compared to the numerical approach. This behavior makes us suppose a diminution in the coolant rate on the experimental apparatus. Harary et al. described that for the undercooling zone the convection heat transfer coefficient for the copper shell around the sample was estimated in h=240 W/m^{2}K and h=370 W/m^{2}K in the solidification zone. However, they don't mention if these values were changed at the end of the solidification process. This asumption is based on the final experimental time. Harary et al. shows in their results that after 900 seconds of experimental time, their cooled sample reaches a minimum temperature of 270.15 K (-3°C), and the temperature does not drop anymore. They final experimental time was 1400 seconds. In addition, another possible factor is that at the end of solidification (below 10% of liquid fraction), the solidification velocity is slower.

Apart the temperature difference after 410 seconds in the remaining 10% of liquid, the general difference in the temperature history does not exceed 5% with respect to the experimental temperature. Neertheless, the time for gallium to reach an average temperature of 268.15 K (-5°C) is significantly different: 548 seconds for the numerical solidification model and 900 seconds to reach the lowest temperature of 270.15K (3°C) in the Harary et al. study.

Another aspect is that liquid gallium is denser than solid gallium (thermophysical properties Table 10). This affects the solidification process inside the shell. The left and bottom walls are cooled, then the phase transformation occurs over these walls. However, the liquid tends to go down. Figure 95 and Figure 96 show the liquid fraction field (left) and temperature color map (right) at 373 seconds and 460 seconds respectively. The solidification front has progressed from the left to the center. However, the bottom solid front advanced around the middle of the sample. Figure 96 shows how the top solid front starts to involve the rest of liquid fraction. This implies that heat extraction goes through the formed solid. The thermal conductivity is the same in liquid and solid phases. At the beginning of phase transformation, the convective fluid increases the heat transfer. However, in advanced stages when the liquid is enclosed in the middle of the sample, the fluid movement is stopped and only the conduction heat transfer mechanism is present in the remained liquid fraction. Assuming equal thermal conductivity in both phases, this leads to less heat transfer.

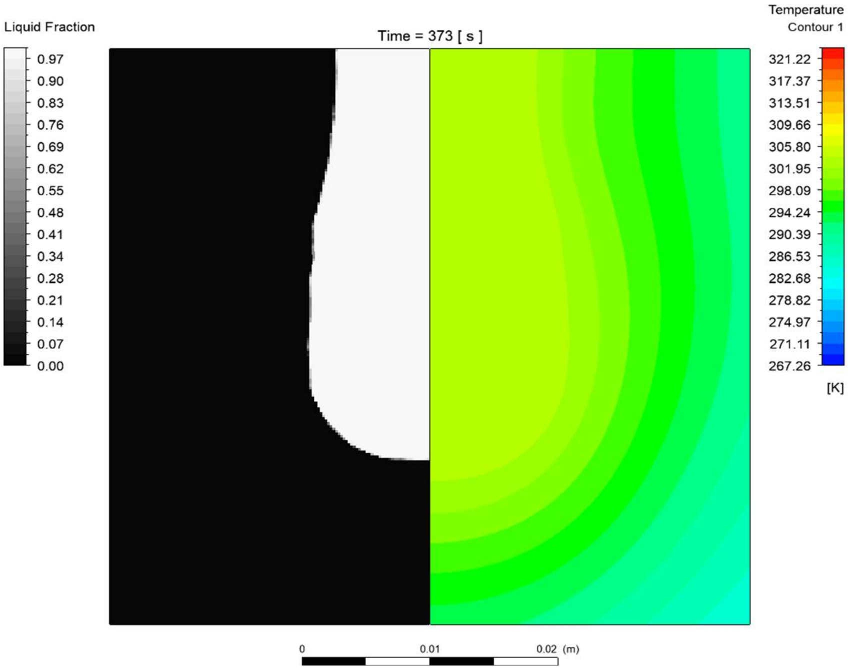

Figure 95 Temperature fields at 373 seconds on the right. Liquid fraction field on the left, black color indicates solid zones. Both correspond to numerical results. Coolant temperature of 268.15 K

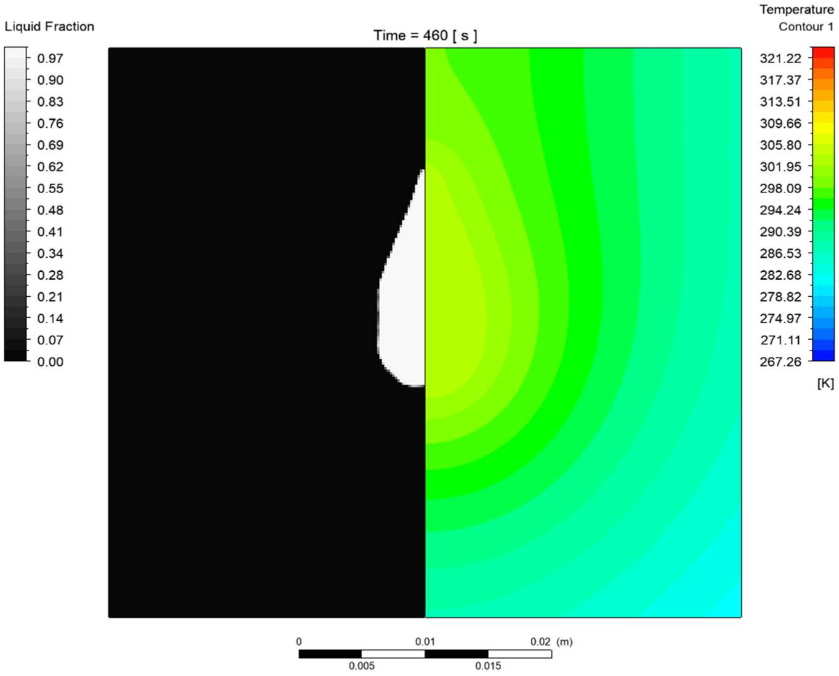

Figure 96 Temperature fields at 460 seconds (on the right), Liquid fraction field on the left, black color indicates solid zones. Both correspond to numerical results. Coolant temperature of 268.15 K

Coolant at 258.15K (-15°C)

Using the same geometry and mesh dimensions, as well as thermophysical properties, the simulation was carried out at a constant coolant temperature of 258.15K. Figure 93 shows the average temperatures at the points identified in Figure 87. The dashed line is the experimental temperature result, and solid line is the numerical temperature result. The vertical error bars correspond to 2% temperature difference with the simuation results. In general, the numerical results do not surpass this difference. The experimental undercooling temperature is approximately 285K and 289K for numerical simulation. The difference is below 1.5%.

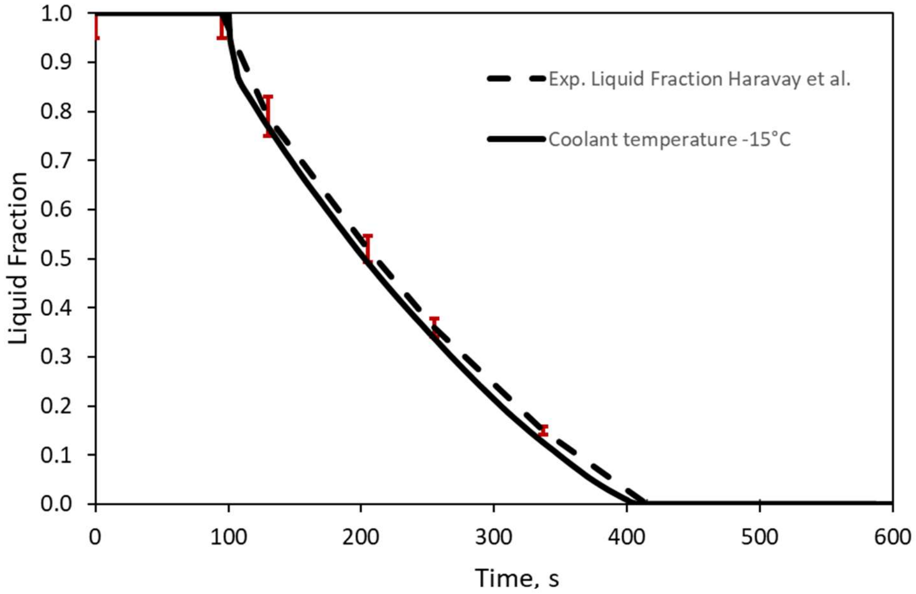

Figure 97 Liquid fraction for coolant temperature of 258.15K, dashed line is experimental results of Harary et al. [196]. Solid line is numerical results. Horizontal error bar respresents a 5% difference

The temperature history has the same behavior as in the case of the coolant temperature of 268.15K. The recalescence process is still faster for the numerical model. This took almost 10 seconds to raise the temperature from the undercooled temperature (289K). On the other hand, in the experimental results reported by Harary et al., this process took approximately 25 seconds. This difference is small when compared with the entire solidification time of 300 seconds. Figure 97 compares the solidification process over time. In comparison with a coolant temperature of 268.15K, the complete numerical solidification process maintains differences below 5% to the results of Harary et al [189]. The solidification velocity is the same 1x10^{-3} m/s. This value seems correct for the coolant temperature of 258.15K, as shown in Figure 97.

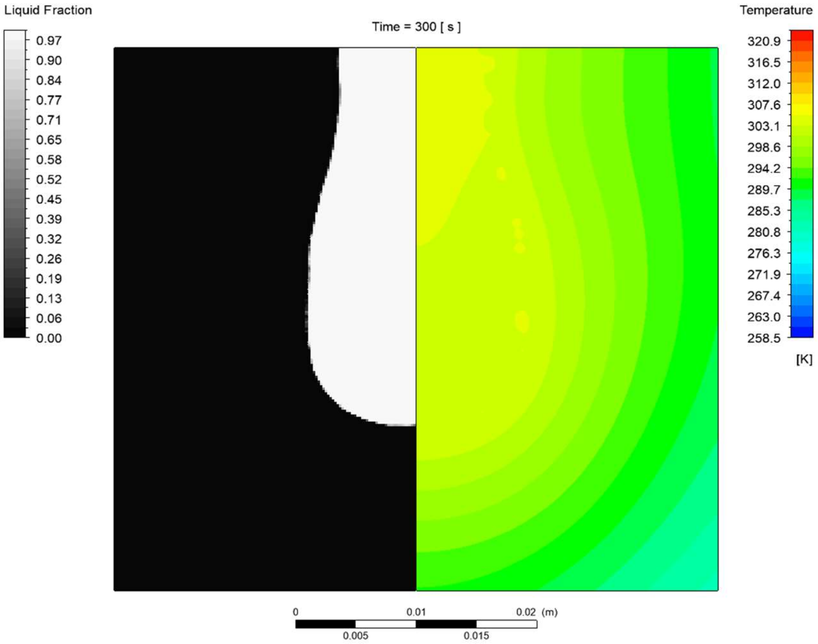

Figure 98 Numerical results for a coolant temperature of 258.15 K. Temperature fields at 300 seconds on the right. Liquid fraction field on the left, black color indicates solidified zone

The temperature history has the same divergence after 300 seconds, and the behavior of the cooling curves is different. This corroborates the same assumption that the cooling rate were diminished on the experimental apparatus. Harary et al [189] reported that after 1000 seconds the average temperature reached 258.15 K. This time is completely contradictory with the 900 seconds needed to reach the lowest temperature for a coolant temperature of 268.15K. In our numerical model the time to reach the lowest temperature was 550 seconds. These cooling times reinforce the idea that the cooling rate during the final stages of solidification was changed in the experimental apparatus of Harary et al.[189]

The solidification front has the same expected behavior. Figure 98 and Figure 99 shows the liquid fraction (left) and temperature color map (right) at 300 seconds and 402 seconds respectively. The solidification front finishes surrounding the liquid fraction. Then the heat transfer mechanism is only by conduction.

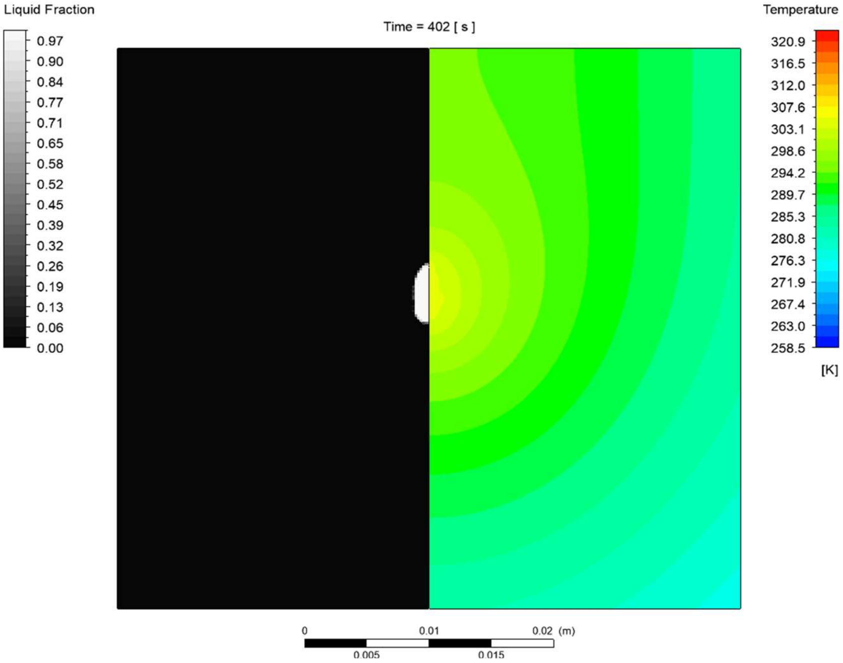

Figure 99 Numerical results for coolant temperature of 258.15 K. Temperature fields at 402 seconds (on the right), Liquid fraction fields on the left, black color indicates solid zones

4.3.2 Isothermal phase change for gallium.

The isothermal phase transformation is limited by its cooling rate to avoid undercooling. The design of LHTES depends on the rate of heat extraction. If the cooling rate-undercooling relation (Equation 87 for gallium) is know, the heat exchanger can be designed to limit the heat extraction and avoid a undercooling degree.

To test Equation 87 and with the same numerical model and thermophysical properties, a numerical isothermal phase transformation is performed. The cooling rate is 0.061 K/s, and it is imposed on the same left and bottom wall. Figure 100 shows simulation results of temperature (continuous line) and the liquid fraction (dashed line). It is clear that the phase change transformation is made between the range of 303.15 and 302.15 K. Both temperatures correspond to the temperature range defined in Table 10.

The first amount solidified in 10 seconds. Almost 27% of liquid transforms suddenly and the phase transformation can occur over all positions in the sample, shown in Figure 101B). At 278 seconds Figure 101 A) shows the liquid fraction (left) and the colormap of temperature (right) in the gallium sample in the seconds before the start of solidification. The uniformity of the temperature, around 304K, is mainly due to three factors:

i) Convective currents inside the sample

ii) The slowness of cooling applied to the sample.

iii) The high thermal conductivity in the gallium.

Due to these three elements, over all the sample it is possible to start the solidification when the temperature is low enough and the kinetic heat transport limits the amount solidified. Solomon et al. in Figure 24 shows the same behavior. In our results, this behavior is shown in Figure 101B), where the first seconds after phase change started, the left side shows how the phase change begins erratically and is influenced primarily by the convective flow. Comparing the paraffin and the gallium isothermal phase transformation, the phase frontier fields are significantly different. For Paraffin transformation the low thermal conductivity limits the heat transport and consequently the variations in its temperature field are significant. For gallium the thermal conduction facilitates heat propagation released by the latent heat. Then all the sample tends to solidifies uniformly.

Figure 101C) shows the state at 3160 seconds. It shows the remaining 10% of liquid fraction in the sample. The mushy region is significantly more extended in comparison with the undercooled gallium. The low heat extraction allows a large solid/liquid boundary. Also, Figure 101C) shows that the last liquid fraction is located in a central position.

Clearly Figure 95, Figure 96, Figure 98 and Figure 99 show the important role of solidification to define the solidification front. However, in isothermal phase transformation the this is drastically different. If a small sample has a high thermal conductivity, the solidification starts practically in all the material and the heat transport is by conduction through all the phase transformation.

Good agreement was found between the results of Harary et al [189]. and our results by reproducing the study on the amount of undercooling caused by the imposition of different cooling

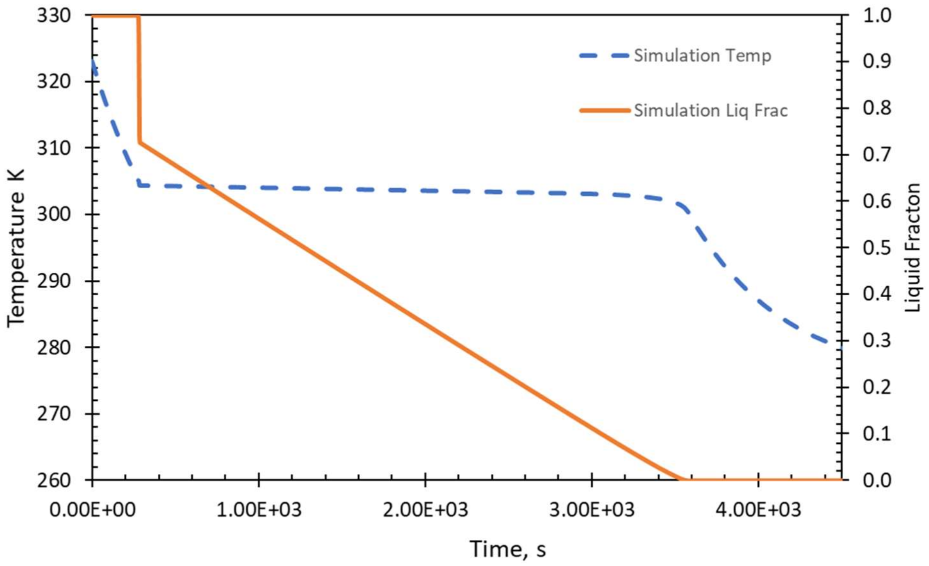

Figure 100 Numerical results of temperature and liquid fraction. Cooling rates of 0.061 [K/s] on the left and bottom boundary walls over all the simulation time

rates. However, Figure 92 and Figure 93 show in the last amount of solidification (remaining 20% of liquid) the temperature behavior was significantly different. As mentioned earlier, it seems that the cooling rate was modified at the end of solidification on the experimental apparatus of Harary et al [189].

Also, for coolant temperature of 268.15 K (-5°C) numerical results show differences in the recalescence process, concluding that the solidification is slower in the experimental results. Figure 94 shows a faster solidification rate in the simulation results compared with the experimental approach. On the other hand, for coolant temperature of 258.15K (-15°C), the constant imposed solidification velocity seems be more consistent with experimental results. Figure 97 shows good agreement in phase transformation rate.

The method for undercooling phase transformation was implemented in the numerical approach described in the previous section. Numerical results show the implementation of Equation 87 to perform simulation considering a undercooling process. Also, shown in Figure 84 for paraffin and Figure 101 for gallium, the melt front is significantly different, despite that both cases perform an isothermal phase transformation. These different behaviors need to be analyzed extensively to optimize the heat extraction during the solidification process.

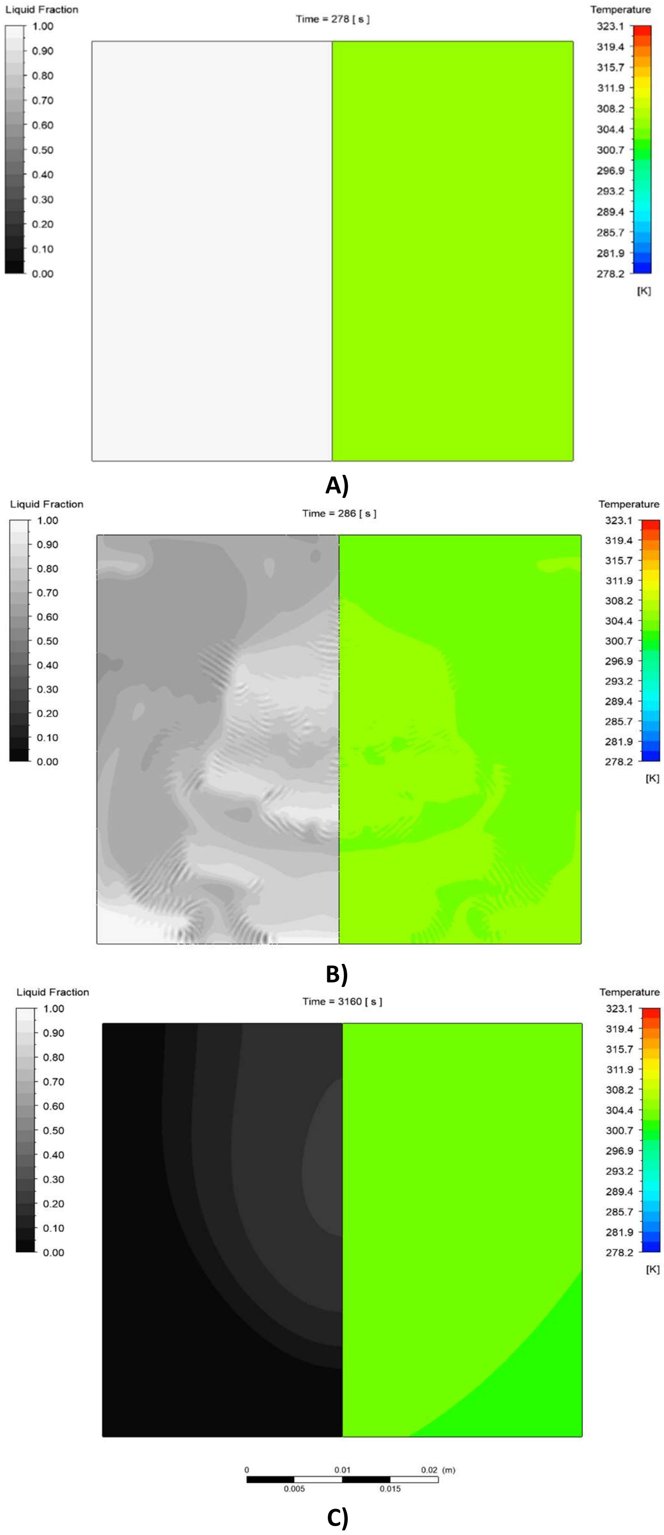

Figure 101 Numerical results. Temperature fields on the right, Liquid fraction fields on the left, black color indicates solid zones. A) At 278 seconds before the phase change starts. B) At 286 seconds, in the 10 first seconds 27% of material has solidified. C) at 3160 seconds, the liquid/solid interface is unclear. Large mushy areas are developed

4.4 Off-eutectic solidification, segregation model

Segregation has been largely studied in casting process, however the randomness and the influenceability of the process make it a complicated and unpredictable phenomenon. Even in the same experimental apparatus two samples can show different amounts of concentration by slight variations in purity or flow convection in the sample under the same conditions, demonstrated in the thesis work of Mahzabeen [191]. The huge complexity to reproduce segregation patterns was described in the doctoral research of Ebrahimi [116]. Therefore, the method proposed in our research does not intend to faithfully reproduce segregation in alloys. Instead, the aim is to reproduce the thermal patterns derived from macrosegregation. To evaluate our method implemented in the numerical approach, some essential characteristics are used to evaluated the segregation model:

- Negative macrosegregation is the low solute concentration with respect to nominal concentration.
- Positive segregation is the high solute concentration with respect to nominal concentration.
- Banded segregation structure is a delimited mixed structure long enough to be easily identified.
- Formation of channel segregates is the result of gravity-driven flow due to change in the density derived by variation in solute concentration and internal temperature (buoyancy effect). The channel is formed at the same time that the solute is rejected.

As mentioned before, the convective fluid flow increases the apparition of segregation. The liquid is moved, in a temperature gradient, from one part of the semi-solid to another transporting latent heat released and rejected solute. Also, the convective flow in the mushy zone combined with solutal concentration and the recalescence process increase the apparition of local macrosegregation zones and eventually the formation of segregation channels. This mechanism is more notorious when long freezing times are involved because at the beginning a small amount of material solidifies, the solutal is rejected and the local temperature fluctuation due to heat release is low. Then the local concentration field (prescribed by the phase diagram) has poorer areas that begin to solidify, and the vicinity remains in solute rich liquid. The rich solutal zone cannot solidify at this temperature. The solidification process continues and the heat released by the solidification in its vicinity increase the local temperature making the solidification process less possible for the zone with the higher temperature and rich solutal concentration. The slow cooling process allows segregated channels to form at an early stage of the solidification that eventually solidify at solute rich concentration because the heat released during solidification is almost entirely absorbed by the alloy. However, this mechanism of segregation depends significantly on convective fluctuation behavior. If the material has a reduced difference in density between liquid and solid, combined with a slow cooling, an equilibrium solidification process can occur. Mainly for this reason, the high density variation during solidification in a binary Sn-Pb alloy [192] is used in the macrosegregation experiment. There is a large increase in density when the temperature decreases along the liquidus line, even with low cooling rates. Also, the dimensions of the sample need to be small to reduce the experimental or simulation time but large enough to allow convective fluid flow.

Many publications have focused on Sn-Pb off-eutectic alloys, and the common sample dimensions are relatively small but enough to allow convective fluid flow. However, research work such as that done by Hebditch et al. [193] Ojha et al [194], Laxmanan et al. [195], Tewari et al. [196], Streat et al [197]. measure the effects of different parameters and how these influence the macrosegregation and result in clear differences in the macrostructure patterns (grain structure) in transverse cross sections. Scheil-Gulliver has been largely validated and these studies show good agreement in the average distribution of solute. However, we can find clear differences in local segregation if these values are reported. A few studies are focused on the macro/micro segregation patterns compared with experimental transverse cross sections (e.g. the PhD work of Ebrahimi [116]).

Simulation setup

Considering the aspects mentioned before, we select the experimental works of Hebditch et al. [193] and Hachani et al. [198]. Their work is based on a binary alloy of Sn-3%Pb in a sample 0.1m in length, 0.06 in height and 0.01m in width.

We have carried out a numerical simulation with Fluent. A two-dimensional model was created to reduce the computational complexity of the simulation. The macrosegregation simulation was performed for a binary alloy at Sn-3%Pb in a 2D rectangular cavity 0.06 m high and 0.1 m long, shown in Figure 102. A constant spatial discretization of $5\text{x}10^{-4}$ m was chosen with a time step of $5\text{x}10^{-2}$ seconds.

Table 12 Thermophysical properties of Sn-3%wtPb alloy

Melting temperature of pure Sn	K	505.15
Eutectic temperature	K	456.15
Eutectic mass fraction	wt%	38.1
Liquidus slope	K/wt%	-1.286
Partition coefficient		0.0656
Initial mass fraction	wt%	3
Specific heat (liquid and solid)	J/kgK	242
Thermal conductivity liquid	W/mK	33
Thermal conductivity solid	WmK	55
Latent heat	J/kg	$6.07\text{x}10^{4}$
Density	Kg/m^3	7130
Thermal expansion coefficient	1/K	$9.5\text{x}10^{-5}$
Solutal expansion coefficient	1/wt%	$5.3\text{x}10^{-3}$
Dynamic viscosity in the liquid phase	Kg/ms	$2\text{x}10^{-3}$

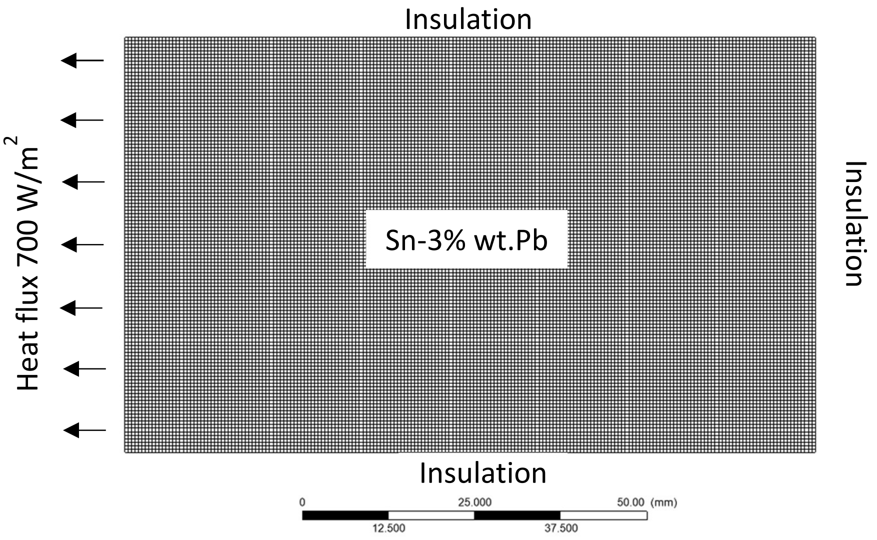

Figure 102 Simulation setup, fixed heat flux of 700 W/m2 applied to the left boundary wall. Dimension of 100 millimeters length and 60 millimeters height. A constant spatial discretization of 0.5 millimeters

The rectangular sample is cooled on the left wall at a fixed heat flux of 7000 W/m^2. The other three sides are thermally insulated. The cooling rate before the beginning of solidification was 3.97x10-2 K/s. This value provided slow cooling and allows the sample to generate convective flows. The thermophysical property data are given in Table 12 [193] [198]. The initial temperature is 510 K.

4.4.1 Model validation

Figure 103 shows time-dependent temperature and liquid fraction, Figure 104 shows the same results but only between the initial time and 1000 seconds. Both are the average values in the sample (temperature and liquid fraction). The solidification process took almost 8x10^3 seconds. The process starts at 162 seconds with an average temperature of 503 K until the end of the phase transformation at 8034 seconds with an average temperature of 451K. The entire simulation took almost 2 days. The average temperature at the start and end of solidification process are the expected and dictated by the phase diagram and the Scheil Gulliver equation.

Unfortunately Hebditch et al. [193] or Hachani et al. [198] do not report cooling temperatures and solid/liquid fraction evolutions. Thus, these particular results cannot be compared with their experimental results.

Figure 105 A) and B) show the final macrosegregation sample from the work of Hachani et al. [198] submitted to a cooling rate of 0.03 K/s. Their results show that:

i) Negative segregation appears in the coolest zone (bottom-left). Solutal rejection results in positive segregation around these zones. Then, the high lead concentration appears in small zones in the equiaxed zones.

ii) The solidification is globally columnar. Equiaxed zones appear in the bottom-left part of the sample. This zone is in the beginning the coolest zone in the sample. Columnar formation takes places at the end of solidification in zones with low cooling rates.

iii) The upstream tilting of the columns is consistent with the existence of a downward flow along the sample. This form bands of macrosegregation.

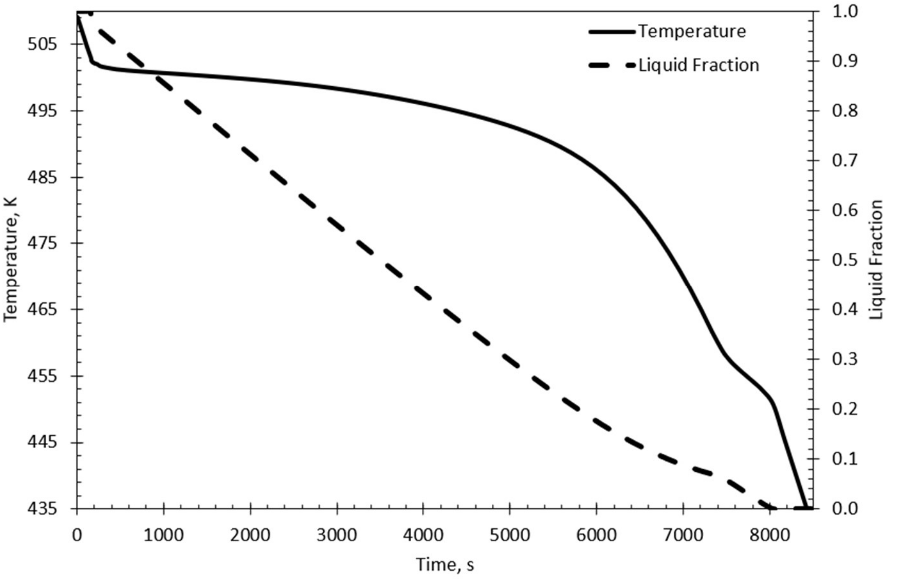

Figure 103 Numerical reslt, solid line is the average tempeature evolution. The dash line is the evolution of liquid fraction during the solidifcation process. The solidification process starts at 162 seconds and end at 8034 seconds

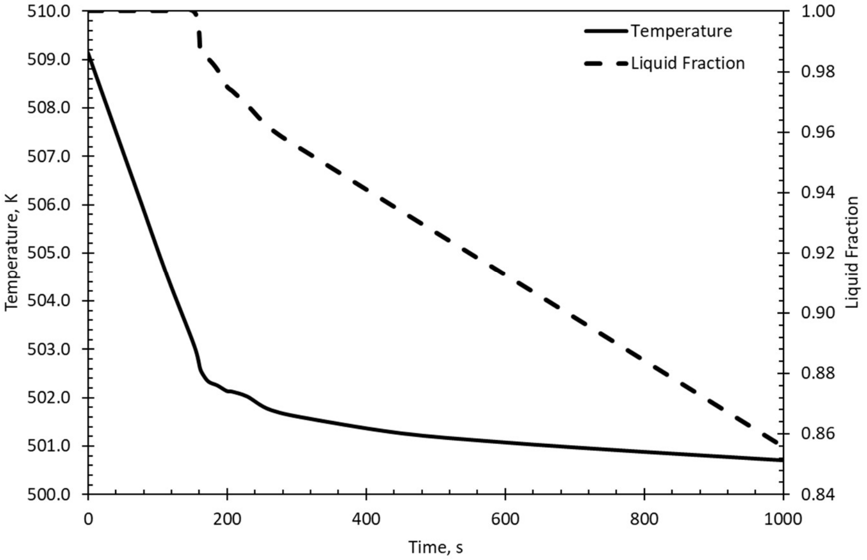

Figure 104 Numerical results, simulation between the initial time to 1000 seconds. Solid line is average temperature evolution in the sample. Dash line is the average liquid fraction evolution in the sample. At the average temperature of 503 K the phase change starts and is finished at the average temperature of 451K

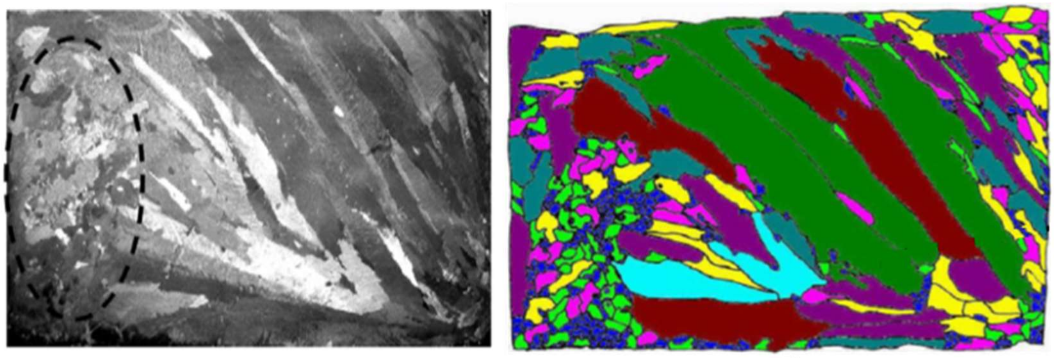

A) B)

Figure 105 Experimental results of Hachani et al. [198] Sn-3%wtPb ingot in the median plane of the sample with a cooling rate of 0.03 K/s. A) Macrostructure, the tiling of the column indicates that convection along the solidification front is downward. B) Grain contour for the same sample

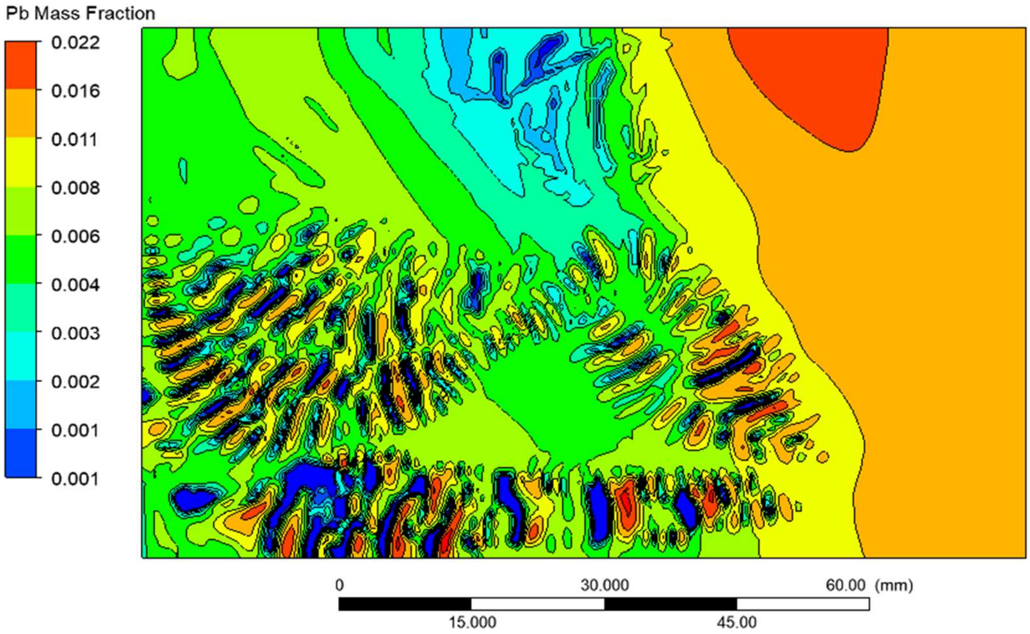

Figure 106 Numerical results of macrosegration patterns of the lead mass fractions at the end of solidification process, average temperature of 445K. As the experimental results of Hachani et al. [198] the tilting of the column follows the downward convection

As mentioned previously, the expected numerical results must include these physical characteristics and be in agreement with the thermophysical behavior. Figure 106 shows the final lead mass fraction from simulation results. This shows the macrosegregation distribution after the solidification process ends at an average temperature of 445 K.

The first characteristics of Hachani et al. Figure 105 is the negative macrosegregation. Figure 106 shows in the bottom-left side the coolest zone. In this zone the solutal rejection appears. This is the first zone to solidify and negative segregation occurs here. Around this zone, the solutal rejection is trapped. Then, during the progress of phase change, this solute-rich zone solidifies forming positive segregation. The latent heat released reduces the cooling rate and modifies the convection flow. These factors slow down solidification formation and also allow large macrosegregation zones. These are shown as large columnar macrostructures.

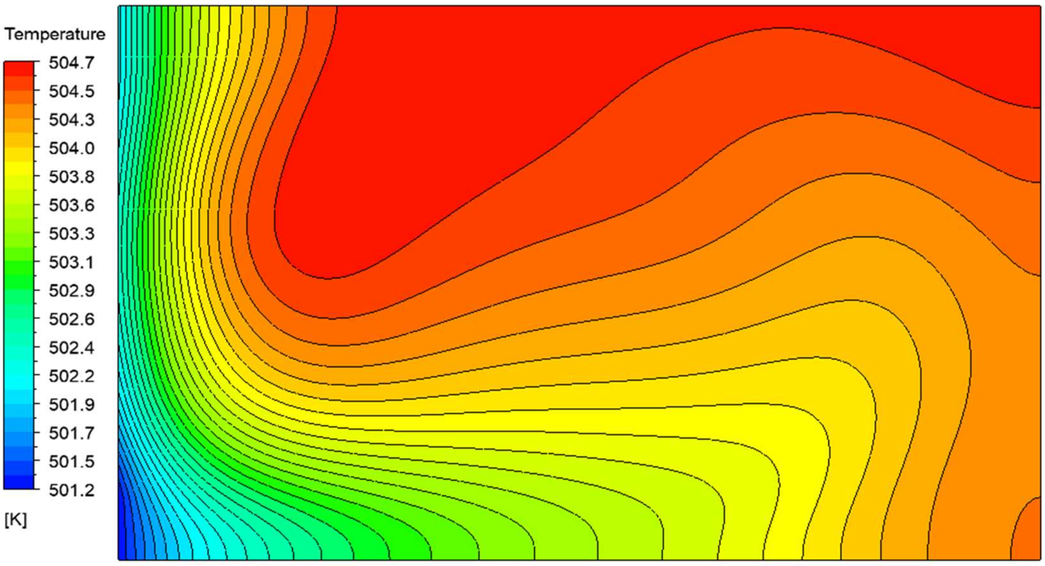

Figure 107 Temperature contour map at the instant previous to the beginning of the solidification process. The convective downward flow drives the temperature patterns

The visual comparison between the experimental results in Figure 105 and simulation result on Figure 106 shows good agreement in its macrosegregation behavior. In both cases, on the coolest wall, small zones show negative and positive segregation of lead. Also, the columnar

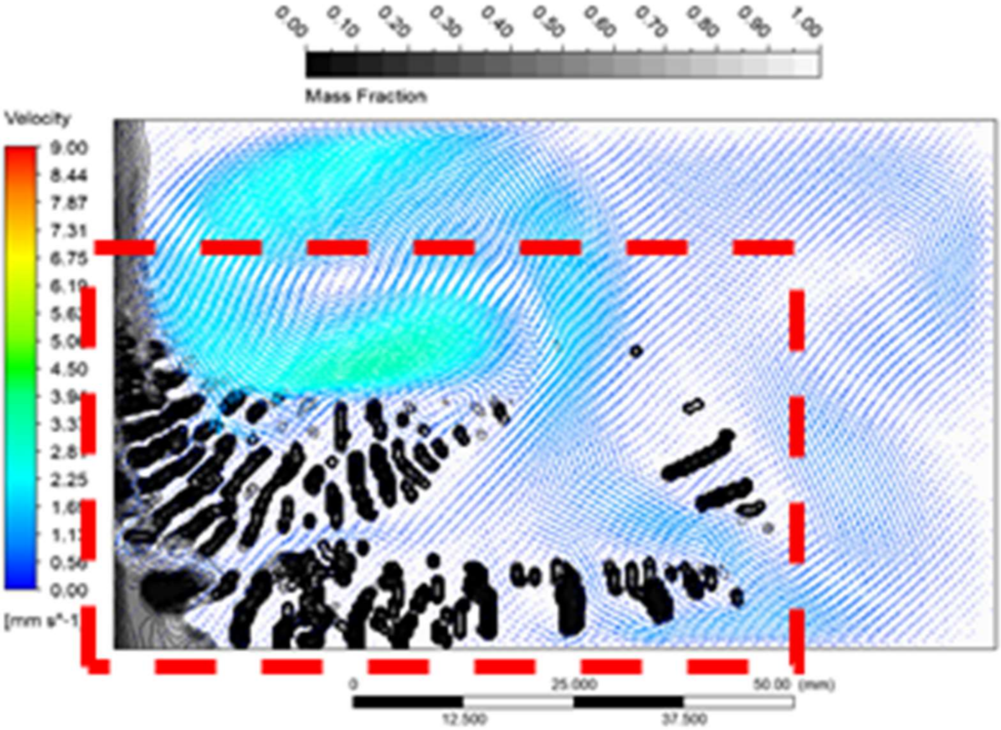

Figure 108 Snapshot of the solid fraction formed at t= 370. Flow field shown by velocity vectors. The local maximum flow velocity is 3.9 mm/seconds

formations are visible on the top, center and right part. The upstream tilting of the columns is consistent with the expected behavior.

The influence of the convective flow is fundamental on macrosegregation, principally in the Sn-Pb alloy. The simulation showed a maximum downward flow velocity field of $8x10^{-3}$ m/s before the start of the solidification. Figure 107 shows the temperature color map at the same instant previous to the phase change. The convective downward flow leads the coolest fluid to the bottom zone. Thus, the first zones to solidify are the lower left to the lower center in the sample. The work of Ahmad et al. [199] demonstrated that the nature of segregation follows the direction of the movement of liquid during solidification. Therefore, these behaviors show good agreement with the expected results. Based on the phase diagram and the Scheil Gulliver formulation, the first solid formed has a low concentration of solute. The advance of the formation of the solid is accompanied with the enrichment of solute.

Figure 108 shows the solid fraction (black zones) at the instant t=370 seconds. 94% of material remains liquid. The velocity vectors in the alloy are observed to be different on the left side. Figure 109 shows the rectangular section defined in Figure 108.

Figure 109a) shows the map of the liquid fraction. Zones 1 and 2 identify the zones where the phase change is being carried out. In these areas, it has solidified approximately 10%. Figure 109b), shows the temperature field and zones 1 and 2 are the hottest areas due to the release of latent heat. This released heat is transported by the convective flow upwards by heating the fluid. Figure 109c) shows the velocity vector interacting with the solid formed. The flow rotation in the upper right side is clearly visible in zone 2. The rise of the heating fluid over the hottest spots generates the counterclockwise flow loop. On the left the cold front extracts the heat transported by the fluid. On the right side the convective flow is slower and the heat transport is considerably reduced. Then, the temperature in this zone is practically homogeneous.

The last characteristic found in macrosegregation is the formation of channel segregation. Zone 3 in Figure 109c), shows the velocity vectors in liquid and mushy zones around the solid formed. Zone 3 shows the cavity formed during the solidification process in which the solute is rejected at the same time that the latent heat is released. The density changes and rich solutal liquid drives the formation and retention of channel segregation. The flow velocity in zone 3 shown in Figure 109c) is below 1×10^{-3} m/s.

However, the heat extraction by the cooled zone reduces the heat transported by the fluid and consequently the channel segregation starts to solidify containing a rich concentration of solute. An interactive local process of solidification takes place on the bottom-left side:

1. The advance of the solid front causes the formation of a solid that abruptly rejects the solute, forming a grain (Figure 109 a).
2. The temperature decreases faster and the vicinity solidifies at a different rate forming another grain but with a significantly different size and concentration than the previously formed solid.
3. The solutal rejection of this new grain is significantly different than the first grain formed. Also, the amount of heat released raises the temperature. Then, the next grain formed has different concentration and solidifies at a different temperature by absorbing a fraction of the heat released.

The continuous exchange between latent heat released, solutal rejection and heat extraction gives the solidification of different concentration grains, as is shown in Figure 105 and Figure 106 on the bottom left side.

As the solidification progresses, fluid flow velocities are reduced. The numerical model predicts a local maximum of $9x10^{-3}$ m/s, and drastically it is reduced to values below $4x10^{-3}$ m / s, as shown in Figure 109c). The rapid reduction in flow velocity in combination with a slow heat extraction changes the solidification process from off-equilibrium to equilibrium. The change in the solidification form is observed by the formation of columnar macrostructure, as shown in Figure 105 and Figure 106 upper-right side.

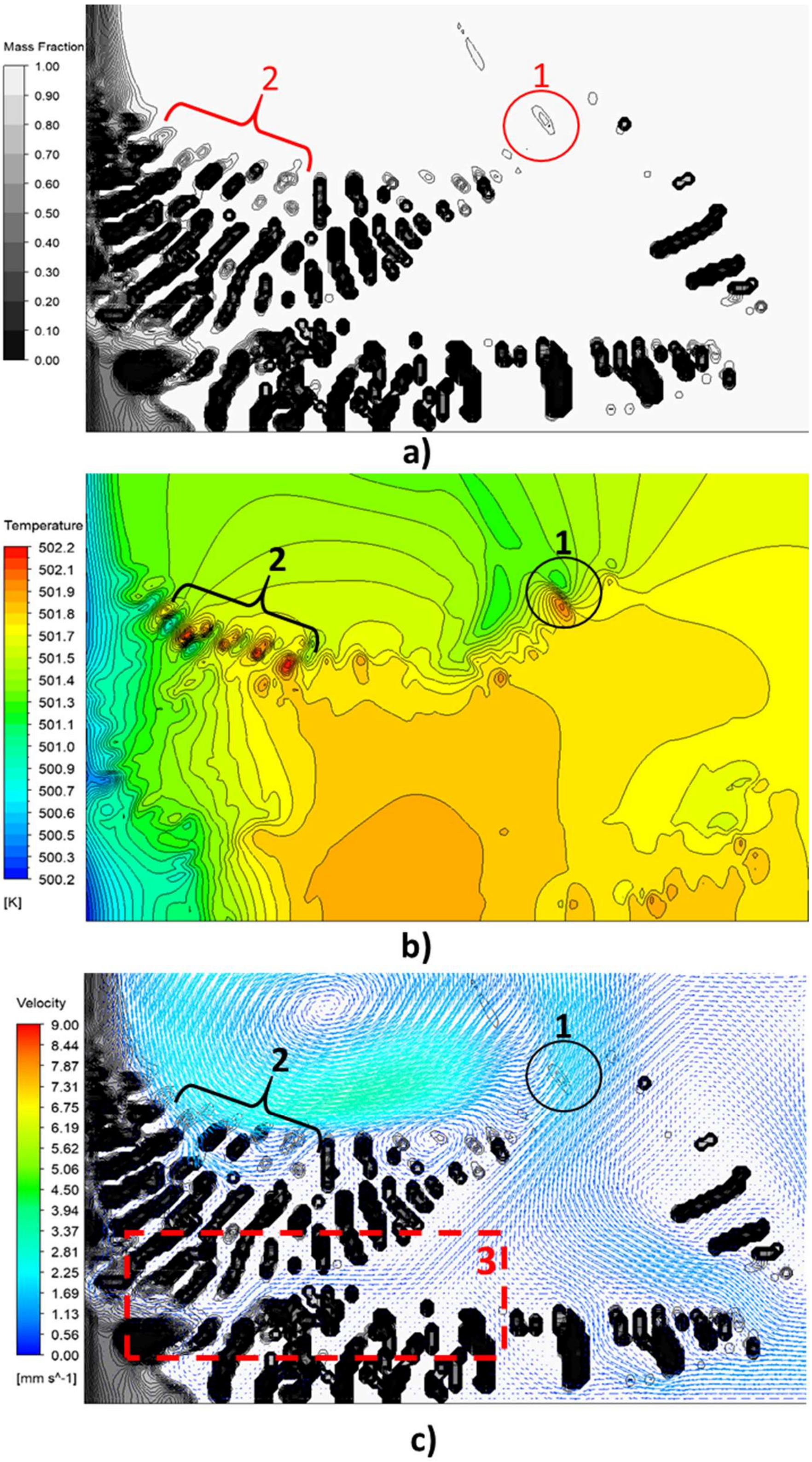

Figure 109 Solidification process at the instant t=370 seconds in the section defined in the previous figure. a) Liquid fraction map in the alloy, white region is liquid, black is solid. b) Temperature color map. The hot spot (red zones) 1 and 2 show the local zone where the phase transformations occurs releasing the latent heat. c) Liquid fraction map and velocity vectors. Maximum velocity value is 3mm/s

4.4.2 Conclusions

The method has been applied to a numerical problem for an alloy at Sn-3%Pb to model macrosegregation. The results obtained show good agreement with the experimental results of Hebditch et al. [193] and Hachani et al. [198]. The numerical solution shows the characteristic elements found in experimental macrosegregation:

- Negative segregation appears in the coolest zone, Figure 106.
- The upstream tilting of the columns is consistent with the existence of a downward flow along the sample as shown in Figure 109c).
- The solidification is globally of columnar type with equiaxed zones in the sample, shown in Figure 106.
- High lead concentration appears in small zones, derived from the rejection of solute (see Figure 106).

At the beginning of solidification, the temperature fields are entirely governed by the convective flow. Affecting the convective flow can considerably alter the solidification process. Also, the macrosegregation problem is unstable due to the interaction of change in temperature (heat released during the solidification) and convective flows. The instability problem is derived from the constant interaction between momentum transport, energy and solute transport through the buoyancy force. The high jump in concentration (solutal rejection) and local thermal fields (latent heat release) increase the nonlinearities of macrosegregation problems. The complexity is augmented changing the material properties that can result in specific particularities (e.g. inverse segregation problems in Ag-Cu and some aluminum alloys, which are not considered in our method).

In materials with large changes in density due to the influence of temperature, they will have higher velocities in the flow and consequently, thermal transport will be even more significant on the solidification transport. Thus, container geometry is an important element to consider. For example, in materials with high density variation due to thermal changes, extracting the heat from the top will favor convective flow to the interior and increase the heat extraction. In

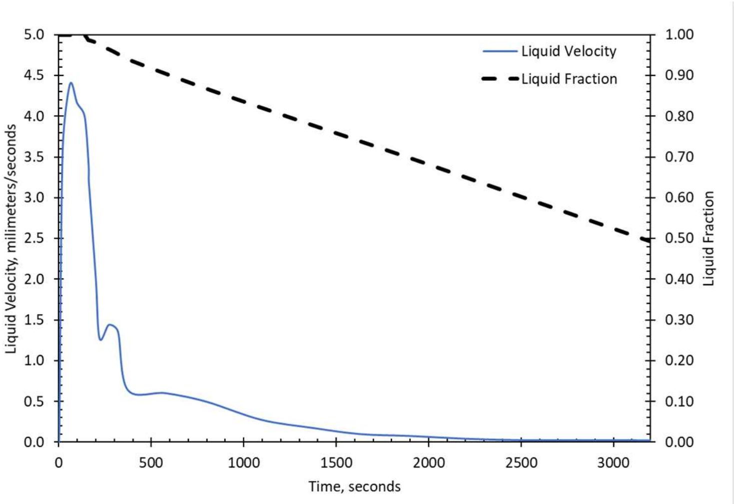

Figure 110 Evolution of the average liquid flow velocity compared with the liquid fraction remaining in the material

this way, the expected start of solidification on the side of the geometry and the latent heat released would be transported by the convective flow to the upper part where it would be extracted. The lowest density in the liquid will push to the top zone the remaining liquid to extract the latent heat that remains. However, if the material has a higher thermal conduction in the solid phase, it may be the optimal solution to extract the heat from the bottom assure that solidification process starts at the wall where the stored heat is extracted. The higher thermal conductivity in the solid phase increase the heat extraction.

From the results obtained, the following aspects for the LHTES are concluded:

1. If the material presents important variations in the density of the material between the solid and liquid phase, important convective flows derived from the change on densities are expected.
2. In situations with significant convective flows, thermal transport will be important and determinant to identify the area where the material begins to solidify and consequently the macrosegregation increases.
3. Macrosegregation influences the solidification process. If there are significant convective flows, macrosegregation will be present even in low cooling rate conditions.
4. In macrosegregation solidification, the convective flow is drastically reduced by increasing small amounts of solid fraction as is shown in Figure 109c). Figure 110

shows the drastic decrease in the average velocity with low amount of solid fraction. With a remaining 50% of liquid fraction, the flow velocity inside of the alloy is practically null.

4.5 **Al-Si alloy**

Al-Si alloy is an excellent option for energy storage. Table 13 shows in detail the comparison with others alloys and common materials used as PCMs [25], [200]. It can be seen that Al Si has one of the highest amounts of latent heat, only below the Si/Mg eutectic alloy, although the difference in melting point between Al/Si and Si/Mg is evident.

The last column of Table 13 shows the amount of latent heat per m^3. These values define the volume of the phase change material needed. Although the Si/Mg alloy overcomes the rest of the materials, its high melting point restricts its use. The Al/Cu alloy is another excellent option, despite having a lower amount of latent heat, it exceeds the Al/Si eutectic alloy in density. To put into context, in France three-room apartment consumes on average 110 liters of hot water per day [1], [3]. This corresponds to 40.1 m^3 of water at 40°C per year. For this volume of water an amount of energy of 4180x10^6 [J] per year is required to raise the temperature from 15 ° C to 40 ° C. If we consider the Al/Si eutectic alloy, 3.3 m^3 of this binary alloy would be needed to supply the energy to heat the water per year without considering the sensible heat or thermal losses of the LHTES. For the same amount of energy needed, a volume of 4m^3 of eutectic Al/Si alloy would be necessary to increase the temperature of 15 apartments (three-room type) for around a month.

Additionally, common binary alloys improve the thermal conductivity compared to other materials, which optimizes the discharge/charge process of the LHTES. On the other hand as mentioned previously, undesirable phenomena such as undercooling occur. In the literature, no information regarding the relationship between cooling rate and the amount of undercooling for the Al/Si alloy was found. Considering its energy storage capacities and the lack of information in literature, the Al-Si eutectic alloy was chosen to use the method described previously in Chapter 3 represented by the algorithm architecture in Figure 35 and a numerical simulation model of this alloy, in Ansys Fluent, was developed.

Based on the analysis described in section 4.1, one of the first elements to analyze is the variation of latent heat and composition using the phase diagram to identify variations that can significantly affect the simulation model. Figure 111 shows the maximum, minimum and average values of the partition coefficient at different hypo-eutectic composition. It can be seen that the maximum variation of the partition coefficient is around the silicon solubility limit. However, this this differs from the results shown in Figure 79. In this, the maximum variation of the amount of latent heat is found between 0.05 and 0.07 mol% Si. Figure 112 shows the phase diagram of Si-Al.

The eutectic composition at Al-12% wt Si, does not present variations derived from the phase diagram. This avoids the variations in the amount of latent heat shown in Figure 79. In literature, scientific data about the undercooling phenomena of Al/Si alloy in samples that allow natural convection cannot be found. Only experimental works performed on samples smaller than 30 millimeters where the microstructure and undercooling are analyzed [106], [107], [201]–[203] could be found. The size of these samples suggests the absence of convective flow. Also, in most cases the information relative to the experimental conditions or the size of the sample it is not detailed, making it difficult to reproduce in numerical simulations.

Table 13 Thermophysical properties of some binary alloys and PCMs [25], [200]

Material	Composition [wt%]	Melting temperature [°C]	Latent Heat [J/kg]x10^3	Density (kg/m^3)	Latent heat x Density [J/m3]x10^6
Si/Mg	56/44	946	757	1900	1438.3
Al/Si	87.7/12.3	560	498	2540	1264.9
Al/Cu	66.9/33.1	548	372	3600	1339.2
Aluminum	100	661	388	2700	1047.6
Zn/Mg	53.7/46.3	340	185	4600	851.0
Zn/Al	96/4	381	138	6630	914.9
Paraffin wax	Paraffin	64	173.6	853	148.1
RT 70 HC	Paraffin	70	260	825	214.5
HiTech	Salt	142	83.7	1762	147.5
LiCl–LiOH	Inorganic PCM	262	485	1550	751.8
NaNO3	Inorganic PCM	308	199	2257	449.1

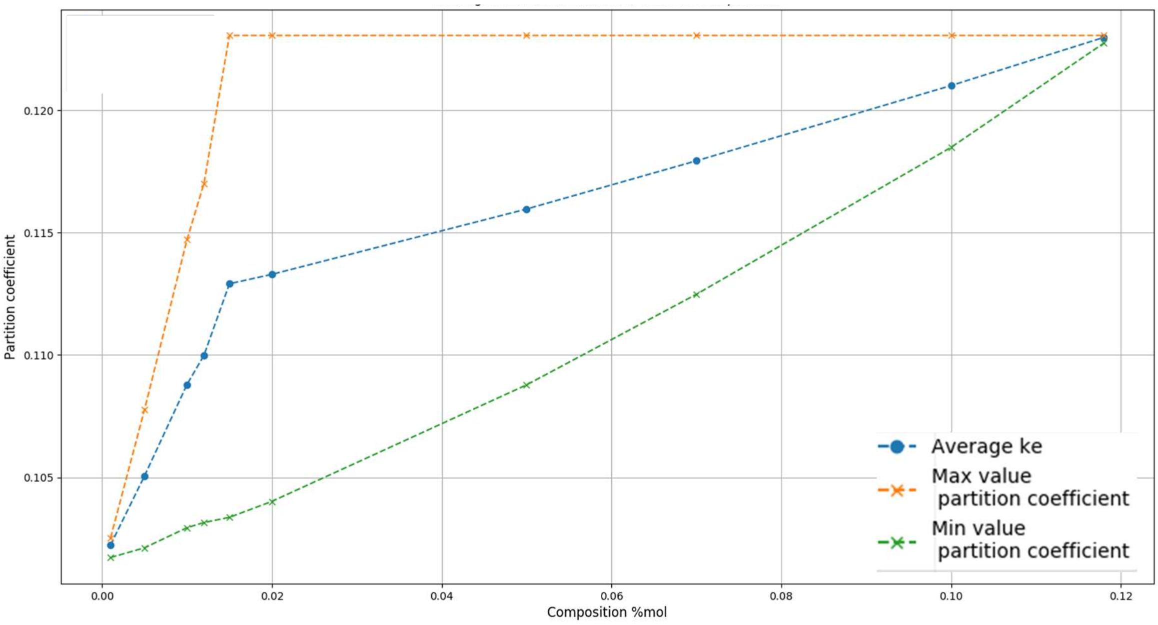

Figure 111 Variation of the partition coefficient for hypo-eutectic Al-Si alloy

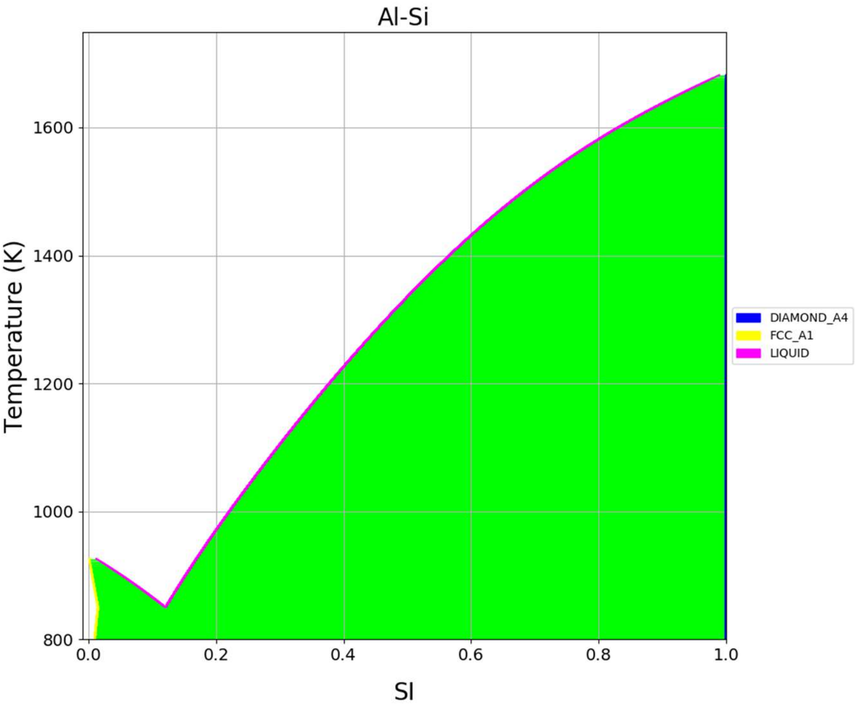

Figure 112 Phase diagram of Al-Si alloy

Table 14 Thermo-physical properties and parameters of Al-12 wt% Si[204]–[208].

Melting temperature	K	849.15
Eutectic mass fraction	wt%	12
Liquidus slope	K/wt%	-700
Partition coefficient		0.113
Specific heat	J/kgK	894
Molar Specific heat	J/molK	47.2
Thermal conductivity	W/mK	Sol 234.7-Liq 89.4
Latent heat	J/kg	$4.18\text{x}10^5$
Molar Latent heat	J/molK	29.8
Density	Kg/m^3	2683.7
Molar mass Si	Kg/mol	0.0281
Molar mass Al	Kg/mol	0.027
Thermal diffusivity	$\text{m}^2\text{/s}$	$2.53\text{x}10^{-5}$
Thermal expansion coefficient	1/K	$2.17\text{x}10^{-5}$
Solutal expansion coefficient	1/wt%	$10.9\text{x}10^{-3}$
Dynamic viscosity	Kg/ms	$3.23\text{x}10^{-3}$
Gibbs-Thomson coefficient, Γ	Km	$0.125\text{x}10^{-6}$
Diffusion coefficient, D	$\text{m}^2\text{/s}$	2.80E-08
Diffusion speed, VD	m/s	5.2

Table 14 shows thermophysical properties at Al-12% wt Si alloy used in the simulation model.

As mentioned in Section 2.5.2 Microstructure and solidification velocity by undercooling effects, Figure 27 shows the relationship between cooling rate, solidification velocity and microstructure. The equations described in Table 4 uses the dendrite tip radius. Therefore, the Langer and Muller-Krumbhaar (L-M) criterion is applied [112], [159], [209]. This considers equal the dendrite tip radius (R) and the eutectic spacing (λ). Then all equations listed in Section 3.2.8 are used with λ in the calculation of Al-Si eutectic alloy. The eutectic spacing (λ) is also called in literature: lamellar spacing, interflake spacing, dendrite arm spacing and inter-phase spacing [112], [210]–[213].

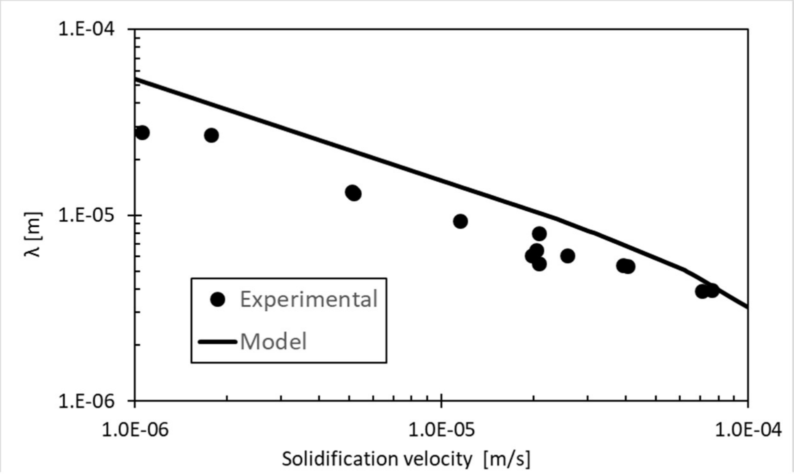

Figure 113 Comparison of calculated and experimental data [214-216] for lamellar spacing of Al-Si eutectic alloy at different solidification rates

From the experimental work of R. Elliott et al [214], Jun-Min Liu et al. [215] and L.M. Hogan et al. [216] experimental results are used to obtain the variation of microstructure depending on the solidification velocity. Figure 113 compares these experimental results of λ and the calculated results using the FB k non-equilibrium to determine λ as a function of solidification velocity. The behavior shown in the figure is as expected. With the increase in solidification velocity, the material's grain size decreases. This is the same behavior described for Ag-Cu alloy in Figure 26. Although the model describes the same behavior. The size of λ is overestimated. However, from solidification velocities of 7.5x10^{-5} m/s, the model rapidly decreases in size by λ. The objective of this work is not to match results or compare the different models to estimate λ. The FB-k non-equilibrium uses the local non-equilibrium diffusion model (LNDM) [154], and the diffusivity value is the key element in this model. In our calculations, the value of diffusion is considered constant because of the lack of information. However, this value can be varied depending on the temperature (described above in section Section 2.5.2) and thus this value can be adjusted to bring the results closer to the experimental values.

Figure 114 shows the comparative numerical results using the FB-undercooling with those of R. Elliott et al [214], Jun-Min Liu et al. [215] and L.M. Hogan et al. [216]. It can be seen that

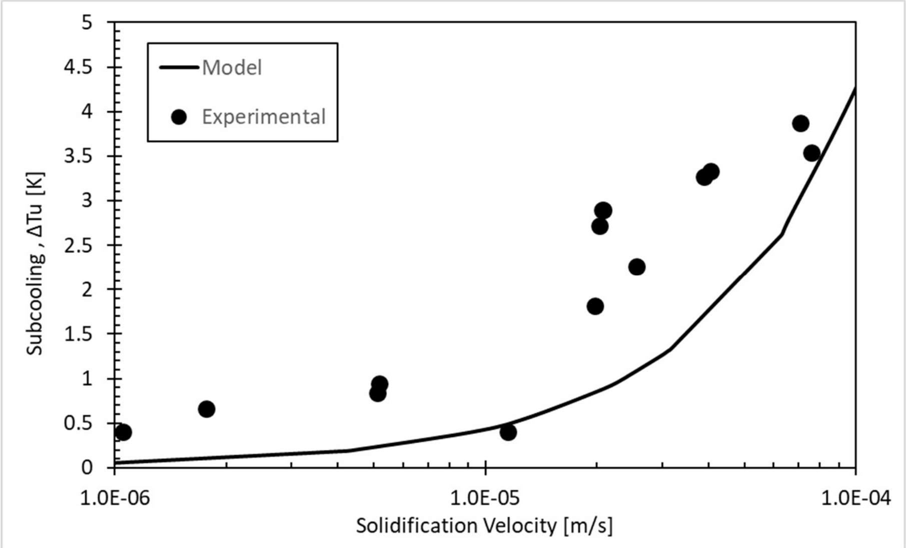

Figure 114 Comparison of calculated and experimental data [209-211] for undercooling degree of eutectic Al-Si at different solidification rates

the proposed model estimates an average of 1 K below the experimental results although this difference decreases as the solidification velocity increases.

The undercooling degree depending on the solidification growth is defined by:

$$\Delta Tu = -6x10^9 Vs^3 - 2x10^6 Vs^2 + 41914Vs + 0.0078 \qquad (88)$$

In literature, an experimental reference that links cooling rate and solidification velocity cannot be found. As it was shown in numerical results for undercooled gallium, cooling rate and solidification velocity are key parameters to correctly predict the behavior of phase change. In the particular case of Al-Si alloy the increase in Si gives a lower λ. Also, the increase of cooling rate reduces λ. Implicitly the reduction of λ increases the solidification velocity. Shivkumar et al. and Drouzy et al [217], [218] propose that λ varies with the cooling rate according to the relation:

$$log(dT/dt) = -\,(log(\lambda) - 2.37)/0.4 \qquad (89)$$

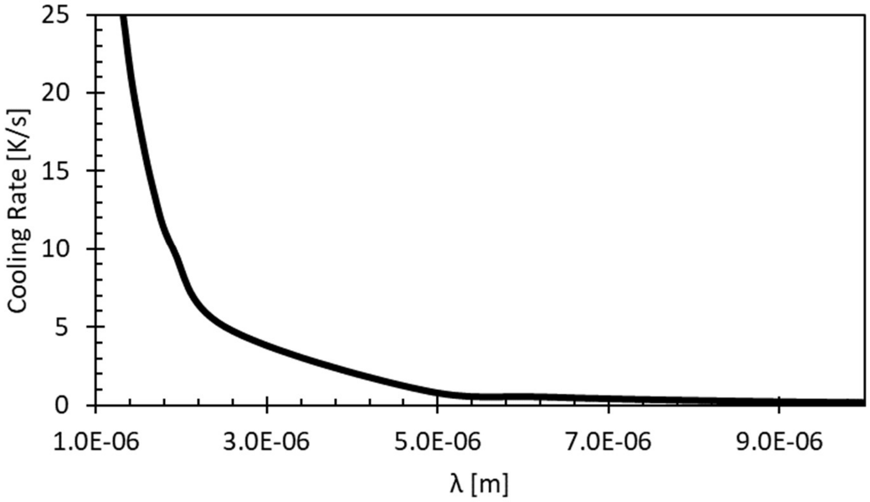

Figure 115 Calculated cooling rate for eutectic Al-Si dependent on the lamellar spacing

where dT/dt is the cooling rate in K/min and λ is in micrometers. Figure 115 shows the cooling rate dependent of λ using the Equation 89 and the results (Figure 113) from the mathematical model in FB-k non-equilibrium.

Then, using the formulation of cooling rate as a function of λ, the polynomial constant terms described on section 2.6 Cooling rate and solidification velocity method (Equation 26) are defined for solidification velocity dependent on the cooling rate as:

$$Vs = 2x10^{-6}CR^3 - 2x10^{-5}CR^2 + 9x10^{-5}CR + 5x10^{-6} \quad (90)$$

The gallium simulation model shows the use of the degree of undercooling dependent on the cooling rate. Then, based in Equations 90 and 88, the undercooling as a function of cooling rate is defined as:

$$\Delta Tu = 0.0458CR^3 - 0.6889CR^2 + 3.4213CR + 0.2416 \quad (91)$$

Figure 116 and Figure 117 show graphically Equation 90 and 91 respectively.

The use of Equations 90 and 91 in the simulation model drives the behavior of the material to define the degree of undercooling and the speed of solidification. These are used according to the algorithm shown in Figure 35 and described in Chapter 3.

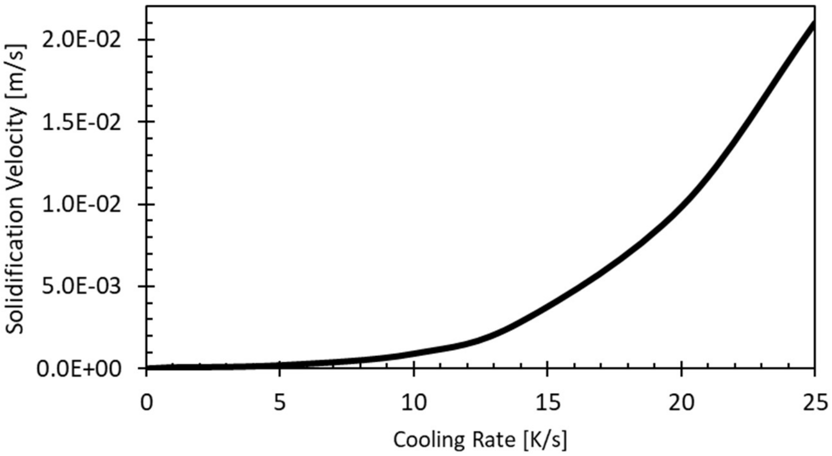

Figure 116 Calculated solidification velocity eutectic Al-Si dependent on cooling rate, Equation 90

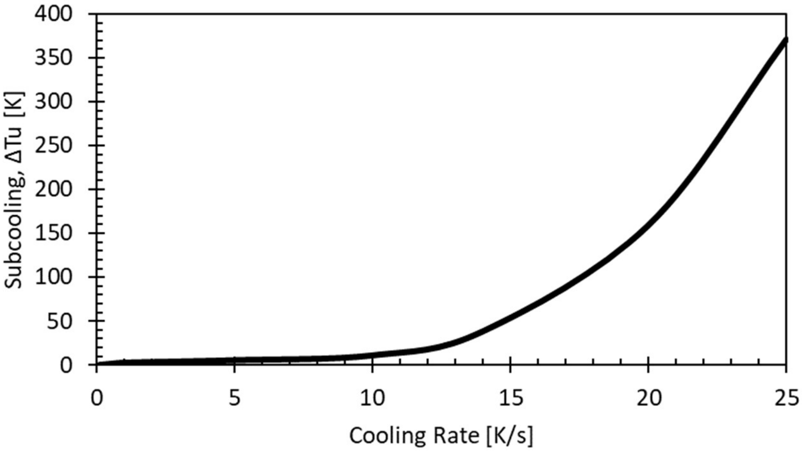

Figure 117 Calculated undercooling degree eutectic Al-Si dependent on cooling rate, Equation 91

4.5.1 Simulation model of Al-Si and results

The geometry and the mesh of the simulation model are shown in Figure 118. A two-dimensional, axial symmetric model was used to reduce the computational complexity of the simulation. Also, both solid and liquid phases are assumed homogeneous and isotropic. The dimensions of the simulation sample are: 100 mm width (modeled with an axis of symmetry) and 50 mm length. A uniform spatial discretization of 0.25 millimeters is applied, giving almost 81K nodes and 40K elements (see Figure 118).

Constant coolant temperature at 473.15 K is set on the left wall and 298.15 K on the bottom wall. For both walls, a constant heat transfer coefficient of $h = 900\ W / m^2K$ was set. The top wall is insulated.

The initial temperature in all the domain is set at 900 K. This is 50 K over the eutectic temperature. Thermophysical properties are detailed on Table 14. The melting interval ΔTs is 1 K, the solidus temperature Ts is 849.15 K and the liquidus temperature is TL = 850.15 K.

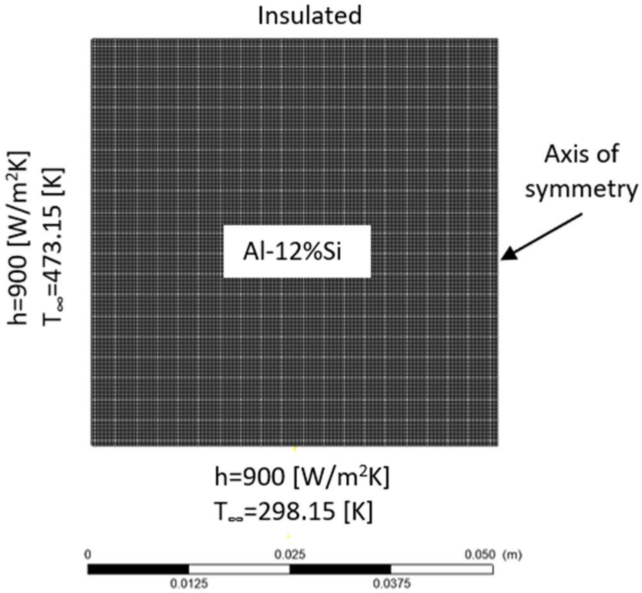

Figure 118 Computational domain and mesh

The simulation took approximately 1-2 days to solve a time of 140 seconds. This time was enough to finish the phase transformation.

Simulation results

Figure 119 shows the position of points used to trace temperatures and liquid fraction results. Figure 120 shows the temperatures at different times at the corresponding points (dashed line). The solid line corresponds to the average temperature of all points. Figure 121 shows results for the first 40 seconds.

The first point P1 shows the strongest cooling rate of 14.17 K/s, wich is the highest value and consequently the zone with the highest undercooling. The point P3 presents the second highest value in the cooling rate (5.92 K/s). These values are at the instant before phase transformation.

As shown in Figure 121, the degree of undercooling for point P1 is 38.8 K. Point P3 shows only a undercooling of 0.2 K.

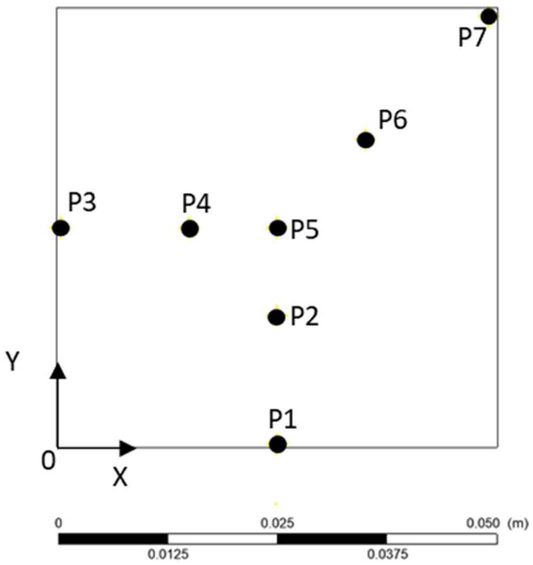

Figure 119 Position in millimeters of points used on results. P1 (25,0.5); P2 (25,15); P3 (0.5,25); P4(15,25); P5(50,50); P6(35,35); P7(49,49)

It can be seen in Figure 120 that the solidification process over the point P1 releases the latent heat and increases the temperature over the points P2, P3 and P4. This increase is not clearly reflected on the average temperature values. Only after 10 seconds a slight increase in the average temperature can be seen. Furthermore, it can be seen at P1 that the latent heat released between seconds 12 and 23 describes a plane of temperature with a slight increase in its temperature although during all the time it remains below the eutectic temperature. The maximum temperature reached is 843 K. In literature [80], [83], [85], [89], this behavior has been observed experimentally as was described in Section 2.5 and 2.6. The latent heat released is extracted by the cooling imposed on the bottom wall and a small fraction is used to barely raise the temperature at the point P1 in the interval from 12 to 23 seconds.

Figure 122 shows the liquid fraction (dashed lines) at the same points indicated in Figure 119 and the average liquid fraction for all points (solid line). Figure 123 plots the first 40 seconds of these results. The points P1 and P3 are the elements at the bottom and left wall respectively. The point P3 starts the solidification process around 4.5 seconds after the point P1, and the solidification process ends approximately 10 seconds after point P1. This is clearly caused by the different solidification velocities.

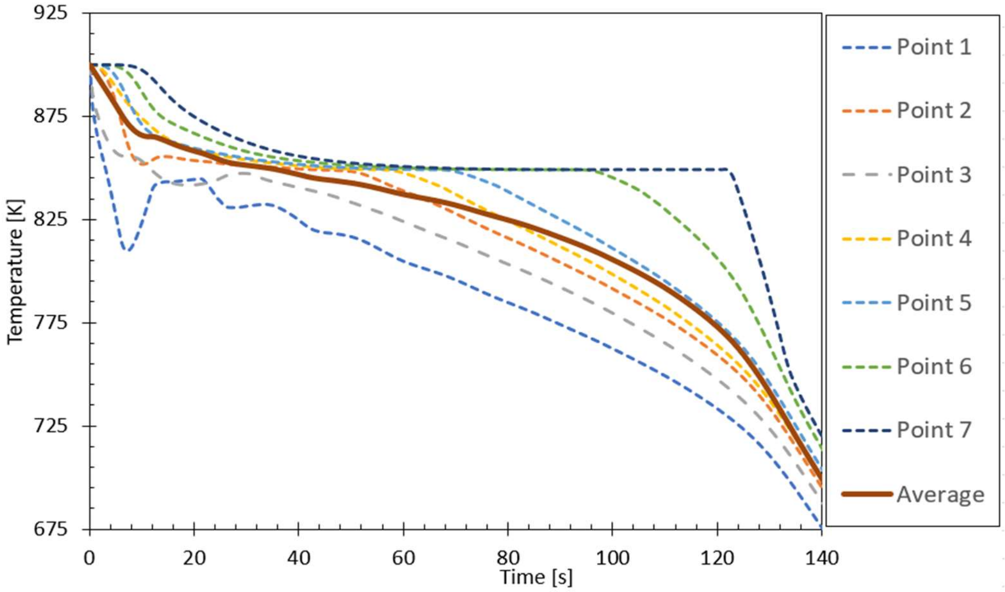

Figure 120 Variation of temperature versus time for P1-P7 points (dashed lines) and average temperature (solid line)

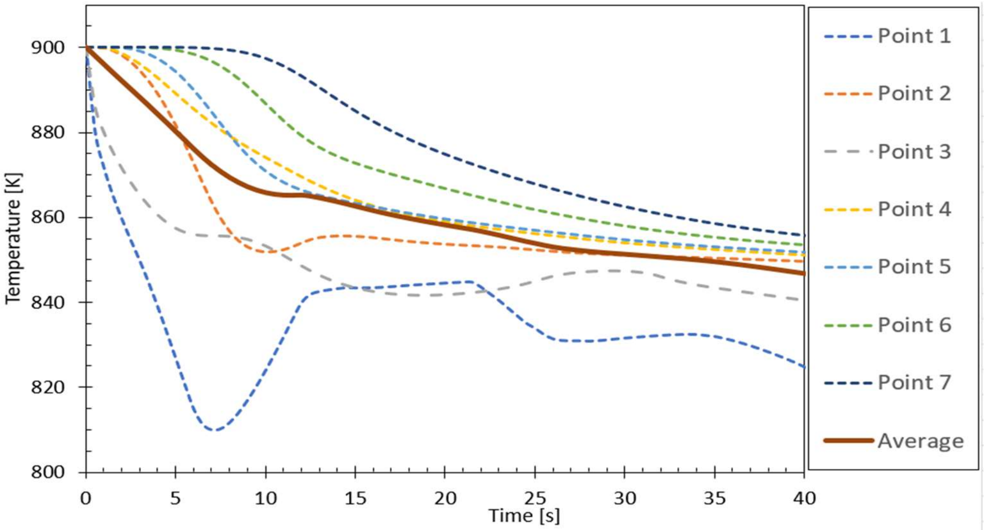

Figure 121 Variation of temperature versus time at the first 40 seconds for P1-P7 points (dashed lines) and average temperature (solid line)

The phase transformation starts almost at the same time all over the bottom wall. This is mainly due to having a virtually constant cooling rate over the entire wall. However, the left wall shows a different cooling rate over the vertical plane. The corner between the bottom and left wall has a different cooling rate than the one located in the corner between the upper and left wall. Figure 124 shows the moment at which point P3 starts to change phase (at 11.5 seconds), Figure 124(A) shows the liquid fractions and the velocity vectors and Figure 124(B) shows the temperature contours. In Figure 124(A) can be seen that the phase change starts at the bottom zone and the solidification continues over the left wall. This behavior is caused by a stronger cooling rate on the lower-left wall. It is also necessary to consider the counterclockwise fluid direction that leads the heat released to the central part of the sample. As shown in the temperature contours of Figure 124(B), the flow circulation (heat flow direction) causes on point P3 to remain at the same temperature. As result, a fraction of the latent heat released in this zone is transferred inside by the convective flow. Thus, the rise in temperature is slower that in other zones (Figure 120), and over the point P2 the temperature increases. However, Figure 121 shows that between seconds 20 and 30, the point P3 increases its temperature more significantly. Also, the solidification rate changes between this interval (as shown in Figure 123). This behavior must be mainly to the advance of the solid/liquid frontier on the left wall of the domain.

Figure 125 shows the phase transformation progress at 20 seconds (top) and at 30 seconds (bottom). Thermal conductivity plays an important role to modify the behavior of the heat extraction. The thermal conductivity is significantly higher in the solid phase (234.7 W/mK) than the liquid phase (89.4 W/mK). The fact that a higher amount of solid phase is present in P3 increases the cooling rate and consequently increases the solidification rate (as seen in Figure 123). Furthermore, increasing the solidification rate results in a greater amount of latent heat released and this causes an increase in P3 temperature (shown in Figure 120). Also, Figure 125 shows the reduction of the convective flow circulation. This reduces the heat transport over the zone P3. This slower convective flow circulation continues transporting the heat released at point P3 to point P1. When P3 increases its solidification rate, the heat released almost stop the cooling in P1 by the heat transported from P3 to P1 (shown in Figure 121). As previously discussed, internal flow circulation is reduced, thermal conduction controls the heat transfer phenomena.

Thus, the cooling rate is maintained almost constantly over the liquid/solid frontier for the rest of the points that have an almost equal solidification rate (see Figure 122).

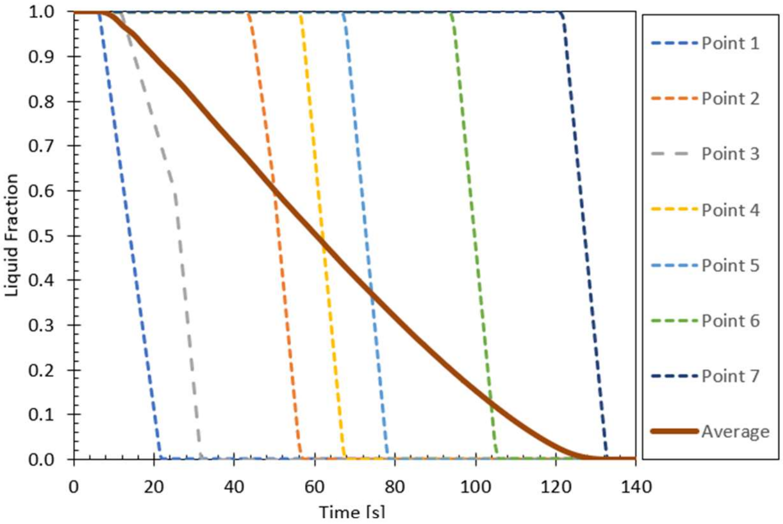

Figure 122 Variation of liquid fraction versus time for P1-P7 points (dashed lines) and average temperature (solid line)

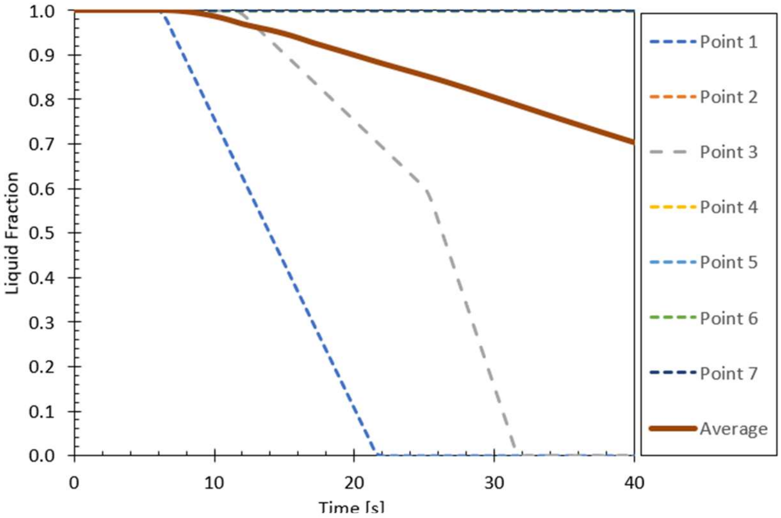

Figure 123 Variation of liquid fraction versus time in the first 40 seconds for P1-P7 points (dashed lines) and average temperature (solid line)

Figure 126(A) and (B) show temperature contours and liquid fraction at the moment when 50% of liquid remains (approximately at 64 seconds). Figure 126(A) shows in the lower zone the solid/liquid frontier is wider compared to the left solid/liquid frontier. Also, the lower solid/liquid frontier shows an advance higher than that shown in the left zone. This is caused by a higher cooling speed on the bottom wall, thus heat extraction accelerates and the solidification rate is higher in the lower zone. This behavior is defined by Equation 90 where the advance of the solid/liquid frontier is controlled by the cooling rate. Figure 126(B) shows the temperature contours and the homogeneity of the temperature in the remaining liquid.

The farthest point P7, in the middle of the sample maintains the eutectic temperature throughout the entire process of phase change as is shown in Figure 120. The rapid decrease in temperature is due to the rapid removal of heat through the surrounding solid phase. At the beginning of the phase transformation (121 seconds) at point P7 the temperature difference between this and the average temperature is 78 K. At point P1 the difference rises to 117 K. These important differences of temperature between the zone P7 and the surrounding zones highlights the importance of the width of the container. It is not efficient to have a zone where the remaining liquid phase has these temperature differences to the cooled wall. With materials with lower thermal conductivities in the solid phase, this thermal difference will be more significant.

The general behavior of the simulation model is similar to described in the experiments mentioned in the second chapter. Figure 35 shows an algorithm able to be simulate alloy phase transformation. Unfortunately, for the Si-Al alloy there were no reliable published results or enough information to compare our results with experimental research. Also, visualizing phase transformation in an alloy sample that allows convective flow is still a challenge, and there is not much available data. However, simulations of the solid/liquid frontier advance, temperature contours and convective flow helps to understand the phenomenon of phase change in alloys. Consequently, this helps improve the design of heat exchangers for applications in LHTES.

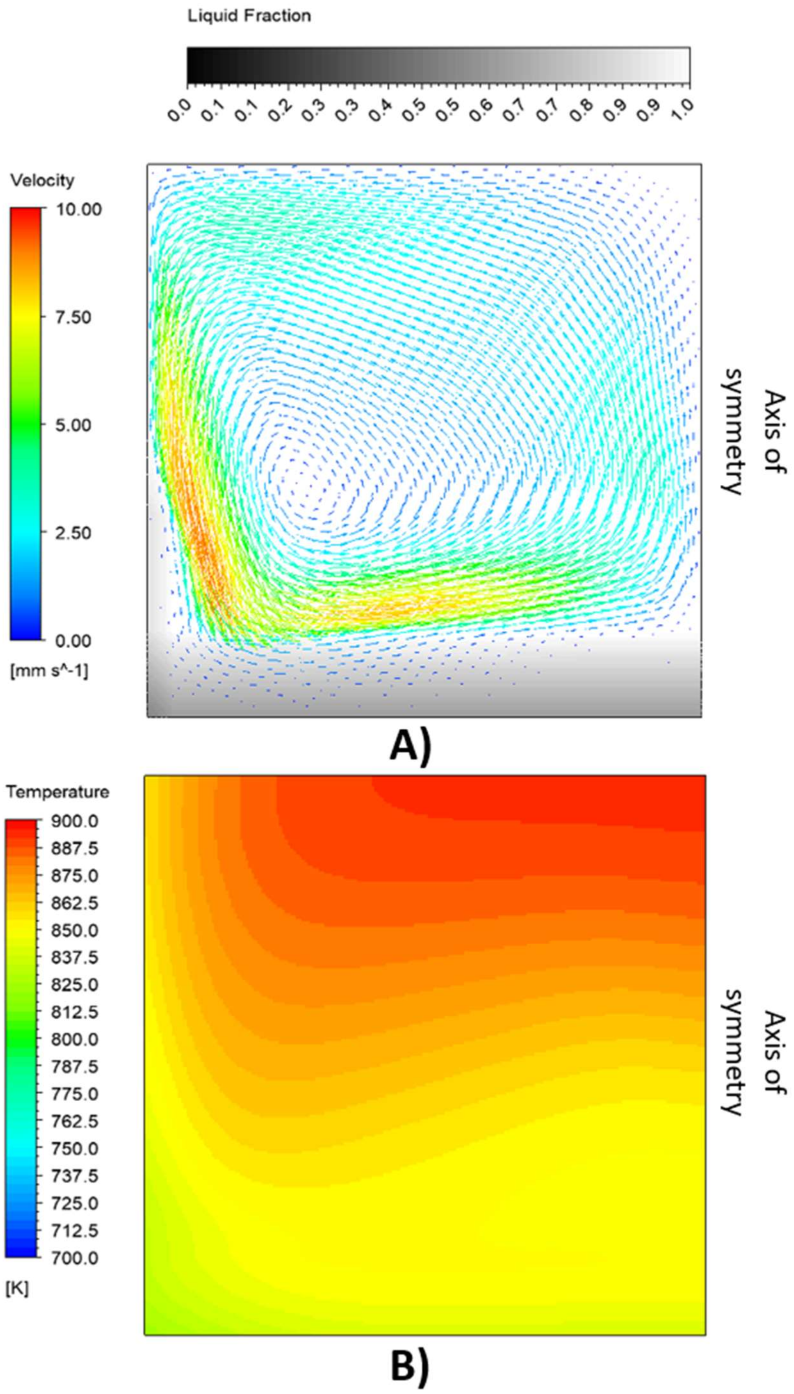

Figure 124 Numerical results at 11.5 seconds. A) Liquid fraction field with the flow field shown by vectors. The local maximum flow velocity is 8.4 mm/s. B) Temperature fields

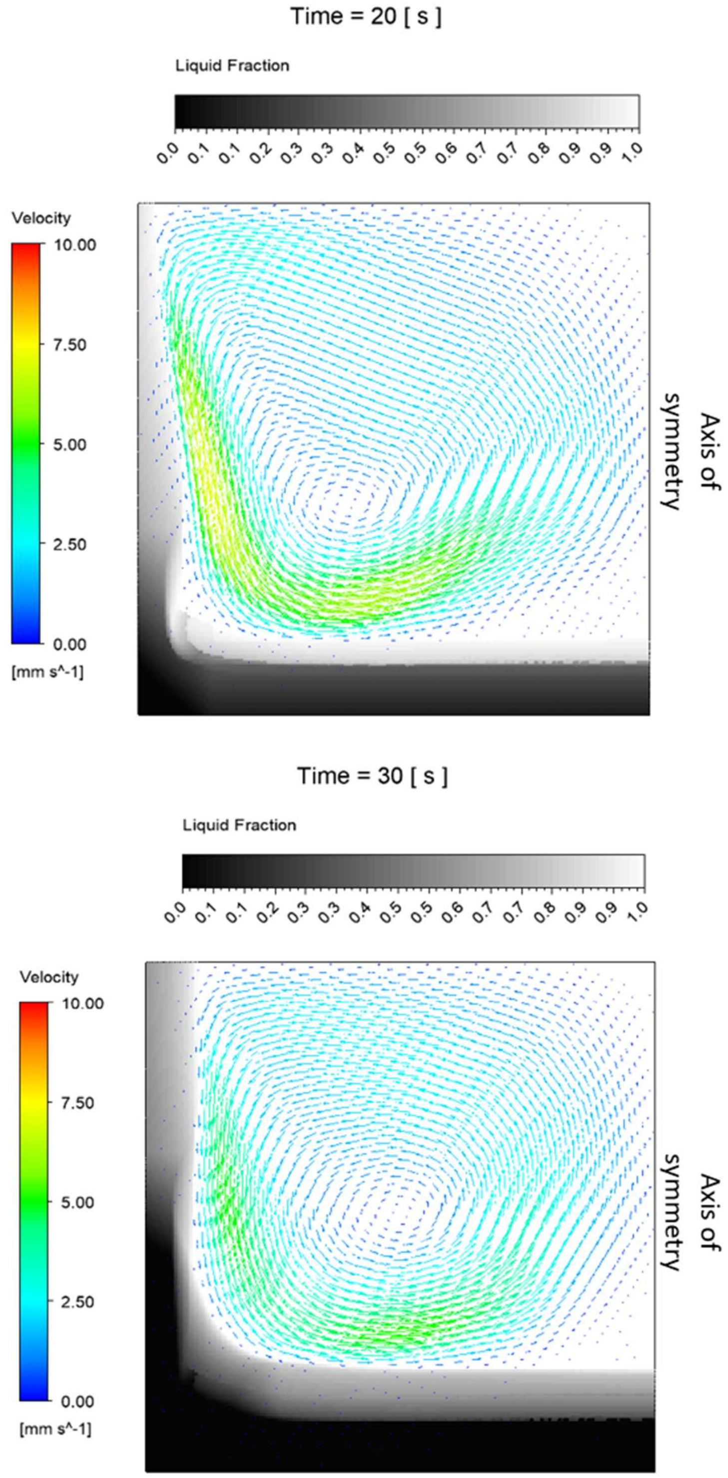

Figure 125 Numerical results of liquid fraction field with flow field shown by vectors at 20 seconds (top) and 30 seconds (bottom). The local maximum flow velocity is 6.8 mm/s. and 5.1 mm/s respectively

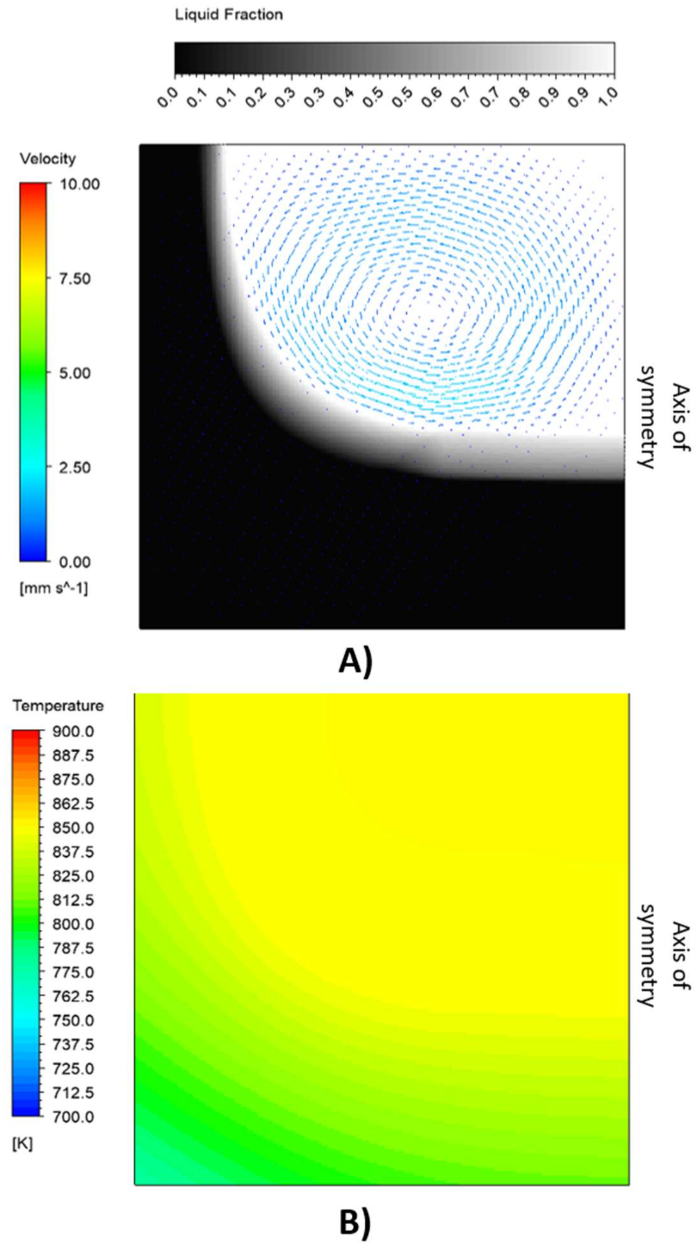

Figure 126 Numerical results at 60 seconds with almost 50% of material solidified. A) Liquid fraction field with the flow field shown by vectors. The local maximum flow velocity is 2 mm/s. B) Temperature fields

Chapter 5 Conclusions and perspectives

5.1 Conclusion

A method was developed in this study to predict the behavior of a binary alloy during phase change, including undercooling, segregation and local compositon variation. This method is represented by the algorithm shown in Figure 35 and is intended for preliminary use in the design of a latent heat thermal storage system. This model can be applied for different cooling rates for binary alloys using phase diagrams and the CALPHAD methodology. This method was divided into functional blocks in order to clearly define the interaction between functions with specific objectives. These functions are the mathematical models that represent the physical phase transformation.

Usually in literature, the CALPHAD methodology is used to define the solid fraction through the lever rule or Scheil-Gulliver formulation. These usually use a constant partition coefficient. Our first approach proposes to calculate the solid or liquid fraction based on the phase diagram to define the influence resulting from a constant or variable partition coefficient. We observe an increase in calculation time when a variable partition coefficient is used and as was shown in Figure 73 and Figure 111, a variable partition coefficient is not always necessary. On the other hand, during the phase change process the variation of composition in the solid formed is used to estimate the quantity of heat transferred. Therefore, this calculation is affected by the use of constant or variable partition coefficient. From the results obtained in Section 4.1.2, we can conclude that the use of a constant partition coefficient is recommended in compositions close to the eutectic point or for pure elements. It is recommended to use a variable partition coefficient in compositions close to the solubility limits. However, a study for each material must be carried out because even on relatively similar phase diagrams such Ag-Cu and Al-Si alloys, the variation in the estimated amount of latent heat was different for both.

Phase change problems in alloys are very complex. To validate the methodology and the algorithm architecture proposed in Figure 35, we created different models reproducing experimental works. These models validate the entire method by parts. In the first part, the Heat

Transfer, Latent Heat and Heat Cpap Functional Blocks showed good agreement with experimental results to solve isothermal phase change.

The second part (as described in Section 4.3 Undercooling degree) included undercooling degree phenomena. Based on the experimental results described before, we propose that the undercooling degree directly depends on the cooling rate. The solidification rate depends on the thermophysical properties and the cooling rate imposed on the sample. Then, numerical simulation of phase change including undercooling is based on the definition of the constant terms in the polynomial Equations 26 and 27. These equations define the solidification rate and the degree of undercooling dependent on the cooling rate, respectively. In Section 4.3, the experimental work of Harary et al. [189] was used to test the method. This numerical model uses the functional blocks for isothermal phase change with the FB-Undercooling and FB-Heat Source. The solidification rate was considered constant and independent of the different cooling rates imposed on the sample. Our results showed a good agreement to predict the undercooling degree. The constant terms were defined by experimental results. However, it can be seen in Figure 94 that the simulation model overestimates the remaining liquid fraction at a cooling rate of 0.31 K/s. On the other hand, for a cooling rate of 0.41 K / s, the model underestimates the remaining liquid fraction. This behavior and difference are mainly explained by the imposition of the same constant solidification velocity in both numerical models. This confirms the importance of defining the solidification rate dependent on the cooling rate. Another important conclusion is the definition of the lower limit of cooling rate to avoid undercooling. From Equation 87 and neglecting up to 5 K of undercooling, the lower limit to prevent undercooling is 96x10-3 [K/s]. This information is significant to improve the heat exchanger and the capacities of the LHTES.

In alloys macrosegregation affects the solidification behavior as was observed in the numerical simulation of section 4.4. These results show good agreement with the experimental results. We can conclude the obvious dependence on macroscale between natural convection and macrosegregation during phase change, largely studied in literature for steels and aluminum alloys. The issues discussed in section 2.4 refer to the complexity of the problem to predict microstructure segregation in alloys during phase change and how this defines the macrosegregation. We include in the method and algorithm architecture the Scheil-Gulliver and LNDM (local non-equilibrium diffusion model [154]) microsegregation models to predict the interaction between composition, segregation and solidification velocity, shown in Figure 27.

These are implemented through FB- K Non-Equilibrium, FB-Undercooling and FB-velocity solidification blocks, wich allow adapting the numerical model to include other models to predict the macrosegregation, undercooling and solidification velocity.

The method described in Chapter 4 represented by the algorithm shown in Figure 35 demonstrated its usefulness to understand the phase change problem for alloys and estimating the degree of undercooling. However, these results should be considered conservatively. The experimental work of G. Wilde et al [101] shows that the degree of undercooling is drastically reduced by impurities in the alloy. The phase change cycles "purify" the alloy and consequently the degree of undercooling increases. Through Equations 26 and 27 it is possible to adjust the model properly and characterize particular conditions of a system from experimental results.

The methodology is tested with the simulation process for an Al-Si eutectic alloy. The dependency of solidification velocity on the cooling rate and how these can be used to predict the behavior of the phase change process was numerically demonstrated. Also, the numerical simulation demonstrated the importance of convective flow during the beginning of phase change. However, the magnitudes of the convective flow are rapidly reduced as the material solidifies. When only 50% liquid remains, heat transfer is primarily driven by conduction. The magnitude of undercooling can vary with solidification progress over the walls, latent heat release and flow direction. The simulation model also showed that the recalescence process is strongly influenced by the convective currents (flow direction) and the heat extraction rate. According to the experimental works of [80], [82], [83], [85] and [167] the cooling rate determines the amount of undercooling. Our numerical model showed the same behavior and dependence described in these works. Our method describes well the interaction of thermophysical properties and phenomena such as segregation and undercooling to define the behavior of the material during phase change.

The method defined in this study in conjunction with the algorithm shown in Figure 35 can be used for preliminary sizing of thermal energy storage systems or to optimize the control of the cooling rates to reduce the undercooling degree. When the proper data is available, the method can be implemented for specific LHTES and optimize the sizing and control of these.

5.2 **Perspectives**

Further evaluation of the assumptions used in the method, such as undercooling degree estimation, should be performed based on experimental results for LHTES. In order to determine the influence of using the CALPHAD methodology and phase diagrams in numerical simulations (discussed in Section 4.1), several more systems should be explored for thermal storage applications. These experimental estimations of alloys under controlled cooling rates will then provide a range of conditions and increase reliability when predecting phase change behavior. Quantifying the effect of undercooling degree and natural convection circulation using numerical simulation will be another aspect to explore with several different alloys.

The use of phase diagrams to calculate liquid fraction and released heat assumes the existence of thermodynamic equilibrium within the mixture, a true conditionfor low cooling rates. The use of the Scheil equation in the calculation of latent heat release requires solving individual species equations for each of the alloy components as was explained in Chapter 3. The results shown in section 4.1 require a more extensive exploration for alloys with a complex phase diagram.

A future task will be to improve the interface and facilitate its use. Thermophysical properties could be included to provide a first approximation of the undercooling degree. The interface could be changed to only require inputing discharge temperature range and cooling rate for the specific LHTES. This process would accelerate alloy selection, proposing different candidates to select the optimum composition for the available energy source.

The results of Chapter 4 show the behavior of the material during phase change. The design of the heat exchanger should take this behavior into account. For example, if the distance between the cooled wall and the area furthest from the cooled wall is increased, it does not necessarily imply an improvement to store energy, and the performance to extract heat can be reduced. Figure 127 shows a typical heat exchanger design [23], this consists of heat transfer fluid pipes submerged in the PCM. It is assumed that the thermal conductivity in solid phase is less than that in the liquid phase. Under this assumption, Figure 127(B) shows the initial condition where the heat transfer fluid extracts heat from the phase change material. The heat extraction is expedited by the higher liquid thermal conductivity and the internal convective flow. Figure 127(A) shows a later time where the liquid/solid boundary advances from the cooled wall. The low thermal conductivity reduces the heat extraction and this keeps reducing with the advance of the solid phase. The latent heat released is mainly absorbed by the remaining liquid. The combination of both aspects reduces the performance of extracting the stored heat. One plausible improvement on this design taking into account the phase transformation process (seen sections 4.3 and 4.5), is moving the duct to the top. Considering a higher density in the solid phase, this higher position will favor the convective flow and maintain a lower advancement of the solidification front. However, as it was shown in section 4.3, when some degree of sub-cooling occurs, the formation of the solid begins on the coldest walls (around the perimeter of the conduct). Consequently, the heat transfer occurs by conduction and this avoid any improvement in the design (assuming that the thermal conductivity in solid phase is less than that in the liquid phase).

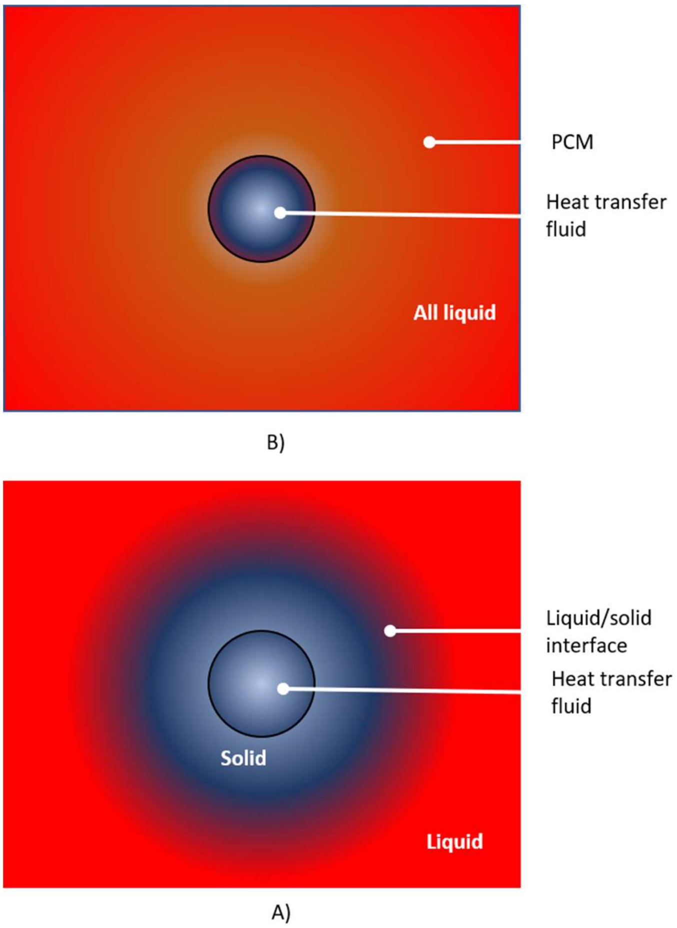

Figure 127 Typical configuration of heat exchanger for LHTES

The most convenient will be to limit the distance between the cooled wall and the opposite one. This distance should be defined as a function of the cooling rate and the solidification velocity. These considerations need to be considered especially in materials where thermal conductivity and density are significantly different between the liquid and solid phases. However, this distance is reduced too much, it will limit the convective flow and consequently will reduce the heat extraction.

Also, additional numerical simulations should be performed to evaluate different heat exchanger designs, then, all enhancements on the LHTES should be evaluated based on the overall system.

References

[1] B. Marc Berthou and D. Bory, "Overview of waste heat in the industry in France," *ECEEE 2012 Summer Study Energy Effic. Ind.*, 2012.

[2] G. P. Panayiotou *et al.*, "Preliminary assessment of waste heat potential in major European industries," *Energy Procedia*, vol. 123, pp. 335–345, Sep. 2017.

[3] "ADEME," *ADEME*. [Online]. Available: http://www.ademe.fr/. [Accessed: 19-Mar-2018].

[4] D. Kurle, C. Schulze, C. Herrmann, and S. Thiede, "Unlocking Waste Heat Potentials in Manufacturing," *Procedia CIRP*, vol. 48, pp. 289–294, Jan. 2016.

[5] A. Kaizawa *et al.*, "Thermal and flow behaviors in heat transportation container using phase change material," *Energy Convers. Manag.*, vol. 49, no. 4, pp. 698–706, Apr. 2008.

[6] "LaTherm - KTG Agrar SE." [Online]. Available: http://www.ktg-agrar.de/geschaeftsfelder/energieproduktion-biogas/latherm.html. [Accessed: 12-Mar-2018].

[7] C. Beghi, Ed., *Thermal Energy Storage: Lectures of a Course held at the Joint Research Centre, Ispra, Italy, June 1–5, 1981*. Springer Netherlands, 1982.

[8] A. Dinker, M. Agarwal, and G. D. Agarwal, "Heat storage materials, geometry and applications: A review," *J. Energy Inst.*, vol. 90, no. 1, pp. 1–11, Feb. 2017.

[9] A. Hoshi, D. R. Mills, A. Bittar, and T. S. Saitoh, "Screening of high melting point phase change materials (PCM) in solar thermal concentrating technology based on CLFR," *Sol. Energy*, vol. 79, no. 3, pp. 332–339, Sep. 2005.

[10] D. Zhou, C. Y. Zhao, and Y. Tian, "Review on thermal energy storage with phase change materials (PCMs) in building applications," *Appl. Energy*, vol. 92, pp. 593–605, Apr. 2012.

[11] R. Y. Zhang, Z. W. Xie, and X. F. Ke, *Phase change materials and phase change energy storage technology*. Science Press, Beijing, 2009.

[12] A. Sharma, V. V. Tyagi, C. R. Chen, and D. Buddhi, "Review on thermal energy storage with phase change materials and applications," *Renew. Sustain. Energy Rev.*, vol. 13, no. 2, pp. 318–345, Feb. 2009.

[13] A. Soupart-Caron, "Stockage de chaleur dans les Matériaux à Changement de Phase," Université Grenoble Alpes, 2015.

[14] F. Li, Y. J. Hu, and R. Y. Zhang, "The Influence of Heating-Cooling Cycles on the Thermal Storage Performances of Al-17 Wt.% Si Alloy," *Adv. Mater. Res.*, vol. 239–242, pp. 2248–2251, 2011.

[15] Z. Wang *et al.*, "Thermal reliability of Al-Si eutectic alloy for thermal energy storage," *Mater. Res. Bull.*, vol. 95, pp. 300–306, Nov. 2017.

[16] N. Saunders and A. P. Miodownik, *CALPHAD (calculation of phase diagrams): a comprehensive guide*, vol. 1. Elsevier, 1998.

[17] "SGTE - Scientific Group Thermodata Europe." [Online]. Available: http://www.crct.polymtl.ca/sgte/. [Accessed: 13-Mar-2018].

[18] "Engineering Simulation & 3-D Design Software | ANSYS." [Online]. Available: //www.ansys.com/. [Accessed: 19-Mar-2018].

[19] C. E. Birchenall and A. F. Riechman, "Heat storage in eutectic alloys," *Metall. Trans. A*, vol. 11, no. 8, pp. 1415–1420, Aug. 1980.

[20] X. Wang, J. Liu, Y. Zhang, H. Di, and Y. Jiang, "Experimental research on a kind of novel high temperature phase change storage heater," *Energy Convers. Manag.*, vol. 47, no. 15, pp. 2211–2222, Sep. 2006.

[21] J. Q. Sun, R. Y. Zhang, Z. P. Liu, and G. H. Lu, "Thermal reliability test of Al–34% Mg–6% Zn alloy as latent heat storage material and corrosion of metal with respect to thermal cycling," *Energy Convers. Manag.*, vol. 48, no. 2, pp. 619–624, 2007.

[22] Z. Zhang and X. Fang, "Study on paraffin/expanded graphite composite phase change thermal energy storage material," *Energy Convers. Manag.*, vol. 47, no. 3, pp. 303–310, Feb. 2006.

[23] B. Cárdenas and N. León, "High temperature latent heat thermal energy storage: Phase change materials, design considerations and performance enhancement techniques," *Renew. Sustain. Energy Rev.*, vol. 27, pp. 724–737, Nov. 2013.

[24] M. K. Rathod and J. Banerjee, "Thermal stability of phase change materials used in latent heat energy storage systems: A review," *Renew. Sustain. Energy Rev.*, vol. 18, pp. 246–258, Feb. 2013.

[25] M. Liu, W. Saman, and F. Bruno, "Review on storage materials and thermal performance enhancement techniques for high temperature phase change thermal storage systems," *Renew. Sustain. Energy Rev.*, vol. 16, no. 4, pp. 2118–2132, May 2012.

[26] S. E. Offerman *et al.*, "Grain nucleation and growth during phase transformations," *Science*, vol. 298, no. 5595, pp. 1003–1005, Nov. 2002.

[27] J. H. Chen, E. Costan, M. A. van Huis, Q. Xu, and H. W. Zandbergen, "Atomic Pillar-Based Nanoprecipitates Strengthen AlMgSi Alloys," *Science*, vol. 312, no. 5772, pp. 416–419, Apr. 2006.

[28] A. Blatter and M. von Allmen, "Reversible Amorphization in Laser-Quenched Titanium Alloys," *Phys. Rev. Lett.*, vol. 54, no. 19, pp. 2103–2106, May 1985.

[29] L. Schultz, "Formation of amorphous metals by mechanical alloying," *Mater. Sci. Eng.*, vol. 97, pp. 15–23, Jan. 1988.

[30] E. Sanz and C. Valeriani, "Crystal-crystal transitions: Mediated by a liquid," *Nat. Mater.*, vol. 14, no. 1, pp. 15–16, Jan. 2015.

[31] R. Kobayashi, "Modeling and numerical simulations of dendritic crystal growth," *Phys. Nonlinear Phenom.*, vol. 63, no. 3, pp. 410–423, Mar. 1993.

[32] L. Thuinet, "Solidification des aciers ternaires : modélisation de la microségrégation en croissance dendritique colonnaire, prise en compte de la réaction péritectique," PhD thesis, Institut National Polytechnique de Lorraine, Vandoeuvre-les-Nancy, INPL, 2005.

[33] Y. Peng *et al.*, "Two-step nucleation mechanism in solid–solid phase transitions," *Nat. Mater.*, vol. 14, no. 1, pp. 101–108, Jan. 2015.

[34] V. Mathot *et al.*, “Flash DSC 1, a power compensation twin-type, chip-based fast scanning calorimeter (FSC): First findings on polymers,” *Thermochim. Acta*, 2011.

[35] E. Zhuravlev and C. Schick, “Fast scanning power compensated differential scanning nano-calorimeter: 1. The device,” *Thermochim. Acta*, vol. 505, no. 1, pp. 1–13, Jun. 2010.

[36] H. L. Lukas, S. G. Fries, and B. Sundman, *Computational thermodynamics: the CALPHAD method*. Cambridge University Press, 2007.

[37] Z. Nishiyama, *Martensitic Transformation*. Elsevier, 2012.

[38] G. E. Totten and M. A. H. Howes, *Steel Heat Treatment Handbook*. CRC Press, 1997.

[39] F. Richter, “Die wichtigsten physikalischen Eigenschaften von 52 Eisenwerkstoffen,” *Stahleisen-Sonderberichte Duesseldorf Verl. Stahleisen 1973*, 1973.

[40] P. Gustafson, “A thermodynamic evaluation of the C− Fe− W system,” *Metall. Mater. Trans. A*, vol. 18, no. 2, pp. 175–188, 1987.

[41] H. Biloni and W. J. Boettinger, “CHAPTER 8 - SOLIDIFICATION,” in *Physical Metallurgy (Fourth, Revised and Enhanced Edition)*, R. W. Cahn and P. Haasen†, Eds. Oxford: North-Holland, 1996, pp. 669–842.

[42] A. Fernández Guillermet, “Critical evaluation of the thermodynamic properties of cobalt,” *Int. J. Thermophys.*, vol. 8, no. 4, pp. 481–510, Jul. 1987.

[43] A. A. Luo, B. R. Powell, and A. K. Sachdev, “Computational phase equilibria and experimental investigation of magnesium–aluminum–calcium alloys,” *Intermetallics*, vol. 24, pp. 22–29, 2012.

[44] N. Moelans, B. Blanpain, and P. Wollants, “An introduction to phase-field modeling of microstructure evolution,” *Calphad*, vol. 32, no. 2, pp. 268–294, Jun. 2008.

[45] D. M. Stefanescu, *Science and Engineering of Casting Solidification*. Springer, 2015.

[46] L. G. Bullard and L. T. Biegler, “Iterated linear programming strategies for non-smooth simulation: A penalty based method for vapor—liquid equilibrium applications,” *Comput. Chem. Eng.*, vol. 17, no. 1, pp. 95–109, 1993.

[47] G. Han and G. P. Rangaiah, “A method for calculation of vapor-liquid and liquid-liquid equilibria,” *Comput. Chem. Eng.*, vol. 21, no. 8, pp. 905–913, 1997.

[48] L. S. Belvèze, J. F. Brennecke, and M. A. Stadtherr, “Modeling of activity coefficients of aqueous solutions of quaternary ammonium salts with the electrolyte-NRTL equation,” *Ind. Eng. Chem. Res.*, vol. 43, no. 3, pp. 815–825, 2004.

[49] G. A. Iglesias-Silva, A. Bonilla-Petriciolet, P. T. Eubank, J. C. Holste, and K. R. Hall, “An algebraic method that includes Gibbs minimization for performing phase equilibrium calculations for any number of components or phases,” *Fluid Phase Equilibria*, vol. 210, no. 2, pp. 229–245, 2003.

[50] M. Castier, P. Rasmussen, and A. Fredenslund, “Calculation of simultaneous chemical and phase equilibria in nonideal systems,” *Chem. Eng. Sci.*, vol. 44, no. 2, pp. 237–248, 1989.

[51] J. Castillo and I. E. Grossmann, “Computation of phase and chemical equilibria,” *Comput. Chem. Eng.*, vol. 5, no. 2, pp. 99–108, 1981.

[52] C. M. McDonald and C. A. Floudas, “GLOPEQ: A new computational tool for the phase and chemical equilibrium problem,” *Comput. Chem. Eng.*, vol. 21, no. 1, pp. 1–23, 1997.

[53] D. Hildebrandt and D. Glasser, "Predicting phase and chemical equilibrium using the convex hull of the Gibbs free energy," *Chem. Eng. J. Biochem. Eng. J.*, vol. 54, no. 3, pp. 187–197, Jul. 1994.

[54] C. B. Barber, D. P. Dobkin, and H. Huhdanpaa, "The quickhull algorithm for convex hulls," *ACM Trans. Math. Softw. TOMS*, vol. 22, no. 4, pp. 469–483, 1996.

[55] "SciPy.org — SciPy.org." [Online]. Available: https://www.scipy.org/. [Accessed: 28-Mar-2018].

[56] J. W. Gibbs, "ART. LII.--On the Equilibrium of Heterogeneous Substances," *Am. J. Sci. Arts 1820-1879*, vol. 16, no. 96, p. 441, 1878.

[57] L. Kaufman and H. Bernstein, "Computer calculation of phase diagrams. With special reference to refractory metals," 1970.

[58] A. A. Luo, "Material design and development: From classical thermodynamics to CALPHAD and ICME approaches," *Calphad*, vol. 50, pp. 6–22, 2015.

[59] J.-C. Zhao and M. F. Henry, "CALPHAD—Is It Ready for Superalloy Design?," *Adv. Eng. Mater.*, vol. 4, no. 7, pp. 501–508, 2002.

[60] A. A. Luo, R. K. Mishra, B. R. Powell, and A. K. Sachdev, "Magnesium alloy development for automotive applications," in *Materials Science Forum*, 2012, vol. 706, pp. 69–82.

[61] J.-O. Andersson, T. Helander, L. Höglund, P. Shi, and B. Sundman, "Thermo-Calc & DICTRA, computational tools for materials science," *Calphad*, vol. 26, no. 2, pp. 273–312, 2002.

[62] C. W. Bale *et al.*, "FactSage thermochemical software and databases," *Calphad*, vol. 26, no. 2, pp. 189–228, 2002.

[63] S.-L. Chen *et al.*, "The PANDAT software package and its applications," *Calphad*, vol. 26, no. 2, pp. 175–188, 2002.

[64] O. Redlich and A. T. Kister, "Algebraic representation of thermodynamic properties and the classification of solutions," *Ind. Eng. Chem.*, vol. 40, no. 2, pp. 345–348, 1948.

[65] G. Cacciamani, R. Ferro, I. Ansara, and N. Dupin, "Thermodynamic modelling of the Co–Ti system," *Intermetallics*, vol. 8, no. 3, pp. 213–222, 2000.

[66] S. Kou and R. Mehrabian, *Modeling and Control of Casting and Welding Processes: Proceedings of the Third Conference on Modeling of Casting and Welding Processes, Sponsored by the Engineering Foundation [and] Held on January 12-17, 1986, in Santa Barbara, California*. Metallurgical Society, 1986.

[67] P. Auburtin, T. Wang, S. L. Cockcroft, and A. Mitchell, "Freckle formation and freckle criterion in superalloy castings," *Metall. Mater. Trans. B*, vol. 31, no. 4, pp. 801–811, 2000.

[68] M. C. Schneider, J. P. Gu, C. Beckermann, W. J. Boettinger, and U. R. Kattner, "Modeling of micro-and macrosegregation and freckle formation in single-crystal nickel-base superalloy directional solidification," *Metall. Mater. Trans. A*, vol. 28, no. 7, pp. 1517–1531, 1997.

[69] W. B. Bald, "On crystal size and cooling rate," *J. Microsc.*, vol. 143, no. 1, pp. 89–102, 1986.

[70] J. H. Perepezko and W. J. Boettinger, "Use of metastable phase diagrams in rapid solidification," *MRS Online Proc. Libr. Arch.*, vol. 19, 1982.

[71] R. Goetzinger, M. Barth, and D. M. Herlach, "Mechanism of formation of the anomalous eutectic structure in rapidly solidified Ni–Si, Co–Sb and Ni–Al–Ti alloys," *Acta Mater.*, vol. 46, no. 5, pp. 1647–1655, Mar. 1998.

[72] W. J. Boettinger, J. H. Perepezko, S. K. Das, B. H. Kear, and C. M. Adam, “Rapidly Solidified Crystalline Alloys,” *TMS-AIME Warrendale PA*, vol. 21, 1985.

[73] Y. Du *et al.*, “Thermodynamic modelling and Gulliver-Scheil simulation of multi-component Al alloys,” *IOP Conf. Ser. Mater. Sci. Eng.*, vol. 27, no. 1, p. 012082, 2012.

[74] T. J. Smith, *Modelling the Flow and Solidification of Metals*. Springer Science & Business Media, 2012.

[75] M. C. Flemings, “Solidification processing,” *Metall. Trans.*, vol. 5, no. 10, pp. 2121–2134, Oct. 1974.

[76] M. C. Flemings, “Behavior of metal alloys in the semisolid state,” *Metall. Trans. B*, vol. 22, no. 3, pp. 269–293, Jun. 1991.

[77] D. Mazumdar and J. W. Evans, *Modeling of Steelmaking Processes*. CRC Press, 2009.

[78] R. S. Rana, R. Purohit, and S. Das, *Reviews on the Influences of Alloying elements on the Microstructure and Mechanical Properties of Aluminum Alloys and Aluminum Alloy Composites*. .

[79] W. Kurz and D. J. Fisher, *Fundamentals of solidification*. Trans Tech Publications, 1986.

[80] L. Huang, E. Günther, C. Doetsch, and H. Mehling, “Subcooling in PCM emulsions—Part 1: Experimental,” *Thermochim. Acta*, vol. 509, no. 1, pp. 93–99, Sep. 2010.

[81] J. Trahan, “A Technical and Economic Comparative Analysis of Sensible and Latent Heat Packed Bed Storage Systems for Concentrating Solar Thermal Power Plants,” *Grad. Theses Diss.*, Jan. 2015.

[82] L. F. Cabeza, A. Castell, C. Barreneche, A. de Gracia, and A. I. Fernández, “Materials used as PCM in thermal energy storage in buildings: A review,” *Renew. Sustain. Energy Rev.*, vol. 15, no. 3, pp. 1675–1695, Apr. 2011.

[83] G. R. Solomon, S. Karthikeyan, and R. Velraj, “Sub cooling of PCM due to various effects during solidification in a vertical concentric tube thermal storage unit,” *Appl. Therm. Eng.*, vol. 52, no. 2, pp. 505–511, Apr. 2013.

[84] “Enhanced thermal performance and study the influence of sub cooling on activated carbon dispersed eutectic PCM for cold storage applications - ScienceDirect.” [Online]. Available: https://www-sciencedirect-com.docelec.u-bordeaux.fr/science/article/pii/S037877881730052X. [Accessed: 27-Jan-2018].

[85] S. Ushak, A. Gutierrez, C. Barreneche, A. I. Fernandez, M. Grágeda, and L. F. Cabeza, “Reduction of the subcooling of bischofite with the use of nucleatings agents,” *Sol. Energy Mater. Sol. Cells*, vol. 157, pp. 1011–1018, Dec. 2016.

[86] D. Turnbull and B. G. Bagley, *Treatise on Solid State Chemistry vol 5 ed NB Hannay*. New York: Plenum) p, 1975.

[87] C. Arkar and S. Medved, “Influence of accuracy of thermal property data of a phase change material on the result of a numerical model of a packed bed latent heat storage with spheres,” *Thermochim. Acta*, vol. 438, no. 1, pp. 192–201, Nov. 2005.

[88] P. Lamberg, R. Lehtiniemi, and A.-M. Henell, “Numerical and experimental investigation of melting and freezing processes in phase change material storage,” *Int. J. Therm. Sci.*, vol. 43, no. 3, pp. 277–287, Mar. 2004.

[89] S.-L. Chen, C.-L. Chen, C.-C. Tin, T.-S. Lee, and M.-C. Ke, “An experimental investigation of cold storage in an encapsulated thermal storage tank,” *Exp. Therm. Fluid Sci.*, vol. 23, no. 3, pp. 133–144, Dec. 2000.

[90] M. Rappaz and C.-A. Gandin, “Probabilistic modelling of microstructure formation in solidification processes,” *Acta Metall. Mater.*, vol. 41, no. 2, pp. 345–360, 1993.

[91] G. F. Zhou, H. J. Borg, J. C. N. Rijpers, and M. Lankhorst, “Crystallization behavior of phase change materials: comparison between nucleation-and growth-dominated crystallization,” in *Optical Data Storage, 2000. Conference Digest*, 2000, pp. 74–76.

[92] S. Okawa, A. Saito, and R. Minami, “The solidification phenomenon of the supercooled water containing solid particles,” *Int. J. Refrig.*, vol. 24, no. 1, pp. 108–117, Jan. 2001.

[93] S. Okawa, A. Saito, and H. Suto, “The experimental study on freezing of supercooled water using metallic surface,” *Int. J. Refrig.*, vol. 25, no. 5, pp. 514–520, Aug. 2002.

[94] F. C. R. Hernandez, J. M. H. Ramírez, and R. Mackay, *Al-Si Alloys: Automotive, Aeronautical, and Aerospace Applications*. Springer International Publishing, 2017.

[95] D. R. H. Jones and M. F. Ashby, *Engineering Materials Volume 2: An Introduction to Microstructures, Processing and Design*. Elsevier, 2013.

[96] E. I. Givargizov, *Oriented Crystallization on Amorphous Substrates*. Springer Science & Business Media, 2013.

[97] P. K. Galenko and D. A. Danilov, “Local nonequilibrium effect on rapid dendritic growth in a binary alloy melt,” *Phys. Lett. A*, vol. 235, no. 3, pp. 271–280, Nov. 1997.

[98] P. Galenko and S. Sobolev, “Local nonequilibrium effect on undercooling in rapid solidification of alloys,” *Phys. Rev. E*, vol. 55, no. 1, pp. 343–352, Jan. 1997.

[99] J. D. Verhoeven, *Fundamentals of physical metallurgy*. John Wiley & Sons Inc, 1975.

[100] G. E. Totten and D. S. MacKenzie, *Handbook of Aluminum: Vol. 1: Physical Metallurgy and Processes*. CRC Press, 2003.

[101] G. Wilde, J. L. Sebright, and J. H. Perepezko, “Bulk liquid undercooling and nucleation in gold,” *Acta Mater.*, vol. 54, no. 18, pp. 4759–4769, Oct. 2006.

[102] S. Zhao, J. F. Li, L. Liu, and Y. H. Zhou, “Cellular growth of lamellar eutectics in undercooled Ag–Cu alloy,” *Mater. Charact.*, vol. 60, no. 6, pp. 519–524, Jun. 2009.

[103] L. Liu, X. X. Wei, Q. S. Huang, J. F. Li, X. H. Cheng, and Y. H. Zhou, “Anomalous eutectic formation in the solidification of undercooled Co–Sn alloys,” *J. Cryst. Growth*, vol. 358, pp. 20–28, Nov. 2012.

[104] J. F. Li, X. L. Li, L. Liu, and S. Y. Lu, “Mechanism of anomalous eutectic formation in the solidification of undercooled Ni–Sn eutectic alloy,” *J. Mater. Res.*, vol. 23, no. 8, pp. 2139–2148, Aug. 2008.

[105] N. H. Pryds and A. S. Pedersen, “Rapid solidification of martensitic stainless steel atomized droplets,” *Metall. Mater. Trans. A*, vol. 33, no. 12, pp. 3755–3761, 2002.

[106] L. Backerud, G. Chai, and J. Tamminen, “Solidification characteristics of aluminum alloys. Vol. 2. Foundry alloys,” *Am. Foundrymens Soc. Inc 1990*, p. 266, 1990.

[107] M. Carrard, M. Gremaud, M. Zimmermann, and W. Kurz, "About the banded structure in rapidly solidified dendritic and eutectic alloys," *Acta Metall. Mater.*, vol. 40, no. 5, pp. 983–996, 1992.

[108] D. M. Anderson, G. B. McFadden, and A. A. Wheeler, "A phase-field model of solidification with convection," *Phys. Nonlinear Phenom.*, vol. 135, no. 1, pp. 175–194, Jan. 2000.

[109] X. Tong, C. Beckermann, A. Karma, and Q. Li, "Phase-field simulations of dendritic crystal growth in a forced flow," *Phys. Rev. E*, vol. 63, no. 6, p. 061601, May 2001.

[110] L. Tan and N. Zabaras, "A level set simulation of dendritic solidification with combined features of front-tracking and fixed-domain methods," *J. Comput. Phys.*, vol. 211, no. 1, pp. 36–63, Jan. 2006.

[111] D. Pal, J. Bhattacharya, P. Dutta, and S. Chakraborty, "An Enthalpy Model for Simulation of Dendritic Growth," *Numer. Heat Transf. Part B Fundam.*, vol. 50, no. 1, pp. 59–78, Mar. 2006.

[112] J. S. Langer and H. Müller-Krumbhaar, "Theory of dendritic growth—I. Elements of a stability analysis," *Acta Metall.*, vol. 26, no. 11, pp. 1681–1687, Nov. 1978.

[113] D. A. Kessler, J. Koplik, and H. Levine, "Steady-state dendritic crystal growth," *Phys. Rev. A*, vol. 33, no. 5, pp. 3352–3357, May 1986.

[114] R. Ananth and W. N. Gill, "Dendritic growth with thermal convection," *J. Cryst. Growth*, vol. 91, no. 4, pp. 587–598, Sep. 1988.

[115] R. Ananth and W. N. Gill, "Self-consistent theory of dendritic growth with convection," *J. Cryst. Growth*, vol. 108, no. 1, pp. 173–189, Jan. 1991.

[116] E. Zohreh, "Micromechanical Phase-Field Model and Simulation of Eutectic Growth with Misfit Stresses," PhD thesis, RWTH AACHEN UNIVERSITY Department of Computer Science, 2010.

[117] I. Loginova, "Phase-field modeling of diffusion controlled phase transformation," Ph.D. Thesis, Royal Institute of Technology, Department of Mechanics, Stockholm, Sweden, 2003.

[118] S. L. Sobolev, "Driving force for binary alloy solidification under far from local equilibrium conditions," *Acta Mater.*, vol. 93, pp. 256–263, Jul. 2015.

[119] M. J. Aziz and T. Kaplan, "Continuous growth model for interface motion during alloy solidification," *Acta Metall.*, vol. 36, no. 8, pp. 2335–2347, 1988.

[120] M. Yao and A. Chait, "An alternative formulation of the apparent heat capacity method for phase-change problems," *Numer. Heat Transf. Part B Fundam.*, vol. 24, no. 3, pp. 279–300, 1993.

[121] J. M. Sturtevant, "Heat capacity and entropy changes in processes involving proteins," *Proc. Natl. Acad. Sci.*, vol. 74, no. 6, pp. 2236–2240, 1977.

[122] M. Salcudean and Z. Abdullah, "On the numerical modelling of heat transfer during solidification processes," *Int. J. Numer. Methods Eng.*, vol. 25, no. 2, pp. 445–473, 1988.

[123] H. Hu and S. A. Argyropoulos, "Mathematical modelling of solidification and melting: a review," *Model. Simul. Mater. Sci. Eng.*, vol. 4, no. 4, p. 371, 1996.

[124] H. T. Hashemi and C. M. Sliepcevich, "A numerical method for solving two-dimensional problems of heat conduction with change of phase," in *Chem. Eng. Prog. Symp. Series*, 1967, vol. 63, pp. 34–41.

[125] V. R. Voller, C. R. Swaminathan, and B. G. Thomas, "Fixed grid techniques for phase change problems: a review," *Int. J. Numer. Methods Eng.*, vol. 30, no. 4, pp. 875–898, 1990.

[126] C. R. Swaminathan and V. R. Voller, “A general enthalpy method for modeling solidification processes,” *Metall. Trans. B*, vol. 23, no. 5, pp. 651–664, 1992.

[127] S. Pang *et al.*, “Effect of cooling rate on the microstructure and mechanical properties of sand-casting Mg–10Gd–3Y–0.5 Zr magnesium alloy,” *Mater. Sci. Eng. A*, vol. 562, pp. 152–160, 2013.

[128] J. Deschamps, M. Georgelin, and A. Pocheau, “Growth directions of microstructures in directional solidification of crystalline materials,” *Phys. Rev. E*, vol. 78, no. 1, p. 011605, 2008.

[129] R. W. Lewis, P. Nithiarasu, and K. N. Seetharamu, *Fundamentals of the finite element method for heat and fluid flow*. John Wiley & Sons, 2004.

[130] M. Deserno and C. Holm, “How to mesh up Ewald sums. I. A theoretical and numerical comparison of various particle mesh routines,” *J. Chem. Phys.*, vol. 109, no. 18, pp. 7678–7693, 1998.

[131] E. Schnetter, S. H. Hawley, and I. Hawke, “Evolutions in 3D numerical relativity using fixed mesh refinement,” *Class. Quantum Gravity*, vol. 21, no. 6, p. 1465, 2004.

[132] A. D. Brent, V. R. Voller, and K. T. J. Reid, “Enthalpy-porosity technique for modeling convection-diffusion phase change: application to the melting of a pure metal,” *Numer. Heat Transf. Part Appl.*, vol. 13, no. 3, pp. 297–318, 1988.

[133] B. Andersson, R. Andersson, L. Håkansson, M. Mortensen, R. Sudiyo, and B. van Wachem, *Computational Fluid Dynamics for Engineers*. Cambridge University Press, 2011.

[134] C. M. Rhie and W. L. Chow, “Numerical study of the turbulent flow past an airfoil with trailing edge separation,” *AIAA J.*, vol. 21, no. 11, pp. 1525–1532, 1983.

[135] H. Gaye and C. H. P. Lupis, “Computer calculations of multicomponent phase diagrams,” *Scr. Metall.*, vol. 4, no. 9, pp. 685–691, 1970.

[136] H. Gaye and C. H. P. Lupis, “Numerical techniques for the calculation of binary phase diagrams,” *Metall. Trans. A*, vol. 6, no. 5, p. 1049, 1975.

[137] J. W. Cahn and W. C. Carter, “Crystal shapes and phase equilibria: a common mathematical basis,” *Metall. Mater. Trans. A*, vol. 27, no. 6, pp. 1431–1440, 1996.

[138] W. C. Carter, “3.016 Mathematics for Materials Scientists and Engineers, Fall 2003,” 2003.

[139] “Welcome to Python.org,” *Python.org*. [Online]. Available: https://www.python.org/. [Accessed: 28-Mar-2018].

[140] D. F. Elger and J. A. Roberson, *Engineering fluid mechanics*. Wiley Hoboken (NJ), 2016.

[141] Y. Nakayama, *Introduction to fluid mechanics*. Butterworth-Heinemann, 2018.

[142] W. Youssef, Y. T. Ge, and S. A. Tassou, “CFD modelling development and experimental validation of a phase change material (PCM) heat exchanger with spiral-wired tubes,” *Energy Convers. Manag.*, vol. 157, pp. 498–510, Feb. 2018.

[143] M. C. Flemings and G. E. Nereo, “MACROSEGREGATION. PT. 1,” *AIME Met Soc Trans*, vol. 239, no. 9, pp. 1449–1461, 1967.

[144] M. C. Flemings, R. Mehrabian, and G. E. Nereo, “MACROSEGREGATION. PT. 2,” *Trans Met Soc AIME*, vol. 242, no. 1, pp. 41–49, 1968.

[145] J. Crank, *Free and moving boundary problems*. Clarendon Press, 1984.

[146] F. Civan, “Limitation in the apparent heat capacity formulation for heat transfer with phase change,” in *Proceedings of the Oklahoma Academy of Science*, 1987, vol. 67, pp. 83–88.

[147] A. V. Veinik, *Thermodynamics for the Foundryman*. Elsevier, 1967.

[148] Z. Leoinid V., “MSE 3050: Thermodynamics and Kinetics of Materials,” University of Virginia, Spring-2018.

[149] W. D. Rolph and K.-Jür. Bathe, “An efficient algorithm for analysis of nonlinear heat transfer with phase changes,” *Int. J. Numer. Methods Eng.*, vol. 18, no. 1, pp. 119–134, 1982.

[150] J. Roose and O. Storrer, “Modelization of phase changes by fictitious-heat flow,” *Int. J. Numer. Methods Eng.*, vol. 20, no. 2, pp. 217–225, 1984.

[151] J. N. Reddy and D. K. Gartling, *The finite element method in heat transfer and fluid dynamics*. CRC press, 2010.

[152] B. R. Baliga and S. V. Patankar, “A control volume finite-element method for two-dimensional fluid flow and heat transfer,” *Numer. Heat Transf.*, vol. 6, no. 3, pp. 245–261, 1983.

[153] J. Lipton, M. E. Glicksman, and W. Kurz, “Dendritic growth into undercooled alloy metals,” *Mater. Sci. Eng.*, vol. 65, no. 1, pp. 57–63, Jul. 1984.

[154] S. L. Sobolev, “Local non-equilibrium diffusion model for solute trapping during rapid solidification,” *Acta Mater.*, vol. 60, no. 6, pp. 2711–2718, Apr. 2012.

[155] G. P. Ivantsov, “GP Ivantsov, Dokl. Akad. Nauk SSSR 58, 567 (1947).,” in *Dokl. Akad. Nauk SSSR*, 1947, vol. 58, p. 567.

[156] Z.-K. Liu and Y. A. Chang, “On the applicability of the Ivantsov growth equation,” *J. Appl. Phys.*, vol. 82, no. 10, pp. 4838–4841, 1997.

[157] G. Müller, J.-J. Métois, and P. Rudolph, *Crystal Growth - From Fundamentals to Technology*. Elsevier, 2004.

[158] P. K. Galenko and K. R. Elder, “Marginal stability analysis of the phase field crystal model in one spatial dimension,” *Phys. Rev. B*, vol. 83, no. 6, p. 064113, 2011.

[159] H. Müller-Krumbhaar, W. Kurz, and E. Brener, “Solidification,” *Mater. Sci. Technol.*, 1991.

[160] J. L. C. Daams, J. R. Rodgers, and P. Villars, “Typical interatomic distances: metals and alloys,” in *International Tables for Crystallography Volume C: Mathematical, physical and chemical tables*, E. Prince, Ed. Dordrecht: Springer Netherlands, 2004, pp. 774–777.

[161] B. Wei, D. M. Herlach, B. Feuerbacher, and F. Sommer, “Dendritic and eutectic solidification of undercooled Co▯ Sb alloys,” *Acta Metall. Mater.*, vol. 41, no. 6, pp. 1801–1809, 1993.

[162] B. T. Bassler, W. H. Hofmeister, G. Carro, and R. J. Bayuzick, “The velocity of solidification of highly undercooled nickel,” *Metall. Mater. Trans. A*, vol. 25, no. 6, pp. 1301–1308, 1994.

[163] K. Eckler, R. F. Cochrane, D. M. Herlach, B. Feuerbacher, and M. Jurisch, “Evidence for a transition from diffusion-controlled to thermally controlled solidification in metallic alloys,” *Phys. Rev. B*, vol. 45, no. 9, p. 5019, 1992.

[164] K. Eckler, D. M. Herlach, and M. J. Aziz, “Search for a solute-drag effect in dendritic solidification,” *Acta Metall. Mater.*, vol. 42, no. 3, pp. 975–979, 1994.

[165] S. A. Khot, N. K. Sane, and B. S. Gawali, “Experimental investigation of phase change phenomena of paraffin wax inside a capsule,” *Int. J. Eng. Trends Technol.*, vol. 2, no. 2, 2011.

[166] J. Tower, “Numerical Development and Optimization of a Phase Change Material Solar Thermal Storage Unit System Model,” 2016.

[167] S. I. Hussain, R. Dinesh, A. A. Roseline, S. Dhivya, and S. Kalaiselvam, “Enhanced thermal performance and study the influence of sub cooling on activated carbon dispersed eutectic PCM for cold storage applications,” *Energy Build.*, vol. 143, pp. 17–24, 2017.

[168] R. Jaffee, *Fundamental Aspects of Structural Alloy Design*. Springer Science & Business Media, 2013.

[169] H. Fredriksson and U. Åkerlind, “Macrosegregation in Alloys,” *Mater. Process. Cast.*, pp. 369–410.

[170] S. Chang and D. M. Stefanescu, “A model for inverse segregation: The case of directionally solidified Al□Cu alloys,” *Acta Mater.*, vol. 44, no. 6, pp. 2227–2235, 1996.

[171] W. R. Osório, D. J. Moutinho, L. C. Peixoto, I. L. Ferreira, and A. Garcia, “Macrosegregation and microstructure dendritic array affecting the electrochemical behaviour of ternary Al–Cu–Si alloys,” *Electrochimica Acta*, vol. 56, no. 24, pp. 8412–8421, 2011.

[172] Q. Z. Diao and H.-L. Tsai, “Modeling of solute redistribution in the mushy zone during solidification of aluminum-copper alloys,” *Metall. Trans. A*, vol. 24, no. 4, pp. 963–973, 1993.

[173] J. LI, M. XIA, Q. HU, and J. LI, “Solutions in Improving Homogeneities of Heavy Ingots,” *Acta Met. Sin*, vol. 54, no. 5, pp. 773–788, 2018.

[174] “Thermodynamic databases - Thermo-Calc Software.” [Online]. Available: http://www.thermocalc.com/products-services/databases/thermodynamic/. [Accessed: 14-May-2018].

[175] M. Hillert, *Phase equilibria, phase diagrams and phase transformations: their thermodynamic basis*. Cambridge University Press, 2007.

[176] M. Bareiss and H. Beer, “An analytical solution of the heat transfer process during melting of an unfixed solid phase change material inside a horizontal tube,” *Int. J. Heat Mass Transf.*, vol. 27, no. 5, pp. 739–746, 1984.

[177] M. Bareiss and H. Beer, “Experimental investigation of melting heat transfer with regard to different geometric arrangements,” *Int. Commun. Heat Mass Transf.*, vol. 11, no. 4, pp. 323–333, 1984.

[178] M. Bareiss and H. Beer, “Influence of natural convection on the melting process in a vertical cylindrical enclosure,” *Lett. Heat Mass Transf.*, vol. 7, no. 5, pp. 329–338, 1980.

[179] K. Katayama *et al.*, “Heat transfer characteristics of the latent heat thermal energy storage capsule,” *Sol. Energy*, vol. 27, no. 2, pp. 91–97, 1981.

[180] T. Saitoh and K. Hirose, “High-performance phase-change thermal energy storage using spherical capsules,” *Chem. Eng. Commun.*, vol. 41, no. 1–6, pp. 39–58, 1986.

[181] S. A. Fomin and T. S. Saitoh, “Melting of unfixed material in spherical capsule with non-isothermal wall,” *Int. J. Heat Mass Transf.*, vol. 42, no. 22, pp. 4197–4205, Nov. 1999.

[182] F. L. Tan, “Constrained and unconstrained melting inside a sphere,” *Int. Commun. Heat Mass Transf.*, vol. 35, no. 4, pp. 466–475, 2008.

[183] E. Assis, L. Katsman, G. Ziskind, and R. Letan, “Numerical and experimental study of melting in a spherical shell,” *Int. J. Heat Mass Transf.*, vol. 50, no. 9–10, pp. 1790–1804, 2007.

[184] “Simplified Formula for Estimating Natural Convection Heat Transfer Coefficient on a Flat Plate,” *Electronics Cooling*, 01-Aug-2001. .

[185] H. Yoshioka, Y. Tada, K. Kunimine, T. Furuichi, and Y. Hayashi, “Heat transfer and solidification processes of alloy melt with undercooling: II. Solidification model,” *Acta Mater.*, vol. 54, no. 3, pp. 765–771, Feb. 2006.

[186] H. Rieger, U. Projahn, and H. Beer, “Analysis of the heat transport mechanisms during melting around a horizontal circular cylinder,” *Int. J. Heat Mass Transf.*, vol. 25, no. 1, pp. 137–147, 1982.

[187] J. M. Khodadadi and Y. Zhang, “Effects of buoyancy-driven convection on melting within spherical containers,” *Int. J. Heat Mass Transf.*, vol. 44, no. 8, pp. 1605–1618, 2001.

[188] F. L. Tan, S. F. Hosseinizadeh, J. M. Khodadadi, and L. Fan, “Experimental and computational study of constrained melting of phase change materials (PCM) inside a spherical capsule,” *Int. J. Heat Mass Transf.*, vol. 52, no. 15–16, pp. 3464–3472, 2009.

[189] I. Harary, V. Dubovsky, E. Assis, G. Ziskind, and R. Letan, “Solidification of subcooled gallium poured into a vertical cylindrical mold,” *Int. J. Thermodyn.*, vol. 19, no. 1, pp. 36–41, 2016.

[190] R. E. Simons, V. W. Antonetti, W. Nakayama, and S. Oktay, “Heat Transfer in Electronic Packages,” in *Microelectronics Packaging Handbook*, Springer, Boston, MA, 1997, pp. 314–403.

[191] T. Mahzabeen, “An Investigation of Manganese Macro segregation in Cast Dual Phase Steels using Micro X-ray Fluorescence Spectroscopy,” University of Waterloo, 2017.

[192] D. R. Poirier, “Densities of Pb-Sn alloys during solidification,” *Metall. Trans. A*, vol. 19, no. 9, pp. 2349–2354, Sep. 1988.

[193] D. J. Hebditch and J. D. Hunt, “Observations of ingot macrosegregation on model systems,” *Metall. Trans.*, vol. 5, no. 7, pp. 1557–1564, 1974.

[194] S. N. Ojha, G. Ding, Y. Lu, J. Reye, and S. N. Tewari, “Macrosegregation caused by thermosolutal convection during directional solidification of Pb-Sb alloys,” *Metall. Mater. Trans. A*, vol. 30, no. 8, pp. 2167–2171, 1999.

[195] V. Laxmanan, “Bulk undercooling, nucleation, and macrosegregation of Pb-Sn alloys,” *Metall. Trans. A*, vol. 19, no. 11, pp. 2651–2658, 1988.

[196] S. N. Tewari and R. Shah, “Macrosegregation during dendritic arrayed growth of hypoeutectic Pb-Sn alloys: influence of primary arm spacing and mushy zone length,” *Metall. Mater. Trans. A*, vol. 27, no. 5, pp. 1353–1362, 1996.

[197] N. Streat and F. Weinberg, “Macrosegregation during solidification resulting from density differences in the liquid,” *Metall. Trans.*, vol. 5, no. 12, pp. 2539–2548, 1974.

[198] L. Hachani *et al.*, “Experimental analysis of the solidification of Sn–3 wt.%Pb alloy under natural convection,” *Int. J. Heat Mass Transf.*, vol. 55, no. 7, pp. 1986–1996, Mar. 2012.

[199] N. Ahmad *et al.*, “Numerical simulation of macrosegregation: a comparison between finite volume method and finite element method predictions and a confrontation with experiments,” *Metall. Mater. Trans. A*, vol. 29, no. 2, pp. 617–630, 1998.

[200] B. Xu, P. Li, and C. Chan, “Application of phase change materials for thermal energy storage in concentrated solar thermal power plants: a review to recent developments,” *Appl. Energy*, vol. 160, pp. 286–307, 2015.

[201] S. Li, J. Zhang, and P. Wu, “A comparative study on migration of a planar interface during solidification of non-dilute alloys,” *J. Cryst. Growth*, vol. 312, no. 7, pp. 982–988, Mar. 2010.

[202] J. A. Kittl, P. G. Sanders, M. J. Aziz, D. P. Brunco, and M. O. Thompson, “Complete experimental test of kinetic models for rapid alloy solidification,” *Acta Mater.*, vol. 48, no. 20, pp. 4797–4811, Dec. 2000.

[203] J. A. Kittl, M. J. Aziz, D. P. Brunco, and M. O. Thompson, “Nonequilibrium partitioning during rapid solidification of Si As alloys,” *J. Cryst. Growth*, vol. 148, no. 1–2, pp. 172–182, 1995.

[204] M. Gupta and S. Ling, “Microstructure and mechanical properties of hypo/hyper-eutectic Al–Si alloys synthesized using a near-net shape forming technique,” *J. Alloys Compd.*, vol. 287, no. 1–2, pp. 284–294, 1999.

[205] S. Tomida, K. Nakata, S. Shibata, I. Zenkouji, and S. Saji, “Improvement in wear resistance of hyper-eutectic Al Si cast alloy by laser surface remelting,” *Surf. Coat. Technol.*, vol. 169, pp. 468–471, 2003.

[206] P. Magnin and R. Trivedi, “Eutectic growth: A modification of the Jackson and Hunt theory,” *Acta Metall. Mater.*, vol. 39, no. 4, pp. 453–467, 1991.

[207] S. Qiu *et al.*, “Process parameters influence on the growth rate during silicon purification by vacuum directional solidification,” *Vacuum*, vol. 125, pp. 40–47, 2016.

[208] M. J. Assael, I. J. Armyra, J. Brillo, S. V. Stankus, J. Wu, and W. A. Wakeham, “Reference data for the density and viscosity of liquid cadmium, cobalt, gallium, indium, mercury, silicon, thallium, and zinc,” *J. Phys. Chem. Ref. Data*, vol. 41, no. 3, p. 033101, 2012.

[209] J. S. Langer and J. Müller-Krumbhaar, “Stability effects in dendritic crystal growth,” *J. Cryst. Growth*, vol. 42, pp. 11–14, 1977.

[210] W. Kurz and D. J. Fisher, “Dendrite growth at the limit of stability: tip radius and spacing,” *Acta Metall.*, vol. 29, no. 1, pp. 11–20, 1981.

[211] E. Toyserkani, A. Khajepour, and S. F. Corbin, *Laser cladding*. CRC press, 2004.

[212] S. Akamatsu, S. Bottin-Rousseau, G. Faivre, and E. A. Brener, “Scaling theory of two-phase dendritic growth in undercooled ternary melts,” *Phys. Rev. Lett.*, vol. 112, no. 10, p. 105502, 2014.

[213] M. B. Amar and E. Brener, “Theory of pattern selection in three-dimensional nonaxisymmetric dendritic growth,” *Phys. Rev. Lett.*, vol. 71, no. 4, p. 589, 1993.

[214] R. Elliott and S. M. D. Glenister, “The growth temperature and interflake spacing in aluminium silicon eutectic alloys,” *Acta Metall.*, vol. 28, no. 11, pp. 1489–1494, 1980.

[215] J.-M. Liu and B.-L. Shang, “Theory and experiments on irregular eutectic growth: investigation on Al-Si eutectic growth,” *J. Mater. Sci.*, vol. 27, no. 8, pp. 2067–2074, 1992.

[216] L. M. Hogan and H. Song, “Interparticle spacings and undercoolings in Al-Si eutectic microstructures,” *Metall. Mater. Trans. A*, vol. 18, no. 4, pp. 707–713, 1987.

[217] S. Shivkumar, L. Wang, and D. Apelian, “Molten metal processing of advanced cast aluminum alloys,” *JOM*, vol. 43, no. 1, pp. 26–32, 1991.

[218] M. Drouzy and M. Richard, “Effet des conditions de solidification sur la qualité des alliage de fonderie de A-U5 GT et A-S7 G, estimation des caractéristiques mécaniques,” *Fonderie.*, vol. 285, 1969.

[219] A. D. Pelton and W. T. Thompson, “Phase diagrams,” *Prog. Solid State Chem.*, vol. 10, pp. 119–155, 1975.

Annex 1 Example of TDB file

Example TDB file used into our software Phase Diagram to construct the Ag-Cu phase diagram

```
$ Database file written 2009-12- 3
$ From database: USER
$......................................................... mass [g/mol]       enthalpy_298    entropy_298
ELEMENT VA   VACUUM                  0.0000E+00      0.0000E+00         0.0000E+00!
 ELEMENT AG   FCC_A1                 1.0787E+02       5.7446E+03         4.2551E+01!
 ELEMENT CU   FCC_A1                 6.3546E+01      5.0041E+03         3.3150E+01!
 FUNCTION GHSERAG    2.98150E+02  -7209.512+118.202013*T-23.8463314*T*LN(T)
     -.001790585*T**2-3.98587E-07*T**3-12011*T**(-1);  1.23493E+03  Y
      -15095.252+190.266404*T-33.472*T*LN(T)+1.412E+29*T**(-9);  3.00000E+03       N !
 FUNCTION GHSERCU    2.98150E+02  -7770.458+130.485235*T-24.112392*T*LN(T)
     -.00265684*T**2+1.29223E-07*T**3+52478*T**(-1);  1.35777E+03  Y
      -13542.026+183.803828*T-31.38*T*LN(T)+3.642E+29*T**(-9);  3.20000E+03       N !
 FUNCTION UN_ASS 298.15 0; 300 N !
 TYPE_DEFINITION % SEQ *!
 DEFINE_SYSTEM_DEFAULT ELEMENT 2 !
 DEFAULT_COMMAND DEF_SYS_ELEMENT VA /- !
 PHASE LIQUID:L %  1  1.0  !
    CONSTITUENT LIQUID:L :AG,CU :  !
   PARAMETER G(LIQUID,AG;0)  2.98150E+02  +11025.076-8.891021*T
  -1.034E-20*T**7+GHSERAG#;  1.23508E+03  Y
   +11508.141-9.301747*T-1.412E+29*T**(-9)+GHSERAG#;  3.00000E+03  N  !
   PARAMETER G(LIQUID,CU;0)  2.98150E+02  +12964.736-9.511904*T
  -5.849E-21*T**7+GHSERCU#;  1.35802E+03  Y
   +13495.481-9.922344*T-3.642E+29*T**(-9)+GHSERCU#;  3.20000E+03  N !
   PARAMETER G(LIQUID,AG,CU;0)  2.98150E+02  +17323.4-4.46819*T;
  6.00000E+03   N  !
   PARAMETER G(LIQUID,AG,CU;1)  2.98150E+02  +1654.38-2.35285*T;
  6.00000E+03   N  !
 TYPE_DEFINITION & GES A_P_D FCC_A1 MAGNETIC  -3.0    2.80000E-01 !
 PHASE FCC_A1  %&  2 1    1 !
    CONSTITUENT FCC_A1  :AG%,CU% : VA :  !
   PARAMETER G(FCC_A1,AG:VA;0)  2.98150E+02  +GHSERAG#;   6.00000E+03   N
   PARAMETER G(FCC_A1,CU:VA;0)  2.98150E+02  +GHSERCU#;   6.00000E+03   N
   PARAMETER G(FCC_A1,AG,CU:VA;0)  2.98150E+02  +36061.88-10.44288*T;
  6.00000E+03   N !
   PARAMETER G(FCC_A1,AG,CU:VA;1)  2.98150E+02  -4310.12;   6.00000E+03   N   !
```

Annex 2 Phase Diagram Software

Main menu with 6 submenus.

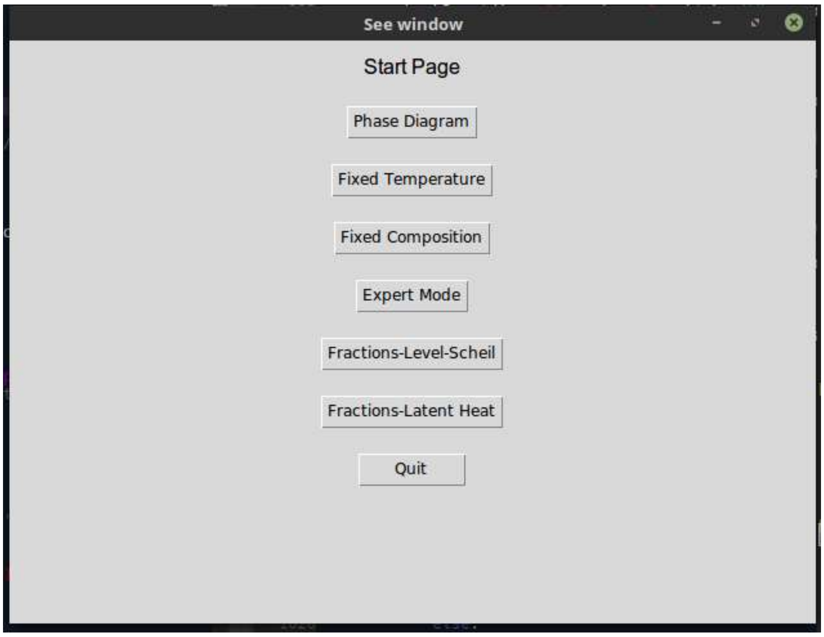

Submenu Phase Diagram used to generate the phase diagram.

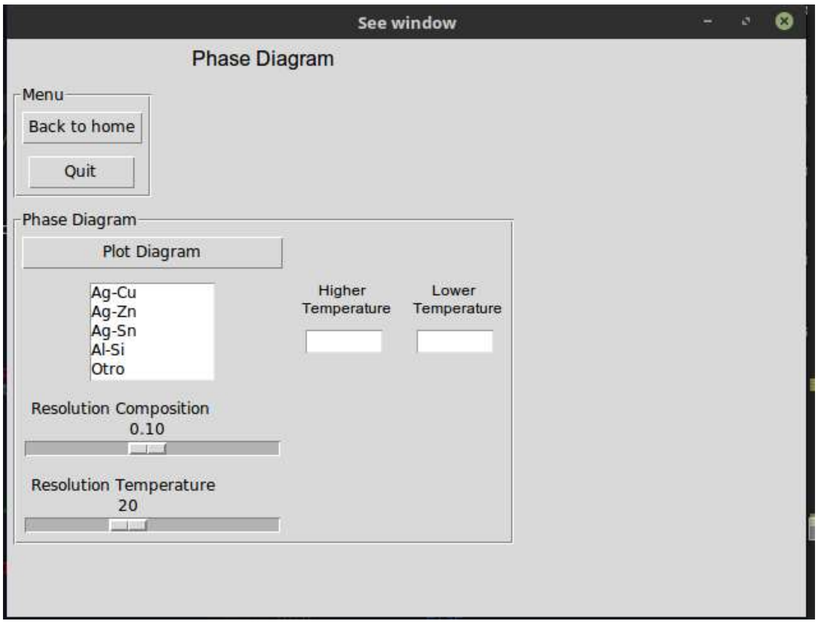

Resolution Composition
0.10

Resolution Temperature
20

Submenu Phase Diagram, Selection of binary alloy from the database SGTE, range of temperature and resolution of composition and temperature.

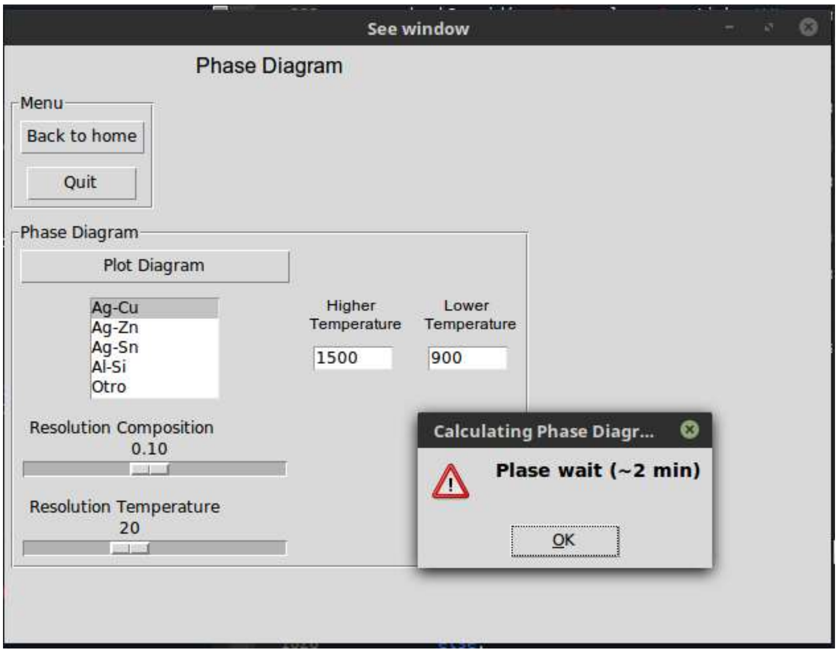

Higher Temperature 1500

Lower Temperature 900

Resolution Composition 0.10

Resolution Temperature 20

Calculating Phase Diagr...

Plase wait (~2 min)

Submenu Phase diagram; Phase diagram result.

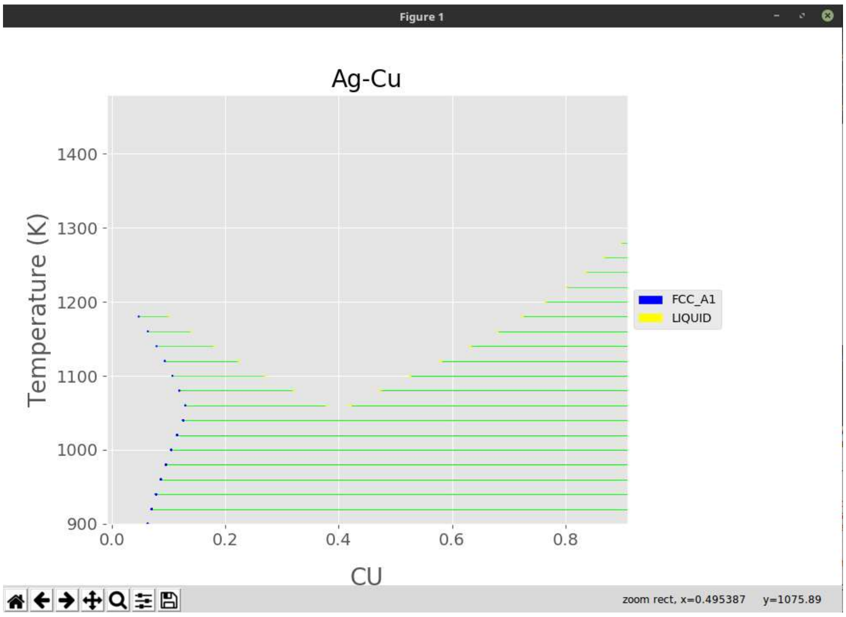

Submenu Fixed composition. With a fixed composition and selected binary alloy the Giibbs free energy, enthalpy, chemical potential, heat capacity and liquid fraction are traced in function of temperature.

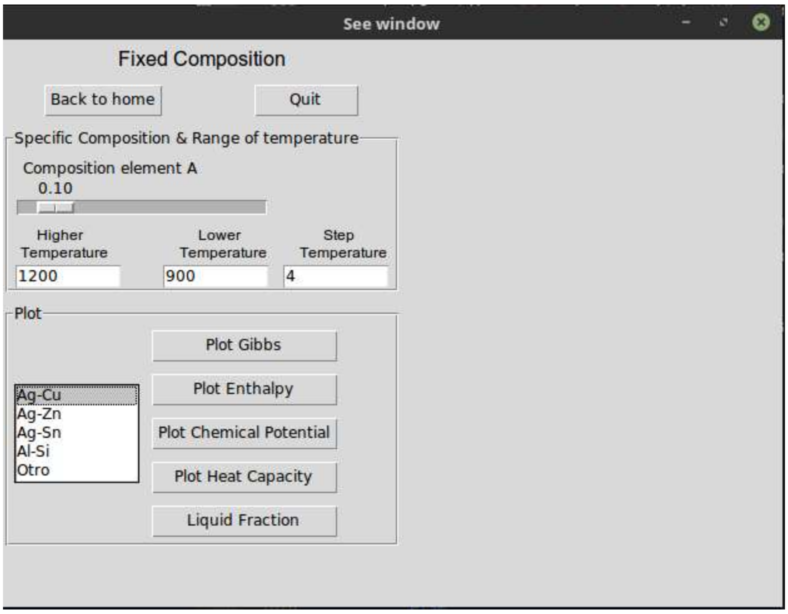

See window

Fixed Composition

Specific Composition & Range of temperature

Composition element A 0.10

Higher Temperature 1200

Lower Temperature 900

Step Temperature 4

Plot

Submenu Fixed composition; The information generated can be exported in a txt file.

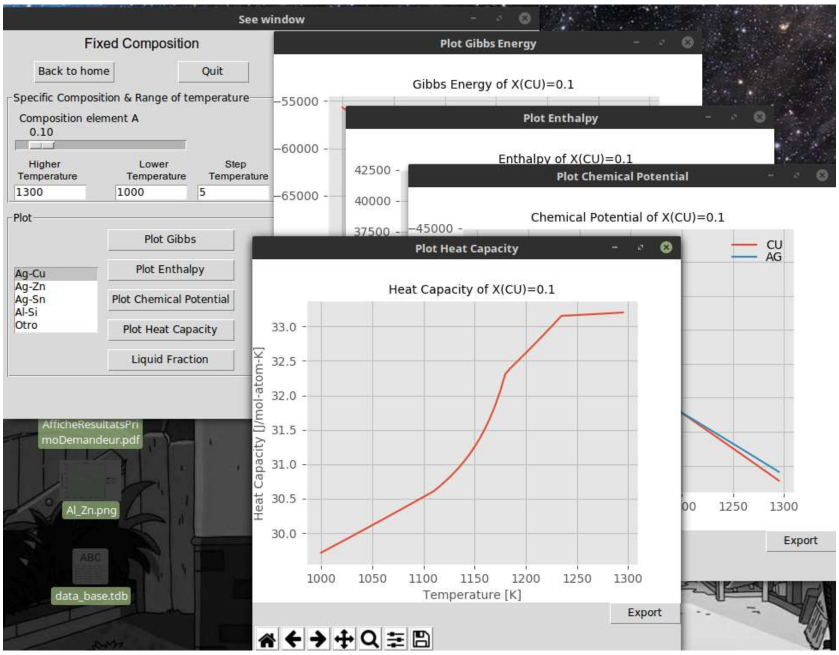

See window

Fixed Composition

Specific Composition & Range of temperature

Composition element A 0.10

Higher Temperature 1300

Lower Temperature 1000

Step Temperature 5

Submenu Expert mode. Based in the theory of Pelton [219], the phase diagram can be traced in function of 6 constants.

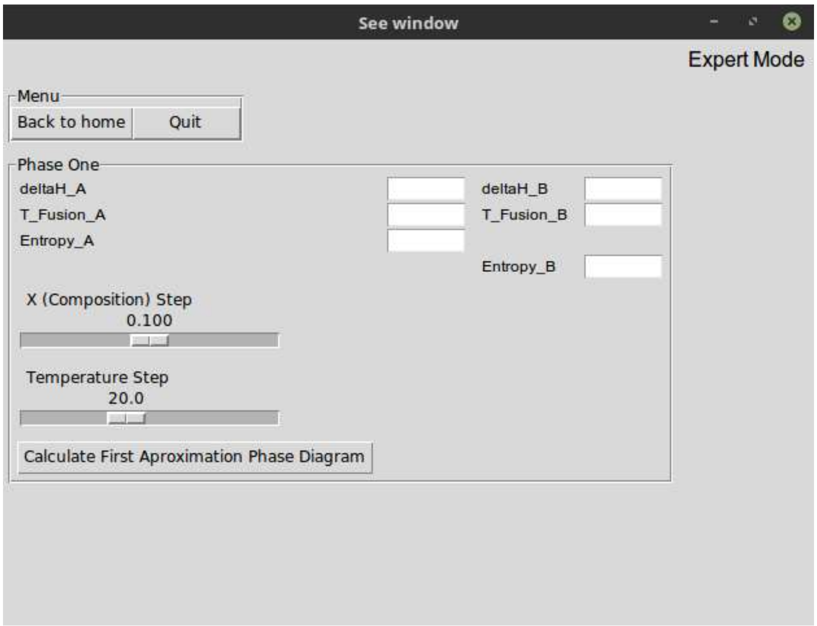

X (Composition) Step 0.100

Temperature Step 20.0

Submenu Fractions-Level-Scheil. Fixing a composition and selecting a binary alloy the lever rule and Scheil Gulliver formulation are used to compare the solidification evolution.

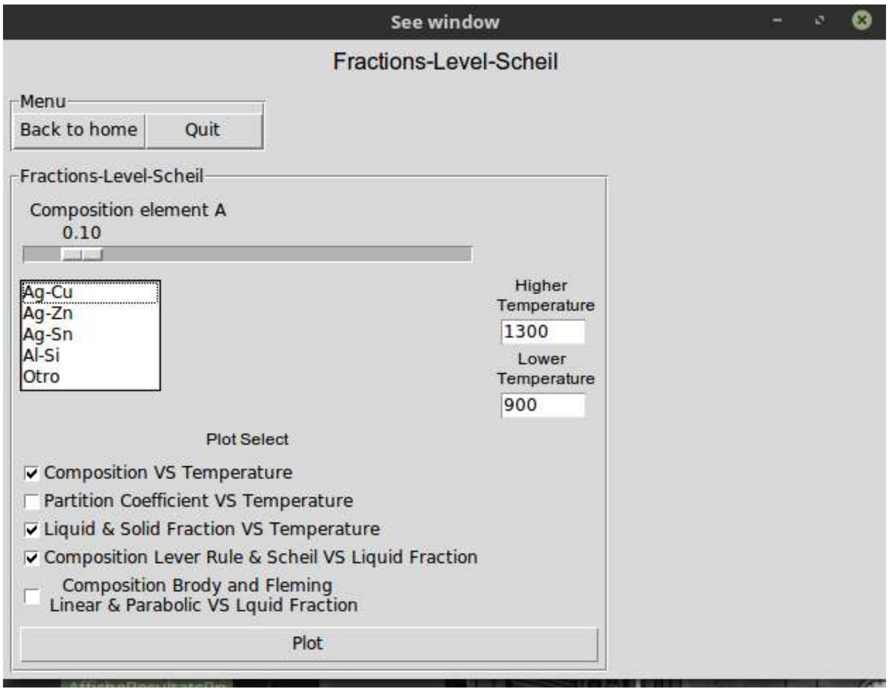

Composition element A 0.10

Higher Temperature 1300

Lower Temperature 900

☑ Composition VS Temperature
☐ Partition Coefficient VS Temperature
☑ Liquid & Solid Fraction VS Temperature
☑ Composition Lever Rule & Scheil VS Liquid Fraction
☐ Composition Brody and Fleming Linear & Parabolic VS Lquid Fraction

Submenu Fraction-Latent heat. Selecting a binary alloy and one or two initial composition the latent heat released is compared with lever rule and Scheil Gulliver formulation for the temperature range selected.

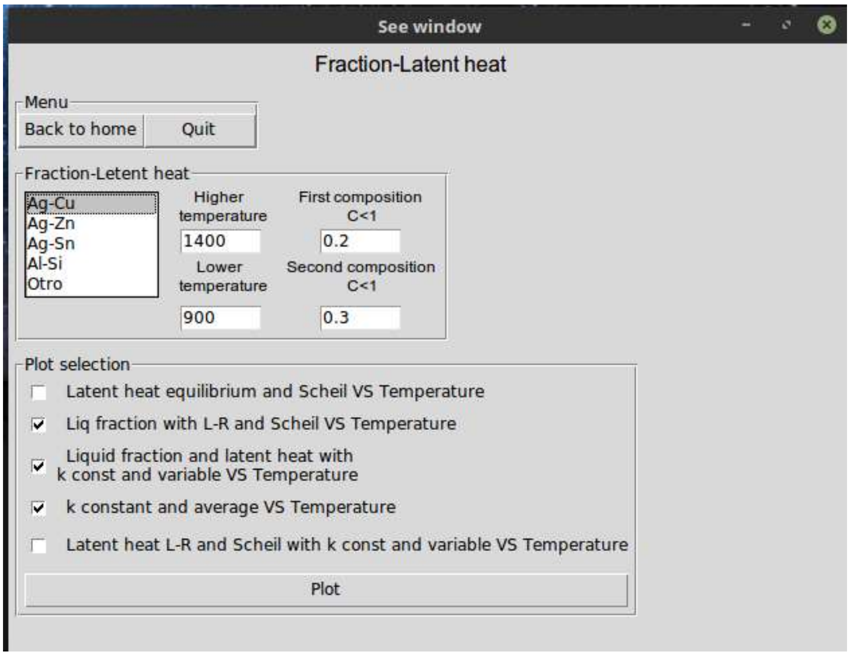

Fraction-Latent heat

Fraction-Letent heat

- Ag-Cu
- Ag-Zn
- Ag-Sn
- Al-Si
- Otro

Higher temperature: 1400

Lower temperature: 900

First composition C<1: 0.2

Second composition C<1: 0.3

Plot selection

☐ Latent heat equilibrium and Scheil VS Temperature
☑ Liq fraction with L-R and Scheil VS Temperature
☑ Liquid fraction and latent heat with k const and variable VS Temperature
☑ k constant and average VS Temperature
☐ Latent heat L-R and Scheil with k const and variable VS Temperature

Annex 3 UDF File

```
/* ======CHECKPOINTS=======
Solid_16 = Incluye para el source en Y
1. Bracket Compatibility
2. Influence of mixture terms
3. Definition of variables
4.  Define user defined memory locations
*/
/* Validation problem from Incropera
   C_UDMI(c,t,0) -- Latent heat content (delta H)
   C_UDMI(c,t,1) -- Latent heat content for last timestep
   C_UDMI(c,t,2) -- Liquid fraction
   C_UDMI(c,t,3) -- Liquid fraction for last timestep
   C_UDMI(c,t,4) -- 0 indicates solid zone
                                                    1 indicates liquid zone
   C_UDMI(c,t,5) -- Last time step temperature
*/
/* Thermal properties AlSi12
Tmelting=576°C
LH=560 000   [J/kg]
Density Al_Sol = 2712
Density Al_Liq = 2375   [at 2000 K = 2623.49]
Density Si_Sol = 2329
Density Si_Liq = 2570
Cp_Liq= 1740
Cp_Sol= 1038
Volume expansion [1/K]=63.9e-6
TherCond Al_Sol = 237   [at 933 kelvin = 208]
TherCond Al_Liq = 92.1   [at 2000 kelvin = 114]
TherCond Si_Sol = 148
TherCond Si_Liq = 50

*/
#include "udf.h"
/* =========== USER INPUTS START ================ */
#define Cmor              1.0e+07  /* Morphological Constant */
#define Tiny              0.001     /* Small number to avoid div by zero */
#define lamda             0.01      /* Relaxation factor for latent heat update */
#define TMELT             849.15    /* Eutectic point in Kelvin  at */
#define TMELT_Alu         933.15    /* in Kelvin  */
#define Latent_Heat       4.18e5     /* Latent heat in J/kg */
#define Cp_Liq                                  1740                /*  Heat capacity liquid  */
#define          Cp_Sol                                 1038                /*          Heat
capacity solid    */
#define beta_thermal      2.6e-06  /* Thermal expansion coefficient of AlSi12 */
#define startSol                       2.79                             /*  time  to  start  solidification
[seg] */
#define speedSol                       0.01                     /* solidification velocity [m/s]*/
#define speedSol_Y                     0.005                    /* solidification velocity [m/s]*/
#define deltaX                                  0.001                 /* delta X en metros*/
#define Co_Si                                   0.0148                /* Amount of silicon */
#define ke                                           0.113                 /*      Partition
coefficient */
#define mesh                                    15251     /*taille mesh node */
#define          Tliquidus                      -Co_Si*700.+TMELT_Alu;
#define          FLeutectic                     pow((TMELT_Alu-Tliquidus)/(TMELT_Alu-TMELT),1/(1-ke));
/*#define FLeutectic                   0.361322   /*taille mesh node */
/* =========== USER INPUTS END ============== */
/*=========== INITIALIZING ==============*/
/* Identify the cells in the mushy zone (initial state is either solid or liquid – write for that) */
DEFINE_INIT(initialize7,d)
{ cell_t c;
  Thread *t;
```

```
  int i;
  thread_loop_c(t,d)   /* Loop over all cell threads in domain */
  {
    begin_c_loop(c,t)  /* Loop over all cells in a cell thread*/
    {
         C_UDMI(c,t,0) = 0.;   /* Latent heat presente */
       C_UDMI(c,t,1) = 0.;   /* Latent heat pasado */
       C_UDMI(c,t,2) = 1.0;
       C_UDMI(c,t,3) = 1.0;
                          C_UDMI(c,t,4) = 2.0;  /* Liquid region */
                          C_UDMI(c,t,5) = C_T(c,t); /* last temperature */
                          C_UDMI(c,t,6) = 0.;     /*  Cooling rate  */
                          C_UDMI(c,t,7) = 0.;                /* Contador, puesto en execute at end  */
                          C_UDMI(c,t,8) = 1-Co_Si;        /* composition_liquid aluminium*/
                          C_UDMI(c,t,9) = 0.;                /* composition_solid aluminium */
                          C_UDMI(c,t,10) = Co_Si;         /* composition_liquid Si*/
                          C_UDMI(c,t,11) = 0.;              /* composition_solid Si */
                          C_UDMI(c,t,12) = 0.;              /* Liquidus temperature per node */
                          C_UDMI(c,t,13) = Co_Si;         /* composition_liquid Si OLD*/
                          C_UDMI(c,t,14) = 0.;              /* composition_solid Si OLD */
         }
    end_c_loop(c,t)
  }
}
/*=========== DEFINING SOURCE TERMS==============*/
/* X-Momentum Source Term */
DEFINE_SOURCE(x_source, c, t, dS, eqn)
{ real con, source, lfrac;
  lfrac = C_UDMI(c,t,2);
  con = -Cmor*(1.0-lfrac)*(1.0-lfrac)/((lfrac*lfrac*lfrac) + Tiny);
  source = con * C_U(c,t);     /* CHECK IF V or U which denote velocity components */
  dS[eqn] = con;
  return source;
}
/* Y-Momentum Source Term (instead of Teut write Tmelt) */
DEFINE_SOURCE(y_source, c, t, dS, eqn)
{ real con, source, lfrac, thermal;
  lfrac = C_UDMI(c,t,2);
  con = -Cmor*(1.0-lfrac)*(1.0-lfrac)/((lfrac*lfrac*lfrac) + Tiny);
  /*source = con * C_V(c,t);*/
  /* Boussinesque terms */
  thermal = C_R(c,t)*9.81*beta_thermal*(C_T(c,t)-TMELT);
  source += thermal;
  dS[eqn] = con;
  return source;
}
  /* Energy Source Term (second one is ignored as no velocity in solid zone*/
DEFINE_SOURCE(eng_source7, c, t, dS, eqn)
{ real source, timestep;
  cell_t  c0, c1;
  Thread *tc0, *tc1, *ft;
  face_t f;
  int numbf;
  timestep = RP_Get_Real("physical-time-step");
  source   = C_R(c,t)*C_UDMI(c,t,0)/timestep;   /* Check definition of latent heat content*/
  dS[eqn]=0.0;
  return source;
}
/* Defining Adjust function. Here enthalpy will be updated*/
DEFINE_ADJUST(my_adjust7, d)
{
       real timestep, timeflow,LiqF_aut, LiqFracT, LiqFracT2, Tliquidus, volume,FLeutectic;
       real x_sol;
       real x[ND_ND];
       real xval, yval;
       real source_energ;
       int n, i;
       cell_t c;
```

```
    Thread *t;
    cell_t c2;
    Thread *t2;
    int curr_ts;
    timestep = RP_Get_Real("physical-time-step");
    curr_ts= RP_Get_Integer("time-step");
    timeflow = RP_Get_Real("flow-time");
    x_sol    = speedSol*(timeflow-startSol);
    thread_loop_c(t,d)     /* Loop over all cell threads in domain*/
    {
        begin_c_loop(c,t)
        {
            C_UDMI(c,t,7) = 5000;
            C_CENTROID(x,c,t);
            xval=x[0];
            yval=x[1];
            C_UDMI(c,t,8) = xval;
            source_energ = Latent_Heat;
            LiqFracT = 0.;
            /* Calcular la fraccion que hay*/
            thread_loop_c(t2,d)
            {
                begin_c_loop(c2,t2)
                {
                    LiqFracT2 += C_UDMI(c,t,2)*C_VOLUME(c,t);
                    volume += C_VOLUME(c,t);
                }
                end_c_loop(c2,t2)
            }
            LiqFracT =LiqFracT2/ volume;
            C_UDMI(c,t,7) = 2000.;
             /* Definir si puede o no solidificar, utiliza scheil para
             calcular la cantidad de fraccion que puede solidificar*/
             if (C_T(c,t)> Tliquidus)
            {LiqF_aut=1;}
            else if (C_T(c,t)> TMELT-2)
            {LiqF_aut = pow((TMELT_Alu-Tliquidus)/(TMELT_Alu-C_T(c,t)),(1/(1-ke)));}
            else{LiqF_aut = pow((TMELT_Alu-Tliquidus)/(TMELT_Alu-TMELT),(1/(1-ke)));}
            C_UDMI(c,t,12) = LiqF_aut;
            /* Identify the cells in the mushy zone */
            if(C_UDMI(c,t,3)<=0.0001) /* Solid  region */
                {
                    C_UDMI(c,t,4) = 0.0;
                    C_UDMI(c,t,0) = 0;
                    C_UDMI(c,t,2) = 0.0;
                    C_UDMI(c,t,11) = C_UDMI(c,t,14);
                    C_UDMI(c,t,9) = 1-C_UDMI(c,t,11);
              /* Cs alu */
                }
            /* LiqFracT > FLeutectic */
            else if (C_T(c,t) <= Tliquidus && timeflow >= startSol && (xval<=x_sol || yval<=x_sol)) &&
LiqF_aut <= LiqFracT  && LiqFracT > FLeutectic && C_UDMI(c,t,3)>0.0001)
            {
                C_UDMI(c,t,4) = 5.;
                C_UDMI(c,t,0) = source_energ*speedSol*timestep/deltaX;
                C_UDMI(c,t,7) = 10;
                if (C_UDMI(c,t,0) >= source_energ)
                {
                    C_UDMI(c,t,0) = source_energ;
                    C_UDMI(c,t,7) = 20;
                }
                if ((C_UDMI(c,t,0) + C_UDMI(c,t,1)) > source_energ)
                {
                    C_UDMI(c,t,7) = 30;
                    C_UDMI(c,t,0)=source_energ-C_UDMI(c,t,1);
                }

              /* Calculate liquid fraction */
```

```
                                        C_UDMI(c,t,2) = 1-((C_UDMI(c,t,0)+C_UDMI(c,t,1)) / source_energ);
                                        C_UDMI(c,t,7) = 40;
                                        if (C_UDMI(c,t,2) <= 0)
                                                {               C_UDMI(c,t,2) = 0.0;
                                                                C_UDMI(c,t,4) = 0.0;
                                                                C_UDMI(c,t,11) = ke*Co_Si*pow(LiqFracT,ke-1);      /* Cs_Si
*/
                                                                C_UDMI(c,t,9) = 1-C_UDMI(c,t,11);
                                       /* Cs alu */
                                                                C_UDMI(c,t,10) =0.;                        /* Cl Si*/
                                                                C_UDMI(c,t,8) = 0.;                                /* Cl alu*/
                                                                C_UDMI(c,t,7) = 50;
                                        }
                                                else
                                                {
                                                                C_UDMI(c,t,11) = 0;                    /* Cs_Si  */
                                                                C_UDMI(c,t,9)  = 0;
                                         /* Cs alu */
                                                                C_UDMI(c,t,10) =  Co_Si*pow(LiqFracT,ke-1);     /* Cl Si*/
                                                                C_UDMI(c,t,8)  = 1-C_UDMI(c,t,10);            /* Cl alu*/
                                                                C_UDMI(c,t,7) = 60;
                                                }

                                       }
                                       /* Eutectic  region */
                                       else   if(C_T(c,t)   <=   (TMELT+2.)   &&   timeflow   >=   startSol   &&   xval<=x_sol   &&
C_UDMI(c,t,3)>0.0001 && LiqFracT <= FLeutectic) /* Eutectic  region */
                                                {
                                                                if (C_T(c,t) >= (TMELT-2.))
                                                                {
                                                                                C_UDMI(c,t,4) = 10;
                                                                                C_UDMI(c,t,0)                                    =
lamda*C_CP(c,t)*(C_UDMI(c,t,5)-C_T(c,t));
                                                                                if (C_UDMI(c,t,0)< 0)
                                                                                                {C_UDMI(c,t,0) =  0.0;}
                                                                                else
                                                                                {
                                                                                if    ((C_UDMI(c,t,0)    +    C_UDMI(c,t,1))    >=
source_energ)

         {C_UDMI(c,t,0)=source_energ-C_UDMI(c,t,1);}
                                                                                }
                                                                }
                                                                else
                                                                {
                                                                                C_UDMI(c,t,7) = 70;
                                                                                C_UDMI(c,t,0)                                    =
source_energ*speedSol*timestep/deltaX;
                                                                                if (C_UDMI(c,t,0) >= source_energ)
                                                                                                {
                                                                                                C_UDMI(c,t,0)                    =
source_energ;
                                                                                                C_UDMI(c,t,7) = 73;
                                                                                                }
                                                                                if    ((C_UDMI(c,t,0)    +    C_UDMI(c,t,1))    >
source_energ)
                                                                                                {
                                                                                                C_UDMI(c,t,7) = 75;

         C_UDMI(c,t,0)=source_energ-C_UDMI(c,t,1);
                                                                                                }
                                                                }
                                                                /* ------------Calculate liquid fraction-------------------------- */
                                                                C_UDMI(c,t,2)     =     1-((C_UDMI(c,t,0)+C_UDMI(c,t,1))     /
source_energ);
                                                                if (C_UDMI(c,t,2) <= 0)  /*---ya es solido---*/
                                                                                {C_UDMI(c,t,2) = 0.0;
                                                                                C_UDMI(c,t,4) = 0.0;
```

```
                                                        C_UDMI(c,t,11) = Co_Si;          /* Cs_Si  */
                                                        C_UDMI(c,t,9) = 1-C_UDMI(c,t,11);   /* Cs alu
*/
                                                        C_UDMI(c,t,10) =0.;                        /*     Cl
Si*/
                                                        C_UDMI(c,t,8) = 0.;
         /* Cl alu*/
                                                        C_UDMI(c,t,7) = 80;
                                                        }
                                                 else   /* es eutectico*/
                                                 {
                                                        C_UDMI(c,t,11) = 0.;
                              /* Cs_Si  */
                                                        C_UDMI(c,t,9) = 0.;
                              /* Cs alu */
                                                        C_UDMI(c,t,10) = Co_Si;;            /* Cl Si*/
                                                        C_UDMI(c,t,8)      =          1-C_UDMI(c,t,8);
       /* Cl alu*/
                                                        C_UDMI(c,t,7) = 90;
                                                 }

                                          }


                              else    /* Liquid region */
                                          {
                                          C_UDMI(c,t,0) =  0.0;
                                          C_UDMI(c,t,4) = 20;
                                          C_UDMI(c,t,7) = 100;
                                          if (C_T(c,t)>Tliquidus && C_UDMI(c,t,2)==1.)
                                          {
                                                 C_UDMI(c,t,11) = 0.;          /* Cs_Si  */
                                                 C_UDMI(c,t,9) = 0.;    /* Cs alu */
                                                 C_UDMI(c,t,10) = Co_Si;;                /* Cl Si*/
                                                 C_UDMI(c,t,8) =  1-C_UDMI(c,t,8);
         /* Cl alu*/
                                                 C_UDMI(c,t,7) = Tliquidus;
                                          }
                                          else
                                          {
                                                 C_UDMI(c,t,11) = 0;                     /* Cs_Si  */
                                                 C_UDMI(c,t,9)  = 0;
                               /* Cs alu */
                                                 C_UDMI(c,t,10) = Co_Si*pow(LiqFracT,ke-1);      /* Cl Si*/
                                                 C_UDMI(c,t,8)  = 1-C_UDMI(c,t,10);           /* Cl alu*/
                                                 C_UDMI(c,t,7) = FLeutectic;
                                                 C_UDMI(c,t,2) = C_UDMI(c,t,3);
                                          }
                                          }
                              C_UDMI(c,t,6) = (C_T(c,t) - C_UDMI(c,t,5))/timestep;
                       }
        end_c_loop(c,t)
     }
   }
   DEFINE_EXECUTE_AT_END(execute_at_end)
   {
    Domain *d;
    Thread *t;
    cell_t c;
    d = Get_Domain(1);   /* single phase*/

    thread_loop_c (t,d)
      {
         begin_c_loop (c,t)
                              C_UDMI(c,t,1) += C_UDMI(c,t,0);
                              C_UDMI(c,t,3) = C_UDMI(c,t,2);
                              C_UDMI(c,t,5) = C_T(c,t);
                              C_UDMI(c,t,13) = C_UDMI(c,t,10);              /* composition_liquid Si OLD*/
```

```
                                   C_UDMI(c,t,14) = C_UDMI(c,t,11);                  /* composition_solid Si OLD */

        end_c_loop (c,t)
    }
}
/*=========== DEFINE PROPERTY==============*/
DEFINE_PROPERTY(cell_conductivity,c,t)
{
real k_cond,k_cond_s_Si,k_cond_l_Si,k_cond_s_Al,k_cond_l_Al;
k_cond_s_Si = 148.0;
k_cond_l_Si = 50.0;
k_cond_s_Al = 237.0;
k_cond_l_Al = 92.1;
real k_cond_l ;
real k_cond_s ;
k_cond_l = (C_UDMI(c,t,8)*k_cond_l_Al)+((1-C_UDMI(c,t,8))*k_cond_l_Si);
k_cond_s = (C_UDMI(c,t,9)*k_cond_s_Al)+((1-C_UDMI(c,t,9))*k_cond_s_Si);
if (C_UDMI(c,t,2) > 0.0001)
        {k_cond = k_cond_l*C_UDMI(c,t,2) + (1.-C_UDMI(c,t,2))*k_cond_s*0.9;
        }
else
        {k_cond = k_cond_s;}
return k_cond;
}
DEFINE_PROPERTY(cell_viscosity,c,t)
{
real mu_lam, mu_liq;
mu_liq = 3.233e-3; /* value aluminium viscosity*/
if (C_UDMI(c,t,2) > 0.0001)
        {mu_lam = mu_liq + (1.-mu_liq)*pow(C_UDMI(c,t,2),3)*(6*pow(C_UDMI(c,t,2),2)-8*C_UDMI(c,t,2)+3);
        }
else
        {mu_lam = 1e4;}
return mu_lam;
}
DEFINE_SPECIFIC_HEAT(my_cp,T)
{
real cp;
if (Co_Si == 0.12)
{
        if (T > 576.0+2.)
                        cp = Cp_Liq;
        else if (T > 576.)
                        cp = 0.5*(0.5*Latent_Heat+Cp_Liq+Cp_Sol);
        else
                        cp = Cp_Sol;
}
else
{
        if (T > 576.0+2.)
                        cp = Cp_Liq;
        else if (T > 576.)
                        cp = 0.5*(0.5*C_UDMI(c,t,2)*Latent_Heat+Cp_Liq+Cp_Sol);
        else
                        cp = Cp_Sol;
                        C_UDMI(c,t,2)=0.0;
}
return cp;
}
/**************************************************************************
UDF that computes specific heat and sets the sensible enthalpy
to the referenced value
***************************************************************************/

/*************************
/****Parafine*********
#include "udf.h"
DEFINE_SPECIFIC_HEAT(my_cp,T)
```

```
    {

    real cp;
    if (T > 288.)
        cp = 2800.;
    else if (T > 286.)
        cp = 47500.*T-3.e-6;
    else
        cp = 2000.;
    printf("Valor Cp= %f",cp);

    return cp;
    }
    ****************/

    #include "udf.h"
    /* =========== USER INPUTS START ================ */
    #define TEUT                849.15    /* Eutectic point in Kelvin  at */
    #define TMELT_Alu           933.15    /* in Kelvin  */
    #define Latent_Heat_T       4.67e5                    /* Latent heat in J/kg */
    #define LB                                                          1.80e6                    /*
        LH Si*/
    #define LA                                                          3.97e5                    /*           LH
Aluminium*/
    #define Cp_Liq                                              1740                    /*  Heat capacity liquid  */
    #define             Cp_Sol                                          1038                    /*          Heat
capacity solid    */
    #define Co_Si                                               0.05                    /* Amount of silicon */
    #define ke                                                          0.14                    /*      Partition
coefficient */
    /* =========== USER INPUTS END ============== */

    DEFINE_SPECIFIC_HEAT(my_cp,T)
    {
    real cp, LH, fl_L;
    if (Co_Si == 0.12)
    {
        if (T > 576.0+2.)
                    cp = Cp_Liq;
        else if (T > 576.)
                    LH=(LB-LA)*Co_Si+LA;
                    cp = 0.5*((1/2)*LH+Cp_Liq+Cp_Sol);
        else
                    cp = Cp_Sol;
    }
    /*=======Lineal========*/
    fl_L=(TL-T)/(TL-TEUT)
    /* ======Equilibirum=====*/
    else
    {
        if (T > 576.0+2.)
                    cp = Cp_Liq;
        else if (T > 576.)
                    cp = 0.5*((1/2)**Latent_Heat+Cp_Liq+Cp_Sol);
        else
                    cp = Cp_Sol;
                    C_UDMI(c,t,2)=0.0;
    }
    return cp;
    }
    /*
    DEFINE_SPECIFIC_HEAT(my_cp,T)
    {
    real cp;
    if (Co_Si == 0.12)
    {
        if (T > 576.0+2.)
                    cp = Cp_Liq;
```

```
	else if (T > 576.)
			cp = 0.5*(0.5*Latent_Heat+Cp_Liq+Cp_Sol);
	else
			cp = Cp_Sol;
}
else
{	if (T > 576.0+2.)
			cp = Cp_Liq;
	else if (T > 576.)
			cp = 0.5*(0.5*C_UDMI(c,t,2)*Latent_Heat+Cp_Liq+Cp_Sol);
	else
			cp = Cp_Sol;
			C_UDMI(c,t,2)=0.0;
}
return cp;
}  */
```

Thermal storage modeling in phase change binary alloy materials submitted to a controlled cooling rate

The thesis focuses on the numerical modeling of a binary alloy to simulate the phase change behavior for thermal energy storage and discharge application. It includes effects of cooling rate, solidification rate, segregation, free convection and undercooling. The aim is to optimize the material heat storage capacity. In the present work, the temperature range for which phase change occurs are estimated thanks to the phase diagram of a binary alloy and the CALPHAD methodology, that return the phases of an alloy, including isothermal transformation. The Gibbs free energy minimization is computed in a homemade numerical code and gives the steady phases. For a given temperature range, the code supplies the heat discharge and the corresponding alloy composition for equilibrium and off equilibrium situations. In the present method, first, the system cooling rate gives the solidification rate. This latter leads to the relation between the global kinetics and the microstructure. From the local off-equilibrium model, that depends on the partition coefficient variation and the operating cooling rate, the undercooling degree is predicted. With data from bibliography, numerical comparisons are carried out to ensure the relevance of our numerical code and to identify the heat released during several materials phase change, including specific phenomena, such as undercooling and recalescence.

Keywords: Latent heat, thermal energy storage, CALPHAD, phase change, undercooling, cooling rate, solidification rate, segregation, alloy phase change, Gibbs energy, phase diagramme

Modélisation du stockage de chaleur par changement de phase d'alliages à composition binaire soumis à un refroidissement contrôlé

La thèse est centrée sur la modélisation de la physique du comportement d’un alliage binaire et l’implémentation du meilleur modèle mathématique pour simuler le changement de phase liquide solide en tenant compte de la vitesse de refroidissement, la vitesse de solidification, la ségrégation, la convection naturelle et la surfusion afin d’optimiser la capacité de stockage de chaleur d'un tel matériau. Dans le présent travail, les températures pour lesquelles le changement de phase s'opère sont estimées grâce aux diagrammes des phases et la méthodologie CALPHAD qui retraduisent les différentes phases d'un alliage binaire, y compris la transformation isotherme. Pour cela, la minimisation de l'énergie de Gibbs est résolue dans un code de calcul développé à cette occasion et aboutit à l'identification des phases stables du matériau. Pour un intervalle de température souhaite le code permet d'estimer rapidement la décharge de chaleur pour la composition de l'alliage sélectionné en équilibre ou hors équilibre. Dans la méthode proposée, la vitesse de refroidissement du système permet de calculer la vitesse de solidification. Puis, celle-ci établit la relation entre la cinétique globale et la microstructure. Basé sur le modèle de non-équilibre local, qui dépend de la variation du coefficient de partition, le degré de surfusion est prédit à partir de la vitesse de refroidissement appliquée. Une étude bibliographique a été réalisée pour amener une comparaison numérique et assurer la capacité de notre méthode à reproduire le changement de phase, en incluant des phénomènes spécifiques tels que la surfusion et la recalescence.

Mots clés: Chaleur latent, stockage d’énergie thermique, CALPHAD, changement de phase, surfusion, vitesse de refoidissement, vitesse de solidification, segregation, changement de phase des alliages, énergie de Gibbs, diagramme de phase.

I2M - Institut de mécanique et d'ingénierie
Université de Bordeaux
ENSCBP bât A, 16 avenue Pey-Berland, 33607 PESSAC Cedex